Université catholique de Louvain

Faculté des Sciences

Département de Physique

The interior structure of terrestrial planets
An application to Mars

Attilio Rivoldini

Thèse présentée en vue de l'obtention du grade de
Docteur en Sciences

Janvier 2012

À mon père

Remerciements

Je tiens à remercier les différentes personnes qui ont rendu ce travail possible. En premier, je remercie Véronique Dehant qui a accepté d'encadrer cette thèse et de m'avoir ainsi permis de travailler dans ce domaine passionnant. Ses conseils, sa disponibilité et son expérience dans ce domaine de recherche m'ont permis de mener ce travail à bien. Je remercie particulièrement Tim Van Hoolst pour son grand investissement dans l'encadrement de ma thèse, nos nombreuses discussions, ainsi que ses nombreux conseils et sa disponibilité.

Je tiens à remercier les membres de mon jury, Yves Félix, Véronique Dehant, Tim Van Hoolst, Jean-Pierre Antoine, Pascale Defraigne, Michel Menvielle et Antoine Mocquet, d'avoir accepté ce rôle et d'avoir lu en détail mon manuscrit.

Une partie importante de ce travail est le fruit des nombreuses réunions de travail que j'ai partagées avec les autres membres du Mars Interior Network Team (MINT). Dans ce contexte, je remercie Gaël Choblet, Véronique Dehant, Tim Van Hoolst, Michel Menvielle, Antoine Mocquet, Pascal Tarits, Pierre Vacher et Olivier Verhoeven.

Je remercie particulièrement aussi mes collègues de bureau avec qui j'ai eu de nombreuses discussions intéressantes et enrichissantes: Antony, Aurélien, Laurence, Marie, Mikael, Olivier, Ozgür, Pascale, Pascal et Sébastien.

Je pense ensuite à toutes ces personnes qui participent à l'ambiance de l'Observatoire et qui en font un endroit agréable pour travailler. Un grand merci à Alexis, Antony, Aurélien, Bogdan, Justine, Laurence, Lébi, Matt, Maria, Michel, Mikael, Nicolas, Ozgür, Pascal, Quentin, Rose-Marie, Sébastien, ainsi qu'à ceux qui ont séjourné à l'Observatoire plus ou moins longtemps pendant la durée de ma thèse: Gregor, Jacques, les deux Nicolas, les deux Olivier, Sandrine, Séverine, Sébastien, Stéphanie et Valéry.

Enfin, je souhaite également adresser mes remerciements à mes parents, ma famille et à mes amis pour leur soutien, leurs encouragements et leur présence et tout spécialement à Claude qui m'a soutenu avec patience durant ces années de travail.

Contents

Preface **1**

I Global models from geodetic data **13**

1 Introduction **15**

2 Interior structure equations **17**
2.1 Governing equations 17
2.2 Practical considerations 20
2.2.1 Initial singularity 20
2.2.2 Reformulation of boundary value problems into standard forms . 21

3 The crust and the mantle **23**
3.1 The Crust 23
3.2 The mineralogy of the mantle 24
3.3 Temperature inside the mantle 29
3.4 Thermodynamics of the mantle 29
3.5 The electrical conductivity of the mantle 35
3.6 Electromagnetic induction 36
3.6.1 Introduction 36
3.6.2 Assumptions of the Magneto induction method 37
3.6.3 Applications 38
3.6.4 The conductivity of the Earth's mantle 43
3.7 Modeling uncertainties due to laboratory measurement errors 48
3.7.1 Uncertainties on electromagnetic and elastic laboratory constants 48
3.7.2 Monte-Carlo error propagation 48
3.7.3 Conclusions 49

4 The core **53**
4.1 Introduction 53
4.2 Core composition of terrestrial planets 55
4.3 Thermodynamics and equations of state for the solid core 58
4.4 Modeling the liquid core 61
4.4.1 Introduction 61
4.4.2 Solution modeling 62
4.4.3 Solution models for the fluid part of planetary cores 64
4.5 Melting 75

4.5.1 Introduction . . . 75
4.5.2 Melting data . . . 77
4.5.3 Melting laws . . . 79
4.5.4 Practical melting law . . . 85
4.5.5 Differentiation of the core of Mars . . . 89
4.6 Liquid core versus solid core . . . 90
4.7 Modeling uncertainties due to error-bound laboratory measurements . . . 93
4.7.1 Uncertainties on EoS parameters . . . 93
4.7.2 Monte Carlo error propagation . . . 94
4.7.3 Conclusions . . . 94

5 Tides **99**
5.1 Introduction . . . 99
5.2 Love Numbers . . . 99
5.3 Governing equations . . . 100
5.3.1 Linear perturbation . . . 102
5.3.2 Scalar equations . . . 104
5.3.3 The static solution . . . 107
5.3.4 Numerical integration . . . 109
5.3.5 Analytical solutions . . . 111
5.4 Phenomenology of deformation . . . 112
5.5 Non elastic rheology and dissipation . . . 112
5.5.1 From elasticity to viscoelasticity . . . 113
5.5.2 Global dissipation and Q . . . 114
5.6 Love number menagerie . . . 116
5.6.1 Planet size and average composition . . . 116
5.6.2 Forcing period . . . 118
5.6.3 Solid core size . . . 120
5.6.4 Liquid core size . . . 122
5.6.5 Inner core size . . . 124
5.6.6 Relative parameter influence . . . 127

6 The interior structure of Mars **131**
6.1 Introduction . . . 131
6.2 Chemical composition . . . 133
6.2.1 Meteorites, chondrites, and SNC meteorites . . . 134
6.2.2 Mars bulk models . . . 135
6.3 Thermal state . . . 137
6.4 The mineralogy of the mantle . . . 139
6.5 Models for the interior structure of Mars . . . 145
6.6 Discussion and conclusions . . . 156

II Mantle models from combined geophysical data sets **157**

7 Introduction **159**

8 Bayesian Inversion **163**
8.1 Introduction . . . 163
8.2 Bayesian inference . . . 165
8.2.1 The basics . . . 165
8.2.2 Inverting conditional probabilities . . . 167
8.2.3 Expectations . . . 168
8.2.4 Functions of random variables . . . 169
8.2.5 The Likelihood function . . . 170
8.2.6 Priors . . . 173
8.2.7 The posterior distribution . . . 174
8.2.8 Examples . . . 175
8.3 Sampling probability distributions . . . 185
8.3.1 Pseudo-random-numbers . . . 185
8.3.2 The inverse sampler . . . 185
8.3.3 The rejection sampler . . . 186
8.3.4 MCMC samplers . . . 186
8.4 An illustrative example . . . 194
8.4.1 Forward problem . . . 194
8.4.2 Direct inversion . . . 195
8.4.3 Bayesian inversion . . . 197
8.4.4 Sampling and other practical considerations . . . 198
8.4.5 Results . . . 201
8.4.6 Wrap up . . . 203

9 Joint inversion of electromagnetic, geodetic, and seismic data **207**
9.1 Introduction . . . 207
9.2 The forward problem and the model parameters . . . 208
9.3 The data . . . 211
9.4 The posterior probability density function . . . 214
9.4.1 The likelihood . . . 214
9.4.2 The prior information . . . 215
9.4.3 The posterior . . . 217
9.4.4 Simulating the posterior probability density . . . 217
9.5 Inversion results . . . 218
9.5.1 Smoother bias . . . 218
9.5.2 Data availability . . . 234
9.5.3 Depth dependent data availability . . . 242
9.5.4 Increased data uncertainties . . . 249
9.6 Extension to the other mantle minerals . . . 257
9.7 Conclusions . . . 266

A Affinities of chemical elements **269**

Conclusion and outlook **271**

Preface

The goal of this thesis is to study the interior structure of terrestrial planets. This knowledge is fundamental to our understanding of the solar system and for our comprehension of the formation and evolution of those planets. Furthermore, knowledge about terrestrial planets provides important insights to our understanding of the future evolution of the Earth. To learn about the interior structure of terrestrial planets, we first devise a method to construct detailed interior structure models applicable to terrestrial planets and second we show how data provided from space missions, earth-bound measurements, and laboratory experiences from high pressure physics can be used to infer knowledge about the interior structure. We apply our method to two studies related to the planet Mars. The main aim of the first study is to constrain the state, size, and composition of the core by using geodesy data. The objective of the second study is to ascertain whether the composition and the thermal state of the Martian mantle can be inferred by jointly using geodesy, seismic, and magnetic induction data. These data are expected from a future surface network mission to Mars. Our choice of Mars is motivated by two reasons: improved geodesy data and new data about thermoelastic and melting properties of core constituents at pressures and temperatures relevant to the core of Mars.

Primary insight into the understanding of the interior structure of planets is provided by the mechanisms of their formation. According to the prevailing theory [e.g. *Armitage*, 2009] planets form in a gaseous protoplanetary disk that orbits a central star in the late stages of its formation. The cooling of the initial hot protoplanetary disk eventually results in the formation of dust grains that coagulate into small kilometer-sized planetesimals. If the accretion disk is massive enough, the planetesimals can grow to planetary embryos that can be about as large as the size of present Mars. Finally, violent collisional merging of the planetary embryos gave rise to the terrestrial planets (i.e. Earth-like) of our solar system: Mercury, Venus, Earth, and Mars. For the formation of giant planets two scenarios have been extensively studied: gravitational collapse and planetesimal accretion with subsequent gravitational accumulation of gas. If the protoplanetary nebula is extremely dense, unstable clumping results and giant planets can form by gravitational collapse just like the Sun itself. Giant planet formation according to the second scenario can only occur further out in the accretion disk where the temperature is low enough so that the formation of ice becomes possible: planetesimals made principally of ice grow until they are several times more massive than the terrestrial planets of the inner solar system. Only the most massive icy planetesimals start to accrete hydrogen and helium from the protoplanetary disk and give rise to gas giants Jupiter and Saturn. For the remaining giant planets, Uranus and Neptune, it is thought that their icy cores formed too late to accrete significant amounts of hydrogen and helium.

A major event occurring during planet accretion is the formation of the core. Core

formation can already start in planetesimals and planetary embryos when significant parts of them are molten because of impact melting and of heat released by decaying radioactive elements like aluminum-26 [e.g. *Chambers*, 2004]. Due to the large density difference between iron and silicates, molten iron segregates to form a core and an overlying silicate shell. In the same way, a terrestrial planet that grows by collisional merging of planetary embryos experiences extensive surface melting. The molten metal brought in by the embryos sinks to the center of the planet after temporarily accumulating in large ponds at the bottom of the silicate magma ocean. Depending on the pressure and temperature conditions at the bottom of the magma ocean as well as on the chemical composition of the magma, different chemical elements can be dissolved into liquid iron [e.g *Poirier*, 1994]. The identity and the amounts of the elements dissolved can have a profound effect on the dynamics and evolution of the planet. For instance, heat produced by the decay of radioactive potassium-40 slows down core cooling and provides a supplemental energy source to power the planetary dynamo. Moreover, light elements like sulfur significantly reduce the melting temperature of iron [e.g. *Fei et al.*, 1997] and thus delay the onset of inner core formation through the solidification of iron rich materials. Core formation ends when the temperature inside the core is sufficiently low so that the whole core freezes.

The terrestrial planets that we observe today have a high average density (Fig.[1]) indicating that a significant fraction of their mass is provided by iron. Besides terrestrial planets, another category of solid planetary bodies consists of the somewhat less dense rocky satellites. They comprise the Moon, and the Jovian satellites Europa and Io. They are principally made of silicate rocks and have smaller fractions of bulk metal and ice, though Europa has a significant fraction of ice. The least dense group of solid planet-like bodies in our solar system consists of the dwarf planets Ceres, Pluto, Haumea, Makemake, and Eris, the two other Galilean satellites Callisto and Ganymede, and the largest satellite of Saturn, Titan. Their average density is about $2000\mathrm{kg/m^3}$, indicating that they contain substantial amounts of water ice besides silicates.

Tab.[1] compares main characteristic properties of terrestrial planets and the Moon. Fig.[2] provides a visual comparison of their size, average density, core size, and core mantle boundary pressure. We now give a brief description of each terrestrial planet.

	Mercury	Venus	Earth	Moon	Mars
Radius	0.383	0.949	1	0.272	0.533
Mass	0.055	0.815	1	0.012	0.107
Density	0.984	0.951	1	0.605	0.713
Normalized moment of inertia	n.d.	n.d.	0.331	0.393	0.364
Rotation period [days]	58.8	−244.	1	27.4	1.03
Global magnetic field	yes	no	yes	no	no
Number of satellites	0	0	1	0	2

Table 1: Terrestrial planetary properties relative to Earth. The moment of inertia of Mercury and Venus are unknown. (n.d.=no data)

Mercury is the terrestrial planet closest to the Sun. In appearance, its surface resembles that of the Moon. It has large mare like plains that are heavily cratered indicating

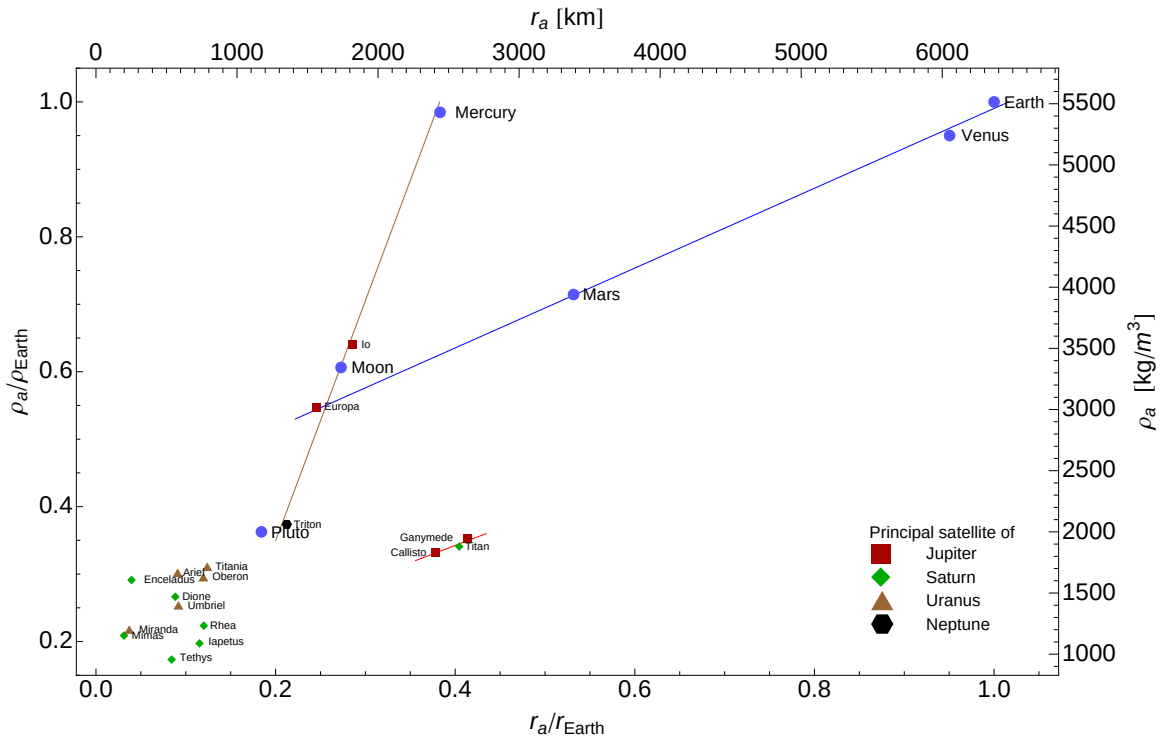


Figure 1: Solid planets and main satellites of the solar system as a function of radius and density relative to Earth.

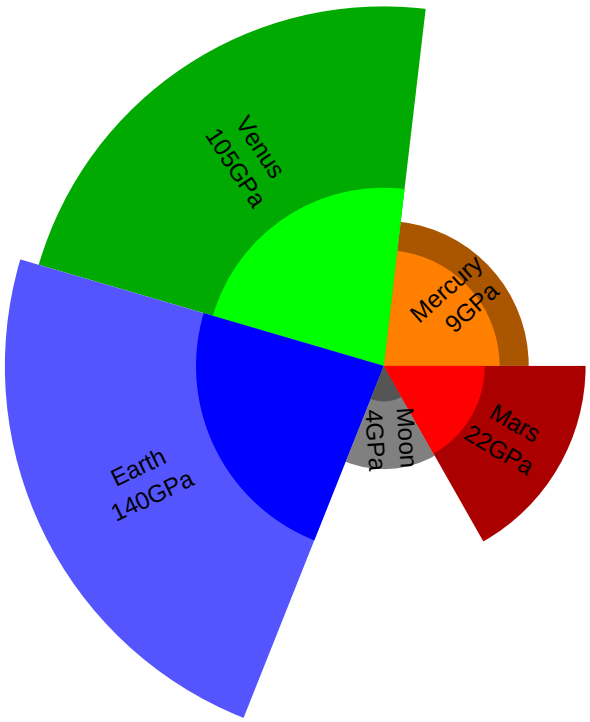


Figure 2: Earth normalized radius and core size of terrestrial planets and the Moon and estimates of core mantle boundary pressure. The angular width is proportional to the density of the planet.

that Mercury has been geologically inactive for billions of years. The surface of Mercury shows large curved cliffs, also known as lobate scarps that can be a few kilometers high and hundred kilometers long. They probably formed when Mercury contracted due to cooling [e.g. *Solomon*, 2003]. Mercury has almost no atmosphere, and daytime temperatures are too hot for liquid water to be sustainable on the surface. However, it is possible that Mercury harbors water ice in craters that are never exposed to the Sun. Very little is known about the interior structure of Mercury. Its relative large mass and small size indicate [*Anderson et al.*, 1987] that Mercury has a large dense core (Fig.[1]). If the core is made of pure iron its radius would be about 3/4 of the radius of the planet which is significantly larger than for the other terrestrial planets (Fig.[2]). During their flybys of Mercury, the spacecraft Mariner 10 and Messenger have observed an external magnetic field. If this magnetic field is of internal origin then Mercury most likely has a liquid outer core and a solid inner core. Additional evidence for a partially liquid core is provided by earthbound radar measurements [*Margot et al.*, 2007], which show that observed rotation variations are larger than expected for an entirely solid planet. The precise size of the core, its composition, the size of the inner core (if present), the thickness and density of the crust, and the density of the mantle are unknown. Ongoing and forthcoming missions to Mercury (Messenger and BepiColombo) will provide strong constraints on those unknowns.

Venus, the second planet, has a very dense atmosphere that is principally made of carbon dioxide and sulfur dioxide. Both gases generate a strong greenhouse effect, creating surface temperatures that are in excess of 450°C. The thick dense atmosphere creates pressure at the surface about ninety times larger than on the surface of the Earth [e.g. *de Pater and Lissauer*, 2001]. It is possible that in the past, much like the Earth, Venus had large amounts of liquid water on its surface. However, it evaporated into the atmosphere because of the large surface temperatures. The water then most likely dissociated and the hydrogen escaped to interplanetary space [*Kasting*, 1988]. The upper layer of Venus' atmosphere is covered with highly reflective clouds hiding its surface in the visible spectrum. Radar measurements of the surface made by the Magellan spacecraft revealed that 80% of Venus' surface is covered with volcanic plains, by a relative small number of almost pristine craters, and that Venus appears to be devoid of plate tectonics [*Basilevsky and Head*, 1994]. The small number of craters and their pristine condition indicate that Venus underwent a recent global resurfacing event (about $300 - 600$ million years ago). The fact that Venus is similar to Earth in terms of density and size (Fig.[1] and Tab.[1]) suggests that both share a similar differentiated interior structure [e.g. *Sohl and Schubert*, 2007]. However, Venus has no intrinsic magnetic field, but measured tides indicate that it has an appreciable liquid layer inside its core [*Konopliv and Yoder*, 1996]. It is unknown whether the core is fully molten or whether it harbors a solid inner core. The concentration and identities of light elements in the core and the composition of the mantle are also unknown.

The third planet of the inner solar system is the Earth. Its most remarkable external features are its dense atmosphere, the large surface reservoirs of liquid water, the active volcanoes, and the global geomagnetic field. The crust comes in two types: continental and oceanic. The lithosphere (crust and upper rigid part of the mantle) is broken up in several tectonic plates that are continuously recycled at subduction zones and at mid-ocean ridges. The plates float on the asthenosphere, a highly viscous and mechanically

weak region of the upper part of the mantle of the Earth [e.g. *Anderson*, 2005]. Seismic data have revealed that the Earth is made of a solid inner core, of a liquid outer core, and of a solid silicate shell. The presence of an outer liquid layer inside the core has been deduced on the basis of absence of seismic shear waves propagating through that region. Independently of shear wave propagation, the presence of a liquid layer inside the core can also be deduced from vibrational modes of the whole Earth, from Earth's deformational response due to tidal forcing, and from studying Earth's rotation. In addition to structural information, seismic data have also provided precise radial profiles of the density and elastic properties [*Dziewonski and Anderson*, 1981]. Those profiles with data obtained from chemical analysis, from studies of isotopes of terrestrial and extraterrestrial rock samples, and from cosmochemical considerations have led to strong constraints on Earth's mineral composition. On the basis of those results, we know that Earth's silicate shell is made of magnesium rich and iron poor minerals. The upper mantle consist mostly of the mineral olivine, and the lower mantle of the mineral magnesium perovskite [e.g. *Stixrude*, 2007]. The core is significantly denser than any rocky surface material and a few percent less dense than pure iron (about 10% of the total weight or 10wt%) at the pressure and presumed temperature conditions inside the core [e.g. *Vočadlo*, 2007]. Since iron is the only element abundant enough in the universe with that density and since the elastic properties of the core are close to those of pure iron the consensus is that the Earth's core is principally made of iron. Besides iron, it is thought that the core also contains a small fraction (less than about 10wt%) of the denser element nickel since nickel is often found together with iron in iron meteorites. Because both the inner and outer core are a few percent less dense than pure iron, they have to contain a small but appreciable fraction of light elements. The identity of those elements is still debated, but the most prominent are sulfur, silicon, oxygen, and carbon [e.g. *Poirier*, 1994]. The efficient cooling of the core results in large scale convective movements inside the liquid core [e.g. *Nimmo*, 2007]. The convective movements are the result of the cooling itself, and the consequence of buoyancy forces acting on the light elements that are released at the inner core-outer core boundary when iron rich material solidifies. Electrical currents in the rotating and convective outer core are responsible for inducing Earth's global magnetic field [e.g. *Roberts*, 2007].

Mars is the farthest terrestrial planet from the Sun. It has about the size of the Earth's core (see Fig.[2]). Many features on the Martian surface are similar to features on Earth. Mars also has an atmosphere, harbors large polar caps, and is home to the largest volcanoes, highest mountains, and deepest canyons of the solar system. In contrast with the Earth, volcanism is probably extinct. The tenuous atmosphere is mostly made of CO_2 and the surface of Mars does not exhibit any sign of activity related to tectonic plates.

Mars' crust exhibits a crustal dichotomy [*Zuber*, 2001]: the northern hemisphere is almost flat and covered with lava whereas the southern hemisphere is 6km higher and cratered by ancient impacts. Spacecraft based spectral measurements and surface features indicate that Mars had large amounts of liquid water on its surface in the very distant past. Nowadays, water on the surface is mostly found in the form of solid water ice below the CO_2 ice covered polar ice caps. Compared to Mercury and Venus, significantly more is known about Mars' interior structure. The topography data and the static gravity field measured by orbiting spacecraft have been used to estimate the crustal thickness

and density [e.g. *Wieczorek and Zuber*, 2004]. The moment of inertia of Mars has been determined with a high precision [*Konopliv et al.*, 2011] from the static gravity field and from Mars precession rate. The precession has been measured by tracking orbiting spacecraft and landers on the surface of Mars [*Folkner et al.*, 1997; *Konopliv et al.*, 2011]. If we assume a simple two layer model of the interior structure, the moment of inertia and the average density require that the core of Mars should be at least about 40% of the planet radius if it is made of pure iron and that it can be significantly larger if it contains large amounts of the light elements (see Fig.[4]). Tidal measurements show that Mars' core is at least partially liquid [*Yoder et al.*, 2003]. Besides, the absence of a global geomagnetic field suggests that even today Mars' core is completely molten. The mineralogical composition of Mars' mantle is not known precisely but is constrained by the chemical and isotopic composition of a set of igneous meteorites of Martian origin (see Fig.[3]).

The most conclusive deductions about the interior structure of a planet can be obtained from seismic measurements. They allow us to derive the elastic properties and the density of the materials within the planet and gather knowledge about their identity. Moreover, since liquid media do not support shear deformations, shear waves can be used to precisely determine the extension of liquid material reservoirs within a planet. Seismic data have been extensively used to determine major features within the Earth, such as the state of the outer core, the depth of the core mantle boundary, and the size of the inner core. However, with the exception of the Moon, seismic data for other planets are not available. Therefore, inferences about their interior structure are indirect and not as precise.

Besides seismic data, depth dependent constraints on the mantle of a planet are also provided by electromagnetic induction data. Induction data are either measured on the surface or by an orbiting spacecraft. The measured electromagnetic field variations are the result of induced electrical currents in the mantle from a source that is localized in the planetary magnetosphere. The source has its origin in the interaction of the magnetosphere with the solar wind. The penetration depth of the electromagnetic field and the depth where the currents are induced increase with the wavelength of the field. Therefore, induction data allow to determine the electrical conductivity of the mantle to a depth depending on the frequency spectrum of the source. Since the electrical conductivity of a given material is a function of the local temperature, its fraction of melt, and its composition, induction measurements provide constraints on those quantities.

In the absence of seismic measurements the state of the core (solid or liquid) can be deduced from the presence of a planetary magnetic field, from the deformational response of the planet to the gravitational attraction of the other celestial bodies (solid tides) or from the variations in its rotation. The global magnetic field within a planet is generated inside its rotating and convecting electrical conducting liquid core. Convection in the core is either purely thermal or combined thermal and compositional. Dynamos can only be sustained if the core efficiently cools which is ultimately controlled by the mantle's capacity to transport heat to the surface. It is thought that after formation all planetary bodies with a liquid core could have experienced a short episode of a thermally driven dynamo. On the other hand, a thermo-chemical dynamo occurs after the planet has cooled enough for core material to start solidifying and induce the formation of an inner core. Therefore, the presence of a planetary magnetic field is evidence for a liquid outer

core and a strong indication for the presence of a solid inner core. Conversely, the absence of a planetary magnetic field indicates that either the core is solid or the liquid part of the core is not convecting. Both tides and rotation are significantly different if a planet is completely solid or if it has internal liquid layers. For instance, a planet with a liquid core is more easily deformable than the same planet with a solid core and therefore has larger tides. Similarly, a solid planet rotates as a whole whereas a planet with a liquid core can experience differential rotation between the shell and the core. Thus, one can deduce the state of the core by measuring tides and the rotation of the planet and obtain constraints on the core size, its density, and on the density of the shell.

Unlike seismic and induction data, geodesy data (tides, rotation, and gravity field) do not provide direct quantitative insights into the interior structure of a planet. To obtain those informations one basically follows a two step process. First, a precise model of the interior structure has to be constructed, i.e., a mathematical relation between the parameters of the model and the data. Second, parameter values are sought that result in computed data that most accurately match the measured data. The procedure is here illustrated with a simple model for the interior structure of a terrestrial planet. We assume a spherically symmetric two-layer planet made of a core and an overlying silicate shell. The parameters of the model are the core radius, the core density, and the density of the shell. In order to infer knowledge about the parameters we use as data the mean density of the planet and its moment of inertia. Fig.[3] and Fig.[4] illustrate the resulting relations between core radius and shell and core density for Mercury, Venus, the Moon, and Mars. For the Moon and Mars we took the uncertainty on the moment of inertia into account. Because of this uncertainty, the curves that graphically represent the relations between the model parameters broaden up to surfaces whose widths depend on the uncertainty of the moment of inertia. For comparison, the figures also include densities of plausible planet forming materials. From the data about Mars, we deduce for instance that chondrite meteorites are plausible representatives for the density of the Martian shell (Fig.[3]) and that the radius of the core of Mars is between 1350km and 2050km if it is made of an iron-sulfur alloy that has less than about 33wt% (weight percent) of sulfur (the weight fraction of sulfur in FeS) (see Fig.[4]). If the density of the core were known precisely, the core radius could be determined with a precision only limited by the precision on the moment of inertia (assuming a negligible uncertainty on the average density). On the other hand, if this knowledge is not available the data do not allow for a reduction of the prior assumed model parameter ranges, even if the moment of inertia were known exactly.

This simple example of a model of the interior structure of a terrestrial planet illustrates two typical problems encountered when doing modeling. First, the number of model parameters is generally larger than the number of data and the data are usually only known up to a certain precision. As a result, there is no unique parameter value set that reproduces the data and *direct inversion* techniques are generally not applicable. In this thesis, we will apply methods that explore the parameter value space and retain only those parameter values that result in calculated data that compare favorably to the measured data. Second, we have to make usage of prior knowledge (that is independent of the data) in order to reduce the parameter value space. For this, we use geophysical plausible values for the parameters or values that result from previous studies dedicated to constraining those parameters.

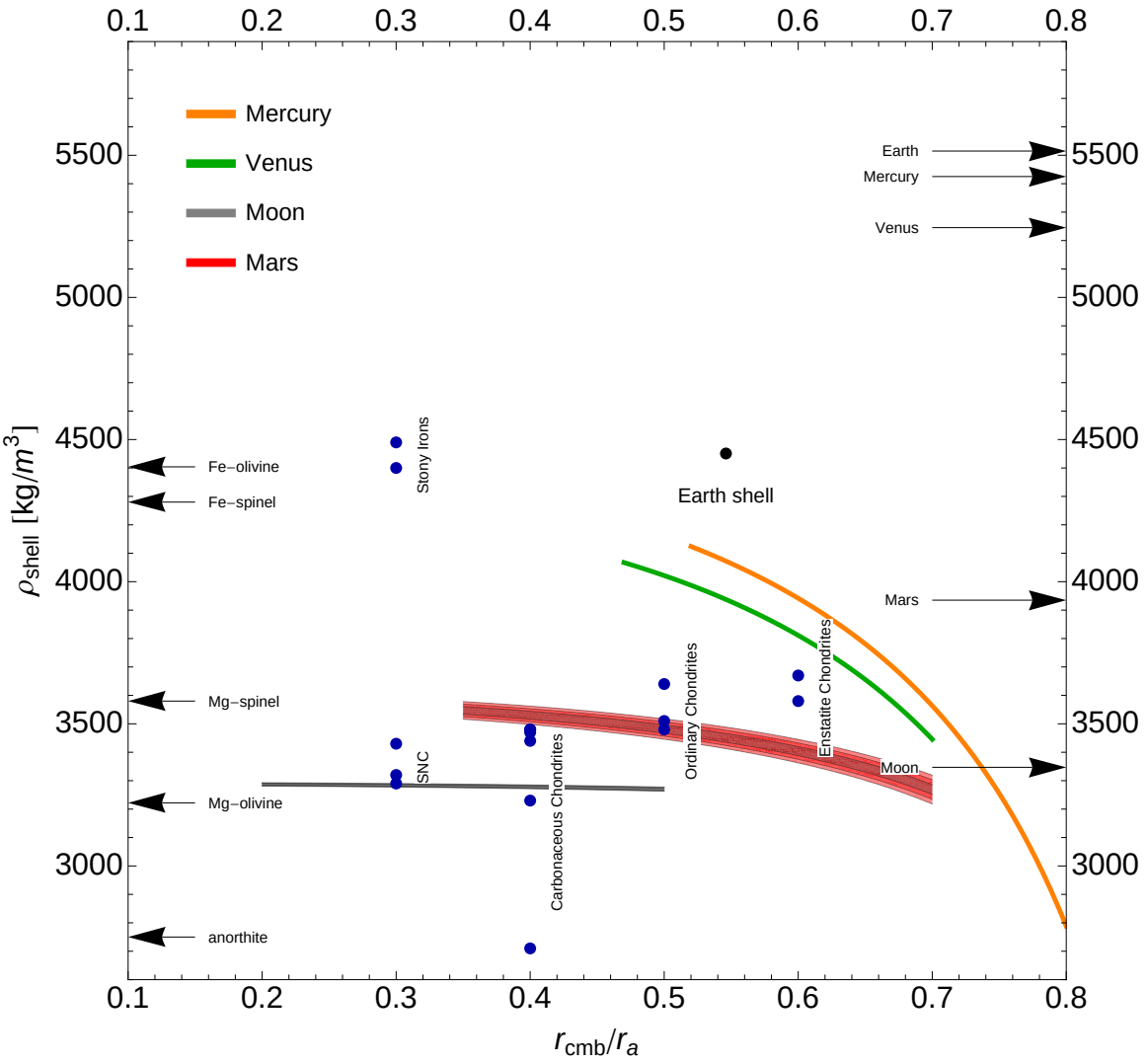


Figure 3: Relation between core size and average planet shell density for a two layer model for terrestrial planets and the Moon. Right-pointing arrows indicate average planetary densities and left-pointing arrows give ambient condition densities of the mineral olivine and of the oxides spinel and anorthite. The dark-blue dots indicate average grain densities of Mars originating meteorites (SNC), chondrite meteorites, and stony iron meteorites. Fe-olivine and Mg-olivine corresponds to olivine without magnesium and to olivine without iron. Fe-spinel and Mg-spinel corresponds to spinel without magnesium and to olivine without iron. For Mercury and Venus, the value of the MOI has been set to 0.33. For the Moon and for Mars, the uncertainties on the MOI were taken into account.

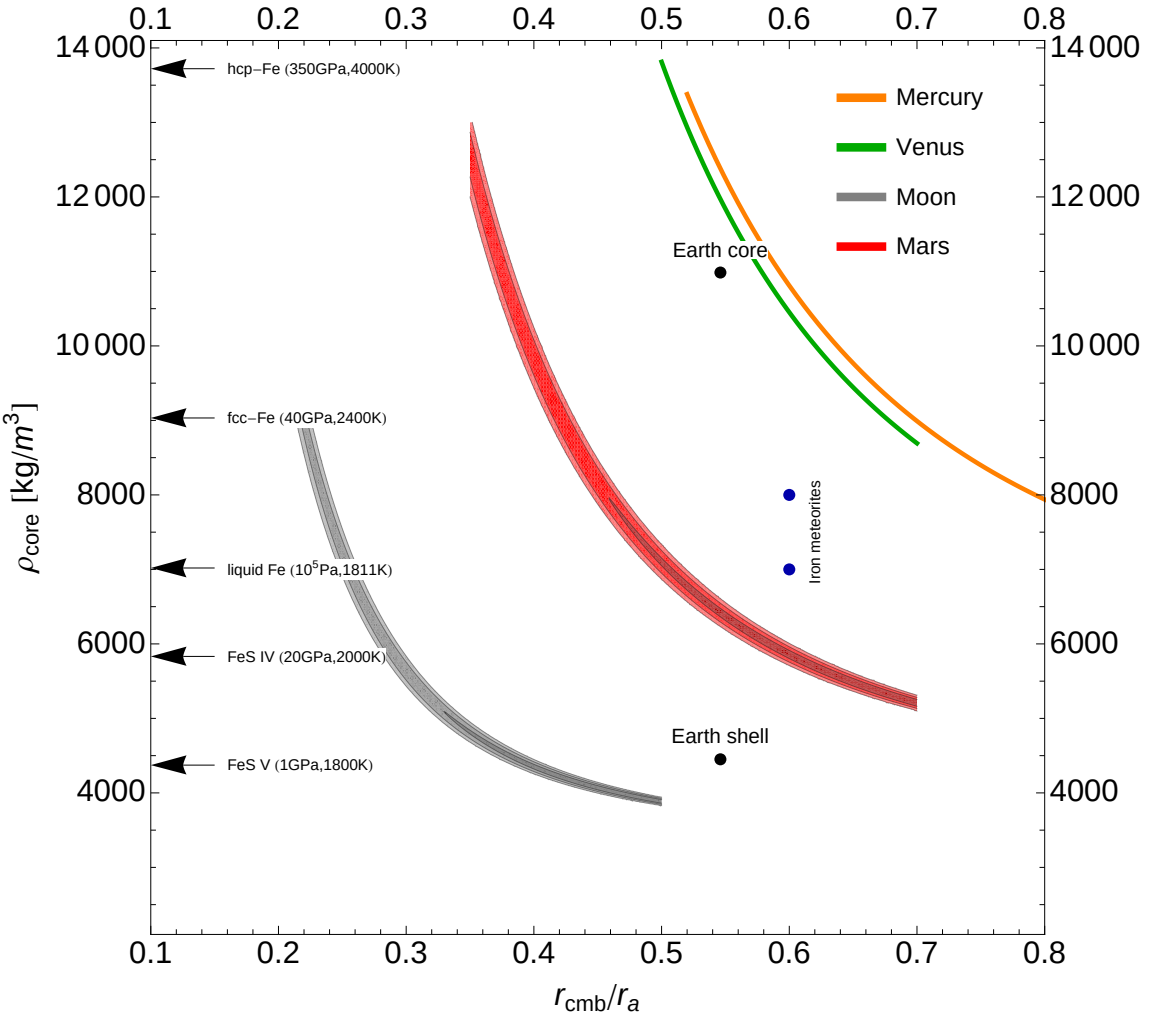


Figure 4: Relation between core size and average core shell density for a two layer model for terrestrial planets and the Moon. Left pointing arrows indicate densities of iron and iron-sulfur at different pressure and temperature conditions. hcp-Fe at approximatively Earth core center conditions, fcc-Fe at approximatively Mars' core center conditions, FeS IV at Mars core mantle boundary conditions, FeS V at Moon center conditions, and ambient pressure molten iron. The blue dots correspond to measured densities of iron meteorites. For Mercury and Venus, the value of the MOI has been set to 0.33. For the Moon and for Mars, the uncertainties on the MOI were taken into account.

Unlike the simple two layer interior models discussed above, the models we devise in this thesis take into account the composition and thermal state of the planet. From the composition of the mantle and from its temperature profile we determine the local mantle mineralogy by using phase diagrams of the relevant mantle minerals. We then use thermodynamic relations to compute for each mineral the density and the elastic properties as a function of local pressure and temperature within the mantle, as well as the electrical conductivity at those conditions. From those results we determine the density, the seismic pressure and shear wave velocities, the bulk sound velocity, and the electrical conductivity at each depth in the mantle. Likewise, we use thermodynamic relations to determine the state of the core (solid, liquid, or solid with a liquid part), its density, and seismic velocities at the core relevant pressures and temperatures. The planetary mass, moment of inertia, its response to tidal forcing, and surface electromagnetic induction data can then be calculated.

In this thesis, we assume that sulfur is the only light element in the core of Mars. There are several reasons for considering only sulfur. First, sulfur is found in iron-meteorites, the remains of the cores of differentiated planetesimals and the likely building blocks of Mars. Second, Martian meteorites, which are representative of the Martian mantle, are depleted in sulfur compared to chondritic meteorites, which means that large amounts of sulfur are probably confined in the Martian core. Third, among the other plausible siderophile light elements, large amounts of sulfur can already be dissolved into liquid iron at relatively low pressure. The other candidate light elements, oxygen and silicon, are almost immiscible into liquid iron-sulfur at pressures and temperatures that are smaller than those prevailing at the bottom of Mars' magma ocean. Finally, of all the light element candidates, sulfur most significantly reduces the melting temperature of iron and therefore provides an explanation for a small planetary body like Mars to still have a liquid core.

In our first study (Chapt.[6]) we infer the interior structure of Mars by using geodesy data (mass, moment of inertia, and tides). By interior structure we mean the size of the core, its state (solid, liquid, or both), the core's sulfur concentration, and the density and thickness of the crust. We do not infer the temperature, and mineralogy of the mantle since there is a strong correlation between mantle mineralogy and temperature. Those correlations cannot be disentangled by geodesy data. Even if the density and the elastic properties of the mantle were known, as is the case for the Earth from seismic measurements, the ambiguities between mantle mineralogy and temperature could not be resolved [e.g. *Matas et al.*, 2007]. In order to estimate the mantle temperature and mineralogy, additional independent observables like the mantle electrical conductivity are necessary [e.g. *Verhoeven et al.*, 2009]. We therefore use two end-member temperature profiles that have been deduced from studies dedicated to the thermal evolution of Mars and use several mantle mineralogy compositions that have been proposed for the mantle of Mars. Our results show that within our model assumptions the geodesy data imply that Mars has no solid inner core and that the liquid core contains a large fraction of sulfur. The absence of a solid inner core is in agreement with the absence of a global magnetic field. Our estimated core size is 1616 ± 137km and the core sulfur concentration is 12 ± 6wt%.

In the second study (Chapt.[9]) we investigate whether the mineralogical composition of the mantle, and its temperature can be inferred from the mantle's bulk sound velocity

and electrical conductivity profiles. For Mars those data are not yet available but are expected to be measured by future missions that deploy a network of landers on its surface. We thus use simulated data sets in order to validate our method. Unlike the first study where the number of parameters was small and parameter values were sought by systematic exploration of the parameter space, parameter inference in the second study is done with a *Bayesian inversion* method (Chapt.[8]). It is well suited to handle the non-linear relation between parameters and data of our model and can accommodate the larger number of parameters i.e. the parameters defining the mineralogy and the temperature values at a given set of depths in the mantle. Our results show that the temperature of the mantle and its mineralogical composition can be determined with a high confidence from seismic and electrical conductivity data. In order to test the robustness of our method we also discuss different scenarios where data sets are missing) or where the data is not available for the whole depth of mantle).

Part I

Global models from geodetic data

Chapter 1

Introduction

The aim of the first part of this thesis is to devise interior structure models of telluric planets and constrain the parameters governing the models through geodetic observations. The how and what of the interior structure that is modeled depends on the nature of data that are available. Usually for terrestrial planets, the only data related to the deep interior that are available is of geodetic origin and comprise the size of the planet, its mass, its moments of inertia, and for all terrestrial planets beside Mercury, the tidal Love number k_2.

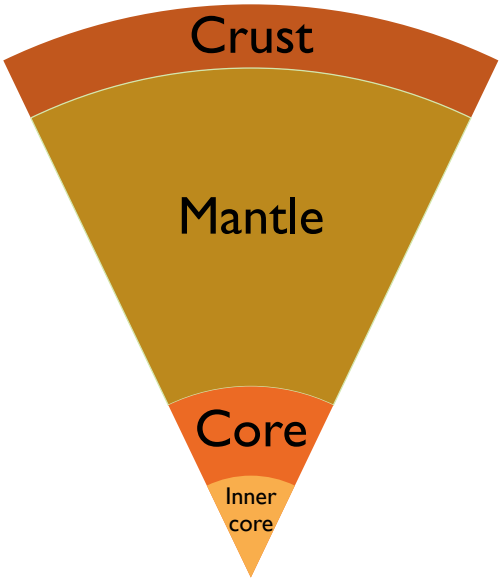


Figure 1.1: Section of a terrestrial planet.

Here, it is assumed that the planet is spherical, isotropic, non-rotating, and in hydrostatic equilibrium. For modeling the interior structure of a terrestrial planet it is convenient to delineate the interior structure in three layers: the crust, the mantle, and the core (Fig.[1.1]). Those layers are made of different materials and have therefore, different densities and different elastic properties. The silicate upper layer, comprising crust and mantle is principally made of silicate rocks, and the core is presumably principally made of iron. With the exception of the core, the crust and the mantle are assumed a

solid. The core, depending on the temperature inside the planet is either fully liquid, has a solid inner core with a liquid outer core, or is completely solid.

In order to calculate the mass and the moment of inertia of a planet one needs to know its density as a function of depth inside each individual layer. The Love number k_2 describes the external gravity potential variations resulting from the mass redistribution inside the planet due to tides. The gravitational forcing of the Sun and of the other bodies cause periodic deformation of the planet and with it internal mass redistribution. The deformational response depends on the mechanical properties of the individual layers and of their dimensions. The deformability of each layer is related to its density and to its capacity to withstand compression and shear deformation. The deformational properties are also related to the state of the layer. If the layer is a liquid, it has no shear strength and planets containing a liquid layer are more easily deformed than planets that are fully solid and so the internal mass redistribution more important and with it the external potential variations. Ultimately, the thermoelastic properties (density, incompressibility, rigidity) of each layer depend on the materials they are made of. The thermoelastic properties of a specific material inside a given layer are related to the local pressure and temperature. Consequently, by measuring the mass, the moment of inertia, and k_2 it is in principle possible to constrain the interior structure, in terms of layer thickness, composition, and temperature.

To achieve this goal detailed models of the interior structure of terrestrial planets are constructed. First, in Chapt.[2] the *structure* differential equations allowing to calculate pressure and temperature inside the planet from the density profile and from other thermodynamic quantities are introduced. Then, starting with the silicate layer comprising crust and mantle it is detailed how, given a chemical composition, one determines a composition in terms of minerals (Chapt.[3]). From the mineralogy, and by using thermodynamic relations, the density and the elastic properties inside the mantle are calculated for each depth. In Sect.[3.6] we describe how given the interior structure of the planet and given its mineralogy composition and associated conductivity structure, one derives the electromagnetic inductional response resulting from an ionospheric ring current. After modeling the mantle, the modeling of the solid and of the liquid core is introduced in Chapt.[4]. The liquid part of the core is modeled by a thermodynamic coherent solution model (Sect.[4.4]). An empirical melting law for the iron sulfur system is derived in Sect.[4.5] from recent melting data. Depending on the pressure and the temperature at the bottom of the mantle it is then possible to calculate the pressure, the temperature, the density, and the elastic moduli inside the core and with the melting law decide on the presence of an inner core. In Chapt.[5], we study in great detail how the different interior parameters influence the Love numbers. In the final chapter of the first part (Chapt.[6]), the previously introduced interior models are then applied on data originating from geodetic observation in order to determine the interior structure of the planet Mars.

Chapter 2

Interior structure equations

2.1 Governing equations

For interior modeling we assume a spherically-symmetric planet in which the interior physical quantities only depend on the radial distance to the center, or equivalently on the local pressure and temperature. For clarity in the notation the implicit dependence on r or P, T of the structure quantities is suppressed.

The planet is assumed to be in hydrostatic equilibrium:

$$\frac{d\,P}{dr} = -\rho\, g, \tag{2.1}$$

where P is the pressure, ρ the mass density, and g the gravity. The gravity is related to the density by the Poisson equation, which can be expressed as

$$\frac{d\,g}{dr} = 4\pi G\rho - \frac{2}{r}g, \tag{2.2}$$

where G is the universal gravitational constant. For illustration, we have calculated the hydrostatic pressure profile for the Earth associated to the density profile of the model AK135 of *Kennett et al.* [1995].

Equations (2.1) and (2.2) depend on the mass density ρ, which we calculate from an equation of state (EoS) specifying the dependence of the density on pressure and temperature. The EoS will be discussed in Chapt.[3] and Chapt.[4].

The temperature profile can be calculated by assuming that the planet is in thermal equilibrium and by specifying at each location the primary method of energy transfer. Thermal equilibrium is the balance between the energy lost by outward energy flux and the internal energy generation and can be expressed as

$$\frac{d\,q}{dr} = \rho\epsilon - 2\frac{q}{r}, \tag{2.3}$$

where q is the outward heat flux per unit area and unit of time and ϵ the specific heat production rate. If energy is transported mainly by convection, the temperature gradient can be approximated by the adiabatic temperature gradient [e.g. *Stacey and Davis*, 2008]

$$\frac{d\,T}{dr} = -\frac{\gamma}{K_S}\rho g T, \tag{2.4}$$

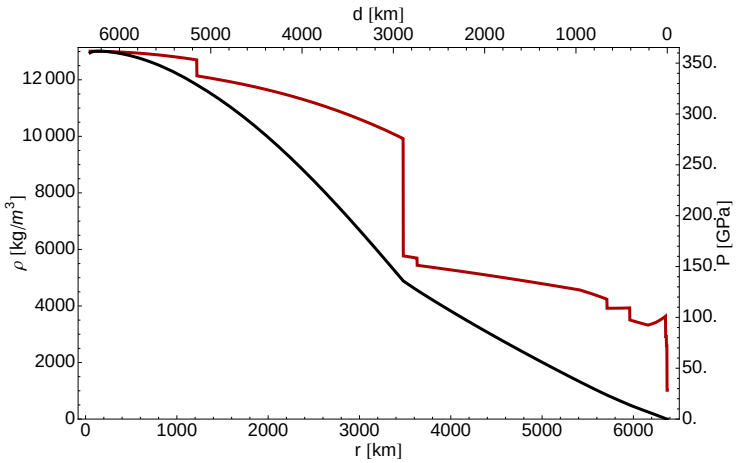


Figure 2.1: Hydrostatic pressure profile (black curve) associated to the Earth density profile of the model AK135 (red curve) [*Kennett et al.*, 1995]

where $\gamma = \alpha K_S/\rho C_P$ is the thermodynamic Grüneisen parameter, K_S the adiabatic bulk modulus, C_P the specific heat at constant pressure and α the thermal expansion coefficient. The meaning of those thermodynamic quantities will be discussed in Chapt.[3] and Chapt.[4].

For conduction, the thermal gradient is given by

$$\frac{dT}{dr} = -\frac{q}{k}, \tag{2.5}$$

where k is the thermal conductivity.

The temperature is difficult to determine because it depends on the thermal history of the planet, the unknown amount of radio-active elements in the core, mantle, and crust and the fraction of light elements in the core. Therefore, we here do not solve differential Eqs. (2.3) and (2.4) (or (2.5)) for the thermal quantities q and T in the mantle, but use instead published mantle temperature profiles from studies dedicated to the thermal evolution of the planet.

The mantle model can then be determined as follows. By assuming a given crust thickness and an average crust density Eqs. (2.1) and (2.2) are integrated from the surface to the bottom of the crust, starting from the boundary conditions at the surface $r = r_a$

$$P(r_a) = 0, \tag{2.6}$$

$$g(r_a) = \frac{GM}{r_a^2}. \tag{2.7}$$

The resulting pressure and gravity at the mantle-crust boundary are the boundary conditions to integrate Eqs. (2.1) and (2.2) from the bottom of the crust to the core-mantle boundary. These equations have to be supplemented with phase diagrams, determining the composition as a function of pressure and temperature, and equations of state to include pressure-induced compression and thermal expansion effects on the thermoelastic properties. The EoS used for the mantle are discussed in Sect.[3.4]. In essence, equations of state are used and material properties at reference temperature and pressure are corrected to actual mantle temperature and pressure by following first an isobaric and then an isentropic thermodynamic path.

For the core the temperature profile is calculated from the temperature at the core-mantle boundary. We assume that there are no radio-active elements in the core and that both the liquid outer core and the solid inner core (if present) are convecting and use Eq. (2.4) for the adiabatic temperature gradient to calculate the temperature in the core. The three governing equations are then given by (2.1), (2.2), and (2.4) for P, g, and T. At the center, the initial condition reads

$$g(0) = 0. \tag{2.8}$$

At the core-mantle boundary, the three quantities P, g, and T must be continuous.

If an inner core is present, boundary conditions have to be applied at the inner core boundary (icb) radius $r_{\rm icb}$. Firstly P, g, and T are to be continuous at the icb. Secondly, depending on where in the core the temperature first drops below the melting temperature upon cooling (see Sec.[4.5]), the inner core grows either by solidification of iron from the center outwards or from solid iron expelled from the outer core solution at the top of the core precipitating towards the center. For the first case the temperature at the icb must be equal to the melting temperature T_m of the outer core liquid:

$$T(r_{\rm icb}) = T_m(x_{\rm oc}, P(r_{\rm icb})), \tag{2.9}$$

where $x_{\rm oc}$ is the sulfur concentration in the liquid part of the core. For the second case the melting temperature of the solution at the core mantle boundary (cmb) is the temperature at the core mantle boundary, therefore the sulfur concentration in the outer core solution can be determined from the pressure and temperature at the cmb

$$x_{\rm OC} = T_m^{-1}(P(r_{\rm cmb}), T(r_{\rm cmb})), \tag{2.10}$$

where $T_m^{-1}(P,T)$ is the function expressing the sulfur fraction of melting as a function of pressure and temperature. The melting law and the EoS relevant to the core are discussed in Chapt.[4].

In practice one encounters 4 different settings. Each case satisfies 2 surface conditions (2.6) and (2.7) and condition (2.8) in $r = 0$. For the crust and the mantle Eqs.(2.1,2.2) are integrated, and for the core and the inner core Eqs.(2.1,2.2,2.4). The differential equations give rise to either 7 or 10 integration constants depending on the presence of an inner core. One can distinguish between two different cases:

- The size of the core is determined from the boundary conditions. The differential equations for the crust (2), mantle (2) and core (3) or (6) have to be integrated simultaneously as the size of the core is unknown.

    1. Solid core or liquid core with given core sulfur fraction:
    The resulting 7 integration constants (2 crust+2 mantle+3 core) together with the core size are determined from the 2 surface boundary conditions, 2 continuity conditions at the top of the mantle, 3 continuity conditions at the core mantle boundary, the condition in $r = 0$.
    2. Liquid core with precipitating inner core of given size:
    The resulting 10 integration constants (2 crust+2 mantle+3 outer core+3 inner core) together with the core size are determined from the 2 surface boundary

conditions, 2 continuity conditions at the top of the mantle, 3 continuity conditions at the cmb, 3 continuity conditions at the icb, and one condition in $r = 0$. The outer core sulfur fraction is obtained from the melting temperature at the cmb (2.10).

- The core size is given and the core composition is determined from the boundary conditions. The differential equations of the crust (2) and the mantle (2) can be integrated separately from those of the core. For the core, the two following configurations exist:

  1. Liquid core:
     The 3 integration constants, resulting from the integration of the differential equations of the core, and the unknown core sulfur fraction, are determined from 3 conditions at the cmb and from the condition in $r = 0$.

  2. Liquid core with with crystallizing inner core:
     The 6 integration constants, resulting from the integration of the differential equations of the outer core and of the inner core, together with the unknown outer core sulfur fraction and the location of the icb, are determined from the 3 conditions at the cmb, 3 continuity conditions at the icb, the condition in $r = 0$ and from the melting temperature at the icb (2.9).

Once the equations for the structure of the planet are solved, the density profile in the whole planet is known. The resulting mass and moment of inertia of spherical volumes with radius r are then calculated from

$$m = 4\pi \int_0^{r_a} dr\ \rho(r) r^2, \tag{2.11}$$

$$I = \frac{8}{3}\pi \int_0^{r_a} dr\ \rho(r) r^4, \tag{2.12}$$

and the normalized moment of inertia MOI is

$$\mathrm{MOI} = \frac{I}{m_a r_a^2}. \tag{2.13}$$

2.2 Practical considerations

2.2.1 Initial singularity

Since the Poisson equation (2.2) is singular at the origin the numerical integration cannot be started from the origin on, but is rather started at the surface of a small sphere with radius δr. The solutions at δr are computed by solving analytically the differential equations for constant thermoelastic properties, i.e. $\rho_0 = \rho(P(0), T(0))$, $K_{S,0} = K_S(P(0), T(0))$,

and $\gamma_0 = \gamma(P(0), T(0))$. The solutions in δr are then:

$$g(\delta r) = \frac{4}{3}\pi G \rho_0 \, \delta r \tag{2.14}$$

$$P(\delta r) = P(0) - \frac{2}{3}\pi G \, \delta r^2 \rho_0 \tag{2.15}$$

$$T(\delta r) = T(0) \exp\left(-\frac{2\pi \, G}{3} \frac{\gamma_0 \, \rho_0}{K_{S,0}} \, \delta r^2\right) \tag{2.16}$$

$$\tag{2.17}$$

2.2.2 Reformulation of boundary value problems into standard forms

The above differential equations and boundary conditions (BCs) have to be rewritten in order to solve them with standard boundary condition solver. We consider three different cases.

Unknown parameter:
When the value of a parameter (e.g. the core sulfur fraction) has to be determined together with the dependent variables of the differential equations, we introduce according to the standard procedure, an additional differential equation for the unknown parameter:

$$\frac{d\,x}{dr} = 0. \tag{2.18}$$

The value of the parameter is then found by solving for the extended system of differential equations.

Unknown integration boundary:
For the case, where the boundary of the integration domain is unknown but specified through the boundary conditions (e.g. given core composition and unknown core size) the integration variable r is substituted with

$$r \to t \, r_{\rm cmb}, \quad \text{with} \quad t \in (0, 1]. \tag{2.19}$$

With this substitution the integration domain of r from $(0, r_{\rm cmb}]$ is remapped to $(0, 1]$. After substitution, the system of ordinary differential equations (ODEs)

$$\frac{d\,\boldsymbol{y}(r)}{dr} = \boldsymbol{f}(\boldsymbol{y}, r) \tag{2.20}$$

for the structural ODEs, where $\boldsymbol{y} = (P, T, g)^T$, then reads

$$\frac{d\,\tilde{\boldsymbol{y}}(t)}{dt} = r_{\rm cmb} \tilde{\boldsymbol{f}}(\tilde{\boldsymbol{y}}, t), \tag{2.21}$$

where $\tilde{y}_i(t) = y_i(r_{\rm cmb} t)$ and $\tilde{f}_i(t) = f_i(y_i(r_{\rm cmb} t), r_{\rm cmb} t)$ for $i = 1 \ldots n$ and n is the number of differential equations. To find the solution of this new set of ODEs together with $r_{\rm cmb}$, they are integrated over $(0, 1]$ with the supplementary ODE for $r_{\rm cmb}$

$$\frac{d\,r_{\rm cmb}}{dt} = 0 \tag{2.22}$$

Unknown special point:
For the case, where a boundary condition is formulated at an unknown point (the size of the inner core is the location where the temperature is equal to the melting temperature). We consider the case where the outer core sulfur fraction has to be found together with the location of the icb from the boundary conditions and from the melting law. The ODEs for the inner and outer core read

$$\frac{d\,\boldsymbol{y}}{dr} = f_{ic}(\boldsymbol{y}, r), \quad 0 \leq r \leq r_{\text{icb}} \tag{2.23}$$
$$\frac{d\,\boldsymbol{y}}{dr} = f_{oc}(\boldsymbol{y}, r), \quad r_{\text{icb}} \leq r \leq r_{\text{cmb}}, \tag{2.24}$$
$$\tag{2.25}$$

where *ic* subscript stands for the structural ODEs for the inner core, and *oc* for the same structural ODEs for the liquid core. The integration interval $(0, r_{\text{cmb}}]$ is remapped in the following way in order to obtain the standard boundary value problem formulation

$$t = \begin{cases} \frac{r}{r_{\text{icb}}}, & 0 \leq r \leq r_{\text{icb}} \\ \frac{r_{\text{cmb}} - r}{r_{\text{cmb}} - r_{\text{icb}}}, & r_{\text{icb}} \leq r \leq r_{\text{cmb}} \end{cases} \tag{2.26}$$

Then with $\boldsymbol{y_1}(t) = \boldsymbol{y}(r)$ for $0 \leq r \leq r_{\text{icb}}$ and $\boldsymbol{y_2}(t) = \boldsymbol{y}(r)$ for $r_{\text{icb}} \leq r \leq r_{\text{cmb}}$,

$$\begin{aligned} \frac{d\,\boldsymbol{y_1}(t)}{dt} &= r_{\text{icb}} \boldsymbol{f_{ic}}(r_{\text{icb}} t, \boldsymbol{y_1}(t)) \\ \frac{d\,\boldsymbol{y_2}(t)}{dt} &= -(r_{\text{cmb}} - r_{\text{icb}}) \boldsymbol{f_{oc}}((r_{\text{icb}} - r_{\text{cmb}})t + r_{\text{cmb}}, \boldsymbol{y_2}(t)) \\ \frac{d\,r_{\text{icb}}}{dt} &= 0 \\ \frac{d\,x}{dt} &= 0. \end{aligned} \tag{2.27}$$

The continuity conditions at the icb are then

$$\boldsymbol{y_1}(1) = \boldsymbol{y_2}(1), \tag{2.28}$$

the initial condition in $r = 0$

$$y_{1,3}(0) = g(0) = 0 \tag{2.29}$$

the BCs in $r = r_{\text{cmb}}$

$$\begin{aligned} y_{2,1}(0) &= P(r_{\text{cmb}}) = P_{\text{cmb}} \\ y_{2,2}(0) &= T(r_{\text{cmb}}) = T_{\text{cmb}} \\ y_{2,3}(0) &= g(r_{\text{cmb}}) = g_{\text{core}}, \end{aligned} \tag{2.30}$$

and the melting constraint at the icb

$$y_{1,2}(1) = T(r_{\text{icb}}) = T_m(y_{1,1}(1), x) = T_m(P(r_{\text{icb}}), x). \tag{2.31}$$

The 8 ODEs are then simultaneously integrated over $(0, 1]$. The resulting 8 integration constants are determined from the condition in $r = 0$, the 3 continuity condition, the 3 boundary conditions at the cmb and from the melting law contraint.

Chapter 3

The crust and the mantle

The crust and the mantle of the Earth have been extensively sampled over the last 100 years. From seismic measurements, we do not only know the average crust thickness and the depth of the mantle, but we also have precise estimates of the radial profiles of density, adiabatic bulk modulus, and shear modulus [*Dziewonski and Anderson*, 1981]. However even with large amounts of in-situ rock samples, without further assumptions, like cosmochemical considerations it is presently not possible to infer unequivocally the bulk composition of the silicate shell of the Earth. Even if the bulk composition of the Earth mantle were known, it would be difficult to infer the mineralogy profile and the temperature profile of the mantle.

For planets, it is even more difficult to get an insight on their interior structure and on their mantle composition. Besides the Moon, neither seismic data nor rock samples unequivocally attributable to the planetary body in question are available. Nevertheless, some scientists have inferred bulk composition from cosmochemical considerations, and for Mars, from precise chemical and isotopic analyses of the SNC meteorites presumably originating from Mars.

In this chapter we will discuss how, given a composition of the mantle, a thickness of the crust, and the depth of the core-mantle boundary, the density and the elastic moduli inside the mantle can be calculated at each depth. For this, it is assumed that the mantle and the crust are hydrostatic spherical shells. We first discuss how the mantle mineralogical profile can be obtained, then the thermodynamic quantities relevant for the calculation of the thermoelastic properties are introduced. Then we explain how the electrical conductivity of the mantle is calculated from the mantle mineralogy and detail the relation between the electrical conductivity and the surface electromagnetic field variations that are induced by external geomagnetic sources. Finally, we assess how uncertainties on thermoelastic and electrical conductivity parameters obtained from in-situ laboratory measurements induce uncertainties on calculated density, elastic moduli, and electrical conductivity profiles.

3.1 The Crust

Here, crust is defined as the upper layer of a planet reaching down to the *Mohorovičić discontinuity* (Moho). It is the seismologically defined boundary between the uppermost layer of the planet and of the mantle [e.g. *Anderson*, 2005, Chap. 8]. Note that other

definitions of the crust are in usage. For instance, with the petrological definition of the Moho, the Moho can occur inside the mantle as the location where the transition from mafic to ultramafic[1] rocks occurs.

Typically the crust formation can occur in three different steps. Firstly, during planetary differentiation a floating crust forms on a differentiating magma ocean or molten mantle. Secondly, the secondary basaltic crust forms when hot material from the convecting mantle partially melts and moves upwards by volcanic eruption or through mid-ocean ridges. And finally, recycling of basaltic crust and water inside the mantle results in partial melting of the secondary crust. This type of crust constitutes the bulk of the continental crust of the Earth. Lastly, the ternary crust forms through the recycling of secondary crust by plate tectonics, i.e., slaps of secondary crust subduct at ocean trenches and are molten in the mantle to later reemerge at ocean ridges as magmatic extrusions.

In principle, given the bulk composition of the upper silicate shell (crust and mantle) of a planet and given a temperature profile, the mineralogy at each depth inside the crust can be calculated. Next from the resulting mineralogy and from the temperature the density and the elastic moduli can be calculated. However, because of the fact that the crust is relatively thin with respect to the size of the planet, the moment of inertia calculated from the average crustal density or from a depth changing density will only be marginally different. Similarly, the deviations of the fine grained elastic properties of the crust from homogeneity have a negligible effect on the deformational resulting from a tidal forcing. Consequently, for modeling planetary interiors we will hence assume that the crust is homogeneous and parameterize it by its average density, thickness, and by average elastic properties.

3.2 The mineralogy of the mantle

The mantle of terrestrial planets is composed mainly of silicates. In analogy with the knowledge acquired relative to the mantle of the Earth one assumes, similarly to *Verhoeven et al.* [2005], that the mantles of terrestrial planets are made principally of those minerals occurring inside the mantle of the Earth. The Earth upper mantle minerals here considered are olivine, orthopyroxene, clinopyroxene, and garnet. As the pressure inside the mantle of terrestrial planets is much lower than inside the mantle of Earth (with the exception of Venus), not every high pressure phase transition occurring inside the mantle of the Earth will occur in planetary mantles.

Schematically, in the olivine (α) system at about 10GPa, Fig.[3.1], olivine progressively transforms to ringwoodite (γ phase) and to wadsleyite (β phase). At pressures above about 16GPa only ringwoodite prevails. Finally at pressures about 20GPa ringwoodite transforms to perovskite and magnesium wüstite.

The location of the phase transition from olivine to its high pressure β and γ phases does not only dependent on pressure and temperature but also on the bulk iron number Fe#. The iron number Fe#[2] is the ratio of ferrous iron atoms to the sum of magnesium

[1] A mafic rock is a silicate mineral that is rich in magnesium and iron. Ultramafic rocks have $< 42\%$ silica content. The Earth's mantle is composed of ultramafic rocks.

[2] The magnesium number Mg#=1-Fe#

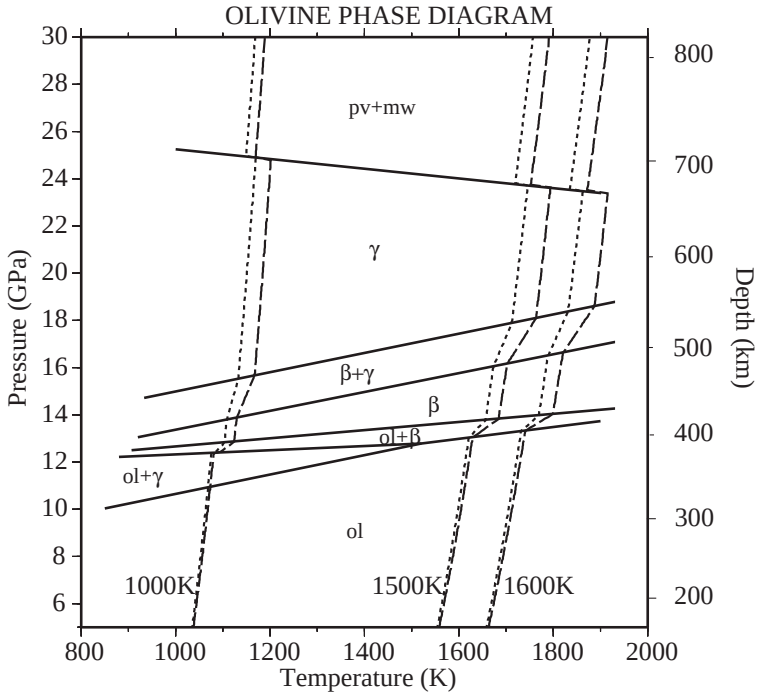


Figure 3.1: Phase diagram of olivine ($Mg_{0.89}, Fe_{0.11}$) from *Vacher et al.* [1998]. ol: olivine, β: wadsleyite, γ: ringwoodite, pv: perovskite, mw: Mg-wüstite.

atoms and ferrous iron ions

$$\text{Fe\#} = \frac{n(\text{Fe}^{2+})}{n(\text{Mg}) + n(\text{Fe}^{2+})} \tag{3.1}$$

of the bulk mantle composition. As can be seen in Fig.[3.2], the pressure where the transition of olivine-α to β and γ occurs strongly decreases with increasing iron number. Consequently, for Mars, as the the bulk mantle iron weight fraction is higher, about 20wt%, than for the Earth, about 8wt%, the phase transition of olivine to its high pressure polymorphs occurs at a lower depth compared to the Earth [*Mocquet et al.*, 1996].

The garnet-pyroxene system is somewhat more complicated. Schematically, the low pressure phases orthopyroxene and low pressure pyroxene transform to high pressure pyroxene at pressures above about 6GPa Fig.[3.3]. At pressures above 12GPa and below about 15GPa, high pressure pyroxene progressively transform to majorite Fig.[3.3]. Finally starting from about 22GPa, majorite starts to transform to the minerals akimotoite (previously called ilmenite) and perovskite.

The chemical formulas of the mantle minerals are those used by *Verhoeven et al.* [2005] and given in Tab.[3.1]. Note that the high pressure polymorphs of the low pressure minerals have identical chemical formulas, however, their associated thermoelastic properties are significantly different Tab.[3.2] and Tab.[3.3]. The properties of the individual minerals depend explicitly on the fraction of iron atoms. The fraction of iron atoms in each mineral depends on the bulk iron number. In general, the fraction of iron atoms within each mineral is a function of local pressure and temperature and depends on the other minerals occurring at that pressure and temperature, i.e., iron can be partitioned

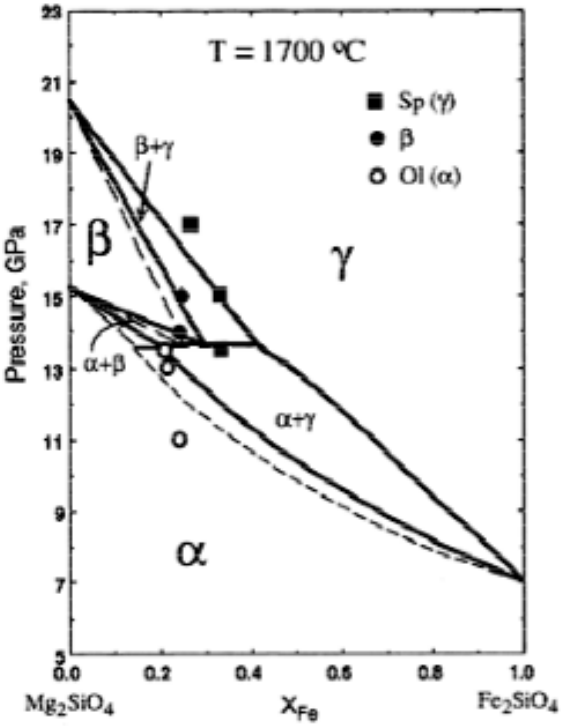


Figure 3.2: Isothermal phase relations of the $Mg_2SiO_4 - Fe_2SiO_4$ system at 1996K [*Bertka and Fei*, 1997] as a function of Fe#.

differently between the individual minerals. Following *Verhoeven et al.* [2005] it is here assumed that the mantle is chemically homogeneous and that the partitioning of iron in the individual minerals is identical. For pure mineral phases the atomic fraction of iron atoms is then identical to Fe#. During phase transition, i.e., the pressures and temperatures domains where both phases are present, the fraction of iron atoms within each mineral phase is calculated from phase diagrams. For instance in the olivine system, see Fig.[3.2], Mg_2SiO_4 and Fe_2SiO_4 from a solid solution. When only one phase is present the fraction of each compound is determined through the Fe#. However, when a phase transition occurs, the relative proportion of Mg_2SiO_4 and Fe_2SiO_4 in each phase (i.e. the Fe#) is determined by the lever rule from the phase diagram.

Note that if the bulk mantle composition contains aluminum it will most likely be incorporated into pyroxenes, garnet, akimotoite, and perovskite. Here we will however assume that the fraction of aluminum of the bulk mantle composition is small enough (below 1%) that the aluminum bearing phases can be neglected. Finally, as done in *Verhoeven et al.* [2005], the calcium contribution in calcium bearing garnet phases resulting from the phase transition of Ca-pyroxene to garnet and from initial low pressure garnet is also neglected.

Following *Verhoeven et al.* [2005], given the iron number and for given fractions of the low pressure minerals olivine, pyroxenes, and garnet, herein also called mantle bulk composition, the depth dependent fractions of mineral polymorphs and high pressure phases are determined from experimentally established phase diagrams.

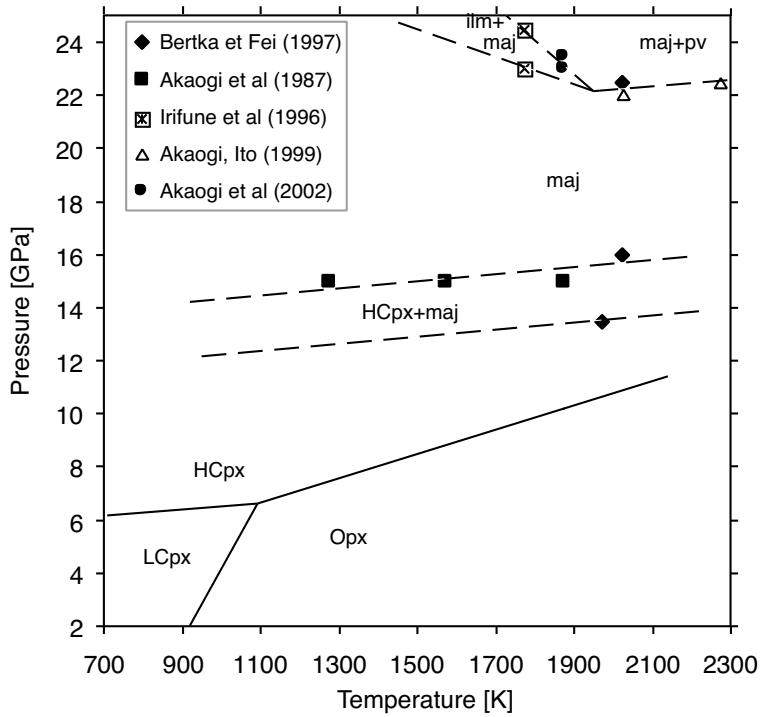


Figure 3.3: Phase diagram of pyroxenes and garnets. Solid [*Ulmer and Stalder*, 2001] and dashed curves correspond to well-determined and less constrained boundaries, respectively. The positions of the latter boundaries are discussed in the text. The letters *ilm*, *maj*, *pv*, *HCpx*, *LCpx* and *Opx* represent ilmenite (akimotoite), majorite, perovskite, high-pressure clinopyroxenes, low-pressure clinopyroxenes and orthopyroxenes, respectively.

Phase	Abbr.	Formula	Chemical formula
olivine	ol	$(Mg_{1-y}Fe_y)_2SiO_4$	$(Mg_{1-y}Fe_y)_2SiO_4$
wadsleyite	wad	$(Mg_{1-y}Fe_y)_2SiO_4$	$(Mg_{1-y}Fe_y)_2SiO_4$
ringwoodite	ring	$(Mg_{1-y}Fe_y)_2SiO_4$	$(Mg_{1-y}Fe_y)_2SiO_4$
clinopyroxene LP	LCpx	$(Mg_{2(1-y)}Mg_{2(1-y)}Fe_{2y}Fe_{2y})Si_4O_{12}$	$(Mg_{1-y}Fe_y)SiO_3$
clinopyroxene HP	HCpx	$(Mg_{2(1-y)}Mg_{2(1-y)}Fe_{2y}Fe_{2y})Si_4O_{12}$	$(Mg_{1-y}Fe_y)SiO_3$
orthopyroxene	opx	$(Mg_{4(1-y)}Fe_{4y})Si_4O_{12}$	$(Mg_{1-y}Fe_y)SiO_3$
Ca-pyroxene	Ca-px	$Ca_2(Mg_{2(1-y)}Fe_{2y})Si_4O_{12}$	$Ca(Mg_{1-y}Fe_y)Si_2O_6$
akimotoite	ak	$(Mg_{1-y}Fe_y)SiO_3$	$(Mg_{1-y}Fe_y)SiO_3$
garnet	gt	$(Mg_{3(1-y)}Mg_{(1-y)}Fe_{3y}Fe_y)SiSi_3O_{12}$	$(Mg_{1-y}Fe_y)SiO_3$
Mg-perovskite	pv	$(Mg_{1-y}Fe_y)SiO_3$	$(Mg_{1-y}Fe_y)SiO_3$
Mg-wüstite	mw	$(Mg_{1-y}Fe_y)O$	$(Mg_{1-y}Fe_y)O$

Table 3.1: Chemical formulas of mantle minerals.

	ρ_0 g/cm^3	$\rho_{0,Fe}$ g/cm^3	a_0 K^{-1}	b_0 K^{-2}	c_0 K	$\gamma t h_0$	$K_{S,0}$ GPa	$K_{S,0,Fe}$ GPa	$\left(\frac{\partial K_{S,0}}{\partial P}\right)_S$	$\left(\frac{\partial K_{S,0}}{\partial T}\right)_S$ GPa/K
ol	3.222	1.182	2.832	0.758	0.	1.14	$129. \pm 1.3$	0.	4.2 ± 0.13	-0.016 ± 0.0027
wad	3.472	1.24	2.711	0.6885	0.5767	1.32	$172. \pm 1.8$	0.	4.5 ± 0.23	-0.016 ± 0.004
ring	3.548	1.30	1.872	0.421	0.6537	1.21	$185. \pm 1.9$	35.	4.1 ± 0.41	-0.024 ± 0.0048
Mg-pv	4.108	1.07	1.17	1.51	0.	1.31	$264. \pm 2.6$	0.	4.0 ± 0.2	-0.015 ± 0.003
Mgw	3.584	2.28	3.0	1.2	0.	1.45	$163. \pm 1.6$	$-15.$	4.0 ± 0.4	-0.019 ± 0.0038
cpx LP	3.208	0.80	2.86	0.72	0.	1.05	$112. \pm 2.2$	$-5.$	6.6 ± 1.4	-0.012 ± 0.003
cpx HP	3.297	0.82	2.86	0.72	0.	1.05	$112. \pm 2.2$	$-5.$	6.6 ± 1.4	-0.012 ± 0.003
opx	3.194	0.81	2.86	0.72	0.	1.05	$109. \pm 2.2$	$-5.$	7.0 ± 1.4	-0.012 ± 0.003
Ca-px	3.277	0.38	2.32	1.88	0.	1.06	$105. \pm 1$	13.	$6.2 - 1.9x_{Fe} \pm 0.62$	-0.013 ± 0.0032
aki	3.810	1.1	2.27	0.682	–0.385	1.38	$212. \pm 2.1$	0.	5.6 ± 1.12	-0.017 ± 0.0042
maj	3.565	0.76	2.08	1.43	0.	1.17	$171. \pm 1.8$	15.	4.4 ± 0.44	-0.021 ± 0.0042

Table 3.2: Thermoelastic constants at STP conditions ($P = 10^5$Pa, $T = 298$K) [*Verhoeven et al.*, 2005] for the mantle. ρ, K_S, and μ are the density, the bulk modulus, and the shear modulus. ρ_{Fe} and $K_{S,\mathrm{Fe}}$ give the iron content dependence of the density and bulk modulus. The coefficients a_0, b_0 and c_0 govern the expansion of the thermal expansivity $\alpha(T) = a_0 + b_0\, T - c_0\, T^{-2}$. Abbreviations: cpx: Ca-pyroxene, gt: garnet, ol: olivine, opx: orthopyroxene, LP: low pressure, HP: high pressure.

	G_0 GPa	$G_{0,Fe}$ GPa	$\left(\frac{\partial G_0}{\partial P}\right)_S$	$\left(\frac{\partial G_0}{\partial T}\right)_S$ GPa/K
ol	$81. \pm 0.81$	$-31. \pm 0.31$	1.4 ± 0.098	-0.014 ± 0.00238
wad	$112. \pm 1.68$	$-40. \pm 0.60$	1.5 ± 0.150	-0.014 ± 0.00350
ring	120.4 ± 1.81	$-28. \pm 0.42$	1.3 ± 0.195	-0.015 ± 0.00300
Mg-pv	$175. \pm 3.50$	$0. \pm 0.00$	1.8 ± 0.270	-0.029 ± 0.00725
Mgw	$130. \pm 2.60$	$-77. \pm 1.54$	2.3 ± 0.470	-0.024 ± 0.00500
cpx LP	$75. \pm 1.50$	$10. \pm 0.20$	1.6 ± 0.240	-0.012 ± 0.00300
cpx HP	$75. \pm 1.50$	$10. \pm 0.20$	1.6 ± 0.240	-0.012 ± 0.00300
opx	$75. \pm 1.50$	$10. \pm 0.20$	1.6 ± 0.240	-0.012 ± 0.00300
Ca-px	$67. \pm 1.34$	$-6. \pm 0.12$	1.7 ± 0.255	-0.010 ± 0.00250
aki	$132. \pm 2.64$	$-41. \pm 0.82$	1.7 ± 0.255	-0.017 ± 0.00425
maj	$92. \pm 1.84$	$7. \pm 0.14$	1.4 ± 0.210	-0.010 ± 0.00250

Table 3.3: Thermoelastic constants and associated uncertainties at STP conditions (STP: $P_0 = 10^5$ Pa, $T_0 = 298$ K) [*Cammarano et al.*, 2003]. G_0 is the shear modulus and $G_{0,Fe}$ gives the iron content dependence of the density bulk and shear modulus. LP refers to low pressure, HP to high pressure.

3.3 Temperature inside the mantle

The thermal state of a planet depends on the gravitational energy gained during its formation, on the concentration of radiogenic elements, on the mantle rheology, on the thermal properties of its constituents, and on the fraction of light elements inside the core. If all those conditions were known, than the temperature profile inside the planet could be calculated. Here we will however not calculate the temperature inside the planet, but use instead published mantle temperature profiles from studies dedicated to the thermal evolution of planets.

3.4 Thermodynamics of the mantle

As indicated in Sect.[3.2] given a bulk mantle composition and a mantle temperature profile the fractions of each of the above introduced phases can be calculated at each pressure inside the mantle. By means of an equation of state and from the thermoelastic properties of each mineral known at reference pressure and temperature conditions, see Tab.[3.2], the density and elastic moduli of each phase are then calculated at local temperature and pressure. The density and elastic moduli at a given depth of the aggregate is calculated by the Hashin-Strikman average.

To calculate the thermoelastic properties of mineral phase i at a given pressure and temperature inside the mantle we proceed as follows: Since each mineral phase of our model is a solid solution among two species, e.g. olivine is a solid solution of forsterite (Mg_2SiO_4) and fayalite (Fe_2SiO_4), the thermoelastic properties of each phase are calculated from the thermoelastic properties of its species. The fraction of iron atoms within each phase determines the concentration of the iron end-member species. Following *Vacher et al.* [1998] and *Verhoeven et al.* [2005] we assume that for each phase i only the density $\rho_{0,i}$, the adiabatic incompressibility $K_{S0,i}$, and the shear modulus $G_{0,i}$ depend on

the fraction of iron atoms and that the dependence on the iron fraction is approximatively linear:

$$\rho_{0,i}(P_0, T_0) = \rho_i(P_0, T_0) + y\ \rho_{0,\mathrm{Fe},i}(P_0, T_0) \tag{3.2}$$
$$K_{S0,i}(P_0, T_0) = K_{S,i}(P_0, T_0) + y\ K_{S0,\mathrm{Fe},i}(P_0, T_0) \tag{3.3}$$
$$G_{0,i}(P_0, T_0) = G_i(P_0, T_0) + y\ G_{0,\mathrm{Fe}}(P_0, T_0),, \tag{3.4}$$

where the subscripts "$_0$" means that those quantities are calculated at reference conditions, i.e., at P_0 and T_0, usually ambient conditions and the quantities to the right-hand side of the equality sign refer to the magnesium end-member species and to an iron fraction proportional correction.

Second, each individual phase i is heated at constant pressure, P_0, from the reference temperature T_0 to an intermediary temperature ϑ_i, called the foot of the adiabat (to be defined later). From the definition of the thermal expansivity α [e.g. *Poirier*, 2000]

$$\alpha = -\left(\frac{\partial\ \log\rho}{\partial T}\right)_P \tag{3.5}$$

the density of phase i at temperature ϑ_i is then calculated from the density at reference condition (3.2)

$$\rho_i(P_0, \vartheta_i) = \rho_{0,i}(P_0, T_0)\ \mathrm{e}^{-\int_{T_0}^{\vartheta_i} dT\ \alpha_i(P_0,T)}, \tag{3.6}$$

where α_i is the temperature dependent thermal expansivity of mineral i, see Tab.[3.2]. Following *Trampert et al.* [2001], the adiabatic bulk modulus at ϑ_i is calculated from

$$K_{S,i}(P_0, \vartheta_i) = K_{S0,i}(P_0, T_0)\left(\frac{\rho_i(P_0, \vartheta_i)}{\rho_{0,i}(P_0, T_0)}\right)^{\delta_{S0,i}}, \tag{3.7}$$

where δ_{S0} is the *Anderson-Grüneisen* parameter, defined as follows [e.g. *Stacey and Davis*, 2008]

$$\delta_{S0,i} = -\frac{1}{\alpha_i(P_0, T_0)}\left(\frac{\partial\ \ln K_{S,i}}{\partial T}\right)_{P_0}. \tag{3.8}$$

Eq. (3.7) can be readily derived from the definition of δ_{S0} by using the definition of the thermal expansivity (3.5). The value of the Anderson-Grünesien parameter is to a very good approximation independent of temperature [*Anderson*, 1988]. Therefore, the value calculated at reference condition is used for all T.

The dependence on temperature of the shear modulus is measured to be approximatively linear. The shear modulus at the foot of the adiabat for phase i is then

$$G_i(P_0, \vartheta_i) = G_{0,i}(P_0, T_0) + \left(\frac{\partial\ G_i}{\partial T}\right)_P (\vartheta_i - T_0). \tag{3.9}$$

The derivative of the shear modulus with respect to temperature is given in Tab.[3.2].

Next, each phase is compressed adiabatically from reference pressure P_0 and temperature ϑ_i to local mantle pressure and temperature (P, T). To calculate the density and the adiabat incompressibility in (P, T) we use a finite strain fourth-order *Birch-Murnaghan*

equations of state [e.g *Stacey and Davis*, 2008, Chap. 18]. The Birch-Murnaghan equations read

$$P = -3K_S(P_0,\vartheta)(1-2\varepsilon)^{5/2}\left(\varepsilon + \frac{3}{2}\left[4-K'_S\right]\varepsilon^2\right) \tag{3.10}$$

$$K_S(P,T) = K_S(P_0,\vartheta)(1-2\varepsilon)^{5/2}\left\{1+\left[5-3K'_S\right]\varepsilon - \frac{27}{2}\left[4-K'_S\right]\varepsilon^2\right\}, \tag{3.11}$$

where $K'_S = \left(\frac{\partial K_S}{\partial P}\right)_T$ and ε is the the Eulerian strain and defined by

$$\varepsilon = \frac{1}{2}\left(1-\left[\frac{\rho(P,T)}{\rho(P_0,\vartheta)}\right]^{2/3}\right). \tag{3.12}$$

One way to derive the Birch-Murnaghan equation of state is to assume a functional expression for the mutual potential energy of neighboring atoms within the crystal lattice of a mineral. By assuming a specific crystal structure, the potential energy can be related to the total bond energy of the crystal. Fundamental thermodynamic definitions relate the derivatives of the total energy to thermodynamic state functions. The state function of pressure is defined as minus the first derivative of the total energy with respect to the volume and the bulk modulus is the volume times the second derivative of the total energy with respect to volume. (3.10) are then obtained by using fourth order polynomial in the ratio of the zero pressure atomic separation to the atomic separation [e.g. *Stacey and Davis*, 2008, Chap. 18].

In the above notation the thermodynamic quantities refer to those of each phase, to unclutter the notation the subscript i has been dropped.

Unlike pure compression, pure shear deformation does not result in a temperature rise. Therefore the isothermal and the adiabatic shear modulus are identical. The equation describing the pressure dependence of the shear modulus are based on second-order elasticity theory and not from finite strain theory [e.g. *Stacey and Davis*, 2008, Chap. 18]. The pressure and temperature corrected $G(P,T)$ are, in the notation of *Cammarano et al.* [2003],

$$G = (1-2\varepsilon)^{5/2}(M_1 + M_2\varepsilon + M_3\varepsilon^2) \tag{3.13}$$

with $M_1 = G_0$, $M_2 = 5M_1 - 3K_{S0}G'$, and $M_3 = 9K_{S0}^2G'' - 3M_2(K'_S-4) + 5M_1(3K'_S-5)$. This functional form of the dependence of the shear modulus on pressure can be derived by expanding the atomic bond potential to second order in atomic bond length about the equilibrium bond length (the bond length at reference pressure) [e.g. *Stacey and Davis*, 2008, Chap. 18].

In the equations (3.10), (3.11), and (3.13) for ρ, K_S, and G first and second derivatives with respect to pressure at (P_0,ϑ) are used. They can be calculated as follows. The first derivatives with respect to pressure of the elastic moduli are to be evaluated in (P_0,ϑ). Following *Jackson* [1998], it is assumed that the poorly determined second mixed derivative $\partial^2 K_S/\partial T\partial P$ is constant. Therefore, K'_S at (P_0,ϑ) is approximated by its value at reference conditions:

$$\left(\frac{\partial K_S}{\partial P}\right)_{\{P_0,\vartheta\}} \approx \left(\frac{\partial K_S}{\partial P}\right)_{\{P_0,T_0\}}. \tag{3.14}$$

The validity of this approximation for G' is also assumed, albeit this has not yet been established [*Trampert et al.*, 2001]. The second derivative of G with respect to pressure is derived form Stacey's relation between shear and bulk modulus [*Stacey*, 1995]

$$G = A\,K_S + B\,P. \tag{3.15}$$

The constants A and B are determined at P_0. The second derivative of G with respect to P is then

$$G''(\vartheta) = A\,K_S''(\vartheta). \tag{3.16}$$

Falzone and Stacey [1980] have established that the bilinear equation relating shear modulus to pressure and bulk modulus (3.15) is a general expression that can be derived from the functional form of the bonding potential and its expansion about the equilibrium atomic bond length within the crystal, see also the discussion in *Stacey and Davis* [2008, Chap. 18].

Finally, although the second derivative of K_S with respect to P is poorly constrained through laboratory measurements it can be calculated from [*Trampert et al.*, 2001]

$$27K_S(\vartheta)\,(K_S(\vartheta)K_S''(\vartheta) - K_S'(\vartheta)\,[7 - K_S'(\vartheta)] + 143/9) = 0. \tag{3.17}$$

This relation between the adiabatic bulk modulus and its derivative with respect to pressure is a natural consistency relation between the coefficients of the polynomial expansion of the total bond energy of the crystal.

The last step of the multistep procedure for calculating the density and the elastic moduli at local pressure and temperature in the mantle is the determination of the foot of the adiabat. The foot of the adiabat is different for each mineral, it is the temperature ϑ_i one would obtain by decompressing mineral i from (P, T) to to reference pressure P_0 adiabatically. Like compression, decompression is dependent on the thermodynamic procedure of each mineral, consequently the foot of the adiabat for each mineral is generally different. See also Fig.[3.4] for a schematic illustration of adiabatic decompression for two different minerals.

The temperature variation along an adiabatic temperature profile as a function of density is described by the thermodynamic Grüneisen parameter γ_{th} [e.g. *Stacey and Davis*, 2008, Chap. 19]

$$\gamma_{\text{th}} = \left(\frac{\partial\ \log T}{\partial \log \rho}\right)_S. \tag{3.18}$$

It has been established by *Anderson* [1979] that within the quasi-harmonic approximation [3] the thermodynamic Grüneisen parameter is inversely proportional to a power of the density

$$\gamma_{\text{th}}(P, T) \sim \rho(P, T)^{-q}, \tag{3.19}$$

where q is a measured constant close to 1. With this approximation (3.18) can be integrated from ϑ to T

$$T(P, \vartheta) = \vartheta\ e^{\frac{\gamma_{th0}(P_0,T_0)}{q}\left[\frac{\rho(P_0,T_0)}{\rho(P_0,\vartheta)}\right]^q\left[1-\left(\frac{\rho(P_0,\vartheta)}{\rho(P_0,T)}\right)^q\right]}. \tag{3.20}$$

[3] In the quasi-harmonic approximation γ is independent on temperature at constant volume [e.g. *Anderson*, 2005, Chap. 18].

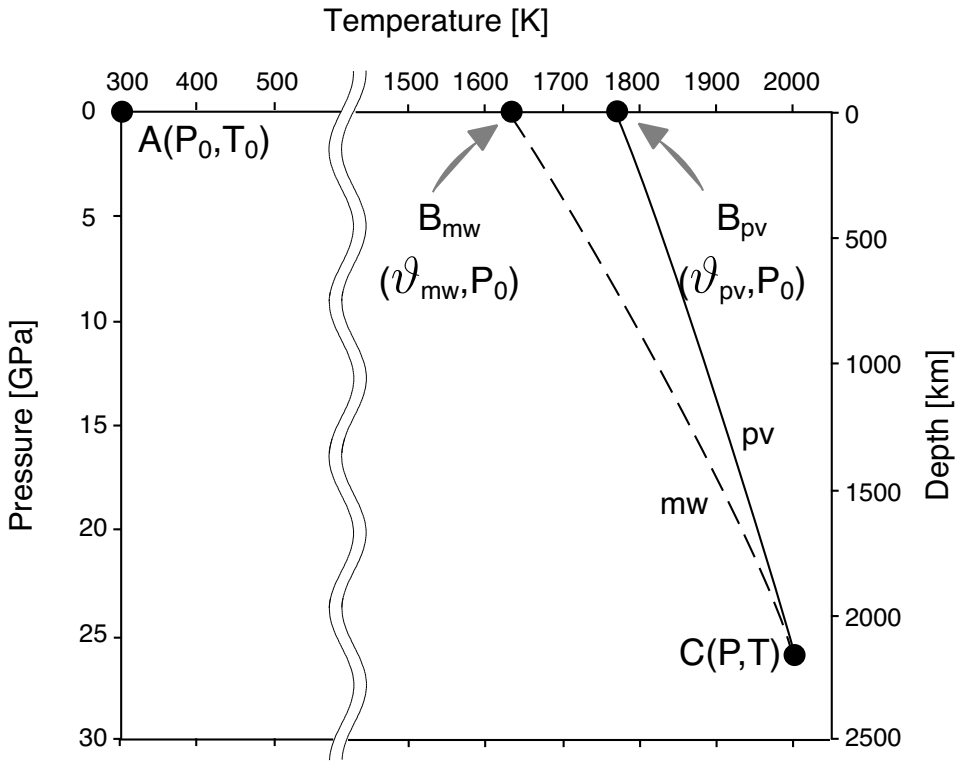


Figure 3.4: Thermodynamic paths, linking reference pressure and temperature (point A) to local pressure and temperature (point C). Illustration for the minerals perovskite (pv) and magnesium-wüstite (mw) drawn as a continuous curve and as a dashed curve. Each mineral, is heated at constant pressure from point A to point B, followed by an adiabatic compression to point C. The temperature ϑ, corresponding to point B, is different for each mineral. It is defined as the temperature at the reference pressure such that an adiabatic compression would bring the mineral from local pressure and temperature in B to conditions in C.

Note that to obtain this equation (3.19) has to be applied a second time in order to relate $\gamma_{\rm th}(P_0, \vartheta)$ to $\gamma_{\rm th}(P_0, T_0)$. Formally (3.20) can be written as

$$T - F(P, T, \tau) = H(\tau). \tag{3.21}$$

The foot of the adiabatic, ϑ, for each mineral is then found by seeking the real root of $H(\tau = \vartheta) = 0$.

Practical summary

We have adopted the following procedure: For a given depth (P, T) inside the mantle, determine the fractions of each phase and the associated iron number from phase diagrams. For each individual mineral, corrected for its atomic iron fraction, solve (3.21) simultaneously with (3.10) and (3.2) to find the density in (P, T) from the reference values (Tab.[3.2]) and the foot of the adiabat. Once the density in (P, T) and the foot of the adiabat are known, the adiabatic bulk modulus and the shear modulus can be calculated from (3.11) and (3.13).

Thermodynamic properties of aggregates

After the density and the elastic moduli of each mineral have been calculated at (P, T) they have to be averaged in order to calculate the density and the elastic moduli at (P, T). The density of a phase aggregate is calculated from the sum of the masses of each constituent. The density of the aggregate is then

$$\rho(P, T) = \sum_{i=1}^{n} \chi_i \rho_i(P, T), \tag{3.22}$$

where the $\chi_i = V_i/V$ are the volume fractions of the minerals, V the total volume of the aggregate, and V_i is the contribution of mineral i to the total volume.

To calculate the elastic moduli of the aggregate we here use the Hashin-Strikman (HS) average [*Watt et al.*, 1976]. The upper K_+ (G_+) and lower HS bounds K_- (G_-) are:

$$K_{-,+} = K_{1,n} + \frac{A_{1,n}}{1 + \alpha_{1,n} A_{1,n}} \tag{3.23}$$

$$G_{-,+} = G_{1,n} + \frac{1}{2} \frac{B_{1,n}}{1 + \beta_{1,n} B_{1,n}}, \tag{3.24}$$

where the $K_- \leq K \leq K_+$ $(G_- \leq G \leq G_+)$. Prior to calculating the HS average the elastic moduli are sorted by increasing order. The component with the minimal elastic moduli is then subscripted with "1" and the component with the maximal elastic moduli with "n" $(M_{1,n})$. The lower bound M_- is then calculated with the minimal elastic moduli and M_+ with the maximal elastic moduli. The coefficients $\alpha_{1,n}$ $(\beta_{1,n})$ and the $A_{1,n}$ $(B_{1,n})$

are defined as

$$\alpha_{1,n} = -\frac{3}{3K_{1,n} + 4G_{1,n}} \tag{3.25}$$

$$\beta_{1,n} = -\frac{3(K_{1,n} + 2G_{1,n})}{5G_{1,n}(3K_{1,n} + 4G_{1,n})} \tag{3.26}$$

$$A_{1,n} = \sum_{i=2,1}^{n,n-1} \frac{\chi_i}{(K_i - K_{1,n})^{-1} - \alpha_{1,n}} \tag{3.27}$$

$$B_{1,n} = \sum_{i=2,1}^{n,n-1} \frac{\chi_i}{\frac{1}{2}(G_i - G_{1,n})^{-1} - \beta_{1,n}} \tag{3.28}$$

Seismic velocities

Once the density and the elastic moduli at a given depth are calculated the seismic velocities can be computed. The p-wave velocity is

$$v_p(P,T) = \sqrt{\frac{K_S(P,T) + \frac{4}{3}G(P,T)}{\rho(P,T)}}, \tag{3.29}$$

where K_S and G are the bulk and the shear modulus of the mineral aggregate. The s-wave velocity is

$$v_s(P,T) = \sqrt{\frac{G(P,T)}{\rho(P,T)}}, \tag{3.30}$$

and the seismic sound velocity

$$v_\phi = \sqrt{\frac{K_S(P,T)}{\rho(P,T)}}. \tag{3.31}$$

3.5 The electrical conductivity of the mantle

The electrical conductivity σ_i of a mineralogical phase i depends on its composition, pressure and temperature, through a *Arrhenius* type equation

$$\sigma_i(T,P) = \sigma_{i,0}\, \mathrm{e}^{-\frac{E_0 + P\Delta V}{k\,T}}, \tag{3.32}$$

where E_0 and σ_0 are the *activation energy* and the *pre-exponential factor*, ΔV is the *activation volume*, and k the Boltzmann constant.

Vacher and Verhoeven [2007] have studied the dependence of the activation energy and of the pre-exponential factor on the iron content y on the mantle minerals and derived the following empirical relations:

$$\log(\sigma_0(y)) = \log(\sigma_{\mathrm{ref}}) + \alpha \log \frac{y}{y_{\mathrm{ref}}} \tag{3.33}$$

$$E_0(y_i) = E_{\mathrm{ref}} + \beta(y - y_{\mathrm{ref}}). \tag{3.34}$$

Vacher and Verhoeven [2007] have set the reference fraction of iron y_{ref} to 0.1. And have defined the reference conductivity σ_{ref} at infinite temperature. E_{ref} is the activation

	$\log(\sigma_{0,\mathrm{ref}}/1\mathrm{Sm})$	$E_{0,\mathrm{ref}}$ eV	α	β eV
olivine	2.69 ± 0.12	1.62 ± 0.04	2.42 ± 0.18	-0.485 ± 0.25
wadsleyite	3.29 ± 0.20	1.29 ± 0.06	2.42 ± 0.18	-0.485 ± 0.25
ringwoodite	2.92 ± 0.04	1.16 ± 0.01	2.42 ± 0.18	-0.485 ± 0.25
Mg-perovskite	1.28 ± 0.12	0.61 ± 0.04	3.56 ± 1.32	-1.72 ± 0.38
Mg-wüstite	2.56 ± 0.10	0.81 ± 0.03	3.14 ± 0.07	0.
clinopyroxene LP	3.19 ± 0.11	1.86 ± 0.02	-1.28 ± 0.51	-1.41 ± 0.35
clinopyroxene HP	3.19 ± 0.11	1.86 ± 0.02	-1.28 ± 0.51	-1.41 ± 0.35
orthopyroxene	3.66 ± 0.10	1.79 ± 0.02	-1.28 ± 0.51	-1.41 ± 0.35
Ca-pyroxene	3.19 ± 0.11	1.86 ± 0.02	-1.28 ± 0.51	-1.41 ± 0.35
akimotoite	3.29 ± 0.18	1.65 ± 0.03	-1.28 ± 0.51	-1.41 ± 0.35
majorite	3.29 ± 0.18	1.65 ± 0.03	-1.28 ± 0.51	-1.41 ± 0.35

Table 3.4: Table of electromagnetic constants entering the forward problem and their uncertainties. $\log \sigma_{0,\mathrm{ref}}$ and $E_{0,\mathrm{ref}}$ are the logarithm of the pre-exponential factor and the activation energy for a 10% iron-bearing mineral, respectively. The constants α and β govern the iron content contribution to the pre-exponential factor and the activation energy, respectively. The experimental uncertainties on $\log \sigma_{0,\mathrm{ref}}$ and on $E_{0,\mathrm{ref}}$ are taken from *Xu et al.* [2000]

energy for the reference fraction of iron y_{ref}. The constants α and β govern the iron content contribution to the pre-exponential factor and to the activation energy. The values here used for the reference quantities for the above introduced mantle minerals are given in Tab.[3.4]. Once, the electrical conductivity of each phase is determined in (P, T) the electrical conductivity of the mantle phase aggregate corresponding to that depth is calculated with the Hashin-Strikman average Sect.[3.4].

3.6 Electromagnetic induction

3.6.1 Introduction

In Magnetic induction studies (MT) the broad spectrum of naturally occurring geomagnetic variations except those originating from the magnetohydrodynamic processes within the Earth's outer core, are used as a power source for electromagnetic induction in the Earth. The most prominent source results from the interaction of the solar wind with the magnetosphere of the Earth. It has been established by *Tikhonov* [1950] and *Cagniard* [1953] that if orthogonal electric and magnetic field variations are measured simultaneously at the surface of the Earth complex ratios (impedances) can be determined that describe the penetration depths of electromagnetic fields within the Earth. The penetration depth of the electromagnetic field depends on its frequency and on the Earth's conductivity, which is related to local temperature, mineralogy, and chemical composition. Here, we summarize the magneto induction method for the Cartesian half space and the spherical configuration and apply it to estimate the conductivity profile of the Earth mantle.

3.6.2 Assumptions of the Magneto induction method

For an overview and a detailed introduction to the subject see for instance *Simpson and Bahr* [2005]. In order to consider the electromagnetic induction inside a planet a number of simplifying assumptions are usually made [e.g. *Cagniard*, 1953]:

1. The Earth does not generate electromagnetic energy by itself (the contribution of an eventual core dynamo is neglected), but only dissipates or absorbs it.

2. All fields are conservative and analytic away from their sources.

3. The natural source field, generated by large scale ionospheric current systems that are relatively far from Earth's surface, are supposed to be uniform, plane-polarized electromagnetic waves impinging on the Earth at near-vertical incidence.

4. Free charges are not expected to accumulate and to be sustained within the layered Earth.

5. Charge is conserved, and the Earth behaves as an ohmic conductor

$$\mathbf{j} = \sigma \mathbf{E}, \tag{3.35}$$

   where $\mathbf{j}$ is the total electric density density (in Am^{-2}), σ is the conductivity of the medium (in Sm^{-1}) and $\mathbf{E}$ is the electric field (in Vm^{-1}).

6. For the MT sounding periods, the electric displacement fields are quasi-static and therefore, time-varying displacement currents are negligible compared with time-varying conduction currents; therefore, electromagnetic induction is treated as a purely diffusion process.

7. Variations in the electrical permittivities and magnetic permeabilities of rocks are assumed negligible compared with variations in bulk rock conductivities.

The incident plane wave electric $\mathbf{E}$ and magnetic field $\mathbf{B}$, with angular frequency ω, initial amplitudes $\mathbf{E_0}$ and $\mathbf{B_0}$ and wavenumber $\mathbf{k}$ are

$$\mathbf{E} = \mathbf{E_0} e^{i(\omega t - \mathbf{k}\cdot\mathbf{r})} \tag{3.36}$$

$$\mathbf{B} = \mathbf{B_0} e^{i(\omega t - \mathbf{k}\cdot\mathbf{r})}, \tag{3.37}$$

where the period $T = 2\pi/\omega$ and the wavelength $\lambda = 2\pi/|\mathbf{k}|$.

Within the assumptions of the MT method, i.e. the negligible time varying displacement currents, the negligible change in the electrical permittivities, ϵ and magnetic permeabilities, μ, compared to changes in rock conductivities, σ, and the assumption of a linear isotropic medium, the Maxwell equations can be written as

$$\nabla \times \mathbf{E} = -\frac{\partial \mathbf{B}}{\partial t} \tag{3.38}$$

$$\nabla \times \mathbf{B} = \mu_0 \sigma \mathbf{E} \tag{3.39}$$

$$\nabla \cdot \mathbf{B} = 0 \tag{3.40}$$

$$\nabla \cdot \mathbf{E} = \eta_f / \varepsilon_0, \tag{3.41}$$

where η_f is the electric charge density and $\mu_0 = 1.2566\,10^{-6}\mathrm{Hm}^{-1}$ and $\varepsilon_0 = 8.85\,10^{-12}\mathrm{Fm}^{-1}$ are the free space electrical permittivities and magnetic permeabilities. By taking the divergence of equation (3.35) and assuming that no current sources exists within the Earth, it follows that

$$0 = \nabla \cdot \mathbf{j} = \nabla \cdot (\sigma \mathbf{E}) = \nabla\,\sigma \cdot \mathbf{E} + \sigma \nabla \cdot \mathbf{E}. \tag{3.42}$$

Furthermore, if σ is homogeneous, i.e. $\nabla\,\sigma = 0$, then $\nabla \cdot \mathbf{E} = 0$.

The diffusion equation for $\mathbf{E}$ is then obtained by taking the curl of equation (3.38). It is

$$\nabla^2 \mathbf{E} = \mu_0 \sigma \frac{\partial \mathbf{E}}{\partial t}, \tag{3.43}$$

or with the plane wave assumption of equation (3.36)

$$\nabla^2 \mathbf{E} = i\omega\mu_0\sigma\mathbf{E}. \tag{3.44}$$

Similarly, by taking the curl of equation [3.39], one has with the plane wave assumption

$$\nabla^2 \mathbf{B} = i\omega\mu_0\sigma\mathbf{B}. \tag{3.45}$$

3.6.3 Applications

In this section, we apply the MT method to three different settings. The homogeneous half-space, the layered half-space, and the layered sphere. The homogeneous half-space and its simplest extension, the layered half-space, are both useful approximations for the conductive structure of planets when the frequency of the incident electromagnetic waves are high, i.e., when the sampling depth is restricted to the upper part of the mantle, and when the analyzed surface patch is small with respect to the size of the planet. In other words, when the sphericity can be neglected the setting is approximatively Cartesian. For smaller planets, and for very low frequencies, i.e. for sounding of the deep mantle, the conductive structure of the planet has to be modeled by a layered sphere.

The homogeneous half-space

In a one-dimensional setting, infinite half-space along the x and y axes, the diffusion equation (3.43) has the following general solution

$$\mathbf{E} = \mathbf{E_1} e^{i(\omega t - q\,z)} + \mathbf{E_2} e^{i(\omega t + q\,z)} \tag{3.46}$$

Since the electric field must remain finite for arbitrary depths, and as we assumed that no internal sources generate electrical energy, $\mathbf{E_2} = 0$. Inserting the general solution in equation (3.44) yields

$$q = \sqrt{i\omega\mu_0\sigma} = \sqrt{\frac{\mu_0\omega\sigma}{2}}(1+i). \tag{3.47}$$

The inverse real part of q,

$$p = \sqrt{2/\mu_0\omega\sigma} \tag{3.48}$$

is the *electromagnetic skin depth* or *penetration depth* of an electric field of angular frequency ω into a half space of electrical conductivity σ. If for the Earth mantle we

assume an average mantle electrical conductivity of $10\mathrm{Sm}^{-1}$ then the sounding depth of the gravest known electromagnetic wave from the ionospheric sheet current (11years) is about 2900km or to the depth of the core mantle boundary.

The inverse of q is denoted as C and also called the *Schmucker-Weidelt transfer function*. For the homogeneous half space problem its real part is equivalent to the half of the skin depth. In general a transfer function establishes a linear relationship between a known input an output. For the electromagnetic sounding problem the transfer function establishes a linear relationship between the measurable orthogonal components of the electric (induced) and magnetic (sum of induced and inducing) field at the surface

$$C \equiv \frac{1}{q} = \frac{E_x}{i\omega B_y} = -\frac{E_y}{i\omega B_x} \tag{3.49}$$

as can be obtained inserting (3.38) and (3.46). The complex impedance is defined as

$$Z \equiv \mu_0 \frac{E_x}{B_y} = i\mu_0\omega C. \tag{3.50}$$

Finally, combining (3.48) and (3.49) yields the relation between the resistivity or the inverse of the conductivity of the homogenous half-space and C:

$$\rho = \frac{1}{\sigma} = |C|^2\mu_0\omega. \tag{3.51}$$

The layered half-space

The layered half-space model consists of a stack of layers of constant electrical conductivity.

The general solutions for the diffusion equation of the electrical field (3.44) and for the magnetic field (3.45), obtained by inserting (3.46) in (3.38), within layer n of conductivity σ_n are

$$\begin{aligned} \boldsymbol{\mathcal{E}}_n(z,\omega) &= \begin{pmatrix} E_{x,n} \\ B_{y,n} \end{pmatrix}(z,\omega) = \begin{pmatrix} e^{-q_n z} & e^{q_n z} \\ -\frac{iq_n}{\omega}e^{-q_n z} & \frac{iq_n}{\omega}e^{q_n z} \end{pmatrix} \begin{pmatrix} E_{1,n}e^{i\omega t} \\ E_{2,n}e^{i\omega t} \end{pmatrix} && (3.52) \\ &= \mathcal{A}_n(z)\ \boldsymbol{a_n}(\omega) && (3.53) \end{aligned}$$

where $q_n = \sqrt{i\mu_0\sigma_n\omega}$. The electromagnetic fields at the top of layer n, in z_{n-1} are then related to the fields at the bottom of layer n, in z_n by

$$\boldsymbol{\mathcal{E}}_n(z_{n-1}) = \mathcal{A}_n(z_{n-1})\mathcal{A}_n^{-1}(z_n)\boldsymbol{\mathcal{E}}_n(z_n). \tag{3.54}$$

If we request that the fields are continuous at the transitions from layer $n+1$ to layer n, we can relate the orthogonal horizontal components of $\boldsymbol{E}$ and $\boldsymbol{B}$ on top of layer $n+1$ to those on top of layer n:

$$\boldsymbol{\mathcal{E}}_n(z_{n-1}) = \mathcal{A}_n(z_{n-1})\mathcal{A}_n^{-1}(z_n)\boldsymbol{\mathcal{E}}_{n+1}(z_n). \tag{3.55}$$

At the surface, $z = 0$, the fields for a stack of N layers is then

$$\boldsymbol{\mathcal{E}}_1(z_0) = \left(\prod_{i=1}^{N} \mathcal{A}_i(z_{i-1})\mathcal{A}_i^{-1}(z_i)\right)\boldsymbol{\mathcal{E}}_{N+1}(z_N). \tag{3.56}$$

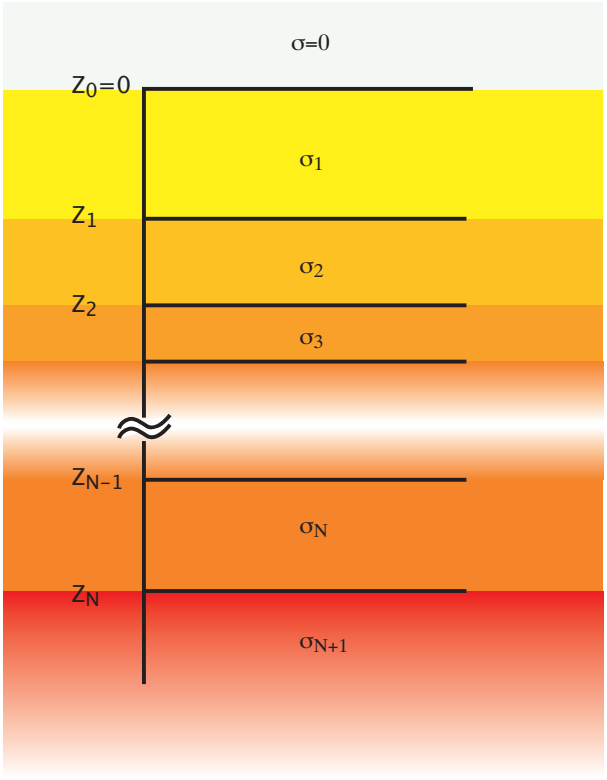


Figure 3.5: $N+1$-layered half-space model

If we assume that the lowermost layer $N+1$ is a homogenous half space, (3.52) with the constraint that $\mathcal{E}$ remains fine for arbitrary depths, reduces to

$$\boldsymbol{\mathcal{E}}_{N+1} = \begin{pmatrix} 1 \\ -\frac{iq}{\omega} \end{pmatrix} E_x \tag{3.57}$$

The surface impedance Z is

$$Z(\omega) = \mu_0 \frac{E_{x,1}(0)}{B_{y,1}(0)} = \mu_0 \frac{\mathcal{Z}_{11} - \frac{iq}{\omega}\mathcal{Z}_{12}}{\mathcal{Z}_{21} - \frac{iq}{\omega}\mathcal{Z}_{22}}, \tag{3.58}$$

where the matrix $\mathcal{Z}$ is defined by

$$\mathcal{Z}(z_0, z_N) = \prod_{i=1}^{N} \mathcal{A}_i(z_{i-1})\mathcal{A}_i^{-1}(z_i) \tag{3.59}$$

Note that surface impedance $Z(\omega)$ only depends on the conductivity of the lowermost half space and not its horizontal electric and magnetic field components.

The apparent resistivity is defined as the resistivity of an equivalent uniform half-space:

$$\rho_a(\omega) = \frac{|Z(\omega)|^2}{\mu_0 \omega}, \tag{3.60}$$

and the *impedance phase* is

$$\phi = \tan^{-1} \frac{E_x}{B_y}. \tag{3.61}$$

Finally, the phase ϕ and the apparent resistivity ρ_a, are linked via a Kramers-Kronig relation [*Weidelt*, 1972].

The stratified sphere

More useful for our purposes, as we deal with very long periods, is the model of the conducting stratified sphere [e.g. *Srivastava*, 1966; *Le Mouël*, 1976].

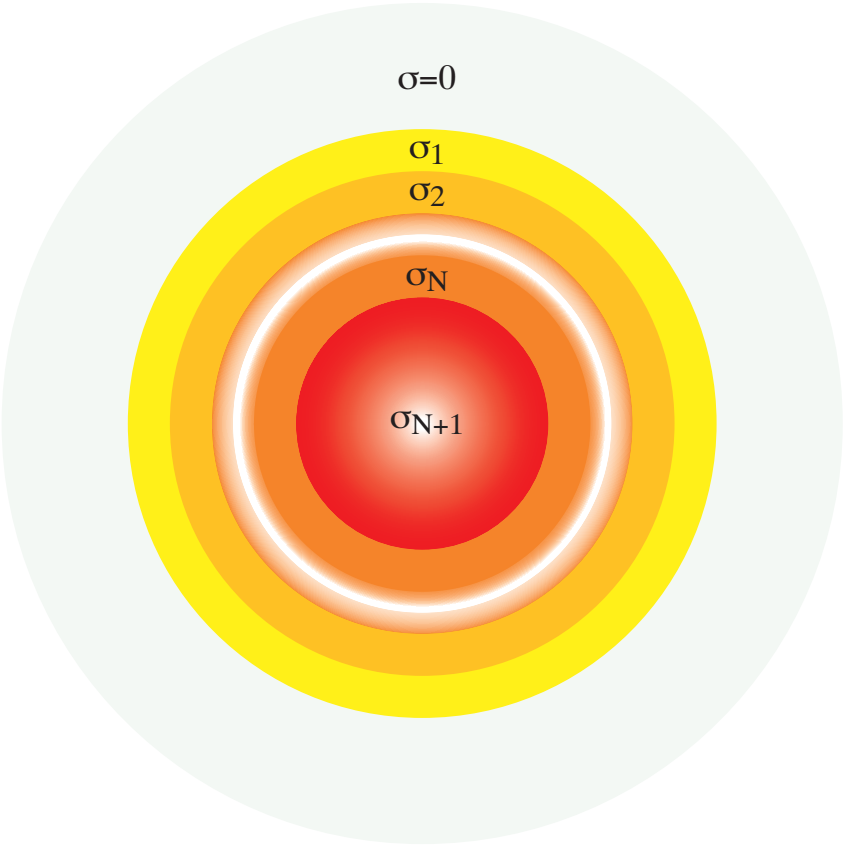


Figure 3.6: Stratified conducting sphere

Again we seek for solutions of the diffusion equations (3.44) and (3.45) inside each spherical shell and apply continuity conditions of the horizontal components of the fields at the transitions of each shell in order to compute the impedance function Z at the surface. This time the diffusion equations are solved in spherical coordinates.

From Maxwell equation $\nabla \cdot \boldsymbol{B} = 0$ it follows that $\boldsymbol{B}$ is solenoidal, in other words it can be represented as the sum of a toroidal and of a poloidal vector field (also known as the *Mie representation* of $\boldsymbol{B}$) [*Backus*, 1986].

$$\boldsymbol{B} = \boldsymbol{T} + \boldsymbol{S}, \tag{3.62}$$

where the vectors $\boldsymbol{T}$ and $\boldsymbol{S}$ are a function of the scalar potentials T and S:

$$\boldsymbol{T} = \nabla \times (T\boldsymbol{r}) \tag{3.63}$$

$$\boldsymbol{S} = \nabla^2 (S\boldsymbol{r}). \tag{3.64}$$

The vector fields $\boldsymbol{T}$ and $\boldsymbol{S}$ are determined uniquely by $\boldsymbol{B}$ in $S(a,b)$, the spherical shell of lower radius a and upper radius b. However, the scalar fields T and S are only determined by $\boldsymbol{B}$ up to an arbitrary additive function in r. One can make the scalar fields unique if they are subjected to the additional conditions that within $S(a,b)$ they are of zero average [*Backus*, 1986].

Within the MT method it is assumed that the inducing $\boldsymbol{B}$ field is purely poloidal. Since the curl of a toroidal field is poloidal [*Backus*, 1986], by equation (3.39) the electric $\boldsymbol{E}$ field is toroidal and the electric and magnetic field can then be written as a function of a common scalar potential f:

$$\boldsymbol{E} = -\nabla \times (\dot{f}\boldsymbol{r}) \tag{3.65}$$

$$\boldsymbol{B} = \nabla \times \nabla \times (f\boldsymbol{r}), \tag{3.66}$$

where the dot stands for the derivative with respect to time. In spherical coordinates, the Fourier transformed components of $\boldsymbol{B}$ and $\boldsymbol{E}$ expanded in spherical harmonics $Y_l^m(\theta,\phi)$ and f_l are:

$$B_r = \frac{l(l+1)}{r} f_l(r) Y_l^m(\theta,\phi) \tag{3.67}$$

$$B_\theta = -\frac{1}{r}\frac{\partial\,(r f_l(r))}{\partial r}\frac{\partial}{\partial\theta} Y_l^m(\theta,\phi) \tag{3.68}$$

$$B_\phi = -\frac{1}{r}\frac{\partial\,(r f_l(r))}{\partial r}\frac{\partial}{\partial\phi}\frac{Y_l^m(\theta,\phi)}{\sin\theta} \tag{3.69}$$

$$E_r = 0 \tag{3.70}$$

$$E_\theta = i\omega f_l(r)\frac{\partial}{\partial\theta} Y_l^m(\theta,\phi) \tag{3.71}$$

$$E_\phi = -i\omega f_l(r)\frac{\partial}{\partial\phi}\frac{Y_l^m(\theta,\phi)}{\sin\theta} \tag{3.72}$$

Note that the toroidal field $\boldsymbol{E}$ is purely tangential, it has no radial component. The r dependent potential function satisfies the following second order differential equation [*Srivastava*, 1966; *Le Mouël*, 1976]:

$$\frac{d^2 f_l(r)}{dr^2} + \frac{2}{r}\frac{d\,f_l(r)}{dr} + \left(q^2(r) - \frac{l(l+1)}{r^2}\right) f_l(r) = 0 \tag{3.73}$$

If the conductivity is constant within a shell then $q = \sqrt{-i\mu_0\sigma\omega}$ and the solution of (3.73) is

$$f_l(r) = A j_l(qr) + B\eta_l(qr), \tag{3.74}$$

where j_l and η_l are spherical Bessel functions of first and second kind of order l. The horizontal orthogonal fields in shell n are then

$$E^l_{\phi,n}(\omega) = -\,i\omega(e_{1,n}(\omega) j_l(q_n r) + e_{2,n}(\omega)\eta_l(q_n r)) \tag{3.75}$$

$$B^l_{\theta,n}(\omega) = \frac{1}{r}\left(e_{1,n}(\omega)\frac{d}{d(q_n\,r)} q_n r\, j_l(q_n r) + e_{2,n}(\omega)\frac{d}{d(q_n r)} q_n r\,\eta_l(q_n r)\right) \tag{3.76}$$

With the notations introduced in the previous section we now have for $\boldsymbol{\mathcal{E}}$ of shell n

$$\begin{aligned}\boldsymbol{\mathcal{E}}^l_n(r) &= \begin{pmatrix} E^l_{\phi,n} \\ B^l_{\theta,n} \end{pmatrix}(\omega) \\ &= \begin{pmatrix} -i\omega j_l(q_n r) & -i\omega \eta_l(q_n r) \\ \frac{1}{r}\frac{d}{d(q_n r)} q_n r\, j_l(q_n r) & \frac{1}{r}\frac{d}{d(q_n r)} q_n r\, \eta_l(q_n r) \end{pmatrix} \begin{pmatrix} e_{1,n} \\ e_{2,n} \end{pmatrix}(\omega) \\ &= \mathcal{A}^l_n(r)\, \boldsymbol{a_n}\end{aligned} \tag{3.77}$$

For the inner most sphere the fields E_ϕ and B_θ need to remain finite in $r = 0$, and as η_l diverges in $r = 0$, e_2 is equal to zero.

$$\boldsymbol{\mathcal{E}}^l_{N+1}(r) = \begin{pmatrix} -i\omega j_l(q\, r) \\ \frac{1}{r}\frac{d}{d(q\, r)} q\, r\, j_l(q\, r) \end{pmatrix} e_1 \tag{3.78}$$

The surface Z impedance for a sphere with N uniformly conducting shells on top of a conducting core

$$Z^l(\omega) = \mu_0 \frac{E^l_{\phi,1}(r_0)}{B^l_{\theta,1}(r_0)} = \mu_0 \frac{-i\omega j_l(q\, r_N)\mathcal{Z}^l_{11} + \left.\frac{d\, q\, r\, j_l(q\, r)}{d(q\, r)}\right|_{r=r_N} \mathcal{Z}^l_{12}}{-i\omega j_l(q\, r_N)\mathcal{Z}^l_{21} + \left.\frac{d\, q\, r\, j_l(q\, r)}{d(q\, r)}\right|_{r=r_N} \mathcal{Z}^l_{22}}, \tag{3.79}$$

where

$$\mathcal{Z}^l(r_0, r_N) = \prod_{i=1}^{N} \mathcal{A}^l_i(r_{i-1})(\mathcal{A}^l_i(r_i))^{-1} \tag{3.80}$$

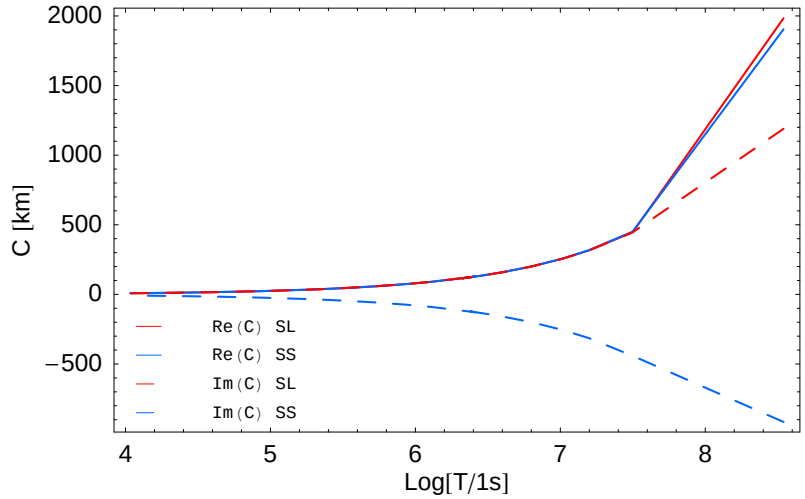
Analogous to the layered half space problem we define the penetration depth for the stratified sphere to be two times the real part of the surface C function. The penetration depth for a sphere of the size of Earth with a homogeneous conductivity of 10S/m is about 3500km for a period of $11a$ and $l = 1$ [4]. This is about 20% deeper then for the case of the homogeneous half space. However, the difference decreases with decreasing period, see Fig.[3.7a].

The period dependent C function for a stratified planet with a core of conductivity $\sigma = 10^4$S/m and a mantle with conductivity $\sigma = 10$S/m is shown in Fig.[3.7a] and Fig.[3.7b]. For comparison we also show C for a half space model with a lower layer that has the same conductivity as the core and an upper layer of the same thickness and conductivity as the mantle. The figures show that the difference of the real part of C of the two models increases with increasing period and increases with decreasing planet size. Also note that the imaginary parts of the two models have opposite sign.

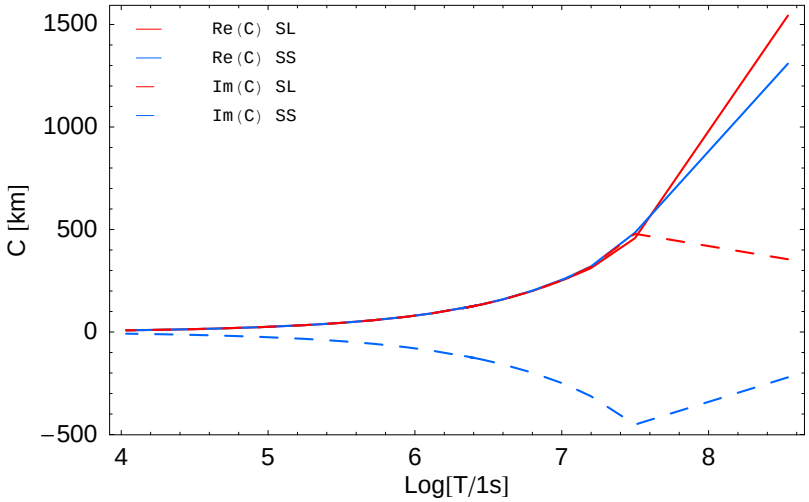
3.6.4 The conductivity of the Earth's mantle

For comparison we also give the C-response values [*Olsen*, 1998] for the Earth, Fig.[3.8]. The periods cover the data range from below one day up to eleven years. The C-response data uncertainties are below 10% for periods below ten days and grow to about 20% for periods up to one year, Fig.[3.8c]. The eleven year signal has a significantly higher associated uncertainty as the acquisition time of induction data is comparatively short when compared to the period of the eleven year signal.

[4] The geometry of the ionospheric sheet current is such that the degree $l = 1$ component of the source field dominates [*Banks*, 1972]



(a)



(b)

Figure 3.7: Real and imaginary (dashed) part of C-response as a function of period. For a layered half-space model (SL, blue curves) and a stratified sphere (SS, red curves). The left figure has Earth size and the right figure has Mars size. The top silicate layer is 2900km (Earth) and 1600km (Mars) thick corresponding to the core sizes for the spherical models of 3471km and 1700km. The conductivity of the top silicate layer (shell) is $\sigma = 10$S/m and of the lower half space (core) is $\sigma = 10^4$S/m.

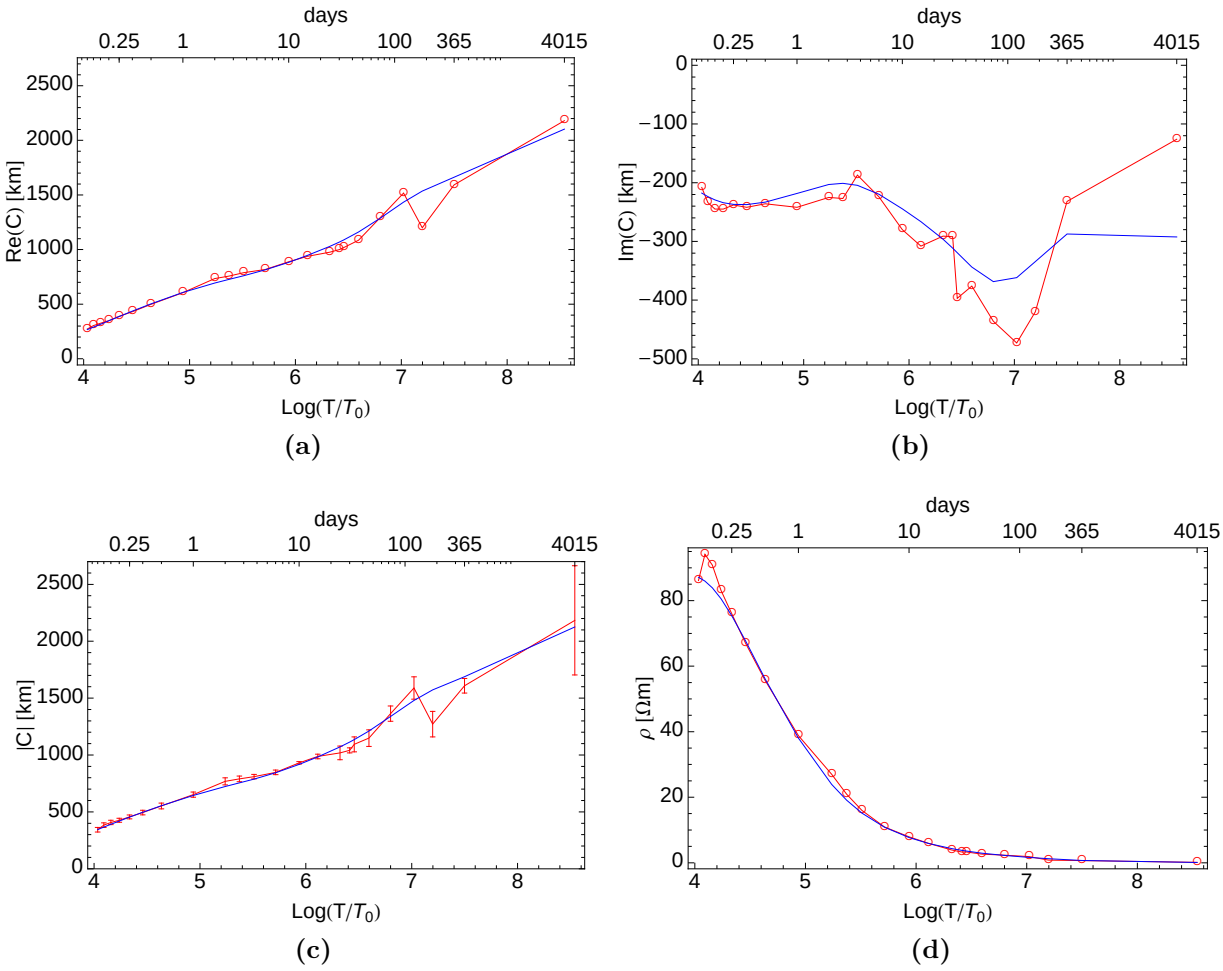


Figure 3.8: Real, imaginary, and absolute part of C-response function and apparent resistivity for the Earth for periods up to 11a (red curves). The uncertainties are given on the absolute value of C. The blue curves are the estimated a posterior averages.

The electrical conductivity profile inside the mantle of the Earth depends on its chemical composition, mineralogy, water content and temperature. It is tempting to build a simple one dimensional model of the Earth's mantle depending on those parameters and infer knowledge about them by inverting induction data. However, due to the sparse data set (about 20 data points) it is difficult to infer reliable results. For that reason we limit ourselves to an inversion of the complex C-response data to infer the conductivity profile of the mantle of the Earth. We assume that the silicate shell above the core is subdivided into 20 layers of variable thickness. The core conductivity is set to 10^4S/m and as usual we assume the ionospheric source current field to be of spherical degree $l = 1$. The data is then inverted with a stochastic sampling procedure by using a reasonable guess on the range of the possible conductivity values ($[10^{-3}, 10^4]$S/m) and requiring smoothness of the electrical conductivity profile. The resulting inferred posterior density on the conductivity profile and layer thickness of the silicate shell is shown in Fig.[3.9]. The 3 different shaded surfaces delineate probabilities of $(0.68, 0.95, 0.997)$. For convenience the posterior density has also be summarized by the mean, the median and the maximum estimator. The figure shows that the electrical conductivity of the silicate shell can be inferred with good confidence down to a depth 1700km.

However, at the 2σ confidence level the data allows to infer the conductivity profile only down to a depth of about 1700km. Note also, that below this depth the estimated median and average profile do not adequately summarize the posterior density as it broadens in a non symmetric way.

In order to assess the quality of the results we have also estimated the average posterior C-response, Fig.[3.8]. As can be seen in the figures the estimated average absolute value of C is mostly within the uncertainty bars of the data. On a closer inspection the result however reveals that the estimate does not very well reproduce the sharp variations of the data. However, it is not clear at this whether those variations are significant or data outliers.

The estimated maximal probable conductivity profile shows that the conductivity of the mantle increases by several orders of magnitude with increasing depth. This is related to the increasing temperature with depth, as the electric conductivity is exponentially dependent on the temperature. The rate of the increase in the conductivity is however not constant because of phase transitions of mantle minerals and changes in local chemistry (iron content). Note that our results to a depth of about 1700km are in good agreement with previous published results [e.g. *Olsen*, 1998].

In conclusion the conductivity profile of the upper mantle and of parts of the lower mantle can be estimated with a good confidence from the available C-response data. The confidence can be further increased when more data with lower uncertainties becomes available. However, to obtain a confident estimate of the conductivity of the lowest part of the mantle, a lower error on the 11year will not be sufficient but data at even longer periods are required, e.g. data related to the 22year cycle of the Sun (from magnetic field reversals).

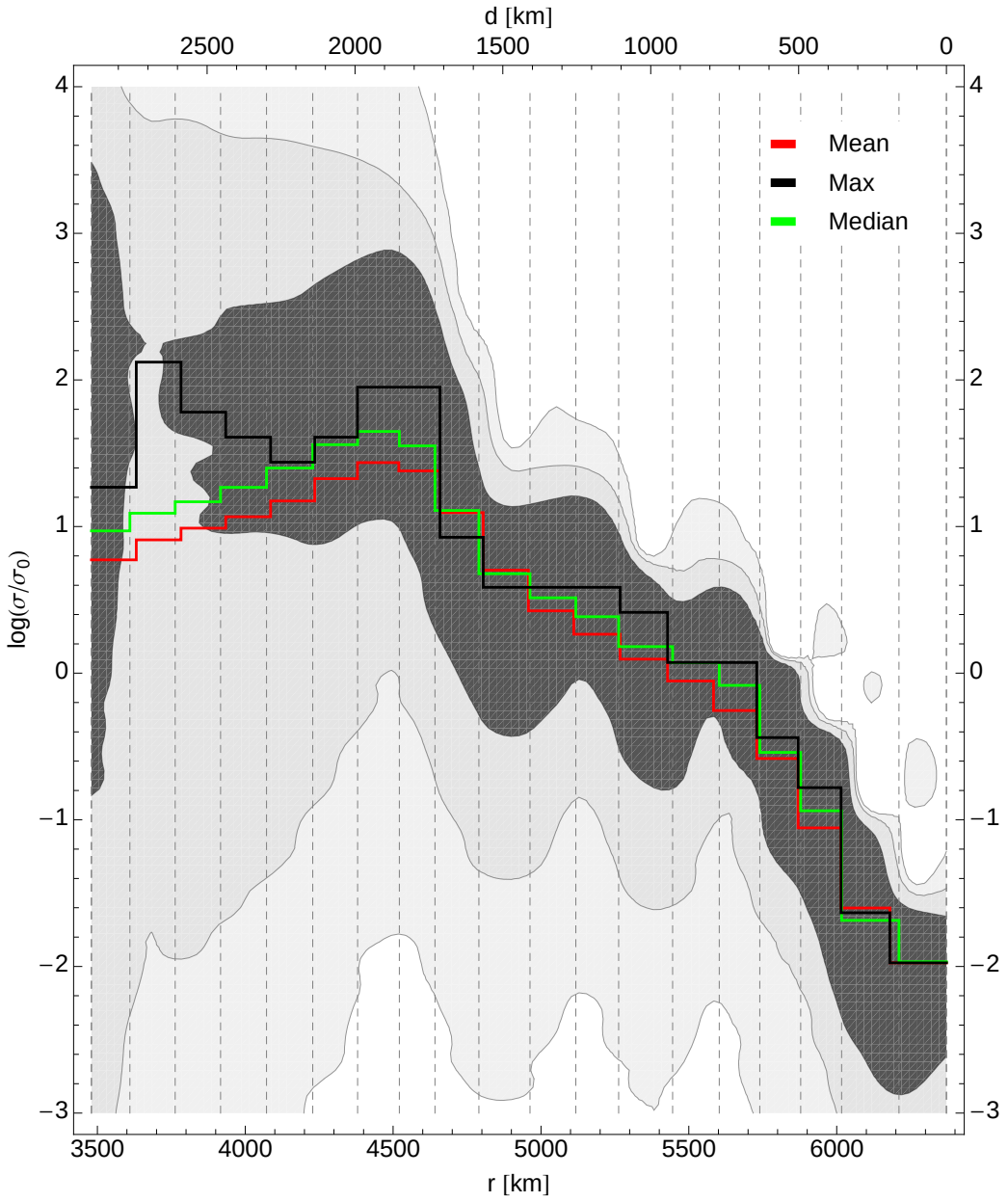


Figure 3.9: Inferred probability density of the conductivity profile of Earth's silicate shell. The contours correspond to probabilities of (0.68,0.95,0.997). The estimated average, median and maximal profiles are given in red, green, and black.

3.7 Modeling uncertainties due to laboratory measurement errors

The thermoelastic parameters and electrical conductivity parameters of minerals are all determined with an associated uncertainty. Those uncertainties are neglected by most scientists studying the interior structure of terrestrial planets. Here we will account for the uncertainties on thermoelastic parameters and electrical conductivity parameters to assess the induced uncertainties on density, seismic velocity, and electrical conductivity profiles inside the mantle. As of today, with the exception of the Earth, those profiles are not yet measured, we will also estimate the uncertainty on the calculated mantle mass and moment of inertia and on the ratio of the planets bulk iron mass to silicon mass.

The error propagation calculation is done for models of the planet Mars. we use two different mantle mineralogies, EH45 and DW, and two different extreme mantle temperature profiles (hot, T_1, and cold, T_2), see Chapt.[6]. Further, to calculate global properties, the crust thickness is set to 100km, the crust density is 2900kg/m^3, the core size is 1600km, and the core is made of iron with a sulfur fraction of 14.2wt%.

3.7.1 Uncertainties on electromagnetic and elastic laboratory constants

The electromagnetic constants and their relative uncertainties are listed in Tab.[3.4]. Tab.[3.2] and Tab.[3.3] display similar information for elastic the constants.

The experimental uncertainties on $\log \sigma_{0,\mathrm{ref}}$ and on $E_{0,\mathrm{ref}}$ are smaller than 10%. Uncertainties on α and β, the parameters that govern the iron content contribution to the pre-exponential factor and the activation energy, result from least square fitting on experimental data performed on samples with different iron contents and are about $40-50\%$ [*Vacher and Verhoeven*, 2007].

The uncertainties reported on the elastic constants are taken from the references cited in *Cammarano et al.* [2003]. Uncertainties on STP values of the density ρ_0 and its derivative with respect to iron-content $\rho_{0,\mathrm{Fe}}$ (Tab.[3.2]), are small and therefore neglected. The uncertainties on the coefficients a_0, b_0 and c_0 (Tab.[3.2]), which govern the thermal expansion of the thermal expansivity α, and uncertainties on the values of Grüneisen parameters $\gamma_{\mathrm{th},0}$ are set to 20%, see [*Cammarano et al.*, 2003] for a discussion.

3.7.2 Monte-Carlo error propagation

We consider the laboratory constants to be random variables of uncorrelated gaussian distribution. The mean value of the individual distribution is set to the measured value and the standard deviation to the associated uncertainty. 5000 sets of different values of laboratory constants have been simulated, and from those laboratory parameters, the profiles of density, seismic velocities, and of the electrical conductivity have been calculated. For convenience, the sets of profiles have been summarized by their mean and their standard deviation (see Figs. [3.10, 3.11, 3.12, 3.13]). The results show that the uncertainties increase with depth, or pressure and temperature. This is due to the fact that the elastic parameters of the high pressure phases have somewhat higher associated error bars than the low pressure phases, see Tabs. [3.2, 3.3, 3.4]. The estimated maximal

errors, at the bottom of the mantle, for ρ are below 0.5%, those for v_p are about below 1%, and those for v_S are about 1%. The estimated average relative mantle mass, moment of inertia and Fe/Si ratio are given in Tab.[3.5]. The estimated error on the mantle mass and on the mantle moment of inertia are on average below 0.3%,the error on Fe/Si is below 2%.

Fig.[3.13] shows that the estimated standard deviation on the logarithm of the electrical conductivity slightly increases with depth. At the bottom of the mantle the error is about 0.3 in log units.

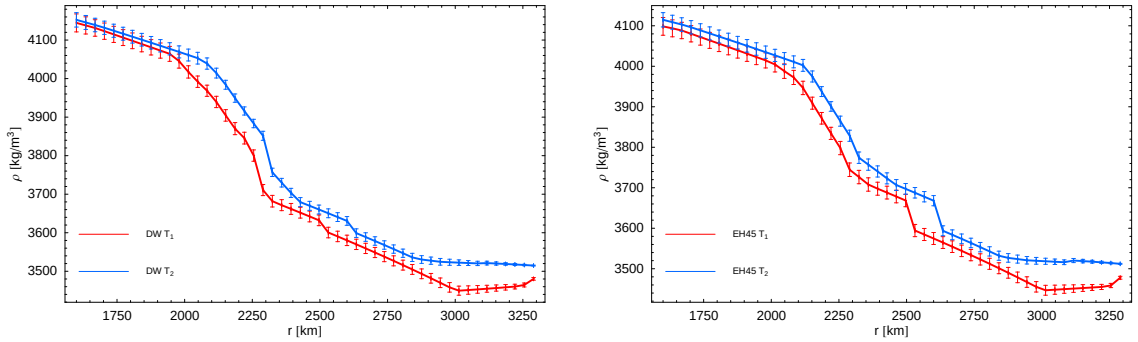


Figure 3.10: Estimated mantle density and associated estimated standard deviation as a function of radius for the hot (red) and cold (blue) Marstherms for the DW (right panel) and EH45 (left panel) mineralogy.

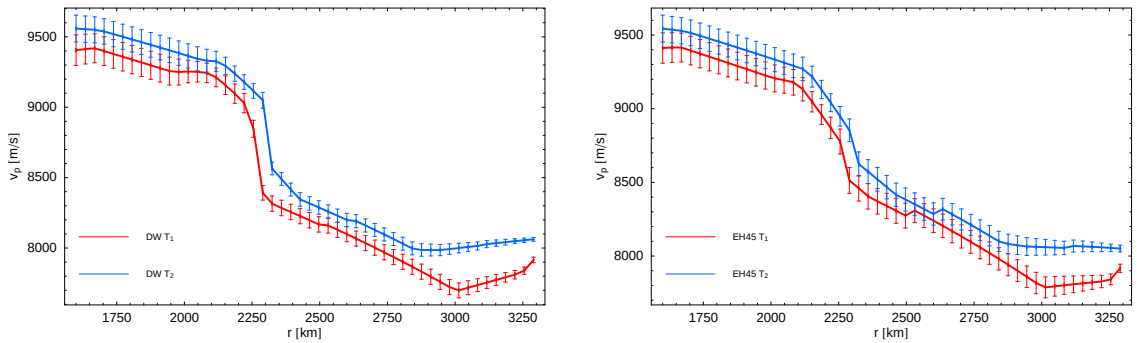


Figure 3.11: Estimated mantle p-wave velocity and associated estimated standard deviation as a function of radius for the hot (red) and cold (blue) Marstherms for the DW (right panel) and EH45 (left panel) mineralogy.

3.7.3 Conclusions

The above results show that despite the errors on the laboratory determined EoS parameters the resulting calculated uncertainties remain low. Similar results have been obtained by *Cammarano et al.* [2003] for the upper mantle of the Earth. Note that the estimated uncertainties on the density profiles are similar to those obtained by evaluating seismic

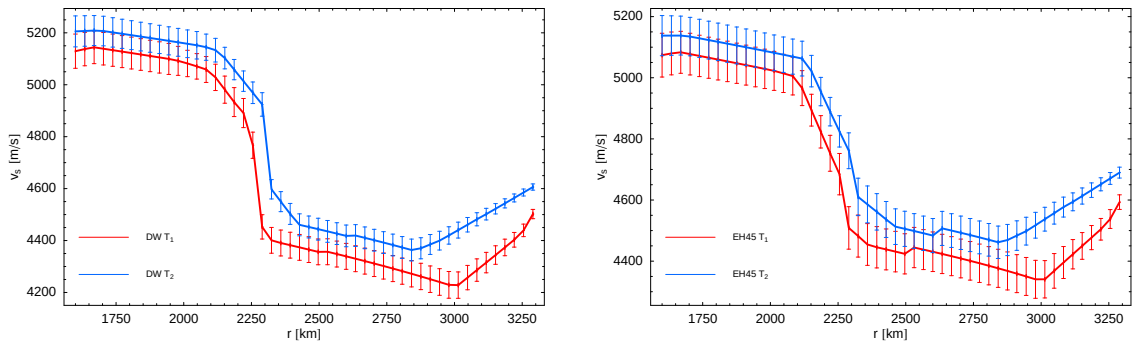


Figure 3.12: Estimated mantle *s*-wave velocity and standard deviation associated estimated as a function of radius for the hot (red) and cold (blue) Marstherms for the DW (right panel) and EH45 (left panel) mineralogy.

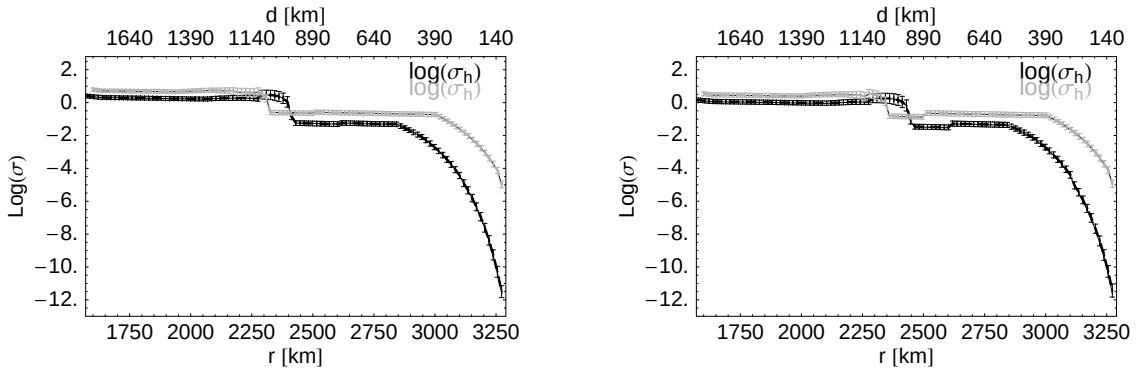


Figure 3.13: Estimated mantle electrical conductivity and associated estimated standard deviation as a function of radius for the hot (black) and cold (grey) Marstherms for the DW (right panel) and EH45 (left panel) mineralogy.

	m_m/m_a	$\sigma(m_m/ma)$	Fe/Si	σ(Fe/Si)	I_m/I_a	$\sigma(I_m/Ia)$
DW T_1	0.749	0.002	1.74	0.02	0.833	0.002
DW T_2	0.758	0.002	1.68	0.01	0.844	0.002
EH45 T_1	0.748	0.002	1.58	0.02	0.832	0.002
EH45 T_2	0.758	0.001	1.52	0.01	0.844	0.002

Table 3.5: Monte-Carlo estimated mantle mass (m_m), moment of inertia (I_m), and bulk Fe/Si ratio for a core composed of Fe and 14.2wt% with a crust of 100km thickness and 2900km/m^3 density. Estimated associated standard deviation are denoted by std.

data for the Earth [*Dziewonski and Anderson*, 1981]. However those on the bulk sound velocity are ten times lower than the values calculated here.

The mass of Mars is known to a very high precision, see Tab.[6.1], the above estimated uncertainty is about 150 times higher! On the other hand, the current uncertainty on the moment of inertia factor (Tab.[6.1]) is about the calculated value. Note that if the mass of the planet is constrained during the calculation, the uncertainty in the estimated global mass will either result in an uncertainty in the core size or core composition. The error on the mantle mass is however very low, the corresponding error on core size or core composition will therefore not be significant.

Chapter 4

The core

4.1 Introduction

Over the past years a wealth of knowledge has been acquired on the nature of the Earth's core. From seismic measurements [*Dziewonski and Anderson*, 1981] we know that the core is made of two parts, a liquid outer core and a solid inner core, and we know the sizes of the inner and outer core with a very high precision. By combining the seismological data with geochemical considerations and laboratory data of thermoelastic properties (e.g. density, compressibility,..) of relevant materials it has been determined that more than 80wt% of the core is made of iron [*McDonough and Sun*, 1995]. If it is assumed that the Fe/Ni ratio of the Earth is chondritic, it can be estimated that the Ni is about 5wt%. The density difference of about 550kg/m^3 at the solid inner core - liquid outer core boundary cannot be explained from the density decrease experienced by iron and nickel on phase change from solid to liquid alone and light elements are required. The possible candidate light elements for the outer core that should be siderophile and abundant enough to be relevant. The most proposed are oxygen, silicon, sulphur, carbon, and hydrogen [*Poirier*, 1994]. Unfortunately, the exact proportion of the light elements in the outer core cannot be constrained from existing mineralogical and seismological data. The only way to characterize the light elements is by modeling the Earth bulk composition and understanding the process of core formation.

Planets of the inner solar system are thought to have accreted from materials of diverse composition and size [*Righter and Drake*, 1996]. The initial material was either primitive (more or less with homogeneous metal dispersion) or already differentiated (with metallic cores). As new material is delivered to the planet surface, chemical re-equilibration, if it takes place, happens at low pressure and temperature. Later re-equilibrations of metallic material at higher pressure and temperatures, during transitions from mantle to the core are also possible. Large metallic blocks will sink quickly to the core with almost no reequilibration, while smaller blobs will sink slowly and re-equilibrate extensively. During accretion and planetary differentiation the surface temperature was high enough to allow for extensive surface and melting at depth within the planet. The reason for melting and early magma ocean formation is due to impact processes and owed to retained heat by an early, dense atmosphere.

Depending on the initial temperature and pressure conditions at the bottom of the early magma ocean and the presumed initial composition, different scientists arrive at

different proportions of light elements. For example, if near-chondritic refractory to lithophile element ratios [*McDonough and Sun*, 1995] are assumed, and based on new laboratory results concerning the partitioning of O, Si, and S between liquid Fe − Ni and liquid silicate at high temperature and pressure conditions, it has been shown that S is more siderophile than O and Si at high pressures while the opposite is true at high temperature [*Li and Agee*, 2001]. As a consequence, if the core composition were largely established by equilibrium partitioning in a deep magma ocean, i.e. under high pressure, then S should be the dominant light element in the Earth's core [*Li and Agee*, 2001].

This accumulated knowledge stands in sharp contrast to what is known about the cores of the other terrestrial planets. With the exception of the Moon, no seismic sounding data are available and what is known is principally deduced from mean density, moment of inertia, and cosmochemical considerations. For some planetary bodies, the data are complemented to some extent with bulk compositional constraints deduced from rock samples or from meteorites originating from the Moon and from Mars. Note that other observables, like for instance the presence or not of an external magnetic field, the deformational response resulting from a tidal potential, and the time variable rotation rate, give further insight in the state of the core and the presence of an inner core.

All terrestrial planets (c.f.Tab.[4.1]), have an average moment of inertia indicating that they have a core of substantial size [1]. Further, their average density is significantly higher than the silicate rich mantle rocks of the Earth. As all terrestrial planets are the result of the same planetary nebula, it is reasonable to assume that the other terrestrial planets cores are similarly to the Earth principally composed of iron and some lower fraction of light elements.

	Merucry	Venus	Earth	Moon	Mars
ρ_a [kg/m^3]	5427	5204	5515	3340	3933
MOI	0.33	0.33	0.3308	0.393	0.3635

Table 4.1: Average density and moment of inertia ratio for terrestrial planets and the Moon, [*de Pater and Lissauer*, 2001], [*Konopliv et al.*, 2006]

In this section, we discuss recent high pressure and temperature laboratory results regarding iron and siderophile light elements and their status as being possible candidates to be incorporated together with iron in the core of the planet Mars. Next, we introduce the necessary thermodynamic notions and the equations of state for calculating the thermoelastic properties at high pressure and temperature inside the core. We explain how the theory of thermodynamic solutions is used as a self-consistent model for the fluid outer core, introduce the concept of melting and explain its relation to the formation of an inner core. Finally, we assess how uncertainties on thermoelastic parameters obtained from in-situ laboratory measurements induce uncertainties on calculated density and seismic sound velocity.

[1] The moment of inertia ratio MOI gives information on the mass distribution inside a planet. It is the ratio of the mean moment of inertia to the mass times the squared size. For a homogeneous spherical planet $MOI = 0.4$, a planet made of a core and a less dense mantle has a MOI value below 0.4, decreasing to zero if all the mass is concentrated at the center.

4.2 Core composition of terrestrial planets

Similarly to the core of the Earth, it is assumed that cores of terrestrial planets are principally made of iron, with a fraction of nickel, and the light elements O, Si, S, C, and H, in binary, ternary, or even more complicated systems. We will here focus on the core and Mars. For a discussion related to the core of Mercury see *Rivoldini et al.* [2009].

The fractions of the possible light siderophile elements cannot be predicted from accretion theory, even in the formation history of the planet were known as the formation process is basically random. Among the light elements sulfur, under the form of FeS, has been found in many nickel-iron-meteorites, and is therefore, ubiquitously invoked as a major candidate for light elements in planetary cores of terrestrial planets. Of all the light elements, if taken alone with iron-nickel, sulfur, and silicon are most easily incorporated into planetary cores of terrestrial planets as their solubility in molten iron is high over an extended pressure range. Oxygen solubility in liquid iron is below 1wt% at ambient pressure and, although increasing with increasing pressure, remains small and below about 1wt% for pressures below 10GPa [*Tsuno et al.*, 2007], close to the pressure at the bottom of the primordial magma ocean.

In ternary iron systems, the solubility of light elements is more complicated. For example, Si does not dissolve into liquid $Fe-S$ at ambient pressure, the first melt to percolate through the silicate matrix during core formation, since at that pressure the $Fe-S-Si$ system exhibits a large region of immiscibility in a temperature composition representation. This miscibility gap only closes at about 14GPa [*Sanloup and Fei*, 2004]. Since the differentiation of Mars took place at pressures of about 14GPa (CMB pressures are about 20GPa for Mars), small amounts of Si could have dissolved in the $Fe-S$ melt and it is therefore unlikely that significant amounts of Si are incorporated into the core. Oxygen, albeit almost immiscible with liquid iron at low pressure, could be dissolved in $Fe-S$ melts since the miscibility increases with increasing temperature, pressure, and sulfur weight fraction [*Tsuno et al.*, 2007]. However, data in *Tsuno et al.* [2007] and *Rubie et al.* [2004] suggest that at the low pressures, characteristic of Mars' differentiation, and with a sulfur concentration of about 14wt%, oxygen too can only be present in small amounts in the planet's core.

Rubie et al. [2004] have invoked the pressure dependent solubility of oxygen in molten iron-nickel as a possible explanation to account for the relative high amount of FeO in the mantle of Mars, about 18wt%, compared to the mantle of the Earth, about 8wt%. If it is assumed that both Mars and Earth have accreted from similar oxidized chondritic material, with an initial FeO content of about $18-22$wt%, the nearly chondritic amount of FeO of the Mars mantle, compared to the lower amount found in the mantle of the Earth, is in agreement with the pressure dependent solubility of oxygen in liquid iron.

As a consequence of the planet's cooling history, a solid inner core might have formed in the initial liquid core of Mars. Light elements are not only dissolved in the liquid $Fe-Ni$ outer core mixture but can also be incorporated in the solid $Fe-Ni$ inner core alloy. The solubility of Si in solid Fe is nearly identical to its solubility in liquid Fe [*Kuwayama and Hirose*, 2004]. The solubility of sulfur inside solid iron is small, increases with decreasing temperature and seems to increase with increasing pressure. The maximal solubility is attained at the *eutectic temperature*[2] (about 1.5wt% for $21\text{GPa} \leq P \leq 40\text{GPa}$

[2]Eutectic comes from the Greek eutektos, meaning easily melted. The melting temperature of a

[*Fei et al.*, 2000; *Li et al.*, 2001; *Stewart et al.*, 2007]. The solubility of S in solid Fe − Ni at the eutectic temperature increases with increasing fraction of Ni and can be about 1wt% larger than inside pure Fe.

The light elements S and Si both have the important property that they lower the melting temperature of the iron system with respect to pure iron, contrary to oxygen which does not significantly depress the melting temperature of Fe [*Boehler*, 1992; *Tsuno et al.*, 2007]. For example, at 21GPa the melting temperature of Fe decreases by about 60K for each additional weight percent of S [*Fei et al.*, 2000] and the temperature decrease for the inclusion of Si is about 10K [*Kuwayama and Hirose*, 2004]. Note that the melting temperature decreases with increasing amounts of nickel [*Stewart et al.*, 2007; *Zhang and Fei*, 2008] (for about 8wt% of Ni at 23GPa it is about 30K).

The above data for binary and ternary iron systems suggest that it is unlikely that Mars' core contains significant amounts of light elements other than sulfur. Moreover, in order to justify the observed liquid outer core of Mars [*Yoder et al.*, 2003], sulfur is a strong candidate as among all the considered light elements, already small amounts allow for strong temperature depression of the melting temperature of the iron-rich core material. On the basis of the above arguments we therefore neglect the effect of other light elements beside sulfur on the thermoelastic properties of the core material. We also neglect Ni, which is likely present up to 10wt% inside the core but its thermoelastic properties are close enough to those of iron to not significantly affect the core density and compressibility at those concentrations.

If the bulk core composition and the pressure and temperature inside the core allow for the presence of an inner core (see Sect.[4.5]) and if the core sulfur fraction is smaller than the eutectic concentration, we will assume that the inner core is made of pure iron, since the here considered core temperatures are significantly above the eutectic temperature. At pressures relevant for the core of Mars (about 18 − 45GPa) the solid iron phase is $\gamma - Fe$[3] Fig.[4.1].

For sulfur fractions larger than the eutectic concentration (see Sect.[4.4]), the inner core is made of iron-sulfur compounds (Fe_3S, $Fe_{3+x}S_2$, Fe_2S, Fig.[4.16]) instead of pure iron (see Sect.[4.4]). If the temperature is low enough to allow for eutectic freezing, the solid core material will be a solid mixture of eutectic composition, see Fig.[4.16].

The laboratory data [4] at reference pressure and temperature, needed for calculating the thermoelastic properties, e.g. density and elastic moduli, at pressures and temperatures inside the core of Mars, for solid iron and the other solid iron-sulfur compounds are given in Tab.[4.2]. The parameters relevant for the liquid outer core are given in Sect.[4.4] Tab.[4.3]. Note that neither the EoS parameters for the iron-sulfur compounds $Fe_{3+x}S_2$ and Fe_2S have been measured nor have the shear modulus for Fe_3S and its derivative with respect to pressure or temperature been determined. The only iron-sulfur compound that

solution depends on the relative proportion of each component. The lowest possible melting temperature, the eutectic temperature, is reached when the proportions of each component is such that the solution is of eutectic composition. See Sect.[4.4].

[3] At ambient pressure and temperature the stable phase of iron is called α and it has a body centered crystal structure (bcc) (Fig.[4.2a]). At high pressures and room temperature the crystal structure changes to hexagonal close packed (hcp) (Fig.[4.2c]) the name of the phase is ε. At pressures and temperatures relevant for the core of Mars and Mercury the stable face of solid iron (γ) has a face centered cubic structure (fcc) (Fig.[4.2b]).

[4] Also called equation of state parameters (EoS).

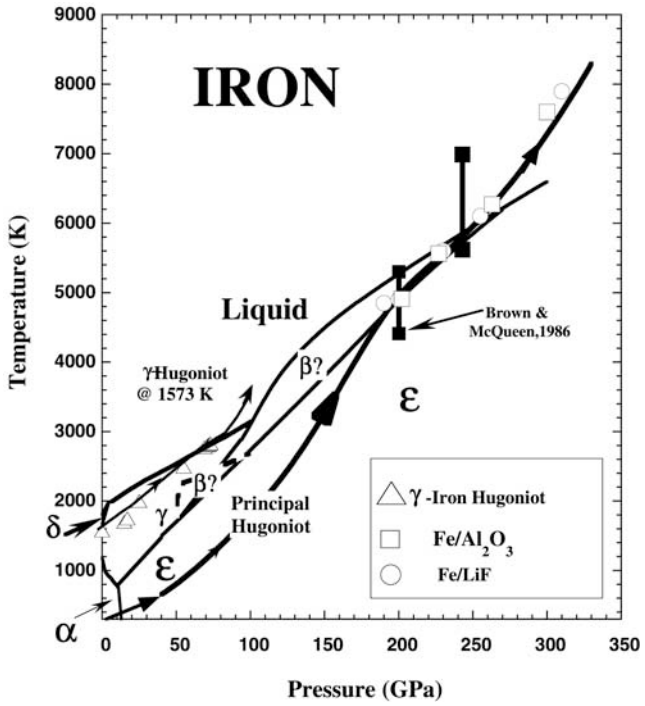
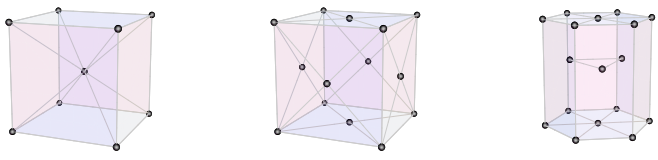


Figure 4.1: Phase diagram of Fe [*Ahrens et al.*, 2002].



(a) bcc **(b)** fcc **(c)** hcp

Figure 4.2: bcc,fcc, and hcp crystal structure.

	ρ kg/m^3	α 10^5/K	K_T GPa	K'_T	dK_T/dT GPa/K	μ GPa	μ'	$d\mu/dT$ GPa/K
$P_{\text{ref}} = 10^5$Pa and $T_{\text{ref}} = 1573$K								
$\gamma - \text{Fe}$	7413.	7.7	103.	5.	-0.020	62.6	2.7	-0.03
$P_{\text{ref}} = 10^5$Pa and $T_{\text{ref}} = 298$K								
Fe_3S	7090	7.01	113	5.2	-0.0375			
$P_{\text{ref}} = 10^5$Pa and $T_{\text{ref}} = 600$K								
$\text{FeS} - \text{IV}$	5121.	$7.16 + 6.08\ 10^{-3}T$/K	62.5	4.	-0.0208			

Table 4.2: Equation of state parameters for the core: $\gamma - \text{Fe}$ from *Ahrens et al.* [2002], Fe_3S from *Seagle et al.* [2006] and *Chen et al.* [2007] (dK_T/dT), $\text{FeS} - \text{IV}$ from *Urakawa et al.* [2004].

is relevant for the core of Mars for which shear data has been measured is $\text{FeS} - \text{IV}$. The significance of the individual EoS parameters is discussed in Sect.[4.3].

4.3 Thermodynamics and equations of state for the solid core

To solve the differential equations introduced in Chapt.[2], the system of ODEs needs to be supplemented with equations of state to calculate the thermoelastic properties of the materials of the mantle and of the core at each depth, or in other words for each pressure and temperature, inside the planet. More specifically, in order to solve the differential equations we need beside the density profile of the whole planet, also the adiabatic incompressibility K_S and the thermodynamic Grüneisen parameter γ as a function of pressure and temperature inside the core for the calculation of the temperature inside the core (2.4). Furthermore, in order to be able to calculate the tidal deformation of the planet we have to calculate the shear modulus and adiabatic incompressibility as a function of depth. All those thermodynamic quantities can only be calculated if the local temperature and the local composition are known. As already stated, we calculate the temperature inside the core from the boundary condition at the core mantle boundary temperature provided by the mantle temperature from dedicated thermal evolution models of the planet, and we assume the composition of the mantle to be known at each depth.

The thermoelastic properties of the mantle minerals and of the core compounds are usually given at reference pressure and temperature conditions (STP). By means of equations of state the thermoelastic properties known at reference conditions are calculated at local temperature and pressure inside the planet. There are different thermodynamically equivalent ways to achieve this goal, as the calculation of a thermodynamic state functions does only dependent on the initial and the final pressure and temperature an not on the specific path followed [*Callen*, 1985].

Here we will use the isothermal approach for the core, meaning that the compounds are first heated to local temperature at constant pressure, followed by an isothermal compression to local pressure. For the mantle, the individual minerals are first heated at constant pressure, but not to local mantle temperature but rather to the foot of the adiabat[5], followed by an adiabatic compression to local temperature and pressure. The

[5]The temperature one obtains by adiabatically decompressing a given mineral from local temperature

reason for choosing different approaches for the core and for the mantle is that for mantle minerals the STP EoS are usually provided for an adiabatic equation of state where those for the core are provided for an isothermal equation of state. On a thermodynamic level the relations between the adiabatic and isothermal EoS parameters are well defined [see *Stacey and Davis*, 2008, Appendix E], however, in practice numerical values are difficult to obtain since some thermodynamic quantities occurring in the equations relating the the two approaches are not yet measured.

Thermodynamic properties of aggregates

In contrast to the mineral assemblages of the mantle, and if the temperature is above the eutectic temperature, the mixture of constituents that forms the solid core is not a mechanical mixture but rather a solid solution, see Sect.[4.4]. Note that at sub-eutectic temperatures the components don't form a solid solution, but rather make a homogeneous solid mixture, an alloy. For the calculation of the thermoelastic properties of this solid aggregate see Sect.[3.4].

For solid solutions of the most simplest kind, ideal solutions, the volume of the solution is simply calculated from the volumes of each individual component. Consequently the density of the solution made of n components is

$$\rho^{-1} = \sum_{i=1}^{n} \frac{x_i}{\rho_i}, \tag{4.1}$$

where ρ_i and $x_i = m_i/m$ are the density and the weight fraction of component i. m_i is the mass of component i and $m = \sum_{i=1}^{n} m_i$ is the total mass. From the definition of the thermal expansivity $\alpha = -\left(\frac{\partial \log \rho}{\partial T}\right)_P$ and from (4.1) the thermal expansivity of the solution reads

$$\alpha = \rho \sum_{i=1}^{n} \frac{x_i\, \alpha_i}{\rho_i}. \tag{4.2}$$

From the definition of the isothermal bulk modulus $K_T = \left(\frac{\partial \log \rho}{\partial P}\right)_T^{-1}$ the isothermal bulk modulus of the solution can be calculated from (4.1). It is

$$K_T^{-1} = \rho \sum_{i=1}^{n} \frac{x_i}{\rho_i\, K_{T,i}}, \tag{4.3}$$

where $K_{T,i}$ is the bulk modulus of component i. The formula for the shear modulus is equivalent. The formulas for the derivatives of the elastic moduli are obtained by deriving (4.3) with respect to pressure at constant temperature

$$\frac{\partial\, K_T}{\partial P} \equiv K_T' = \rho K_T^2 \sum_{i=1}^{n} x_i \frac{K_{T,i}' + 1}{\rho_i\, K_{T,i}^2} - 1 \tag{4.4}$$

where $K_{T,i}'$ is the pressure derivative of the isothermal bulk modulus of component i.

---

and pressure to reference pressure.

Isothermal thermodynamics of the solid core

In principle the thermoelastic properties of the solution can be calculated from the properties of its components at reference condition (P_0, T_0) or at local pressure and temperature (P, T). Since laboratory parameters for core materials are usually not given at the same reference conditions, it is often more convenient to bring each individual component from reference conditions to local conditions and then calculate the thermoelastic properties of the solution.

In contrast to the mantle (see Sect.[3.4]), where for each mineral we have followed an isobaric path from (P_0, T_0) to the foot of the adiabat (ϑ_0, P_0) and then applied and adiabatic compression to (P, T), we here heat the core components from (P_0, T_0) along an isobar to (P_0, T) and then apply an isothermal compression to (P, T).

The density at local temperature is obtained by integrating the definition of the thermal expansivity from the reference temperature T_0 to the local temperature T

$$\rho_0(P_0, T) = \rho_{\rm ref}(P_0, T_0)\ \mathrm{e}^{-\int_{T_0}^{T} dT' \alpha_{\rm ref}(T', P_0)}. \tag{4.5}$$

For the mantle minerals we have used the same equation, however with a different lower integration bound (see (3.6)). The quantities with subscript "ref" refer to the laboratory constants, or EoS parameters, obtained at reference conditions, see Tab.[4.3]. We assume that the isothermal bulk modulus has a linear dependence on temperature

$$K_{T,0} = K_{ref}(P_0, T_0) + \left(\frac{d\,K}{dT}\right)_{\rm ref} (T - T_{\rm ref}). \tag{4.6}$$

For the shear modulus G we also assume a linear temperature dependence and use the same equation as for mantle minerals (3.9).

Once the thermoelastic properties are calculated at T their, compressed values at local P in the core can be determined. Similarly to the minerals of the mantle we use a finite strain fourth-order Birch-Murnaghan equation of state to calculate the density, bulk modulus, and shear modulus at local pressure. For this we use equations (3.10), (3.11), and (3.13) whereby the density, the elastic moduli, and their derivatives with respect to pressure at reference pressure are evaluated at local temperature T rather than at temperature ϑ_0 and the adiabatic bulk modulus is replaced by the isothermal bulk modulus since equations (3.10),(3.11), and (3.13) are identical for adiabatic and isothermal conditions. Analogously to the considerations of the mantle minerals we assume that the derivatives of the elastic moduli with respect to pressure at temperature T can be approximated by their values at reference temperature T_0, see (3.14). The second derivative with respect to pressure of the shear modulus G_0'' appearing in (3.13) is approximated by [*Sohl and Spohn*, 1997]

$$G_0'' \approx -\frac{35}{9}\frac{G_0}{K_{T,0}^2}. \tag{4.7}$$

For the calculation of seismic velocities, one also needs the adiabatic bulk modulus K_S as a function of local pressure and temperature. It is related to the isothermal bulk modulus K_T through the fundamental thermodynamic relation [*Poirier*, 2000]

$$K_S(P, T) = K_T(P, T)[1 + \alpha(P, T)\gamma(P, T)T]. \tag{4.8}$$

The thermal expansivity at (P,T) is calculated from

$$\alpha(P,T)K_T(P,T) \approx \alpha(P_{ref},T)K_T(P_{ref},T). \tag{4.9}$$

This approximate relation is valid whenever the local temperature exceeds the *Debye temperature* [e.g. *Poirier*, 2000, Chap.13], as in terrestrial planetary cores[6]. Note that it is not clear whether the Debye theory for specific heat is valid for metals. According to *Anderson and Zou* [1989] it is valid for close packed minerals with an atomic volume smaller than 5.8cm^3/mol ($V_{a,\mathrm{Fe}} = 7.1$cm^3/mol !). In the Debye theory, above the Debye temperature the heat capacity at constant volume C_V for a volume containing n atoms is

$$C_V = 3nR, \tag{4.10}$$

where R is the gas constant. With this approximation, αK_T, with the definition of the Grüneisen parameter $\gamma = \alpha K_T/\rho C_V$ [e.g. *Stacey and Davis*, 2008, Chap.19] reads

$$\alpha(P,T)K_T(P,T) = 3nR\,\gamma(P,T)\rho(P,T). \tag{4.11}$$

In the quasi harmonic approximation (see Sect.[3.4]) for a given temperature $\gamma\rho$ is approximatively independent of pressure. Consequently (4.9) is approximatively valid.

The Grüneisen parameter γ is computed from the Vashchenko and Zubarev formulation [*Anderson*, 2000]

$$\gamma(P,T) = \frac{\frac{1}{2}K'_T(P,T) - \frac{5}{6} + \frac{2}{9}PK_T^{-1}(P,T)}{1 - \frac{4}{3}PK_T^{-1}(P,T)}, \tag{4.12}$$

The derivative of the isothermal bulk modulus with respect to pressure, K'_T, evaluated at (P,T) is derived from the Birch-Murnaghan equation of state. It is

$$K'_T = K'_{T,0} - 3K_{T,0}K''_{T,0}\varepsilon, \tag{4.13}$$

where ε is given in (3.12) and the second derivative with respect to pressure of the isothermal bulk modulus, K''_T, is obtained from (3.17) by replacing the adiabatic bulk modulus with the isothermal bulk modulus.

With the adiabatic bulk modulus, shear modulus, and density known at local (P,T) the seismic P- and S-wave velocities can be calculated from Eqs. (3.29) and (3.30).

4.4 Modeling the liquid core

4.4.1 Introduction

Depending on the pressure and temperature conditions and on the composition the core can be solid or liquid, or both if it is made of a fluid outer core and a solid inner core. The state of the core is dependent on the amount of light element impurities as those light elements have the property of depressing the melting temperature of iron. Melting point depression dependent on the amount of light elements and melting will be discussed in the next section.

[6]The Debye temperature for iron is 470K [*Kittel*, 2004].

Conceptually, a fluid or a melt is made of disorganized chunks of a solid, and therefore inherit to a certain extent the properties of the solid. To accurately describe the properties of fluid cores it is of important to use properties of the liquid constituents and not of solids. However, due to lack of data most authors use thermoelastic properties of solid constituents for modeling liquid planetary cores [e.g. *Sohl and Spohn*, 1997; *Bertka and Fei*, 1997]. Some authors acknowledge for this inconsistency and correct local densities to account for phase changes [e.g. *Van Hoolst and Jacobs*, 2003; *Zharkov and Gudkova*, 2005]. More recently, with the advent of new laboratory data on rich iron solutions [*Sanloup et al.*, 2000; *Balog et al.*, 2003], *Hauck et al.* [2007] and *Rivoldini et al.* [2009] have fitted polynomial empirical laws to liquid data in order to describe approximatively liquid core materials at reference temperature and pressure conditions. Although, the latter approach uses laboratory established measurements, it lack any sound thermodynamical foundation and it is unclear over which pressure, temperature, and composition domain the modeling is valid.

In this section we propose a consistent modeling for liquid core materials based on thermodynamic solution modeling and explain how EoS parameters can be retrieved from available laboratory data relevant for liquid core constituents.

4.4.2 Solution modeling

Cores of planets are multicomponent systems. The thermodynamic properties of a multicomponent system are coherently described by thermodynamic potentials [e.g. *Callen*, 1985]. The different thermodynamic potentials are equivalent and related to one another by a *Legendre transform* [e.g. *Callen*, 1985]. Here, we use the *Gibbs potential* as our fundamental thermodynamic relation. Once the Gibbs potential is established all thermodynamic properties (density, elastic moduli, thermal expansivity,...) of interest can be derived. The Gibbs potential is defined as

$$\mathcal{G}' = H' - T\mathcal{S}', \tag{4.14}$$

where H' is the enthalpy and $\mathcal{S}'$ the entropy [e.g. *Callen*, 1985]. In what follows "'" subscripted quantities refer to whole system quantities and unprimed quantities refer to molar quantities, e.g. $\mathcal{G}' = n\,\mathcal{G}$, where n is the number of moles in the system.

For a non-interacting multicomponent system the Gibbs potential of the aggregate is simply the sum of the the Gibbs energies of the components, i.e. there are no interactions between the components. Conversely, the multicomponent liquid part of the core and the multicomponent non-eutectic solid inner core form an interacting system, a solution. *Solutions are defined as homogeneous phases produced by dissolving one or more substances in another substance.*

The molar Gibbs energy for an l component solution is [e.g. *Callen*, 1985]

$$\mathcal{G}(P,T) = \sum_{i}^{l} x_i \mathcal{G}_i(P,T) + x_i RT \ln a_i, \tag{4.15}$$

where $\mathcal{G}_i$ is the Gibbs energy of the pure component i and a_i the activity of component i, and R is the gas constant. The x_i are the mole fractions of each species

$$x_i = n_i \left(\sum_{j}^{l} n_j \right)^{-1} = \frac{n_i}{n}, \tag{4.16}$$

where n_i are the number of moles of component i. Equation (4.15) shows that the Gibbs energy of the solution is the sum of the Gibbs energies of each component plus an interaction term depending on the chemical activity a_i. In the most general setting a_i is a function of pressure, temperature, and of the mole fractions of all components. It is conveniently written as

$$a_i \equiv f_i x_i \tag{4.17}$$

where f_i is the activity coefficient, and it has the property that $f_i = 1$ for $x_i = 1$. The activity coefficients are usually determined experimentally or from a more fundamental microscopic theory.

Thermodynamic properties of the solution are calculated by derivation of the Gibbs potential with respect to the state variables P, T, n_i, ... [e.g. *Callen*, 1985]. Note that here we assume the system to be isolated and to be chemically nonreacting so that the x_i are constant. We have

$$\begin{aligned}\mathcal{S} &= -\left(\frac{\partial\, \mathcal{G}}{\partial T}\right)_P = \sum_i^l x_i \mathcal{S}_i - x_i R \ln f_i x_i - x_i R T \left(\frac{\partial\, \ln f_i}{\partial T}\right)_P \\ &= \sum_i^l x_i \mathcal{S}_i - x_i R \ln f_i x_i + x_i \mathcal{S}_{e,i} \end{aligned} \tag{4.18}$$

$$H = \mathcal{G} + T\mathcal{S} = \sum_i^l x_i H_i - x_i T \mathcal{S}_{e,i} = \sum_i^l x_i H_i - x_i H_{e,i} \tag{4.19}$$

$$V = \left(\frac{\partial\, \mathcal{G}}{\partial P}\right)_T = \sum_i^l x_i V_i + x_i R T \left(\frac{\partial\, \ln f_i}{\partial P}\right)_T = \sum_i^l x_i V_i + x_i V_{e,i} \tag{4.20}$$

$$\frac{1}{K_T} = -\frac{1}{V}\left(\frac{\partial^2\, \mathcal{G}}{\partial P^2}\right)_T = \frac{1}{V}\sum_i^l x_i \frac{V_i}{K_{T,i}} - x_i \left(\frac{\partial\, V_{e,i}}{\partial P}\right)_T \tag{4.21}$$

$$V\,\alpha = \left(\frac{\partial^2\, \mathcal{G}}{\partial P \partial T}\right) = \sum_i^l x_i \alpha_i V_i + x_i \left(\frac{\partial\, V_{e,i}}{\partial T}\right)_P, \tag{4.22}$$

where $\mathcal{S}$ is the entropy, V the volume, K_T the isothermal bulk modulus, and α the thermal expansivity of the solution. The symbols with the "i" subscript refer to the corresponding quantities for the pure components. $V_{e,i}$, $S_{e,i}$, and $H_{e,i}$ are the *excessive mixing volume*, *excessive mixing entropy*, and *excessive mixing enthalpy*. The excessive volume expresses the fact that the volume of the solution is generally different from the sum of the volumes of the individual species, i.e. in the solution the volume of each species deviates from its volume as single pure species, it has an effective volume. Note that even when the excessive entropies are zero, the entropy of the solution is not computed from the mole fraction weighted sum of the entropies of the individual species alone but includes supplementary terms ($\sim x_i R \ln f_i x_i$), accounting for the increased number of possible arrangements of the system due to mixing. For a noninteracting mixture, a mechanical mixture, those interaction terms are zero.

A further fundamental quantity is the *chemical potential* [e.g. *Callen*, 1985]. For an l component solution the chemical potential of component i is

$$\mu_i = \left(\frac{\partial\, \mathcal{G}'}{\partial n_i}\right)_{n_{-i},P,T}, \tag{4.23}$$

where n_{-i} are the mole fractions of all other l components without i. The chemical potential is also called the *partial molal* Gibbs potential. The chemical potential of component i in a multicomponent system is [e.g. *Callen*, 1985]

$$\mu_i \equiv \mu_i^0 + RT \ln(x_i f_i), \tag{4.24}$$

where μ_i^0 is the chemical potential for the pure component i (i.e. for $x_i = 1$).

4.4.3 Solution models for the fluid part of planetary cores

The simplest consistent model for solutions is the *ideal solution* model. It is an adaption to liquids of the *ideal gas* mixing model [e.g. *Callen*, 1985].

A solution whose excessive mixing volume and excessive mixing enthalpy are zero is called an ideal solution (i.e. $f_i = 1$ since $\log(a_i) = 0$ for a one component solution). The molar mixing Gibbs potential $\Delta\mathcal{G}$ and entropy ΔS of the solution can then be derived from equations (4.15) and (4.18) as

$$\Delta\mathcal{G} = RT \sum_i^l x_i \ln x_i \tag{4.25}$$

$$\Delta S = -R \sum_i^l x_i \ln x_i. \tag{4.26}$$

By starting from the ideal solution, the significance of the activity coefficients can be illustrated. If $f_i = 1$ the chemical potential of component i in the solution depends only on its mole fraction. If $f_i > 1$, component i acts as if the solution contains more of component i than its mole fraction would suggest. Equivalently if $f_i < 1$, component i acts if less than mole faction x_i is in the solution.

Ideal solution model for the core

We assume that the $\mathrm{Fe} - \mathrm{S}$ system is an ideal solution and calculate the relevant thermoelastic parameters at core pressures and temperatures in the ranges $[18 - 45]$GPa and $[1800 - 2300]$K from the EoS data for liquid Fe [*Anderson and Ahrens*, 1994], liquid $\mathrm{Fe} - 10\mathrm{wt\%S}$ [*Balog et al.*, 2003], and liquid FeS [*Kaiura and Toguri*, 1979]. See Tab.[4.3] for the data values used. We have all needed parameters values for pure iron, but not for sulfur in the solution. However, by assuming an ideal binary solution the relevant EoS data for sulfur in the solution can be calculated from the EoS data of iron, $\mathrm{Fe} - \mathrm{S}$ and $\mathrm{Fe} - 10\mathrm{wt\%S}$ by using equations (4.20), (4.22), and (4.21). In detail, to calculate the molar volume, the bulk modulus, and its derivative with respect to pressure we have used the EoS data of liquid Fe and liquid $\mathrm{Fe} - 10\mathrm{wt\%S}$. The thermal expansivity of S has been computed from the thermal expansivity of liquid Fe and liquid FeS.

Fig.[4.3] shows the density, the thermal expansivity, the bulk modulus, and its derivative with respect to pressure as a function of sulfur concentration for the ideal $\mathrm{Fe} - \mathrm{S}$ solution. The sulfur weight fraction varies from $x_\mathrm{S} = 0$ (pure iron) to $x_S = 0.365\mathrm{wt\%}$ (the weight fraction of sulfur in FeS), and the volume of the solution increases linearly with the amount of sulfur. The density and the bulk modulus and its derivative decrease with increasing amount of sulfur in the solution as they are all inversely proportional to

	ρ kg/m^3	V cm^3/mol	α 10^5/K	K_T GPa	K'_T	dK_T/dT GPa/K
$P_{\text{ref}} = 10^5$Pa and $T_{\text{ref}} = 1881K$						
FeS		12.38	16.28			
Fe		7.96	9.20	85.	5.8	-0.031
Fe $-$ 10wt%S		9.45		63.	4.8	
S in ideal Fe $-$ S solution: $P_{\text{ref}} = 10^5$Pa and $T_{\text{ref}} = 1881K$						
S		17.19	19.2	38.86	3.1	

Table 4.3: Equation of state parameters for ideal Fe $-$ S. Fe from *Anderson and Ahrens* [1994], FeS from *Kaiura and Toguri* [1979], and Fe $-$ 10wt%S from *Balog et al.* [2003]. Estimated EoS parameter for S in Fe $-$ S solution.

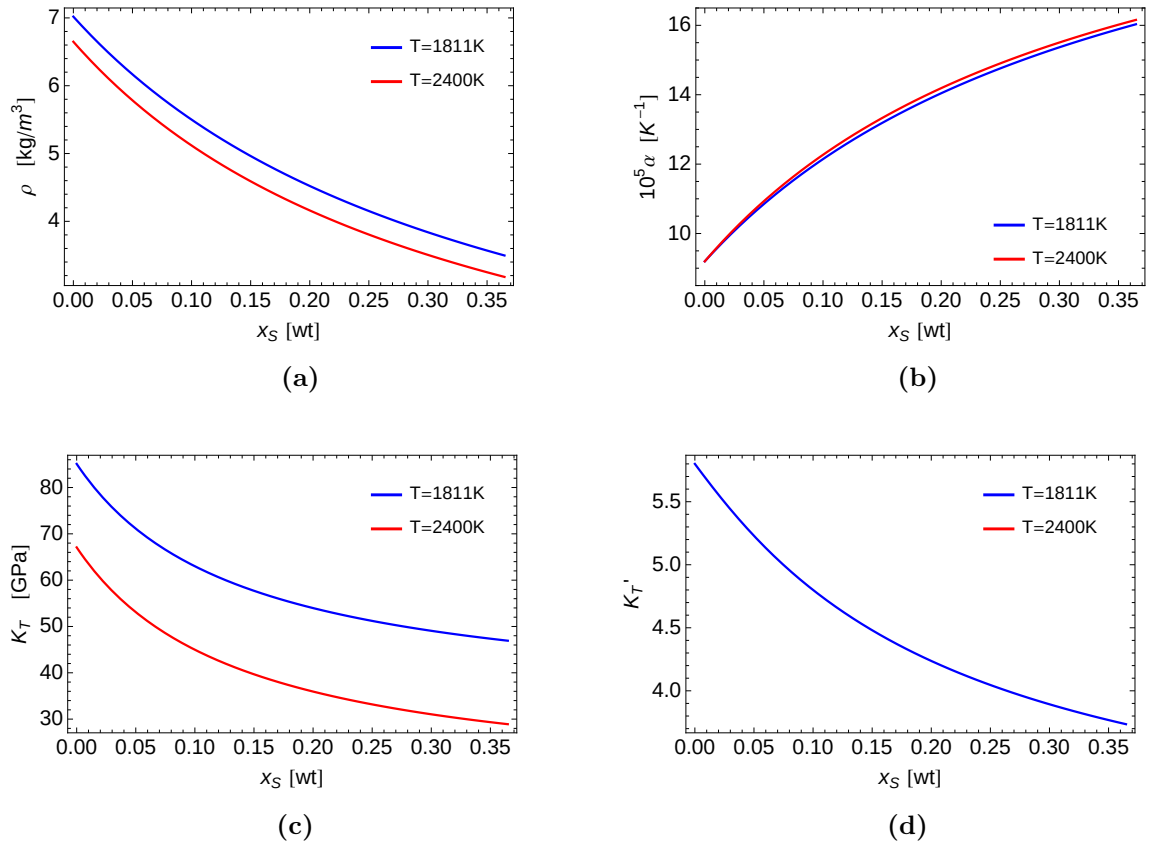


Figure 4.3: Density, thermal expansivity, bulk modulus, and derivative of bulk modulus with respect to pressure for the ideal solution model as a function of sulfur weight fraction at reference pressure for reference temperature ($T = 1811$K) and $T = 2400$K.

the volume of the solution. The thermal expansivity is proportional to the volume of the solution and therefore increases with increasing amount of sulfur in the solution.

Once the thermoelastic properties of the solution are calculated at reference conditions, they have to be corrected to local core conditions. Here, this is done by first through isobaric heating followed by isothermal compression. The density and the bulk modulus at local temperature are calculated from the reference value by (4.5) and (4.6). We assume that the bulk modulus of the $\mathrm{Fe}-\mathrm{S}$ solution depends linearly on temperature, see (4.6). Since the temperature dependence of the bulk modulus of sulfur in the ideal solution cannot be determined from the above introduced EoS data (see Tab.[4.3]) we here assume that the derivative of K_T with respect to temperature of the solution can be approximated by the one of liquid iron. Also, it is assumed that the derivative of K_T with respect to pressure is temperature independent. Fig.[4.3] shows density, thermal expansivity, bulk modulus and its derivative with respect to pressure for two different temperatures, the reference temperature ($T = 1811\mathrm{K}$) and for $T = 2400\mathrm{K}$, for the solution. The temperature dependence of the thermal expansivity is weak as both the thermal expansivity of liquid Fe and S in the solution are independent of temperature, and the dependence is solely a result of the temperature dependence of the volumes of the components and of the solution.

The density, bulk modulus, and the derivative of the bulk modulus are then calculated at local (P, T) by a finite-strain Birch-Murnaghan[7] equation of state Eqs. (3.10, 3.11, 4.13). In order to calculate the pressure wave velocity inside the fluid core layer the adiabatic bulk modulus is calculated from the pressure corrected thermal expansivity and Vashchenko and Zubarev Grüneisen parameter[8] (4.12) from formula (4.8). The two later quantities are also needed to calculate the temperature profile in a convective fluid core, see (2.4).

In order, to assess the influence of different core sulfur concentrations and core mantle boundary temperatures in the ideal solution model on the thermoelastic properties of cores of terrestrial planets we integrate the interior structure differential equations Eqs. (2.1, 2.2, 2.4) for a core of 1600km subjected to a core mantle boundary pressure of 21.5GPa and core mantle boundary temperatures of $T_{\mathrm{cold}} = 1800\mathrm{K}$ and $T_{\mathrm{hot}} = 2200\mathrm{K}$, which are plausible CMB conditions for a planet like Mars. We note that for the colder CMB temperature an iron-sulfur solution only melts for a sulfur weight fraction above about 7wt%.

We have calculated depth dependent pressure. temperature, density, bulk sound

[7]It is here tacitly assumed that the BM EoS can be applied to liquid solutions. For solid minerals, the BM EoS provides an accurate description for calculating density and elastic moduli for pressures significantly higher than those in cores of terrestrial planets. However, it is not adequate as an EoS for liquid silicate melts [*Ghiorso*, 2004]. Since microscopic properties of metals, liquid or solid, are rather different then those of silicates (isolators), it remains to be investigated if the BM equations provide a valid EoS for iron rich liquid solutions.

[8]It remains to be investigated if the Grüneisen parameter derived for solids can be applied to liquids. At high pressures ($> 15\mathrm{GPa}$) the structure of the liquid $\mathrm{Fe}-\mathrm{S}$ approaches the close packed structure of the solid [*Morard et al.*, 2008], see Fig.[4.2c], consequently the solid state formulations of γ might provide a satisfactory formulation for the core of Mars, but not for the upper part of the core of Mercury if a large core is assumed. Further note that the above used formulation for γ was derived under the assumption that the main contribution to thermal pressure is vibrational ($\gamma \sim P_{\mathrm{thermal}}$). This assumption is valid for isolators, however, for metals, the neglected electronic contribution resulting from free electrons is not negligible [*Anderson*, 2000].

velocity for sulfur weight fractions of 0wt%, 5wt%, 10wt%, 14wt% and 20wt%, see Figs. [4.4,4.5,4.6,4.7]. For given temperature and pressure conditions at the core mantle boundary the pressure at the center of the core decreases with increasing sulfur concentration. The pressure in $r = 0$km drops by about 15GPa if the core sulfur weight fractions increases from $x_S = 0$wt% (pure iron) to a $x_S = 20$wt%. The pressure resulting from the colder CMB temperature are slightly larger (relative difference below 2%) than pressure associated with the hotter CMB temperature. The pressure difference increases with pressure and decreases with sulfur concentration.

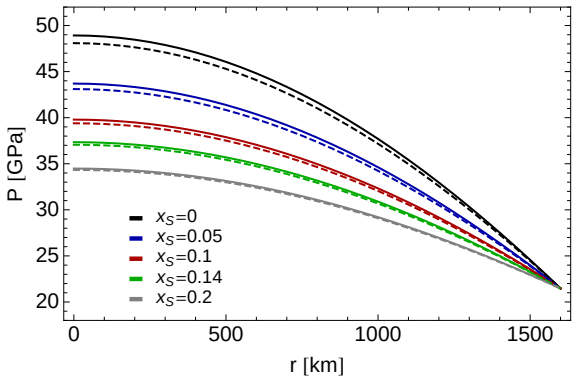
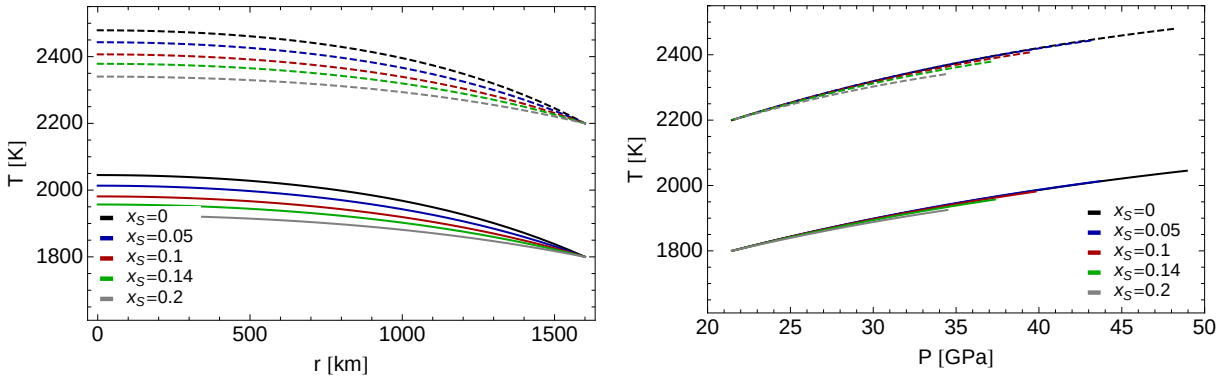


Figure 4.4: Pressure profiles as a function of core size for cold (continuous curves) and hot (dashed curves) core mantle boundary temperatures and different solution sulfur concentrations.

Fig.[4.5a] and Fig.[4.5b] represent the core temperature profile as function of radius and pressure. The results show that for a given CMB temperature; the average core temperature decreases with increasing amount of sulfur. For the hot CMB temperature condition, the temperature increase between the CMB to $r = 0$km is about 300K for 0wt% of sulfur and 150K for 20wt% of sulfur. For the cold CMB temperature condition, the temperature increase is lowered relative to the hot CMB scenario by about 50K. The dependence on the sulfur concentration is mainly due to the different pressure profiles as is illustrated in Fig.[4.5b] where the temperature pressure relation displays only a relatively weak dependence on the solution sulfur concentration.

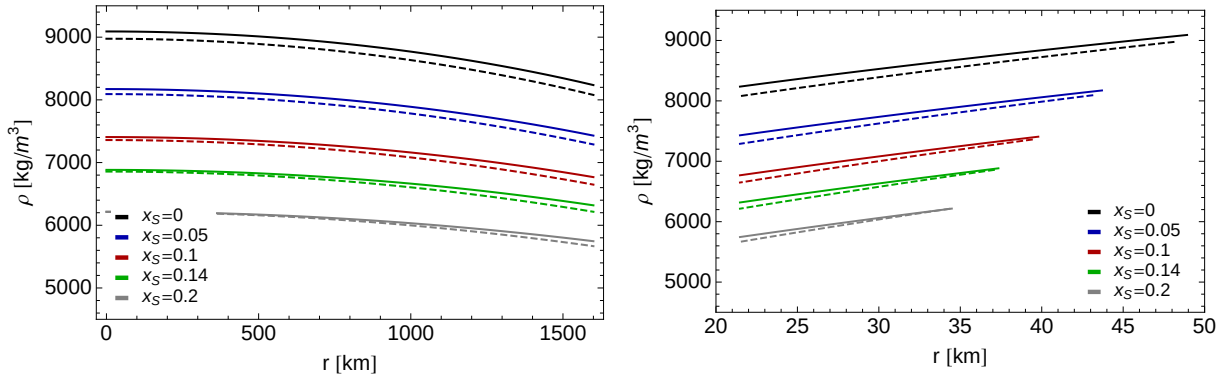
The density profiles as a function of radius and pressure are shown in Fig.[4.6a] and Fig.[4.6b]. Due to thermal expansion, hot CMB configurations have somewhat lower density profiles than those resulting from the cold CMB temperature (the average relative difference is below 2%). The relative difference between hot and cold decreases with increasing pressure and is smaller when the solution contains more sulfur. Since the compressibility is larger for the hot configurations and increases with increasing amount of sulfur (see Fig.[4.8b]). Also, note that the density increases about linearly with increasing pressure and with an approximative sulfur independent slope. On average, the slope is 34 ± 2kg/m^3/GPa for cold CMB temperatures and 39 ± 3kg/m^3/GPa for hot CMB temperatures.

The bulk sound velocity profiles for different fractions of sulfur and the two CMB temperature constraints are shown in Fig.[4.7]. The bulk sound velocity increases almost linearly with pressure and decreases with temperature and sulfur concentration. The rate of decrease with sulfur concentration decreases with increasing sulfur concentration. This results in an overlap of the bulk sound velocity curves at intermediary and high pressures.



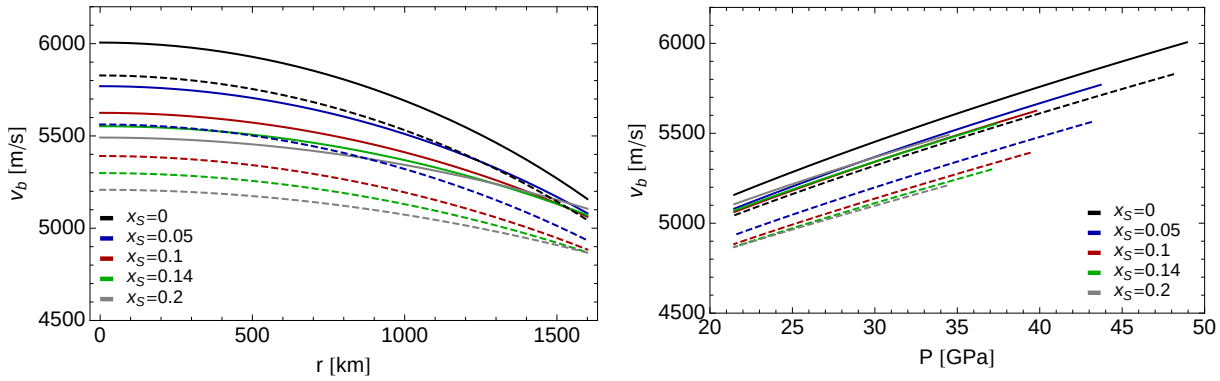
(a) **(b)**

Figure 4.5: Temperature profiles as a function of core size and core pressure for cold (continuous curves) and hot (dashed curves) core mantle boundary temperatures and different sulfur concentrations.



(a) **(b)**

Figure 4.6: Density profiles as a function of radius and core pressure for cold (continuous curves) and hot (dashed curves) core mantle boundary temperatures and different sulfur concentrations.

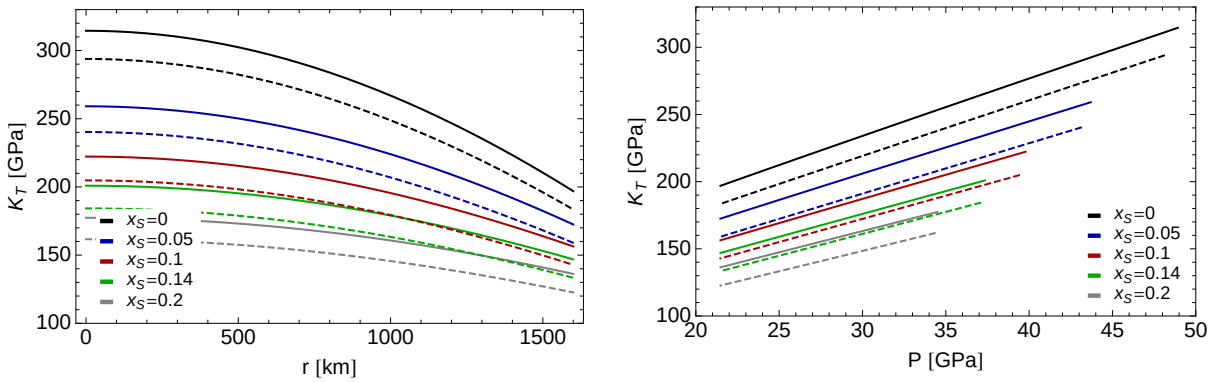


(a) **(b)**

Figure 4.7: Bulk sound velocity profiles as a function of radius and core pressure for cold (continuous curves) and hot (dashed curves) core mantle boundary temperatures and different sulfur concentrations.

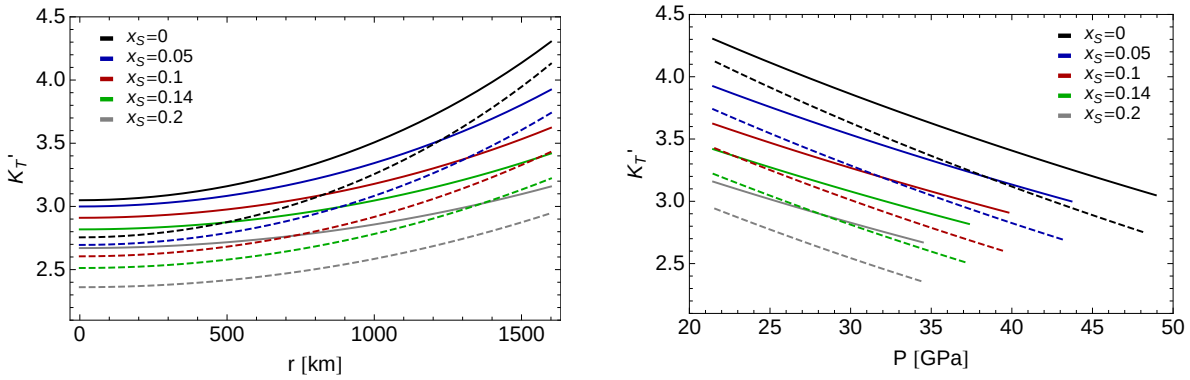
For instance, increasing the sulfur fraction to 5wt% for the hot CMB temperature results in approximatively similar v_b profile as the one obtained for pure iron with the cold CMB temperature.

For completeness we also present the thermoelastic quantities needed to calculate the density and the bulk sound velocity as a function of pressure and temperature (Fig.[4.8]-Fig.[4.12]). The compressibility of the solution increases with increasing amount of sulfur, decreases almost linearly with temperature, and increases with temperature (Fig.[4.8b]). Fig.[4.11] and Fig.[4.12] represent the thermal expansivity and the Grüneisen parameter as a function of radius and pressure. Both quantities are used to calculate the adiabatic bulk modulus (Fig.[4.10]) from the isothermal bulk modulus. The Grüneisen parameter decreases significantly with increasing pressure. Therefore, the common assumption of a more or less constant Grüneisen parameter over a wide pressure range, e.g. for estimating the adiabat temperature gradient inside a convective core, is to be avoided.



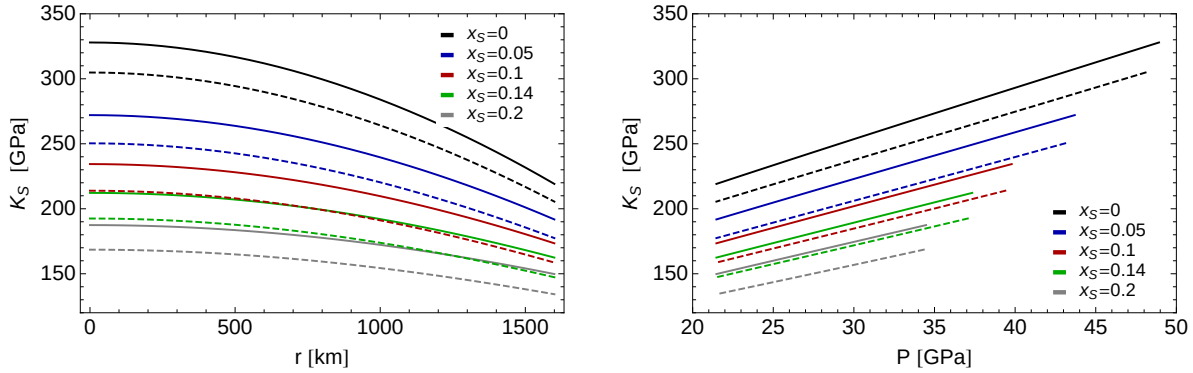
(a) **(b)**

Figure 4.8: Isothermal bulk modulus profiles as a function of radius and core pressure for cold (continuous curves) and hot (dashed curves) core mantle boundary temperatures and different sulfur concentrations.



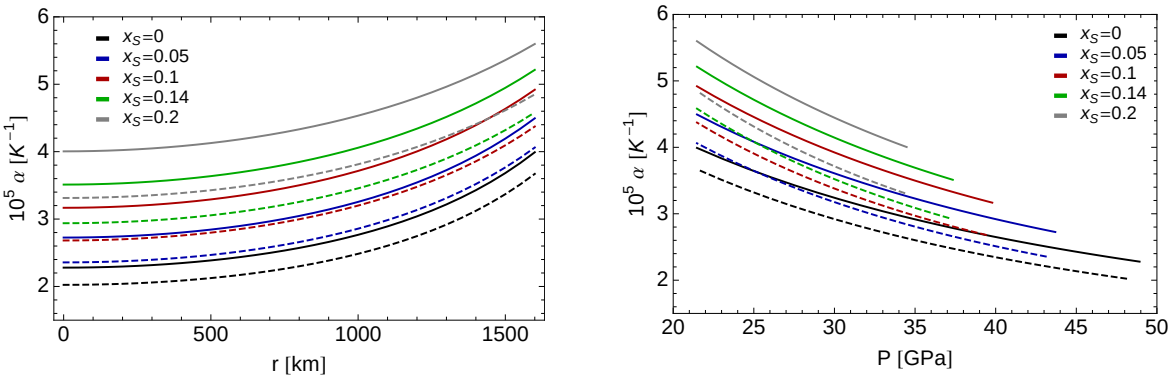
(a) **(b)**

Figure 4.9: Derivative of isothermal bulk modulus with respect to pressure profiles as a function of radius and core pressure for cold (continuous curves) and hot (dashed curves) core mantle boundary temperatures and different sulfur concentrations.



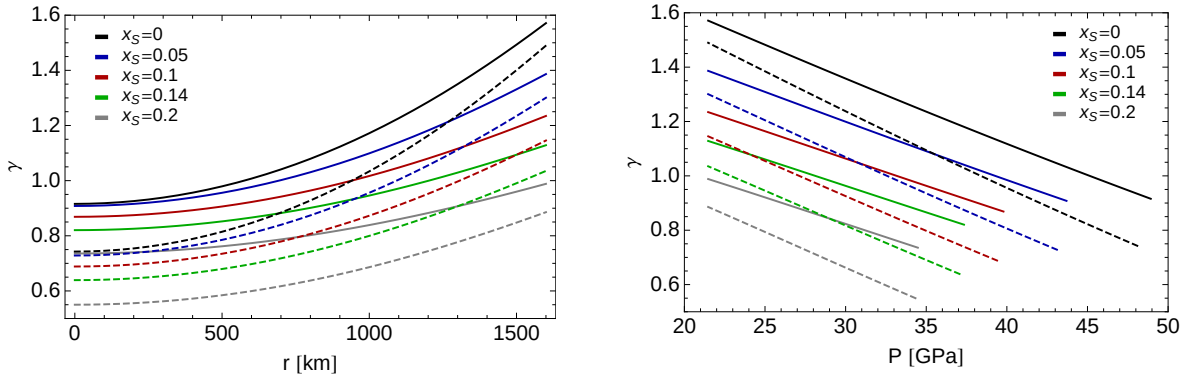
(a) **(b)**

Figure 4.10: Adiabatic bulk modulus profiles as a function of radius and core pressure for cold (continuous curves) and hot (dashed curves) core mantle boundary temperatures and different sulfur concentrations.



(a) **(b)**

Figure 4.11: Thermal expansivity profiles as a function of radius and core pressure for cold (continuous curves) and hot (dashed curves) core mantle boundary temperatures and different sulfur concentrations.



(a) **(b)**

Figure 4.12: Grüneisen parameter profiles as a function of radius and core pressure for cold (continuous curves) and hot (dashed curves) core mantle boundary temperatures and different sulfur concentrations.

Real solutions

The ideal solution model provides the simplest thermodynamic coherent description of solutions. Since the model neglects component interaction, thermodynamic properties of the solution can be calculated from the thermoelastic properties of each individual component. Presently this is the only viable solution as high pressure data relevant for the cores of planets like Mars or Mercury are scarce. However, phase diagrams of $\mathrm{Fe}-\mathrm{S}$ at 3GPa [*Brett and Bell*, 1969], at 10GPa and 14GPa [*Chen et al.*, 2008] to the left of the eutectic (iron rich) display typical non-ideal liquidus curves. Moreover, recent density measurements at 4GPa of $\mathrm{Fe}-\mathrm{S}$ solutions for sulfur fractions up to 50wt% exhibit significant deviations from the ideal solution behavior [*Nishida et al.*, 2008].

The simplest extension towards a more realistic description of real solutions is the *regular solution* model [e.g. *DeHoff*, 2006, page 232]. Compared to the ideal solution model it has the same entropy of mixing (4.26) but it includes a nonzero mixing enthalpy ΔH_{mix}. In the regular solution model the mixing entropy and the mixing enthalpy do not depend on temperature. Since the Gibbs energy is temperature dependent through the fundamental relation (4.14), the Gibbs mixing energy is also temperature dependent. It is

$$\Delta \mathcal{G}_{\mathrm{mix}} = \Delta H_{\mathrm{mix}} - T\Delta S^{\mathrm{id}}_{\mathrm{mix}}, \tag{4.27}$$

$\Delta S^{\mathrm{id}}_{\mathrm{mix}}$ is the mixing entropy of the ideal solution model, see (4.26). In a two component regular solution the mixing enthalpy ΔH_{mix} is

$$\Delta H_{\mathrm{mix}} \equiv \alpha_0 x_1 x_2 \equiv \Delta \mathcal{G}^{\mathrm{xs}}_{\mathrm{mix}}, \tag{4.28}$$

where $\Delta \mathcal{G}^{\mathrm{xs}}_{\mathrm{mix}}$ is the excess Gibbs energy and α_0 a composition independent constant that determines the interaction between component 1 and 2. The expression of the mixing enthalpy depicts the simplest symmetric between component interaction term that is zero for pure components. By using (4.15) and from the definition of the chemical activity (4.17) the mixing enthalpy can be expressed as activity coefficients. For the binary regular solution we obtain

$$f_1 = \mathrm{e}^{\frac{\alpha_0 x_2^2}{RT}} \quad \text{and} \quad f_2 = \mathrm{e}^{\frac{\alpha_0 x_1^2}{RT}}. \tag{4.29}$$

Nishida et al. [2008] have shown that from their measurements of the density of $\mathrm{Fe}-\mathrm{S}$ solutions for different fractions of sulfur, the molar volume as a function of the molar fraction of sulfur (x) is well described at 4GPa pressure by a regular solution model. With the definitions of the activity coefficients (4.17) and the definition of the volume of a binary solution (4.20), the molar volume as function of sulfur fraction at constant pressure reads

$$V = (1-x)V_{\mathrm{Fe}} + xV_{\mathrm{S}} + x(1-x)\beta(P), \tag{4.30}$$

where

$$\beta(P) = \left(\frac{\partial\, \alpha_0}{\partial P}\right)_{T,n_i}. \tag{4.31}$$

Nishida et al. [2008] estimated the molar volume of iron in the solution at 4GPa as $V_{\mathrm{Fe}} = 7.72\mathrm{cm}^3/\mathrm{mol}$, the molar volume of sulfur in the solution as $\mathrm{V_S} = 18.68\mathrm{cm}^3/\mathrm{mol}$ and the interaction coefficient as $\beta(4\mathrm{GPa}) = \beta_0 = -14.27$. Compared to the molar volume of sulfur in the ideal solution model estimated from the EoS data of Tab.[4.3],

the value of V_S in the regular solution model is about 8% lower. However, the difference would only be relevant if the regular solution model were valid for solutions up to 100% of sulfur.

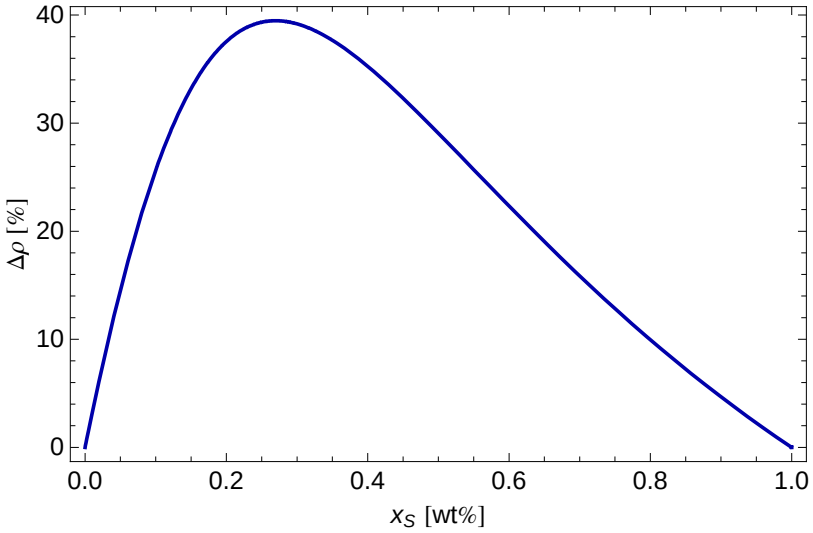


Figure 4.13: Relative deviation of measured density of Fe − S liquid solution compared to an ideal solution.

The relative departure of the solution density from an ideal solution model is shown in Fig.[4.13]. Note that the deviation is shown for no sulfur to 100% sulfur. The model is however strictly speaking only valid for sulfur concentrations up to 36wt%. The result show that the relative deviation can be as high as 40% when the sulfur fraction is about 26wt%. Indicating that the measured volume of the solution is significantly smaller than the one predicted from an ideal solution model fitted on the same data. The effective volume of the sulfur atoms in the solution decreases with increasing amount of sulfur and reaches a maximum at about 26wt%, (40at%). Note that this is about the eutectic composition of sulfur in Fe − S at 4GPa [*Morard et al.*, 2007].

Fig.[4.14] shows the sulfur weight fraction obtained if the density of an Fe − S solution is interpreted in terms of an ideal solution. It shows that if the sulfur concentration is estimated from the density within the framework of an ideal solution model the concentration of sulfur is systematically underestimated. For example, at 4GPa and 1973K, a 2wt% ideal iron-sulfur solution has the same density as a 10wt% iron-sulfur solution.

Beside density data of Fe − S solutions there are also recent measurements at low pressure of isothermal bulk moduli for different fractions of sulfur [*Sanloup et al.*, 2000]. Those measurements, together with the molar volume estimates of *Nishida et al.* [2008] can be used to estimate the bulk modulus of sulfur in ideal and regular solutions. *Sanloup et al.* [2000] have measured the densities of Fe − S solutions for different fractions of sulfur over the $[1.5, 6.2]$GPa pressure range and $[1500, 1780]$K temperature range. From the data they have estimated bulk moduli for their solution with those fractions of sulfur under the assumption that K'_T is between 4 and 7. The data is shown together with the bulk modulus of pure iron (Tab.[4.3]) in Fig.[4.15]. The error-bars result from density measurement errors and from the assumed K'_T range. For the figure, the bulk moduli

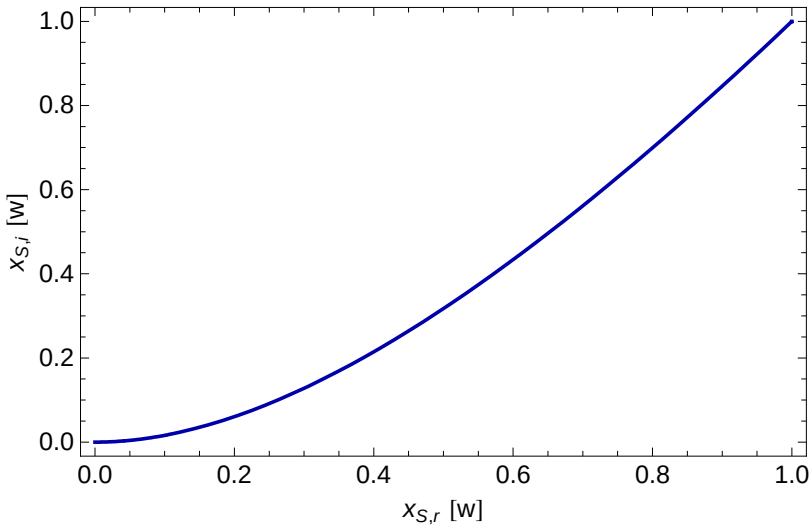


Figure 4.14: Sulfur weight fraction of measured solution interpreted as sulfur weight fraction of ideal solution. $x_{\mathrm{S},r}$ and $x_{\mathrm{S},i}$ are the measured sulfur fraction in the solution and the sulfur fraction of the same solution interpreted as an ideal solution.

have been corrected to the temperature $T = 1923$K, the reference temperature of the data series of *Nishida et al.* [2008]. The data have then been fitted to an ideal solution model K_T and to a regular solution model K_T with an excessive volume depending linearly on pressure. By using the estimated molar volumes for iron, sulfur, and excessive mixing volume from the data of *Nishida et al.* [2008]. The resulting fits are shown in Fig.[4.15]. The estimated isothermal bulk moduli for sulfur in the solutions are 11.3GPa for the ideal solution model and 16GPa for the regular solution model. Note that the K_T for sulfur in the ideal solution model fitted on high pressure EoS data is about 39GPa (Tab.[4.3]). The figure shows that neither the ideal solution model nor the simplest regular solution model, with a pressure independent excessive volume, provides a satisfactory representation of the measured data, especially for high sulfur concentrations.

If a simple solution model is assumed, here ideal or regular, the above discussed data allows to estimate EoS parameters for sulfur in $\mathrm{Fe}-\mathrm{S}$ solutions. If this EoS data is supplemented with thermal expansivity data it can be used to calculate densities and bulk sound velocities for the liquid part of cores of smaller planets (Moon core like).

It is tentative to use the low pressure results and extrapolate them to high pressure. However, as recent data shows [*Morard et al.*, 2008], $\mathrm{Fe}-\mathrm{S}$ liquids are subject to a major structural change at pressures about below 15GPa. The behavior of sulfur in the solution changes from *covalent* to a more compact *interstitial*[9]. The interstitial behavior prevails

[9] A solution can be substitutional or interstitial. In a substitutional solution each, individual atom occupies a lattice site. In an interstitial $\mathrm{Fe}-\mathrm{S}$ solution, sulfur acts as an interstitial impurity, meaning that it preferably occupies locations in the crystal other than the normal lattice sites of $\mathrm{Fe}-\mathrm{Fe}$. The thermodynamic description of interstitial solution is conceptually different from substitutional solutions, because the state of pure solute is often inassessible for the interstitial solution. For instance $\mathrm{Fe}-\mathrm{H}$ forms an interstitial solution, and H does not exist as a stable phase at ambient conditions, but rather H_2. For a description of interstitial solution modeling see for instance *DeHoff* [2006, Chapt. 13] or *Oates and Flanagan* [1981].

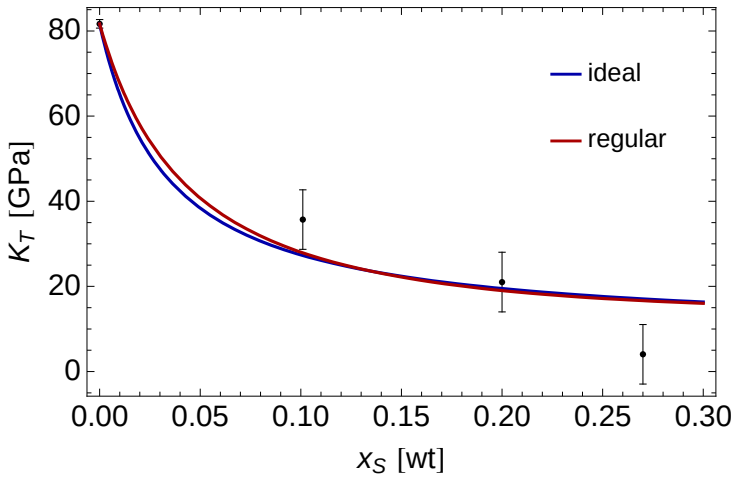


Figure 4.15: Sulfur dependent isothermal bulk modulus as a function of sulfur concentration at 4GPa and $T = 1923$K.

at least up to pressures of 65GPa [*Morard et al.*, 2008]. The structural changes in the solution imply changes in the thermodynamic properties that are not accounted for by basic usage of equations of state. For Mercury, this phase transition might be of relevance, since the presently estimated core size allows for a pressure range inside the core from about 10GPa to about 40GPa [*Rivoldini et al.*, 2009].

4.5 Melting

4.5.1 Introduction

Melting is the transition between two of the principal states of matter, solid and liquid. It is a first order phase transition, which means that it is this is related to discontinuities of first derivatives of the free energy, like volume and entropy[10] (see equations (4.20) and (4.18)). Different theoretical descriptions have been devised to describe the process of melting at microscopical level. A successful melting theory is based on the free proliferation of dislocations in crystals. In this theory melting occurs when the free energy of the undislocated crystal and one saturated with dislocations (the liquid) are equal. As the model is only based on dislocation propagation and does not account for changes in molecular structure of the melt and the solid it cannot for instance describe the melting of water ice. But it has been shown that most metals fit in the theory as long as no major structural changes occur.

Morard et al. [2008] use the term covalent solution to describe the structure of the liquid prior to the transition to the more compact interstitial structure. In a covalent solution, the atoms share their valence electrons. It is however, not clear that by a solution with covalent structure is meant a substitutional solution.

[10]Second order phase transitions are expressed as discontinuities in the second derivatives of the free energy, like the phase transition from β to γ spinel in the upper Earth mantle. During this phase transition the volume and the entropy change continuously, but the elastic bulk modulus changes discontinuously, see (4.21).

In the context of planetary core modeling it is important to know the melting conditions for all pressures and temperatures occurring inside the core as a function of light element concentration. For example, if the core bulk composition and the core mantle boundary pressure and temperature were to be known, then the melting law will not only determine the state of the core, but also determine the size of the inner core, the temperature at the inner core outer core boundary, and the concentration in light elements of the liquid outer an solid inner core.

In this section we will present recently acquired melting data related to core material and discuss the consequences of the limited amount of data. We introduce some tools and theoretical concepts to overcome this shortage.

The state of core material, solid or liquid, depends on the local pressure and temperature and on the composition of the material. The regions of stability of one or more phases, depending on thermodynamic variables, often pressure, temperature and composition are usually represented by phase diagrams.

Fig.[4.16] represents a phase diagram for $Fe-S$ at 21GPa for the thermodynamic variables temperature and sulfur weight fraction [*Fei et al.*, 2000]. The curve between the $'Fe+L'$ field and the $'L'$ field is called the liquidus or melting curve. It represents the melting temperature of an $Fe-S$ solution as a function of sulfur concentration. The melting temperature of pure iron strongly decreases with increasing amount of sulfur. At 21GPa a solution containing about 16wt% of sulfur has its melting temperature reduced by about 900K compared to pure iron. The curve delimiting the $'Fe+L'$ field and the $'Fe+Fe_3S'$ is the solidus. The sulfur concentration of the lowest melting temperature is called the *eutectic concentration*. In a simple two component eutectic system, if the temperature is above the melting temperature, the components form a liquid solution for any proportion of components. If the solution is of eutectic composition and the temperature drops below the eutectic temperature, the solution unmixes and each component crystalizes separately. As long as the system contains liquid the temperature will not lower until all the eutectic liquid has solidified. The resulting solid is not a solid solution, but rather a homogeneous mixture, an alloy. To the left side of the eutectic, when the temperature drops below the liquidus, solid iron is expelled from the solution and the sulfur concentration in the solution increases. Upon further cooling, more solid iron is expelled and the sulfur concentration in the solution increases until the eutectic concentration is reached. During the whole cooling event the local temperature follows the liquidus curve.

For concentrations to the right of the eutectic, the cooling scheme is similar only instead of solid iron solid iron-sulfur compounds solidify and are expelled from the solution and the solution is enriched in iron upon cooling.

When a system made of solid Fe and Fe_3S, with a sulfur concentration to the left of the eutectic, is heated the first melt produced will have eutectic composition and it will melt at the eutectic temperature. As the eutectic liquid contains more sulfur than the solid, the solids sulfur concentration decreases. As long as there is sulfur in the solid the temperature will not increase upon heating (the system moves along the solidus curve). When all the sulfur has molten away (the outermost left on the solidus line) the temperature will rise if the system is further heated and the remaining solid iron will melt when its melting temperature is reached.

Thermodynamically, melting at a given pressure and temperature occurs when the

Gibbs free energy of the solid and the liquid phase are equal. For one component systems the chemical potential and the Gibbs free energy are equal. Formally this two phase equilibrium reads

$$\mathcal{G}^s(P,T) = \mathcal{G}^l(P,T), \tag{4.32}$$

where $\mathcal{G}^s$ and $\mathcal{G}^l$ are the Gibbs energies of the solid and liquid phase. With the definition of the differential form of the Gibbs energy [e.g. *Callen*, 1985]

$$d\mathcal{G}^{s,l} = -S^{s,l}dT + V^{s,l}dP \tag{4.33}$$

the above equilibrium condition results in the *Clausius-Clapeyron equation*

$$\frac{d\,P}{dT} = \frac{\Delta S^{s\to l}}{\Delta V^{s\to l}}, \tag{4.34}$$

where $\Delta S^{s\to l} = S^l - S^s$ is the change in entropy upon melting and $\Delta V^{s\to l} = V^l - V^s$ is the change in volume upon melting. The Clausius-Clapeyron equation gives the slope of the melting temperature and is valid for every two-phase system. In principle the phase boundary between the two phases can be obtained from the Clausius-Clapeyron equation, if the melting volume and entropy are known as a function of pressure and temperature. It is needless to say that this is hardly the case in practice.

The relation between thermodynamical variables, e.g. pressure, temperature, and concentrations of components is formalized by the *Gibbs phase rule*. It is a relation between the number of degrees of freedoms of a system f, the number of components c, and the number of phases p [e.g. *Callen*, 1985]. It reads

$$f = c - p + 2. \tag{4.35}$$

Phases are defined as stable homogeneous parts of the system that are mechanically separable from the system. In the $\mathrm{Fe-S}$ system the phases at 21GPa, are Fe, L, $\mathrm{Fe_3S}$, and the other sulfur-iron compounds. The components are the constituents by which the compositions of the phases can be expressed, here Fe and S. For this particular phase diagram, the pressure is fixed, so that one degree of freedom is lost and the formula reads $f = c - p + 1$.

4.5.2 Melting data

In order to decide on the state of an iron-sulfur core, for planets the size of Mercury or Mars, and on the presence of an inner core, one would need melting data over a range of pressures $[8, 50]$GPa. Useful melting data (in the form of phase diagrams) have been published at discrete pressures values of 10GPa and 14GPa by *Chen et al.* [2008] (Fig.[4.17]), at a pressure of 21GPa by *Fei et al.* [2000], and at 23GPa and 40GPa by *Stewart et al.* [2007]. With the exception of the first authors, who measured the melting temperature for a wide range of sulfur concentrations, the other data, at least for concentrations to the left of the eutectic and temperatures where melting occurs, is limited to concentrations about the eutectic. Most authors then supplement the data by the melting temperature of pure iron [*Boehler et al.*, 1990; *Shen et al.*, 1998] and draw a liquidus curve through the data points with a shape suggesting an underlying ideal solution model

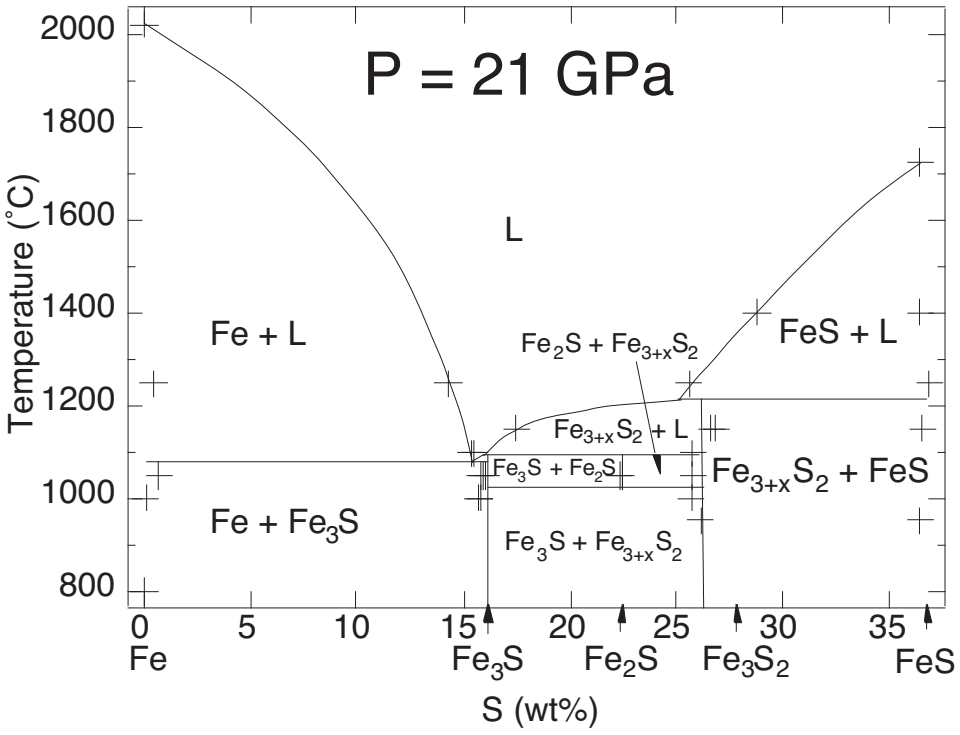


Figure 4.16: Phase diagram of the Fe – S system at 21GPa. The experimental data are represented by '+' symbols. The melting temperature of Fe and FeS are from *Boehler et al.* [1990]; *Boehler* [1992] . The other data points are from *Fei et al.* [2000]. L stands for liquid.

[e.g. *DeHoff*, 2006]. However, at lower pressures, where liquidus temperatures for sulfur concentrations between pure iron and eutectic concentration have been measured, the results show distinctive features suggesting significant deviations from the ideal behavior (see Fig.[4.17]), especially at 14GPa, [e.g. *DeHoff*, 2006]. For instance, at 14GPa, for a sulfur concentration of 6wt% the ideal model predicts a melting temperature of 2050K where the measured values is about 1720K! In this pressure domain liquid and solid iron [*Shen et al.*, 1998, 2004] do not experience any structural changes, so the strong deviation from non-ideality is probably related to a structural change experienced by the eutectic liquid as it evolves toward a more compact structure in the $[13-17]$GPa pressure range [*Morard et al.*, 2007].

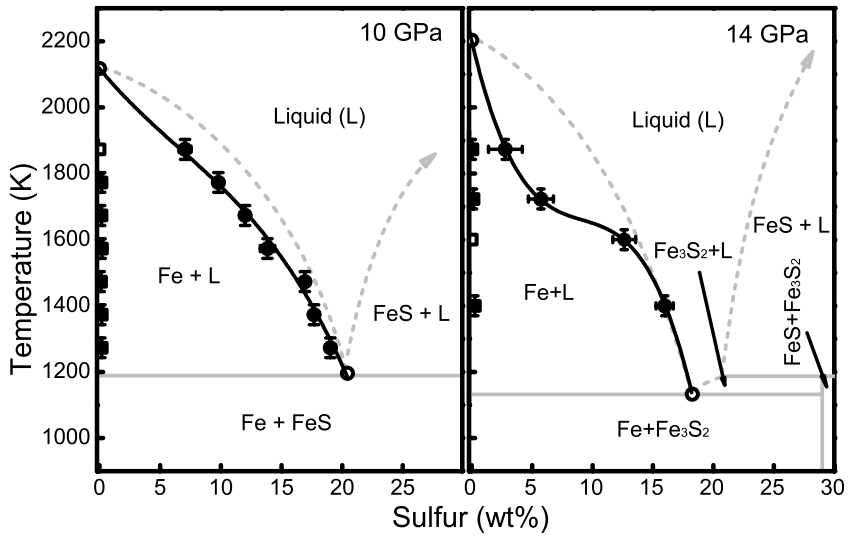


Figure 4.17: Phase diagram of the $Fe-S$ system at 10GPa and 14GPa from *Chen et al.* [2008]. L stands for liquid. The dashed curves suggest ideal solution melting.

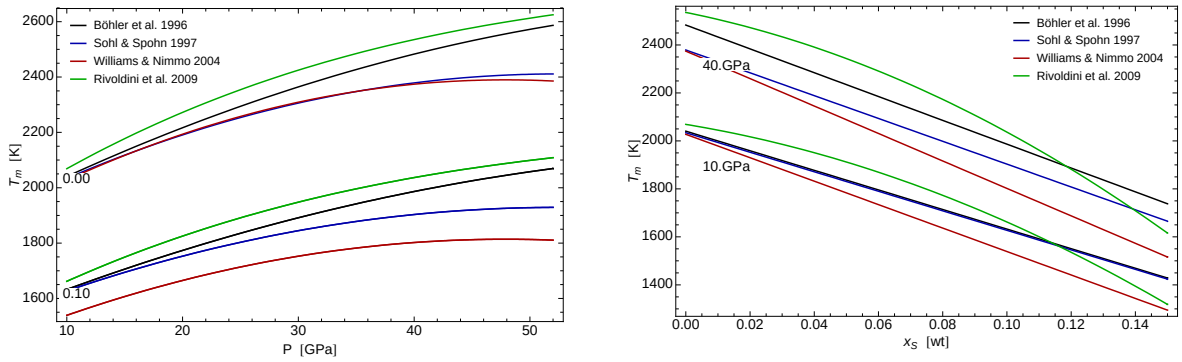
4.5.3 Melting laws

Usually the shortage of melting data is overcome by constructing empirical melting laws summarizing the dependence of the melting temperature on pressure and sulfur concentration through a polynomial expansion of the following type

$$T_m(x,P) = T_{m_0}(1-\alpha_1 x-\alpha_2 x^2+\ldots)(\beta+T_{m_1}P+T_{m_2}P^2+\ldots), \tag{4.36}$$

where it is assumed that the sulfur concentration is not dependent on pressure. The constants in the equation are fitted by using melting temperature data of pure iron, which are relatively well known over a wide pressure range, and data about the eutectic temperature and sulfur concentration. In (4.36) T_{m_0} is the melting temperature of pure iron, and the polynomial depending on pressure is an approximation of the pressure dependence of the melting temperature of iron normalized by the melting temperature of iron at reference condition. Fig.[4.18] shows empirical melting law fits as a function of pressure and sulfur concentration as obtained by different authors. The curves of

Boehler [1996], *Sohl and Spohn* [1997] and *Williams and Nimmo* [2004] used a melting temperature expansion linear in x_S and quadratic in P. *Rivoldini et al.* [2009] have used a quadratic polynomial in x and a cubic polynomial in P (but restrict the validity of their melting law fit to sulfur fractions smaller than 6wt%). Since the different authors have only used the melting data available at the publication time of their article the parameters in the empirical melting law are different. The resulting curves show that the different sets of melting data lead to significantly different melting temperatures. The differences increase with increasing pressure, at 40GPa the difference between the melting law providing the lowest and the melting law providing the highest melting temperature is about 200K for low sulfur concentration. Note that with the exception of *Rivoldini et al.* [2009], the data available by the different authors was measured at pressures below about 21GPa.



(a) **(b)**

Figure 4.18: Empirical melting law as a function of pressure Fig.[4.18a], for 0wt% and 10wt% of sulfur, and as a function of sulfur concentration Fig.[4.18b], for 10GPa and 40GPa.

The reasons for the strong differences between the different empirical polynomial fits are twofold. Firstly, in the light of the complexity of the $Fe-S$ system, as is illustrated for instance in Figs.[4.21,4.22,4.17], the smooth polynomial expansion orthogonal in x and P seems hardly suitable for summarizing the liquidus curve of the $Fe-S$ phase diagram. More general Taylor expansions, with mixed terms in P and x, could provide more faithful representation of the data. However, due to the local character of the Taylor expansion, the expansions are still not able to represent the whole phase diagram satisfactorily with a reasonable amount of expansion terms. The second reason for the strong differences is the general lack of high pressure data over wide ranges in sulfur concentrations. With the exception of the pressure dependent melting temperature of pure iron Fig.[4.19], pressure dependent melting data is generally only provided for the eutectic concentration. Moreover, only recently the eutectic melting temperature and concentration have been measured for the whole pressure range relevant for the core of Mars or Mercury. The eutectic temperature as a function of pressure and sulfur concentration is shown in Figs.[4.21,4.22].

In summary, as long as melting data for iron rich iron-sulfur solutions has not been apprehended one has to resort to similar empirical approaches to represent the melting data. Here we will build an empirical melting law for sulfur concentrations to the left

T_0	a_1	a_2	a_3
1811K	28.945K/P	-0.3236K/P^2	0.00132K/P^3

Table 4.4: Fitted parameter values for the polynomial iron melting curve representation.

of the eutectic by using new data on the pressure dependent eutectic, concentration and temperature, together with the pressure dependent melting data of iron. we will also show how the thermodynamic description of melting together with solution models can be used in principle to find a more physical representation of the melting curve.

Pure iron melting

The melting temperature as a function of pressure for iron is shown in Fig.[4.19]. The data is from *Boehler et al.* [1990] and *Shen et al.* [1998]. The black curve in the figure results from a least square fit of a cubic polynomial on the data (intermediate to the two triple-points δ-γ-liquid and γ-ε-liquid, see Fig.[4.1]):

$$T_m(P) = T_0 + a_1 P + a_2 P^2 + a_3 P^3, \tag{4.37}$$

where the fitted parameter values are given in Tab.[4.4]. As the figure shows, the polynomial gives a faithful representation of the data.

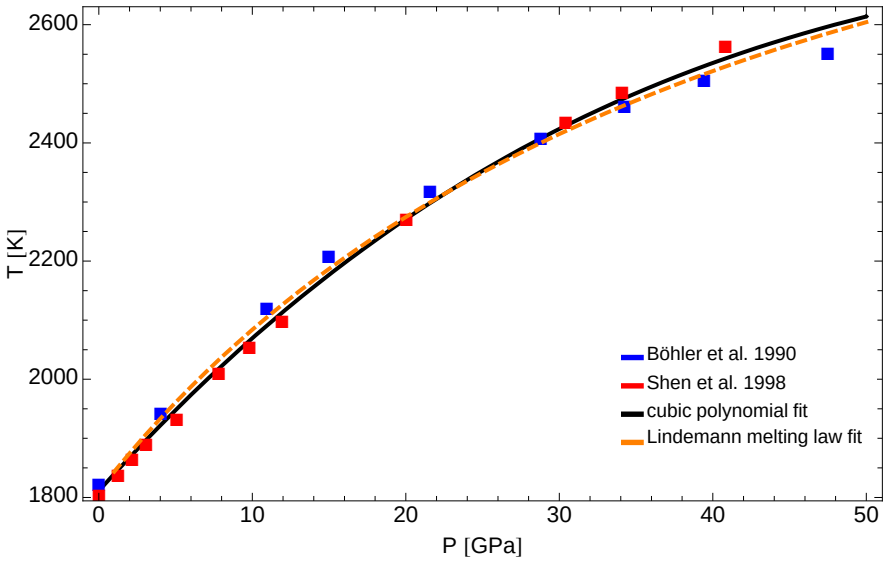


Figure 4.19: Melting temperature of pure iron as a function of pressure. The black curve represents a cubic least square fit of the data and the dashed orange curve is a fit of the Lindeman melting law on the data.

The melting temperature of iron as a function of pressure can in principle be calculated by integrating the Clausius-Clapeyron equation (**??**). However, since the change in volume and entropy upon melting as a function of pressure and temperature are unavailable for the conditions prevalent in terrestrial planets core it cannot be done in practice.

A more convenient way to obtain the melting temperature of iron is provided the *Lindemann melting law* [e.g. *Stacey and Davis*, 2008, page 324]. The differential form of the Lindemann law can be expressed as

$$\frac{1}{T_M}\frac{d\,T_m}{dP} = \frac{2(\gamma - \frac{1}{3})}{K_T}, \tag{4.38}$$

where γ is the Grüneisen parameter and K_T the isothermal bulk modulus. Originally the derivation was based on the assumption that melting occurs when the amplitude of atomic vibration reaches a critical fraction of atomic spacing. In other words the melting temperature description was based only on properties of the solid phase. However, the same expression can be derived from considerations of the melting model based on the propagation and proliferation of dislocations[11] [e.g. *Stacey and Davis*, 2008, page 324-325]. Equation (4.38) can be integrated, by using fundamental thermodynamic relations, to extrapolate the melting temperature $T_m(P_0) = T_0$ from P_0 to P:

$$T_m(P) = T_0 \left\{\frac{\rho(P_0,T_0)}{\rho(P,T_m)}\right\}^{2/3} \exp\left\{\frac{2\gamma(P_0,T_0)}{q}\left[1 - \left(\frac{\rho(P_0,T_0)}{\rho(P,T_m)}\right)^q\right]\right\}, \tag{4.39}$$

where q is a constant [e.g. *Stacey and Davis*, 2008] relating the pressure and temperature dependent density to the Grüneisen parameter:

$$\frac{\gamma(P,T)}{\gamma(P_0,T_0)} = \left\{\frac{\rho(P_0,T_0)}{\rho(P,T)}\right\}^q \tag{4.40}$$

Here we use (4.39) as a compact representation of the melting temperature as a function of pressure. The values of q and γ at pressure P_0 and temperature T_0 have been obtained by fitting (4.39) on the melting data of iron together with the EoS parameters of solid $\gamma - \mathrm{Fe}$. For $P = 10^5$Pa and $T = 1811$K, the melting temperature of iron at ambient pressure, the estimated Grüneisen parameter is $\gamma = 1.54$ and the estimated q value is 2.9. The integrated Lindemann melting curve corresponding to the estimated γ and q values is shown in Fig.[4.19]. The maximal temperature difference between the Lindemann melting curve and the polynomial melting curve is below 16K.

Iron sulfur melting

Next we need to understand how sulfur lowers the melting temperature of iron, if the sulfur concentration is below the eutectic concentration. And how the melting temperature of the first solid iron-sulfur compound to the right of the eutectic increases with increasing amount of sulfur. Depending on the pressure, the first iron-sulfur compound to the right of the eutectic is different. At 10GPa it is FeS (Fig.[4.17]), Fe_3S_2 at 14GPa (Fig.[4.17]), and $Fe_{3+x}S_2$ with at 21GPa (Fig.[4.16]). For higher pressures at least up to 60GPa, it most likely is Fe_3S_2.

To the left of the eutectic, upon melting we have for iron

$$\mu_{\mathrm{Fe},l}(P,T,x_l) = \mu_{\mathrm{Fe},s}(P,T,x_s), \tag{4.41}$$

[11] In the dislocation model of melting, the crystal saturated with dislocations is identified with the liquid. Melting occurs when the free energy of the dislocation free crystal and the one saturated with dislocations are equal. See *Poirier and Price* [1992] for an application to the melting of metals.

where the subscript s and l stand for solid and liquid and x_s and x_l are the fractions of sulfur in the solid and liquid solutions. From this equilibrium condition and by using (4.24) the fraction of sulfur in the liquid phase is obtained from

$$x_l = 1 - (1 - x_s)\frac{f_{\mathrm{Fe},s}(x_s)}{f_{\mathrm{Fe},l}(x_l)}\mathrm{e}^{-\frac{\Delta\mu^{s\to l}_{\mathrm{Fe}}}{RT}}, \tag{4.42}$$

where

$$\Delta\mu^{s\to l}_{\mathrm{Fe}}(P,T) = \mu_{\mathrm{Fe},l}(P,T,0) - \mu_{\mathrm{Fe},s}(P,T,0), \tag{4.43}$$

is the change in free energy of pure iron upon melting. If it is assumed that sulfur is not dissolving in solid iron, and that the solution is ideal, (4.42) simplifies to

$$x_l = 1 - \mathrm{e}^{-\frac{\Delta\mu^{s\to l}_{\mathrm{Fe}}}{RT}}. \tag{4.44}$$

In the first field to the right of the eutectic, upon melting we have for the iron-sulfur compound $\mathrm{Fe}_\alpha\mathrm{S}_\beta$

$$\mu_{\mathrm{Fe}_\alpha\mathrm{S}_\beta,l}(P,T,x_l) = \mu_{\mathrm{Fe}_\alpha\mathrm{S}_\beta,s}(P,T,x_s). \tag{4.45}$$

To obtain the sulfur concentration in the solution we first have to determine the chemical activity of $Fe_\alpha S_\beta$. It can be determined from the following chemical reaction

$$\alpha\mathrm{Fe} + \beta\mathrm{S} = \mathrm{Fe}_\alpha\mathrm{S}_\beta \tag{4.46}$$

together with the property that at chemical equilibrium the chemical potentials of the species Fe, S, and $\mathrm{Fe}_\alpha\mathrm{S}_\beta$ are related by [e.g. *DeHoff*, 2006, chap. 11]

$$\mu_{\mathrm{Fe}_\alpha\mathrm{S}_\beta} = \alpha\mu_{\mathrm{Fe}} + \beta\mu_{\mathrm{S}}. \tag{4.47}$$

The chemical activity of $\mathrm{Fe}_\alpha\mathrm{S}_\beta$ is obtained from (4.47) and (4.24) together with the boundary condition that $a_{\mathrm{Fe}_\alpha\mathrm{S}_\beta} = 1$ when all Fe and S have reacted to form $\mathrm{Fe}_\alpha\mathrm{S}_\beta$. As a function of the activity coefficients of Fe (f_{Fe}) and S (f_{S}) it can be written as

$$a_{\mathrm{Fe}_\alpha\mathrm{S}_\beta} = \frac{f^\alpha_{\mathrm{Fe}}(1-x)f^\beta_{\mathrm{S}}(x)}{f^\alpha_{\mathrm{Fe}}(1-z)f^\beta_{\mathrm{S}}(z)}\frac{(1-x)^\alpha x^\beta}{(1-z)^\alpha z^\beta}, \tag{4.48}$$

where x is the mole fraction of sulfur and z is the mole fraction of sulfur in $\mathrm{Fe}_\alpha\mathrm{S}_\beta$, $z = \beta/(\alpha+\beta)$. Note that chemical activity and the activity coefficients f depend on pressure and temperature.

By using equations (4.45) and (4.48) we obtain the following implicit equation for the fraction of sulfur in the solution

$$(1-x_l)^\alpha x_l^\beta = \frac{f^\alpha_{\mathrm{Fe},l}(1-z)f^\beta_{\mathrm{S},l}(z)}{f^\alpha_{\mathrm{Fe},s}(1-z)f^\beta_{\mathrm{S},s}(z)}\frac{f^\alpha_{\mathrm{Fe},s}(1-x_s)f^\beta_{\mathrm{S},s}(x_s)}{f^\alpha_{\mathrm{Fe},l}(1-x_l)f^\beta_{\mathrm{S},l}(x_l)}(1-x_s)^\alpha x_s^\beta\ \mathrm{e}^{-\frac{\Delta\mu^{s\to l}_{\mathrm{Fe}_\alpha\mathrm{S}_\beta}}{RT}}, \tag{4.49}$$

where

$$\Delta\mu^{s\to l}_{\mathrm{Fe}_\alpha\mathrm{S}_\beta}(P,T) = \mu_{\mathrm{Fe}_\alpha\mathrm{S}_\beta,l}(P,T,0) - \mu_{\mathrm{Fe}_\alpha\mathrm{S}_\beta,s}(P,T,0), \tag{4.50}$$

is the change of free energy of pure $\mathrm{Fe}_\alpha\mathrm{S}_\beta$ upon melting. If the solution is ideal and with $x_s = z$ for the fraction of sulfur in $\mathrm{Fe}_\alpha\mathrm{S}_\beta$, equation (4.49) simplifies to

$$(1-x_l)^\alpha x_l^\beta = (1-z)^\alpha z^\beta\ \mathrm{e}^{-\frac{\Delta\mu^{s\to l}_{\mathrm{Fe}_\alpha\mathrm{S}_\beta}}{RT}}. \tag{4.51}$$

If $\alpha = \beta = 1$ and $z = 1/2$, for melting of FeS, we obtain the following explicit expression for the fraction of sulfur in the liquid

$$x_l = \frac{1}{2} - \frac{1}{2}\sqrt{1 - \mathrm{e}^{-\frac{\Delta\mu^{s\to l}_{\mathrm{FeS}}}{RT}}}. \tag{4.52}$$

From equations (4.42) and (4.49) the fraction of sulfur in the solution can be determined from the activity coefficients and from the differences in chemical potential of the pure solid and liquid phases (Eqs. (4.43) and (4.50)). Or, conversely we can determine the melting temperature of iron and the melting temperature of the first phase to the right of the eutectic as a function of the sulfur concentration. From the intersection of the two melting curves, the sulfur concentration and temperature at the eutectic can be calculated.

In order to calculate the melting temperature as function of sulfur and as a function of pressure we have to know the activity coefficients and the differences in chemical potential of the pure solid and liquid as a function of pressure and temperature. Here we only consider the ideal solution case therefore only the differences in the chemical potentials are required.

To determine the chemical potential at (P, T) from the chemical potential at (P_0, T_0) we first move along an isobar to (P_0, T) and then along an isotherm to (P, T)

$$\Delta\mu(P, T) = \Delta\mu(P_0, T) + \int_{P_0}^{P} dP'\, \Delta V(P', T), \tag{4.53}$$

where ΔV is the difference in volume between the liquid and the solid phase. With equation $\Delta\mu = \Delta H - T\Delta S$ and from [e.g. *Callen*, 1985]

$$\Delta H(P_0, T) = \Delta H_0(P_0, T_0) + \int_{T_0}^{T} dT'\, \Delta C_p(T') \tag{4.54}$$

$$\Delta S(P_0, T) = \Delta S_0(P_0, T_0) + \int_{T_0}^{T} dT'\, \frac{\Delta C_p(T')}{T'}, \tag{4.55}$$

where ΔC_p is the difference in isobaric heat capacity between the liquid and the solid phase, $\Delta\mu(P_0, T)$ can be calculated. If melting occurs at (P_0, T_0), the chemical potentials of the liquid and solid phase are equal and the changes in enthalpy and entropy are related

$$\Delta H_0 = T_0 \Delta S_0 \tag{4.56}$$

and equation (4.53) becomes

$$\begin{aligned}\Delta\mu(P, T) =& \Delta S_0(T_0 - T) + \int_{T_0}^{T} dT'\, \Delta C_p(T') \\ &- T\int_{T_0}^{T} dT'\, \frac{\Delta C_p(T')}{T'} + \int_{P_0}^{P} dP'\, \Delta V(P', T).\end{aligned} \tag{4.57}$$

In summary, within the assumptions of the ideal solution model, we could calculate the phase diagram at each pressure with equations (4.44), (4.51), and (4.57), if we knew for both solid and liquid phases, the melting temperature at P_0, the isobaric heat capacity as a function of temperature, the entropy in (P_0, T_0), and have an equation of state to calculate the volume as a function of pressure.

However, since the EoS parameters of the first iron-sulfur compound to the left of the eutectic are mostly unknown we cannot use the above approach to determine the melting curves and the eutectic as a function of pressure. We can nevertheless; use the above approach to determine the melting curve to the left of the eutectic for the pressures where the eutectic has been determined if we know at least the melting temperature for one sulfur concentration intermediary to pure iron and eutectic concentration. At constant pressure with the assumption that the difference in heat capacity between the solid and liquid phases is approximatively constant with temperature (4.57) simplifies to

$$\Delta\mu(P,T) = \Delta S(P,T_0)(T_0 - T) + \Delta C_p(P,T_0)\left(T - T_0 - T\log\frac{T}{T_0}\right). \tag{4.58}$$

Fig.[4.20] shows melting data and functional fits calculated from (4.44) and (4.58) (two parameter melting model) for the pressures 10GPa, 14GPa, 21GPa, and 23GPa. The figures also shows fits for the case where $\Delta C_p = 0$ (one parameter melting model) and for a model where the melting temperature decreases linearly with increasing sulfur concentration. For those two settings only the melting data of iron and the eutectic where used. The result show that the simplified ideal solution model does not produce a faithful representation of the data. With the exception of the data points at 14GPa, Fig.[4.20b], for sulfur fractions below 10 atomic percents (at%), the simple model underestimates the melting temperatures. The linear model also underestimates the melting temperatures, however to a smaller extend. A better fit is provided from the melting model assuming equations (4.44) and (4.58). The model is however, unable to reproduce the more complicated signature of the 14GPa Fig.[4.20b] data. By assuming a simple regular solution model at 14GPa the fit is only marginally improved (results not shown here).

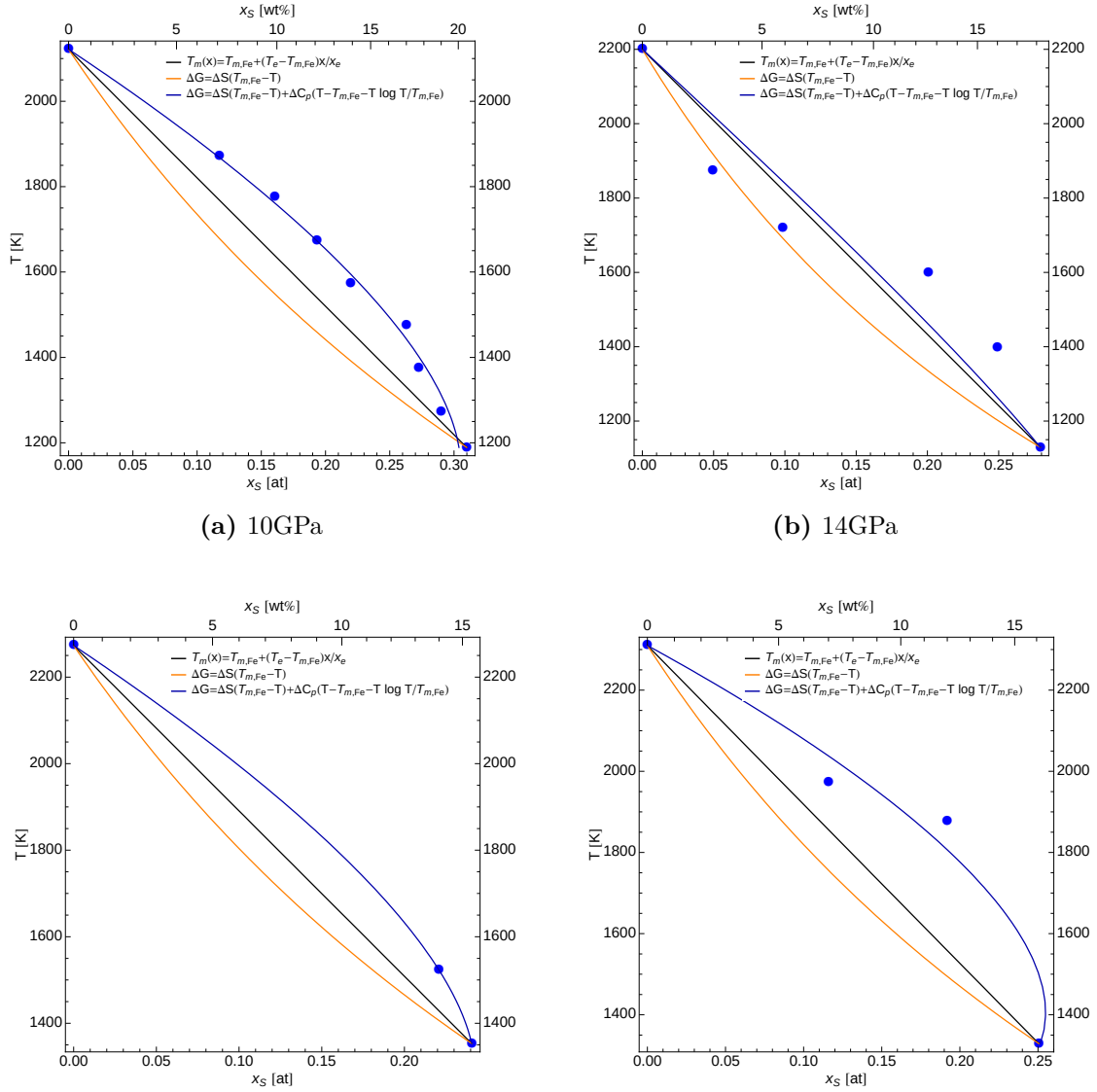
4.5.4 Practical melting law

Since in practice only a limited amount of melting data is available for sulfur concentrations to the left of the eutectic and as the one parameter melting model underestimates the melting temperature, we will here assume that the melting temperature decreases linearly with the sulfur fraction from the melting temperature of iron to the melting temperature of the eutectic at eutectic concentration. The melting temperature as a function of pressure and sulfur fraction x is then

$$T_m(x,P) = T_{m,\mathrm{Fe}}(P) + \frac{T_e(P) - T_{m,\mathrm{Fe}}(P)}{x_e(P)}x, \tag{4.59}$$

where $T_{m,\mathrm{Fe}}$ is the melting temperature of iron and T_e and x_e the eutectic temperature and sulfur concentration.

The data of the eutectic temperature as a function of pressure is shown in Fig.[4.21]. The eutectic temperature decreases with pressure until Fe_2S_3 occurs, and then increase with pressure. The rate becomes smaller after the occurrence of Fe_3S. To model the eutectic temperature as a function of pressure we assume a piecewise linear function with changing slope between intermediary phase occurrence to represent the eutectic. The resulting fitted function is shown in Fig.[4.21] and the fitting coefficients are given in Tab.[4.5].



(a) 10GPa **(b)** 14GPa

(c) 21GPa **(d)** 23GPa

Figure 4.20: Liquidus data (blue dots) for iron rich Fe − S solutions (left side of the eutectic) for 10GPa (4.20a, [*Chen et al.*, 2008]), 14GPa (4.20b, [*Chen et al.*, 2008]), 21GPa (4.20c, [*Fei et al.*, 2000]), and 23GPa (4.20d, [*Stewart et al.*, 2007]). The black curve is a linear interpolation between pure iron melting and eutectic melting. The orange curve and the blue curve are fits of ideal solution models for temperature independent and temperature dependent melting entropy and enthalpy.

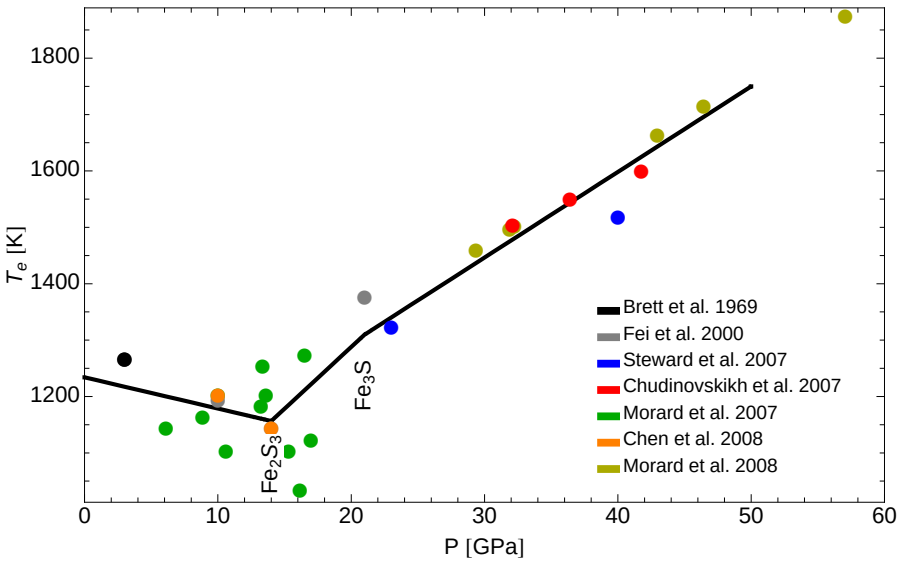


Figure 4.21: Eutectic temperature as function of pressure. The black curve represents a piecewise linear least square fit of the data. The data sets are from *Fei et al.* [2000]; *Stewart et al.* [2007]; *Chudinovskikh and Boehler* [2007]; *Morard et al.* [2007]; *Chen et al.* [2008] and *Morard et al.* [2008]

$T_e(P) = aP + b$	
b [K]	a [K/GPa]
$P < 14$GPa	
1234	-5.5
14GPa $\leq P \leq$ 21GPa	
850.	21.9
21GPa $< P \leq$ 50GPa	
991.	15.2

Table 4.5: Fitted parameter values for for the eutectic temperature as a function of pressure.

$x_e(P) = a\ P^2 + b\ P + c$					
a	[GPa^{-2}]	b	[GPa^{-1}]	c	
0.0000742893		−0.00715268		0.288949	

Table 4.6: Fitted parameter values for for the eutectic sulfur concentration as a function of pressure.

The measured eutectic concentration shows that the eutectic sulfur concentration decreases monotonically with increasing pressure, and seems to stabilize at a value of about 12wt% for $P > 40$GPa (see Fig.[4.22]). We use a quadratic polynomial in pressure to fit the measured data

$$x_e(P) = a\ P^2 + b\ P + c. \tag{4.60}$$

The estimated parameter values are given in Tab.[4.6] and the resulting eutectic concentration as a function of pressure is shown in Fig.[4.22].

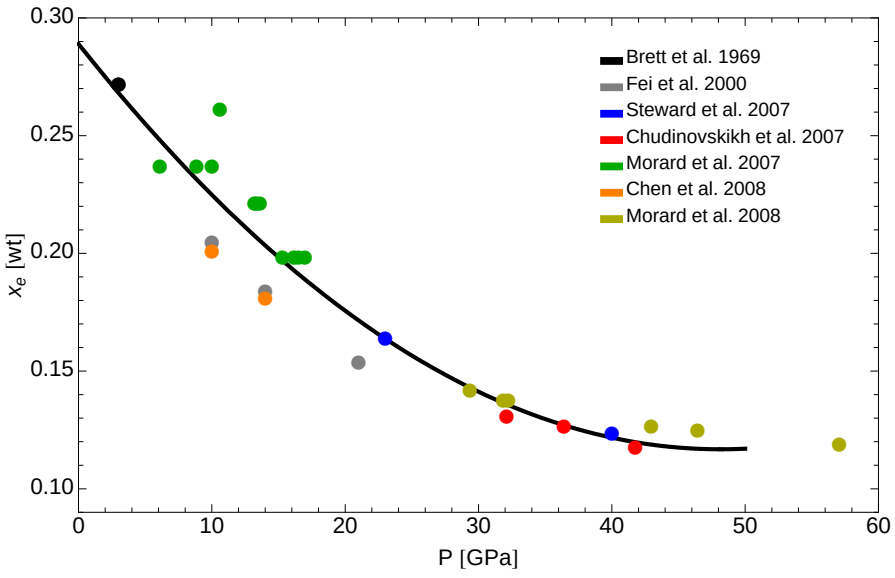


Figure 4.22: Eutectic sulfur concentration as a function of pressure. The black curve represents a quadratic polynomial least square fit of the data.

With the above introduced iron melting temperature, eutectic temperature, and eutectic sulfur concentration as a function of pressure, one can now, by means of equation (4.59), calculate the melting temperature as a function of sulfur fraction x (up to the eutectic concentration) and pressure ($P \leq 50$GPa). Fig.[4.23] shows calculated melting temperatures for different fractions of sulfur as a function of pressure. Note that the functional form of the eutectic temperature and the change in slopes related to the occurrence of the intermediary stable phases Fe_2S_3 and Fe_3S are clearly visible in the melting temperatures down to sulfur fractions of about 2wt%.

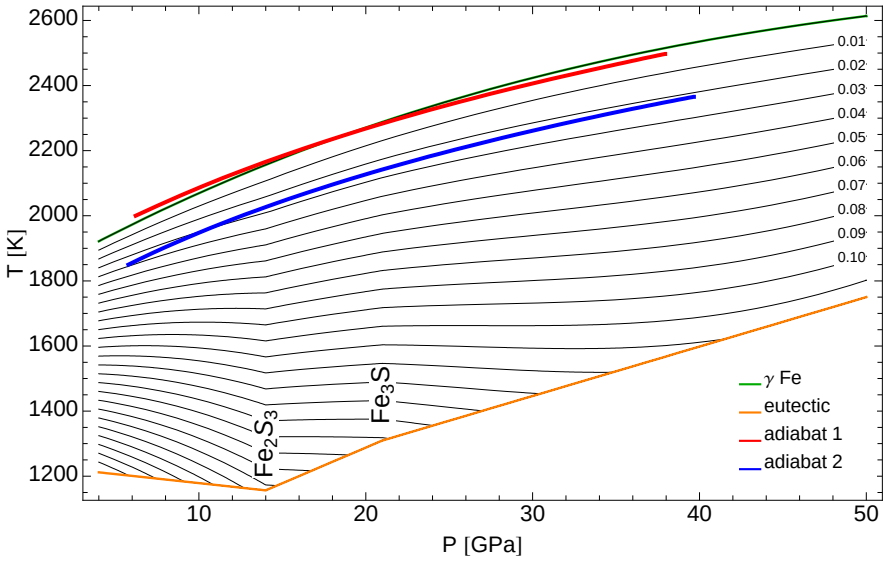


Figure 4.23: Melting temperatures of $Fe-S$ as function of pressure for different fractions of sulfur (black curves). The green curve is the melting temperature of iron and the orange cure is the eutectic temperature. The red and the blue curves are two hypothetical adiabatic temperature profiles for Mercury.

4.5.5 Differentiation of the core of Mars

The differentiation of a planetary core depends on its initial bulk sulfur content. Initially hot and liquid core material solidifies when the local temperature drops below the local melting temperature. The adiabatic core temperature profile (see Fig.[4.23] red curve) will drop below the melting temperature at the location of the highest pressure in the core upon cooling, if the slope of the melting temperature is steeper than the core adiabat. This situation occurs when an initial fluid core with less than about 1wt% of sulfur cools. Solid iron will start to precipitate out of the solution resulting in a solid inner core crystalizing from the center outwards. With the growing inner core the amount of sulfur in the liquid solution increases. As long as the slope of the melting curve associated to this new sulfur concentration is steeper than the adiabat iron will solidify at the location of the highest pressure, i.e., the inner core - outer core boundary (icb). The temperature at the icb is the melting temperature of the solution at icb pressure and outer core sulfur concentration so that the location of the icb can be determined from the intersection of the local temperature with the melting temperature.

If the bulk sulfur concentration in the solution is high enough such that the slope of the local temperature is steeper than the slope of the melting curve, a different situation arises. Upon cooling the local temperature drops below the melting temperature at the location of the lowest core pressure (see Fig.[4.23] blue curve), i.e. the core mantle boundary. Consequently, upon cooling solid iron is expelled from the solution close to the cmb and precipitates or snows towards the center of the core. As long as during downfall the temperature is below the local melting temperature of solid iron, solid iron will accumulate as sediment at the center of the core to form an inner core. While precipitation goes on, the sulfur concentration of the liquid increases, and the precipitation continues as

long as the slope of the temperature remains steeper than the slope of the melting curve and the sulfur concentration smaller than the eutectic concentration. For this inner core growing scenario, the location of the icb cannot be determined from the intersection of the melting temperature with the temperature profile. However, if the temperature and pressure at the cmb are constrained, the outer core sulfur concentration is determined from the melting law and from the cmb pressure and temperature. Consequently, for this outer core sulfur concentration all inner core sizes intermediary to no inner core and to an inner core the size of the core minus a small layer of outer liquid are possible.

More complicated scenarios, combining an initial crystallization phase followed by a snowing phase are conceivable. Or multiple snowing scenarios, due to the kinks in the melting curves appearing at higher sulfur concentrations, where upon cooling the melting temperature drops below the melting temperature at multiple locations. For a discussion of those scenarios and for inner core growing scenarios for solutions with sulfur concentrations above the eutectic see *Stewart et al.* [2007] and *Chen et al.* [2008].

Here, for planetary core modeling of terrestrial planets, we will only consider the inner core crystallization scenario and the one location snowing core scenario separately. Under the assumption that for the snowing core scenario the precipitating solid iron does not re-melt upon downfall. The first case will be applied for core temperatures close to the melting temperature of iron and the second case for cmb temperatures down to 1800K. From Fig.[4.23] one sees that for a cmb pressure of about 20GPa, for the first case inner cores are only possible for sulfur concentrations smaller than about 0.5wt%, and for the second case inner cores are possible for sulfur concentrations up to about 8wt% of sulfur because of the cmb temperature choice of 1800K.

4.6 Liquid core versus solid core

Until recently EoS parameters of liquid $Fe-S$ system, for pressures and temperatures relevant to cores of terrestrial planets, have been unavailable. For this reason, the thermoelastic properties of the liquid part of the cores have been calculated with EoS parameters of solid Fe and solid FeS [e.g. *Sohl and Spohn*, 1997; *Bertka and Fei*, 1998; *Zharkov and Gudkova*, 2005]. Here, we show that core properties, like temperature, density, and seismic sound velocity, calculated with solid EoS parameters are significantly different from those obtained from liquid EoS parameters.

For the calculation with solid EoS parameters, we use the ideal solution model introduced in Sect.[4.4], but instead of using EoS parameters of liquid iron and liquid $Fe-10$wt%S to calculate the EoS parameters of sulfur in the solution, we use solid $\gamma-Fe$ together with solid $FeS-IV$ (model m_1), and $\gamma-Fe$ with Fe_3S (model m_2). The resulting EoS parameters for sulfur in the solution are given in Tab.[4.7] and the EoS parameters for $\gamma-Fe$, $FeS-IV$, and Fe_3S are in Tab.[4.2]. We compare FeS models with Fe_3S models because the former has been used by other scientists and because the latter is, with solid $\gamma-$iron, the solid compound that will constitute the solid core (if Mars core conditions are assumed Fig.[4.16]) if the temperature drops below the eutectic temperature and if the sulfur concentration in the liquid is to the left of the eutectic concentration. For sulfur concentrations larger than the eutectic the solid core material is made of FeS and of other iron-rich sulfur compounds. For lower core pressure conditions

	V	α	K_T	K'_T	dK_T/dT
	cm^3/mol	$10^5/K$	GPa		GPa/K
S in ideal solid $Fe-S$ solution: $P_{ref} = 10^5$Pa and $T_{ref} = 1573$					
$\gamma - Fe$ and $FeS - IV$	14.75	21.3	32.5	3.2	-0.02^*
$\gamma - Fe$ and Fe_3S	9.29	10.77	63.9	4.8	-0.02^*

Table 4.7: Equation of state parameters for ideal for sulfur in solid $Fe - S$ solution. Calculated from $\gamma - Fe$ and $FeS - IV$ and from similar model with $\gamma - Fe$ and Fe_3S. For both models dK_T/dT is from $\gamma - Fe$.

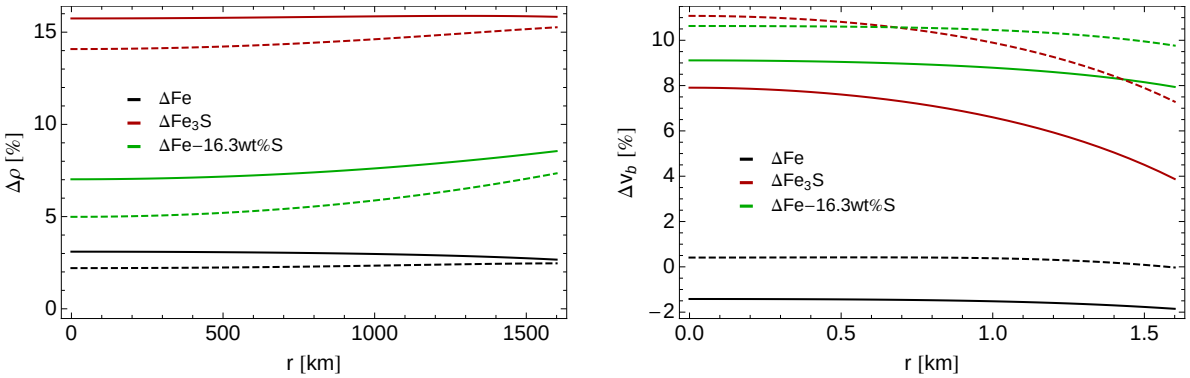
and to the left of the eutectic, the solid compound forming the solid core together with iron is FeS if $P < 14$GPa and Fe_2S_3 if the pressure is between $14\text{GPa} < P < 20\text{GPa}$ (see Fig.[4.17]). To the best of our knowledge EoS parameters of Fe_2S_3 have not yet been measured.

The EoS parameters for sulfur in the solid solution for both models are quite different and also different from the EoS parameters for sulfur in liquid $Fe - S$ (see Tab.[4.3]). The EoS parameters for sulfur in the solution for the m_1 model are closest to the EoS parameters of sulfur in the liquid solution.

In order to assess the differences in the core structure by using solid EoS parameters instead of liquid EoS parameters, the structure equations (see Chapt.[2]) are integrated for a core of 1600km, a core surface boundary pressure of $P = 21.5$GPa and for a cold and a hot core surface temperature (1800K and 2200K). The equations are solved for pure iron, and for models m_1 and m_2 for a solution with 16.3wt% of sulfur. Note that this is the sulfur weight fraction of Fe_3S.

The relative difference in density between the liquid solution model and model m_1 and model m_2 is shown in Fig.[4.24a]. The equivalent results for bulk sound velocity, pressure, and temperature are given in Figs. [4.24b, 4.25a, and 4.25b]. The relative difference in density decreases with increasing temperature (about 1%) and increases with increasing fraction of sulfur. A pure solid iron core is about 2% denser than a liquid iron core. Model m_1 is about 5% denser and model m_2 by more than 15%. Note that the convergence of the curves toward the top of the core results from the pressure and temperature constraints applied at the core surface. The relative differences in core mass and density are given in Tab.[4.8]. For both models, m_1 and m_2 the differences are significant. The difference in mass can also be expressed in difference in core size if the core mass is fixed, and the structure equations are solved for the core size together with the previous quantities. The results show that a solid iron core is about 39km smaller than a liquid core of equal mass. The difference between model m_1 and the liquid solution model is about 130km, and for model m_2 it is larger than 225km (see Tab.[4.9]). Therefore, using solid EoS parameters to describe a liquid core results in large difference in the estimated core size.

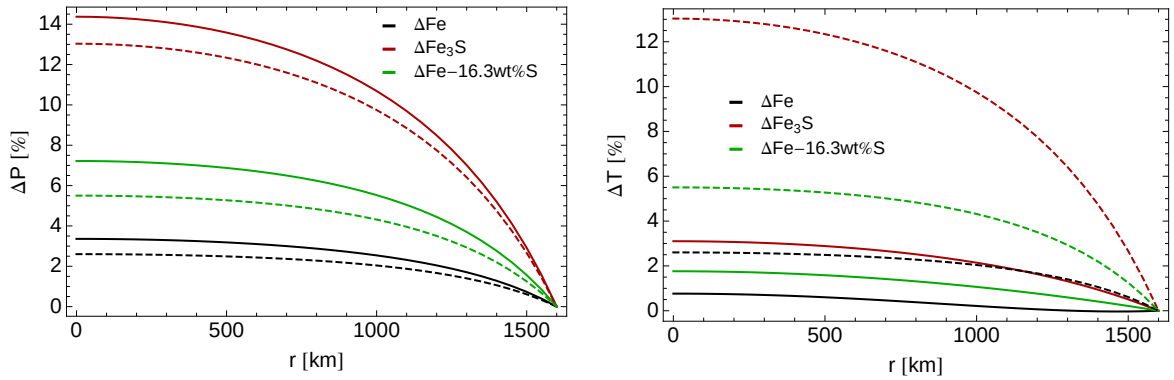
The relative difference in bulk sound velocity is shown in Fig.[4.24b]. At 16.3wt% sulfur concentration the relative difference in sound velocity can be as high as about 10%. As long as there are no seismic soundings, the only measurable quantities that give information about the bulk sound velocity in the liquid core are the Love numbers since they are associated to tidal deformations and to the external gravity changes which are dependent on density and on elastic properties. As will be shown in Chapt.[5], the Love



(a) (b)

Figure 4.24: Relative difference in density Fig.[4.24a] and seismic sound velocity Fig.[4.24b]. Comparisons are between solid and liquid iron, liquid Fe – 16.3wt%S and solid solution Fe – 16.3wt%S (m_1), and liquid Fe – 16.3wt%S and solid Fe_3S. The continuous curves are for an upper core boundary temperature of 1800K and the dashed curves for a temperature of 2200K.

numbers depend only weakly on the core density and the bulk sound velocity. For this reason, it is not expected that the solid EoS parameter formulation of the liquid core leads to significant errors in the Love numbers. However, the significant difference in core density between the solid and liquid EoS formulation results in smaller cores and in a sensibly smaller tidal Love number k_2. Therefore, the interpretation of the Love numbers in terms of core sulfur concentration will be erroneous, since for a given core size the core sulfur concentration deduced from a solid EoS parameter calculation will be significantly larger because those cores are denser.



(a) (b)

Figure 4.25: Relative difference in pressure Fig.[4.25a] and temperature Fig.[4.25b]. Comparisons are between solid and liquid iron, liquid Fe – 16.3wt%S and solid solution Fe – 16.3wt%S (m_1), and liquid Fe – 16.3wt%S and solid Fe_3S. The continuous curves are for an upper core boundary temperature of 1800K and the dashed curves for a temperature of 2200K.

Furthermore, solid and liquid EoS parameters result in sensibly different core pressure and temperature profiles, see Fig.[4.25a] and Fig.[4.25b]. The figures show that the relative differences increase with increasing core sulfur concentration. If the core bound-

	ΔFe	ΔFe_3S	Fe − 16.3wt%S
	%	%	%
		mass	
$T = 1800$K	−3.	−18.8	−9.4
$T = 2200$K	−2.4	−17.4	−10.
		inertia	
$T = 1800$K	−2.9	−18.9	−9.2
$T = 2200$K	−2.5	−17.6	−9.8

Table 4.8: Relative difference in core mass and inertia. Comparisons are between solid and liquid iron, liquid Fe−16.3wt%S and solid solution Fe−16.3wt%S (m_1), and liquid Fe−16.3wt%S and solid Fe_3S.

	ΔFe	ΔFe_3S	Fe − 16.3wt%S
	km	km	km
$T = 1800$K	42.5	240.9	128.5
$T = 2200$K	35.3	225.3	134.2

Table 4.9: Difference in core size. Comparisons are between solid and liquid iron, liquid Fe − 16.3wt%S and solid solution Fe − 16.3wt%S (m_1), and liquid Fe − 16.3wt%S and solid Fe_3S.

ary conditions allow for the presence of an inner core, a calculation done with solid EoS parameters will underestimated the inner core size, or even exclude the presence of an inner core, since those models predict more sulfur and a higher core temperatures.

4.7 Modeling uncertainties due to error-bound laboratory measurements

EoS parameters are determined with associated uncertainties. Here, similarly to Sect.[3.7], we assess how the uncertainties in the laboratory data induce uncertainties in the core pressure, temperature, density, and acoustic wave velocity profiles.

The error propagation is done for a core of 1600km, with a CMB pressure of 22GPa, and a CMB temperature of 2200K. The profiles are calculated by integrating the structure differential equations (see Chapt.[2]) supplemented by the thermodynamic relations of Sect.[4.3] and the EoS parameters for liquids (Tab.[4.3]).

4.7.1 Uncertainties on EoS parameters

The uncertainties, or standard deviations, for liquid Fe and liquid FeS are given in Tab.[4.10]. Since for liquid FeS only uncertainties on density and thermal expansivity are available in the literature, we take the uncertainties for liquid iron for the other parameters. Additionally, in order to account for the non-ideality of the solution, for each weight fraction of sulfur, supplementary uncertainties on the density (50kg/m^3), on K_T

(5GPa), and on K'_T (0.5) are used in the calculation.

	ρ kg/m^3	α 10^{-5}1/K	K_T GPa	K'_T	dK_T/dT GPa/K
Fe	2.	0.14	2.1	0.04	0.007
FeS	26.	3.4	2.1*	0.04*	0.007*

Table 4.10: EoS parameter uncertainties for liquid Fe [*Ahrens et al.*, 2002] and liquid FeS [*Kaiura and Toguri*, 1979]. Starred values are estimated.

4.7.2 Monte Carlo error propagation

The EoS parameters are assumed to be uncorrelated normal distributed random variables, with the mean value set to the measured value and the standard deviation equal to the associated uncertainty. We simulated 50000 sets of EoS parameter and calculated 50000 profiles from those sets. The information has then been summarized by estimated mean values and standard deviations. The error propagation calculation has been done for pure liquid iron, and for iron sulfur solutions of 5wt%, 10wt%, and 14wt%.

The estimated average profiles and associated standard deviations for pressure, temperature, density, and sound velocity are shown in Fig.[4.26]. The figures show that the uncertainties increase slightly with increasing depth, resulting from the increasing relative contribution of the pressure and temperature correction terms to the calculated density and adiabatic bulk modulus. The estimated standard deviations increase also with increasing sulfur concentration, from about 1% for pure iron to about 5% for a solution with 14wt% of sulfur, resulting from the included non ideality uncertainties and from the larger uncertainties on the EoS parametera FeS compared to Fe. Fig.[4.26d] also shows that the induced uncertainties on the seismic velocity profile make it impossible to ascribe a given profile to a specific core sulfur fraction.

Fig.[4.27] show the core mass and the core moment of inertia as a function of core sulfur fraction. The vertical error-bars are estimated standard deviations for specific fixed values of core sulfur. The uncertainties on the estimated core mass and moment of inertia are smaller than 2%. The horizontal error-bars are estimated standard deviations on the core sulfur fraction if the core mass is fixed. On average, EoS parameter uncertainties, induce an error on the core sulfur concentration of about 1wt%. Fig.[4.28] shows the core radius as a function of core sulfur for a fixed core mass. The results show that EoS parameter uncertainties lead to core size uncertainties of about 5km for a pure iron core that increase by about 350m for each wt% of sulfur.

4.7.3 Conclusions

The above results show that uncertainties on laboratory determined EoS parameters lead to small errors on core size (smaller than about 10km). The corresponding uncertainty on core sulfur fraction is also relatively small, about 1wt%, nevertheless, if the boundary conditions at the CMB allow for the formation of an inner core, then a difference of about

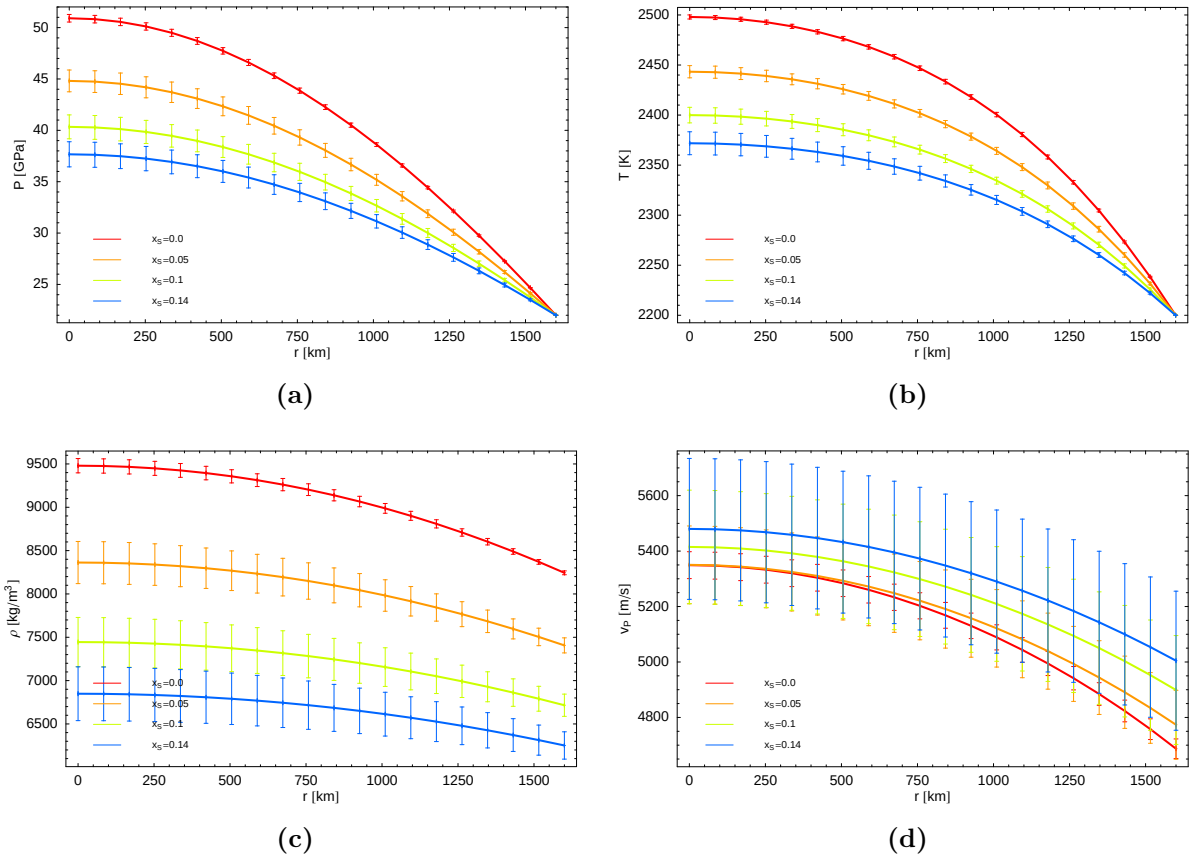
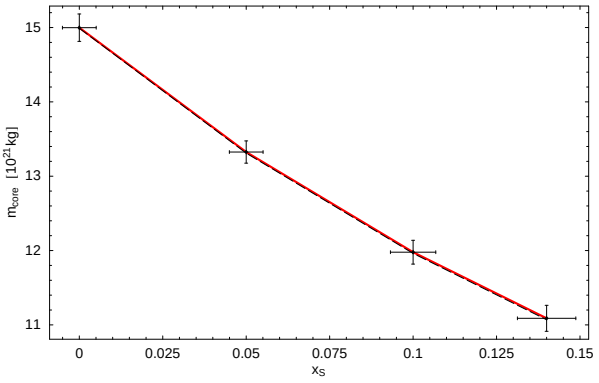
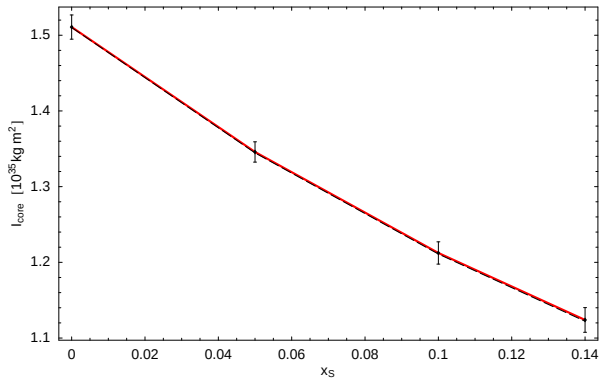


Figure 4.26: Estimated profiles of mean and standard deviation of core pressure (a), temperature (b), density (c) and acoustic wave velocity profiles (d) for liquid cores with 0wt%, 5wt%, 10wt%, and 14wt% sulfur.



(a)



(b)

Figure 4.27: Estimated core mass (a) and core moment of inertia (b) as a function of sulfur fraction. Error-bars are associated estimated standard deviations.

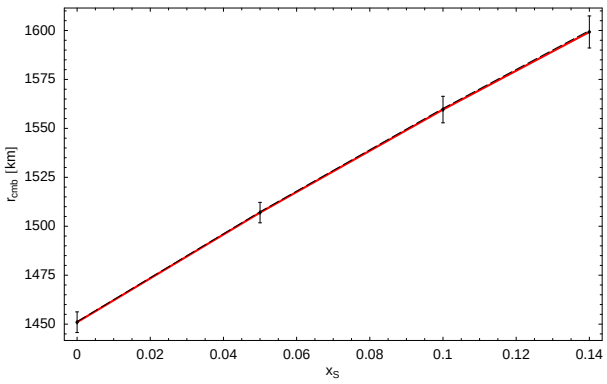


Figure 4.28: Estimated core size as a function of core sulfur fraction. Error-bars are associated estimated standard deviations.

1wt% in the sulfur concentration in the liquid core solution can result in a core with an inner core or no inner core.

The most significant uncertainties are induced on the seismic sound velocity. The overlapping of the error-bars associated to the models with different core sulfur concentrations make it impossible to associate univocally a sulfur concentration to a given seismic velocity profile.

Chapter 5

Tides

5.1 Introduction

A planetary body subject to a changing gravitational tidal potential experiences tidal deformation and changes its external potential due to a different gravitational forcing on different portions of the body. More specifically, the periodic external forcing results in surface displacements (tides) and variations in the planet's gravitational potential field. The reaction of the planet depends strongly on the internal structure of the planet, particularly on the size, and the state of the core. For example, for the planet Mercury, the amplitude of the surface displacements is about 30cm if the core is solid and about 3.5m if the core is liquid and has a size of about 2200km. Thus tides can be used to constrain the interior structure of planets. Tides have been measured for all terrestrial planets except Mercury. To better understand the relation between the internal structure parameters, e.g., core state and size, elastic and rheological properties, and the response of the planet to the tidal forcing we here calculate the reaction of the planet to the periodic tidal forcing for a wide set of internal structure models. The goal of this study is twofold, firstly assess the dependence of tides on the internal structure parameters, and secondly to identify those parameters that can best be constrained through the measurement of tides.

5.2 Love Numbers

We consider a spherically symmetric, isotropic, and non-rotating planet. With these assumptions the reaction of a perturbing potential of degree and order (l, m) is described by a single harmonic (l, m). Moreover, the radial reaction does not depend on the harmonic degree m. For this reason, the frequency dependent tidal potential is conveniently written in the following way

$$V_l^T(r, \theta, \varphi, \omega) = \left(\frac{r}{r_a}\right)^l \sum_{m=-l}^{l} V_{l,m}(\theta, \varphi, \omega) = \left(\frac{r}{r_a}\right)^l V_l(\theta, \varphi, \omega), \tag{5.1}$$

where r_a is the radius of the undeformed planet. The tidal acceleration of a unit of matter, i.e. minus the gradient of the tidal potential, is the difference between local and orbital acceleration. The force associated to the tidal acceleration therefore deforms the planet.

In particular the surface will be displaced with respect to its equilibrium position. Those tidal reactions are customarily described by dimensionless *Love numbers* [*Love*, 1911]. The radial displacements and tangential displacements are expressed by the numbers h and l, and the Love number k describes the external gravity potential variations. For our setting when the surface displacements are small with respect to the size of the planet, the degree l components of the surface displacements vector $\boldsymbol{u}_l$ are written

$$u_{l,r}(r_a,\theta,\varphi,\omega) = -\frac{1}{g_a} h_l(\omega) \sum_{m=-l}^{l} V_{l,m}(\theta,\varphi,\omega), \tag{5.2}$$

$$u_{l,\theta}(r_a,\theta,\varphi,\omega) = -\frac{1}{g_a} l_l(\omega)\, \partial_\theta \sum_{m=-l}^{l} V_{l,m}(\theta,\varphi,\omega), \tag{5.3}$$

$$u_{l,\varphi}(r_a,\theta,\varphi,\omega) = -\frac{1}{g_a} l_l(\omega) \frac{1}{\sin(\theta)}\, \partial_\varphi \sum_{m=-l}^{l} V_{l,m}(\theta,\varphi,\omega), \tag{5.4}$$

where g_a is the surface gravity. Note that the angular dependence on the surface displacement corresponds to the angular dependence of the tidal potential. The variations in the external gravitational potential ΔV are due to the tidal potential itself and to the change in potential resulting from the mass redistribution within the tidally deformed planet:

$$\Delta V_l(r,\theta,\varphi,\omega) = \left[1 + k_l(\omega)\left(\frac{r_a}{r}\right)^{l+1}\right]\left(\frac{r}{r_a}\right)^{l} \sum_{m=-l}^{l} V_{l,m}(\theta,\varphi,\omega). \tag{5.5}$$

In what follows we consider the planet to be in hydrostatic equilibrium, spherical symmetric, isotropic and non-rotating. With this assumptions the reaction of a perturbing potential of degree and order (l,m) is described by a single harmonic (l,m). Whereas for an elliptical planet the response to a single harmonic forcing would also result in a deformation in other harmonics, leading to position dependent Love numbers.

5.3 Governing equations

If the deformations are small all displacements can be described by the linear theory of the free oscillations of the planet. We suppose the planet to be composed of a number of fluid and solid regions that are separated by non-intersecting, smooth closed surfaces. The solid-solid boundaries are welded, such as the crust and the upper mantle. The fluid-solid boundaries, such as between the fluid outer core and the lower mantle, are frictionless.

For the exact details on the derivation of the involved equations one can consult for instance *Dahlen and Tromp* [1998] or *Aki and Richards* [2002]. In what follows we will give a short overview of the governing equations, emphasizing only the important steps needed to obtain the necessary results for calculating Love numbers.

The equation of motion of a small parcel of moving matter of density ρ moving at velocity $\boldsymbol{v}$ is readily obtained from Newton's second law:

$$\frac{d}{dt}\int_{V^t} dV\ \boldsymbol{v}\rho = \mathcal{F} \tag{5.6}$$

where $\mathcal{F}$ is the total external force acting on the *comoving* volume V^t. The comoving volume V^t is time dependent but composed of the same material particles. The external force is the sum of the long range body force $\mathcal{F}_b$ acting on each particle, and the short range surface force $\mathcal{F}_s$ exerted across the boundary ∂V^t. The long range body force $\mathcal{F}_b$

$$\mathcal{F}_b = -\int_{V^t} dV\ \rho\nabla\left(\phi + V\right), \tag{5.7}$$

ϕ is the long range gravitational potential and V the potential. The surface force $\mathcal{F}_s$ is written in terms of the *Cauchy* stress tensor $\boldsymbol{T}$ action upon the boundary

$$\mathcal{F}_s = \int_{\partial V^t} d\Sigma\ \hat{\boldsymbol{n}} \cdot \boldsymbol{T} = \int_{V^t} dV\ \nabla \cdot \boldsymbol{T} \tag{5.8}$$

$\hat{\boldsymbol{n}}$ is the unit vector normal to the surface and the Cauchy stress tensor measures the stress per unit deformed area. The resulting integral obtained by inserting equations [5.7] and [5.8] in [5.6] must be valid for every comoving volume V^t, therefore the integrand must be zero:

$$\rho D_t \boldsymbol{u} - \nabla \cdot \boldsymbol{T} + \rho\nabla\left(\phi + V\right) = 0, \tag{5.9}$$

where $D_t = \partial_t + \boldsymbol{u}\cdot\nabla\cdot$ is the *material derivative*. The equation of motion is supplemented with the equation of continuity

$$\frac{\partial\,\rho}{\partial t} + \nabla \cdot (\rho\ \boldsymbol{u}) = 0, \tag{5.10}$$

derived from the conservation of mass, and with the *Poisson* equation:

$$\nabla^2\phi = 4\pi G\rho \tag{5.11}$$

relating the density distribution ρ to the gravitational potential ϕ inside of the density distribution, and

$$\nabla^2\phi = 0 \tag{5.12}$$

outside of the density distribution. G is the universal gravitational constant. Eqs. (5.9), (5.10), and (5.11) have to be supplemented with a set of boundary conditions (BC) at the surface of the planet and at each internal boundary. First we introduce the practical notation $[f]^+_-$ to represent limiting conditions at boundaries:

$$[f]^+_- = \lim_{\varepsilon\to 0}\left[f(x-\varepsilon) - f(x+\varepsilon)\right]. \tag{5.13}$$

Inside a planet two kinds of boundary conditions are encountered, those between two solid regions and those between a solid and an inviscid[1] fluid region. At a welded boundary between two solids, such as those between the mantle and the crust, the velocity must be continuous

$$[\boldsymbol{u}]^+_- = 0. \tag{5.14}$$

Between a solid and a fluid region, e.g. between the solid inner core and the liquid outer core, tangential slip is allowed at the boundary

$$[\hat{\boldsymbol{n}} \cdot \boldsymbol{u}]^+_- = 0. \tag{5.15}$$

[1]Fluids for which friction is negligible and that don't support shear waves. In what follows fluids are supposed to be inviscid.

The vector $\hat{\boldsymbol{n}}$ is the unit outside normal to the boundary. Beside those kinematical conditions, reflecting (dis)continuity in position, there are dynamical conditions requiring that the traction $\hat{\boldsymbol{n}} \cdot \boldsymbol{T}$ must be continuous across solid welded and across liquid-solid slipping boundaries

$$[\hat{\boldsymbol{n}} \cdot \boldsymbol{T}]^+_- = 0. \tag{5.16}$$

Furthermore, there is no shear traction on the boundary between a solid and fluid region, traction is only perpendicular to the boundary:

$$\hat{\boldsymbol{n}} \cdot \boldsymbol{T} = \hat{\boldsymbol{n}}(\hat{\boldsymbol{n}} \cdot \boldsymbol{T} \cdot \hat{\boldsymbol{n}}), \tag{5.17}$$

On the outer free surface the traction must vanish $\hat{\boldsymbol{n}} \cdot \boldsymbol{T} = 0$. Finally, the gravitational potential ϕ and its normal to the surface gradient are continuous across all density discontinuities

$$[\phi]^+_- = 0, \quad [\hat{\boldsymbol{n}} \cdot \nabla \phi]^+_- = 0, \tag{5.18}$$

which implies the continuity of the gravity vector $\boldsymbol{g} = -\nabla \phi$. All these above conditions are time dependent and must be satisfied at the instantaneous position of the boundaries.

5.3.1 Linear perturbation

For small magnitudes of deformations the equation of motion and the boundary conditions can be linearized about an initial planet in static equilibrium. Prior to the occurrence of a forcing, the planet is in a state of mechanical equilibrium, at rest with respect to a set of Cartesian axes located at the mass center. Points or material particles in the planet or on the boundary surfaces are denoted as $\boldsymbol{x}$.

Let ρ^0 denote the initial density distribution within the planet, and ϕ^0 the initial gravity potential. They are related through Poisson's equation

$$\nabla^2 \phi^0 = 4\pi\, G\, \rho^0 \tag{5.19}$$

within the planet and subject to the boundary conditions

$$\left[\phi^0\right]^+_- = 0, \quad [\hat{\mathbf{n}} \cdot \nabla \phi_{\mathbf{0}}]^+_- = 0. \tag{5.20}$$

The gravitational field $\boldsymbol{g}^0 = -\nabla\, \phi^0$ within a spherical planet points radially downward:

$$\boldsymbol{g}^0 = -g^0 \hat{\boldsymbol{r}} = -\partial_r \phi^0 \hat{\boldsymbol{r}}. \tag{5.21}$$

The equivalent equation to the Poisson equation in terms of g^0 is

$$\partial_r g^0 + \frac{2}{r} g^0 = 4\pi G \rho^0. \tag{5.22}$$

Outside the planet the potential satisfies $\nabla^2 \phi^0 = 0$. The initial stress tensor $\boldsymbol{T^0}$ for a hydrostatic planet is $\boldsymbol{T^0} = -p^0 \boldsymbol{I}$ with initial hydrostatic pressure $p^0 = \frac{1}{3}\mathrm{tr}\boldsymbol{T^0}$. In mechanical equilibrium the equation of motion [5.6] reduces to the condition of hydrostatic equilibrium:

$$\nabla \cdot \boldsymbol{T^0} + \rho^0 \nabla\, \phi^0 = \nabla\, p^0 + \rho^0 \nabla\, \phi^0 = 0 \tag{5.23}$$

To obtain the equations for small displacements $\boldsymbol{s}(\boldsymbol{x},t)$ about the position of equilibrium $\boldsymbol{x}$ the equations [5.9]-[5.11] and the associated boundary conditions are to be expanded about $\boldsymbol{x}$. The position vector $\boldsymbol{r}(\boldsymbol{x},t)$ is written in the form

$$\boldsymbol{r}(\boldsymbol{x},t) = \boldsymbol{x} + \boldsymbol{s}(\boldsymbol{x},t) \tag{5.24}$$

and linearized in $\boldsymbol{s}$, i.e. systematically neglect all terms of order 2 and higher in $||\boldsymbol{s}||^2$. Correct up to first order, the stress tensor is

$$\boldsymbol{T}(\boldsymbol{r},t) = \boldsymbol{T}^0(\boldsymbol{r}) + \boldsymbol{T}^{E1}(\boldsymbol{r},t) = \boldsymbol{T}^0(\boldsymbol{r}) + \boldsymbol{T}^{L1}(\boldsymbol{x},t) - \boldsymbol{s}\cdot\nabla\boldsymbol{T}^0(\boldsymbol{r}), \tag{5.25}$$

where $\boldsymbol{T}^{L1}$ is the incremental Lagragian Cauchy tensor, the density is

$$\rho(\boldsymbol{r},t) = \rho^0(\boldsymbol{r}) + \rho^{E1}(\boldsymbol{r},t), \tag{5.26}$$

and the potential field

$$\phi(\boldsymbol{r},t) = \phi^0(\boldsymbol{r}) + \phi^{E1}(\boldsymbol{r},t). \tag{5.27}$$

Superscript $E1$ on symbols refers to their first order Eulerian perturbation. The resulting equation of motion, continuity equation and Poisson equation correct to the first order in the displacement are then

$$\rho^0\frac{d^2\boldsymbol{s}}{dt^2} - \nabla\cdot\boldsymbol{T}^{L1} + \nabla\left(\rho^0\boldsymbol{s}\cdot\nabla\phi^0\right) + \rho^0\nabla\left(\phi^{E1}+V\right) + \rho^{E1}\nabla\phi^0 = 0 \tag{5.28}$$

$$\rho^{E1} + \nabla\cdot\left(\rho^0\ \boldsymbol{s}\right) = 0 \tag{5.29}$$

$$\nabla^2\phi^{E1} - 4\pi G\rho^{E1} = 0 \tag{5.30}$$

Upon inserting (5.21) in (5.28), expressing ρ^{E1} by means of (5.29) and $\partial_r g^0$ using (5.22), the equation of motion becomes

$$\rho^0\frac{d^2\boldsymbol{s}}{dt^2} = \nabla\cdot\boldsymbol{T}^{L1} - 4\pi G{\rho^0}^2 s_r\ \hat{\boldsymbol{r}} - \rho^0\nabla\left(\phi^{E1}+V\right) - \rho^0 g^0\left[\nabla\, s_r - \left(\nabla\cdot s + \frac{2}{r}s_r\right)\hat{\boldsymbol{r}}\right], \tag{5.31}$$

where $s_r = \hat{\boldsymbol{r}}\cdot\boldsymbol{s}$. The incremental Lagragian Cauchy tensor is expressed by the isotropic constitutive relation

$$\boldsymbol{T}^{L1} = \kappa\nabla\cdot\boldsymbol{s}\boldsymbol{I} + 2\mu\boldsymbol{d}, \tag{5.32}$$

where the deviatoric strain is

$$\boldsymbol{d} = \boldsymbol{\varepsilon} - \frac{1}{3}\nabla\cdot\boldsymbol{s}\ \boldsymbol{I}, \tag{5.33}$$

with the strain $\boldsymbol{\varepsilon} = \frac{1}{2}\left(\nabla\boldsymbol{s} + (\nabla\boldsymbol{s})^T\right)$. With these definitions the equation of motion (5.31) can be written entirely in terms of the displacement $\boldsymbol{s}$ and incremental gravitational potential ϕ^{E1}.

The incremental Cauchy tensor is related to the elastic tensor $\boldsymbol{\Gamma}$ and to the strain by *Hooke's* law:

$$\boldsymbol{T}^{L1} = \boldsymbol{\Gamma} : \boldsymbol{\varepsilon}, \tag{5.34}$$

where ":" stands for the tensor product. For an isotropic solid the elastic tensor can be written as

$$\Gamma_{ijkl} = (\kappa - \frac{2}{3}\mu)\delta_{ij}\delta_{kl} + \mu(\delta_{ik}\delta_{jl} + \delta_{il}\delta_{jk}). \tag{5.35}$$

κ is the isentropic incompressibility or bulk modulus and μ is the rigidity or shear modulus. Note that in the other chapters of this thesis we have used K_S and G to designate the adiabatic bulk modulus and the shear modulus. In the fluid regions of a planet the rigidity μ is identically zero and the incremental Lagragian Cauchy becomes

$$\boldsymbol{T}^{L1} = -\kappa \nabla \cdot \boldsymbol{s}\, \boldsymbol{I} \tag{5.36}$$

The perturbed boundary conditions are

- outer free surface

$$\hat{\boldsymbol{r}} \cdot \boldsymbol{T}^{L1} = 0 \tag{5.37}$$

- solid-solid interface

$$[\boldsymbol{s}]^+_- = 0, \quad \left[\hat{\boldsymbol{r}} \cdot \boldsymbol{T}^{L1}\right]^+_- = 0 \tag{5.38}$$

- inviscid liquid-solid interface

$$[\hat{\boldsymbol{r}} \cdot \boldsymbol{s}]^+_- = 0, \quad \left[\hat{\boldsymbol{r}} \cdot \boldsymbol{T}^{L1}\right]^+_- = \left[\hat{\boldsymbol{r}}(\hat{\boldsymbol{r}} \cdot \boldsymbol{T}^{L1} \cdot \hat{\boldsymbol{r}})\right]^+_- = 0 \tag{5.39}$$

- all interfaces

$$\left[\phi^{E1}\right]^+_- = 0, \quad \left[\hat{\boldsymbol{r}} \cdot \nabla\, \phi^{E1} - 4\pi G \rho^0 \hat{\boldsymbol{r}} \cdot \boldsymbol{s}\right]^+_- = 0 \tag{5.40}$$

5.3.2 Scalar equations

To solve the equations for small deformation about a spherically symmetric initial configuration all scalar and vectors are expanded in spherical harmonics and Fourier-transformed to the frequency domain. The density ρ, the rigidity μ, and the adiabatic incompressibility κ only depend on r in the unperturbed configuration. They are constant in time when the rheology is elastic and become frequency dependent otherwise. The resulting radial second order differential equations are transformed to first order differential equations by introducing auxiliary scalar functions such that derivatives in r of ρ, κ, and μ are avoided. This will result in a set of 8 linear first order differential equations each depending on the frequency ω, on r, and on the degree l and order m.

For the scalar functions one uses

$$f(r, \theta, \phi) = \sum_{l=0}^{\infty} \sum_{m=-l}^{l} f_{l,m}(r) Y_l^m(\theta, \varphi). \tag{5.41}$$

Since V enters the equation of motion only in combination with ϕ^{E1} as $\phi^{E1} + V$ the equations are formally identical to those governing the free oscillation of a planet ($\nabla^2 V = 0$ outside of the body generating the tidal potential) by replacing ϕ^{E1} with $V + \phi^{E1}$. For that reason we define

$$\phi^{E1} + V = \sum_{l=0}^{\infty} \sum_{m=-l}^{l} y_{5l}(r) Y_l^m(\theta, \varphi). \tag{5.42}$$

The vector fields are expanded with the Helmholtz decomposition

$$\boldsymbol{s} = \sum_{l=0}^{\infty} \sum_{m=-l}^{l} \{ y_{1l} Y_l^m(\theta,\varphi)\mathbf{1}_r + y_{3l} \nabla_h Y_l^m(\theta,\varphi) - y_{7l}(\mathbf{1}\times\nabla_h) Y_l^m(\theta,\varphi)\} \tag{5.43}$$

where the horizontal gradient on the unit sphere is

$$\nabla_h = \mathbf{1}_\theta \frac{\partial}{\partial\theta} + \mathbf{1}_\varphi \frac{1}{\sin\theta}\frac{\partial}{\partial\varphi}, \tag{5.44}$$

and

$$\mathbf{1}\times\nabla_h = -\mathbf{1}_\theta \frac{1}{\sin\theta}\frac{\partial}{\partial\varphi} + \mathbf{1}_\varphi \frac{\partial}{\partial\theta}. \tag{5.45}$$

We also expand the traction as

$$\hat{\boldsymbol{n}}\cdot\boldsymbol{T}^{L1} = \sum_{l=0}^{\infty} \sum_{m=-l}^{l} \{ y_{2l} Y_l^m(\theta,\varphi)\mathbf{1}_r + y_{4l} \nabla_h Y_l^m(\theta,\varphi) - y_{8l}(\mathbf{1}\times\nabla_h) Y_l^m(\theta,\varphi)\}, \tag{5.46}$$

where $\hat{\boldsymbol{n}}$ is the unit normal to the undeformed boundary.

The first-order equations for the solid layers can be expressed as (the index l is dropped for clarity):

$$\frac{d\,y_1}{dr} = -2\frac{\kappa-\frac{2}{3}\mu}{\kappa+\frac{4}{3}\mu}\frac{y_1}{r} + \frac{1}{\kappa+\frac{4}{3}\mu}y_2 + k^2\frac{\kappa-\frac{2}{3}\mu}{\kappa+\frac{4}{3}\mu}\frac{y_3}{r} \tag{5.47}$$

$$\begin{aligned}\frac{d\,y_2}{dr} =& \left[-4\rho\,g - \omega^2\rho\,r + \frac{12}{r}\frac{\mu\kappa}{\kappa+\frac{4}{3}\mu}\right]\frac{y_1}{r} - \frac{4\mu}{\kappa+\frac{4}{3}\mu}\frac{y_2}{r} \\ &+ k^2\left[\rho\,g - \frac{6}{r}\frac{\mu\kappa}{\kappa+\frac{4}{3}\mu}\right]\frac{y_3}{r} + k^2\frac{y_4}{r} + \frac{l+1}{r}\rho\,y_5 - \rho\,y_6\end{aligned} \tag{5.48}$$

$$\frac{d\,y_3}{dr} = -\frac{y_1}{r} + \frac{y_3}{r} + \frac{y_4}{\mu} \tag{5.49}$$

$$\begin{aligned}\frac{d\,y_4}{dr} =& \left[\rho\,g - \frac{6}{r}\frac{\mu\kappa}{\kappa+\frac{4}{3}\mu}\right]\frac{y_1}{r} - \frac{\kappa-\frac{2}{3}\mu}{\kappa+\frac{4}{3}\mu}\frac{y_2}{r} \\ &- \left[\omega^2\rho\,r + \frac{2}{r}\mu - \frac{4k^2}{r}\frac{\mu(\kappa+\frac{1}{3}\mu)}{\kappa+\frac{4}{3}\mu}\right]\frac{y_3}{r} - \frac{3}{r}y_4 - \frac{\rho}{r}y_5\end{aligned} \tag{5.50}$$

$$\frac{d\,y_5}{dr} = 4\pi G\rho y_1 - \frac{l+1}{r}y_5 + y_6 \tag{5.51}$$

$$\frac{d\,y_6}{dr} = 4\pi G\rho\frac{l+1}{r}y_1 - 4\pi G\rho\frac{k^2}{r}y_3 + \frac{l-1}{r}y_6 \tag{5.52}$$

$$\frac{d\,y_7}{dr} = \frac{y_7}{r} + \frac{y_8}{\mu} \tag{5.53}$$

$$\frac{d\,y_8}{dr} = \left[-\omega^2\rho\,r + (k^2-2)\frac{\mu}{r}\right]\frac{y_7}{r} - 3\frac{y_8}{r}, \tag{5.54}$$

where $k^2 = l(l+1)$. Note that y_6 defined by equation (5.51) has been selected that way in order to obtain homogeneous boundary conditions at the surface of the planet [*Takeuchi and Saito*, 1972]. In what follows we will discard the toroidal displacement described by

equations y_7 and y_8, as they are decoupled from the other equations and do not contribute to the spheroidal displacements.

In the inviscid fluid layers of the planet, rigidity is zero and consequently the shear traction y_4 is zero and equation (5.50) gives

$$\omega^2 \rho y_3 - \frac{1}{r}\left(\rho\, g\, y_1 + \rho\, y_5 - y_2\right) = 0. \tag{5.55}$$

If $\omega^2 > 0$, the remaining scalar differential equations for the fluid layer can then be written as

$$\frac{d\,y_1}{dr} = \left[-2 + \frac{k^2}{r}\frac{g}{\omega^2}\right]\frac{y_1}{r} + \left[\frac{1}{\kappa} - \frac{k^2}{r^2\omega^2\rho}\right] y_2 + \frac{k^2}{\omega^2}\frac{y_5}{r^2} \tag{5.56}$$

$$\frac{d\,y_5}{dr} = 4\pi G\rho\, y_1 - \frac{l+1}{r} y_5 + y_6 \tag{5.57}$$

$$\frac{d\,y_2}{dr} = \left[-4\rho\, g - \omega^2\rho\, r + \frac{k^2}{r}\frac{\rho\, g^2}{\omega^2}\right]\frac{y_1}{r} - \frac{k^2}{r^2}\frac{g}{\omega^2} y_2 + \left[\frac{k^2}{r}\frac{\rho\, g}{\omega^2} - (l+1)\rho\right]\frac{y_5}{r} + \rho\, y_6 \tag{5.58}$$

$$\frac{d\,y_6}{dr} = 4\pi G\rho\left[(l+1) - \frac{g}{\omega^2}\frac{k^2}{r}\right]\frac{y_1}{r} + \frac{4\pi G}{\omega^2}\frac{k^2}{r^2} y_2 - \frac{4\pi G\rho\, k^2}{r^2\,\omega^2} y_5 + \frac{l-1}{r} y_6 \tag{5.59}$$

where $k^2 = l(l+1)$. The above equations are formally identical to those of [*Dahlen and Tromp*, 1998] if $y_1 \to U$, $y_2 \to R$, $y_3 \to k^{-1}V$, $y_4 \to k^{-1}S$, $y_5 \to -P$, and $y_6 \to -B$. [*Dahlen and Tromp*, 1998] have considered the problem of free oscillations, so that their differential equations for y_5 and y_6 do not contain the tidal potential V.

The boundary conditions on interfaces are

$$[y_1]^+_- = 0 \tag{5.60}$$

$$[y_2]^+_- = 0 \tag{5.61}$$

$$[y_4]^+_- = 0 \tag{5.62}$$

$$[y_5]^+_- = 0 \tag{5.63}$$

$$[y_6]^+_- = 0 \tag{5.64}$$

$$[y_8]^+_- = 0 \tag{5.65}$$

$$\tag{5.66}$$

On solid-solid interfaces, the tangential displacement and the tractions are also continuous: $[y_3]^+_- = 0$ and $[y_7]^+_- = 0$. Tangential slip is allowed on fluid-solid interfaces, y_3 and y_7 can be discontinuous, but tangential tractions are zero: $y_4 = 0$, $y_8 = 0$. At the surface, $r = r_a$, traction must vanish: $y_2(r_a) = y_4(r_a) = y_8(r_a) = 0$. The radial part of the Eulerian perturbation to the potential inside of the planet is

$$\phi_l^{E1}(r) = k_l(r)\left(\frac{r}{r_a}\right)^l V_l, \quad r \le r_a \tag{5.67}$$

and the expression for y_5 is obtained by using (5.1) and (5.42):

$$\phi_l^{E1} + V_l = \left[1 + k_l(r)\right]\left(\frac{r}{r_a}\right)^l V_l = y_5(r) \tag{5.68}$$

Furthermore, on the outside of the planet, we have

$$\phi_l^{E1}(r) = k_l \left(\frac{r_a}{r}\right)^{l+1} V_l, \quad r > r_a \tag{5.69}$$

The continuity of the potential at the surface, $[y_5]_-^+$ implies then

$$1 + k_l(r_a) = \frac{y_5(r_a)}{V_l} = 1 + k_l. \tag{5.70}$$

From the continuity of the radial gradient of the potential at the surface (5.40)

$$\begin{aligned}\left[\frac{d\,y_5}{dr} - 4\pi G\rho y_1\right]_{r=r_a-} &= \left[\frac{d\,y_5}{dr}\right]_{r=r_a+} = \frac{d}{dr}\left[\left(\frac{r}{r_a}\right)^l + k_l\left(\frac{r_a}{r}\right)^{l+1}\right]_{r=r_a+} V_l \\ &= \left(\frac{l}{r_a} - k_l\frac{l+1}{r_a}\right) V_l,\end{aligned} \tag{5.71}$$

with the definition of y_6 from (5.51) and with (5.70) we obtain the surface condition for y_6:

$$y_6(r_a) = \frac{d\,y_5(r_a)}{dr} - 4\pi G\rho(r_a)y_1(r_a) + \frac{l+1}{r_a}y_5(r_a) = \frac{2l+1}{r_a}V_l \tag{5.72}$$

Further, when $r \to 0$ the displacements and the potential tend to zero

$$y_1(0) = 0, \quad y_3(0) = 0, \quad y_5(0) = 0 \tag{5.73}$$

5.3.3 The static solution

Strictly speaking the tidal potentials are always time dependent and the static case, i.e. the forcing frequency $\omega = 0$, is only encountered in loading problems. However, ω can be very small and numerically this is equivalent to setting $\omega = 0$. For solid layers the equations are obtained from equations (5.47)- (5.52) by setting $\omega = 0$. As equations (5.56), (5.58), and (5.59) are singular for $\omega = 0$ we derive the static equations for liquid layers from the solid layer equations by simultaneously setting $\mu = 0$ and $\omega = 0$. We then have

$$\frac{d\,\kappa\,x}{dr} + \rho\frac{d\,y_5}{dr} - \rho\frac{d\,g\,y_1}{dr} + \rho g x = 0 \tag{5.74}$$

$$\kappa x - \rho(-y_5 + g y_1) = 0 \tag{5.75}$$

$$\frac{d^2\,y_5}{dr^2} + \frac{2}{r}\frac{d\,y_5}{dr} - \frac{k^2}{r^2}y_5 = 4\pi G\frac{d\,\rho}{dr}y_1 + 4\pi G\rho x \tag{5.76}$$

where (5.74) and (5.75) are the $Y_l^m(\theta,\varphi)$ and $\nabla_h Y_l^m(\theta,\varphi)$ proportional part of the equation of motion (5.31) and (5.76) is Poisson's equation (5.30).

x is defined through

$$\nabla\cdot\boldsymbol{s}(r,\theta,\phi) = \sum_{l=0}^{\infty}\sum_{m=-l}^{l}\left(\frac{d\,y_1}{dr} + \frac{2y_1 - k^2 y_3}{r}\right) Y_m^l(\theta,\phi) = \sum_{l=0}^{\infty}\sum_{m=-l}^{l} x(r)\,Y_m^l(\theta,\phi). \tag{5.77}$$

Eqs. (5.74) and (5.75) can be written as

$$N^2(r)x(r) = 0, \tag{5.78}$$

where N is the local *Brunt-Väisälä* frequency

$$N^2(r) = -\left(\frac{1}{\rho}\frac{d\,\rho}{dr} + \frac{\rho g}{\kappa}\right) g. \tag{5.79}$$

The Brunt-Väisälä frequency N^2 can also be rewritten in terms of the temperature gradient inside the the fluid layer as follows:

$$N^2(r) = -\alpha g\left(\frac{\rho g \gamma T}{\kappa} + \frac{d\,T}{dr}\right), \tag{5.80}$$

where α is the thermal expansivity and γ the Grüneisen parameter[2].

Thus according to (5.78) in a fluid layer, with $\omega = 0$, one either has $x = 0$, i.e. the static flow of the fluid is incompressible, or $N^2 = 0$, or both. The condition $N^2 = 0$ is equivalent to the statement that the *Adams Williamson* equation holds in the fluid layer. Which states that the fluid is homogeneous, that its layering is isentropic, and that according to (5.80) and (2.4) the temperature gradient in the fluid layer is adiabatic. If this is not the case the static deformation in the fluid has to be solenoidal, e.g., $x = 0$.

By using (5.78) Eq.(5.76) can be rewritten as

$$\frac{d^2\,y_5}{dr^2} + \frac{2}{r}\frac{d\,y_5}{dr} - \left[\frac{k^2}{r^2} - 4\pi G\rho\left(\frac{N^2}{g^2} + \frac{\rho}{\kappa}\right)\right] y_5 = 0. \tag{5.81}$$

Furthermore, by using (5.75) and $y_2(r_a) = 0$, the surface boundary condition (5.72) can be rewritten as

$$\frac{d\,y_5(r_a)}{dr} - \frac{4\pi G\rho(r_a)}{g(r_a)} y_5(r_a) + \frac{l+1}{r_a} y_5(r_a) = \frac{2l+1}{r_a} V_l. \tag{5.82}$$

Hence if $\omega = 0$, in a liquid y_5 decouples from the displacement equations y_1 and y_3.

For a solenoidal deformation, this implies that the radial and tangential displacements, y_1 and y_3, are completely determined by y_5. With $x = 0$ we obtain from equations (5.74) and (5.75)

$$y_1 = \frac{y_5}{g} \tag{5.83}$$

$$y_3 = \frac{1}{k^2}\left(\frac{2}{g} y_5 + r\frac{d\,y_5/g}{dr}\right). \tag{5.84}$$

Furthermore, for y_2 and y_4 one has

$$y_2 = \kappa x = 0 \tag{5.85}$$

$$y_4 = 0. \tag{5.86}$$

[2] To derive the above relation we have used that $P = P(\rho, T)$, the expressions for the thermal expansivity $\alpha = -\left(\frac{\partial\,\log\rho}{\partial T}\right)_P$ and the isothermal bulk modulus $K_T = \left(\frac{\partial\,\log\rho}{\partial P}\right)_T^{-1}$, and the relation (4.8) between K_T and the adiabatic bulk modulus κ.

Thus, for a fully liquid planet a general solution exists if the deformation is solenoidal. However, in a more general setting, i.e., a solid planet with a fluid layer or fluid core, there is no general static solution. For $\omega > 0$, for a planet made of a solid inner core, a liquid outer core, and a solid mantle, one has a system of 6 ODEs in the solid parts and 4 ODEs in the liquid layer, if $\omega \neq 0$. This results in 16 free constants that have to be determined from the boundary conditions. From the 6 solutions in the inner core only 3 are regular, at the solid-liquid/liquid-solid interfaces 5 of the scalar solutions are continuous, at the surface the tractions y_2 and y_4 vanish and a final constant is determined through the continuity of the potential y_5. This determines the 16 free constants. However, if $\omega = 0$, there are only 2 free constants in the liquid layer, consequently, a planet with a liquid layer (or core) of incompressible flow cannot in general have a static solution. This has already been pointed out by *Longman* [1963], i.e., there are no static solutions for a planet with a liquid non-neutrally stratified layer featuring a solenoidal displacement field. See also *Denis et al.* [1998] for a detailed discussion.

For a fully fluid planet with $N^2 = 0$ the potential y_5 can also be calculated from (5.81) and (5.82), but the radial and tangental displacements y_1 and y_3 as a function of depth are undetermined. However, unlike the incompressible flow setting, a solution for the more general setting, i.e., a solid planet with a fluid layer or liquid core, can be obtained. At a fluid solid interface b a first vector is constructed with the solutions of $y_5^l(b)$ and $y_6^l(b)$ and by setting the remaining $y_i^s(b) = 0$. A second vector is build by setting $y_1^s(b) = 1$, $y_6^s(b) = -4\pi G\rho(b)^{(l)} y_1^s(b)$, $y_2^s(b) = \rho(b)^{(l)} g(b) y_1^s(b)$, and the remaining $y_i^s(b) = 0$. The third solution accounts for possible tangential slip at the fluid-solid boundary: $y_3^s(b) = 1$ and the remaining $y_i^s(b) = 0$.

5.3.4 Numerical integration

Prior to numerical integration the system of linear differential equations is rewritten in terms of undimensional quantities. The following rescalings have been applied:

$$\begin{aligned}
(y_1, y_3) &\rightarrow r_a(y_1, y_3) \\
(y_2, y_4) &\rightarrow \kappa_0(y_2, y_4) \\
(y_5, y_6) &\rightarrow y_{5,0}(y_5, y_6/r_a) \\
y_{5,0} &= G r_a^2 \rho_a \\
\rho &\rightarrow \rho_a\, \rho \\
g &\rightarrow g_0\, g \\
(\kappa, \mu) &\rightarrow \kappa_0(\kappa, \mu) \\
\omega &= \omega_0 \omega \\
\kappa_0 &= G r_a^2 \rho_a^2 \\
g_0 &= G r_a \rho_a \\
\omega_0^2 &= G \rho_a,
\end{aligned} \tag{5.87}$$

where ρ_a is the average planetary density. The resulting equations are formally identical to the dimension bearing equations if G is set to 1. For the planet Mars with $r_a = 3390$km

and $\rho_a = 3934\text{kg/m}^3$ one has for instance:

$$\begin{aligned} \kappa_0 &= 11.87\text{GPa} \\ g_0 &= 0.89\text{m/s}^2 \\ \frac{2\pi}{\omega_0} &= 3.41\text{h} \end{aligned} \tag{5.88}$$

The numerical integration is best started at the center from a solution that satisfies the initial condition in $r = 0$, and done separately for each layer delineated by discontinuities in state, fluid or solid, or/and discontinuity in ρ, κ or μ. For the initial conditions of a given layer the solutions at the top of the previous layer are to be employed. At the surface of the planet a specific linear combination of the solutions vectors will accommodate with the surface conditions.

The 6 ODE's describing the spheroidal displacements and traction in a solid planet have 6 independent solutions, however, only 3 are regular in $r = 0$. This can be seen from the analytical solutions for a homogenous planet [e.g. *Gilbert and Backus*, 1968]. Half of the solutions are regular in $r = 0$, they either are proportional to powers of r or to radial Bessel functions, the remaining functions diverge for $r \to 0$ and are proportional to negative powers of r and to radial Neuman functions.

As the ODE's have an apparent singularity in $r = 0$, it is advisable to start the numerical integration at $r = \varepsilon$. And use as initial solution the 3 regular analytical solution at the surface a sphere of size ε. At solid-solid interfaces each of the six scalar functions are continuous. In fluid layers, the tangential traction $y_4 = 0$ and y_3 can be expressed as an algebraic equation (5.55). Only 2 combinations of the 3 solid solution vectors satisfy the boundary condition $y_4 = 0$. The 2 independent solutions are propagated by the 4 fluid ODE's in y_1, y_2,y_5, and y_6 to the surface of the next interface. At fluid-solid interfaces, the two 4 dimensional fluid solution vectors are extended with $y_3 = 0$ and $y_4 = 0$ and comprise 2 independent initial solution vectors for the solid layer integration. A third solution, which allows for possible tangential slip at the fluid-solid boundary is:

$$y_i = 0, \quad y_3 = 1, \quad i = 1, 2, 4, 5, 6 \tag{5.89}$$

At the surface of the planet, when there is no final fluid layer, there will be 3 independent six dimensional solution vectors, $\boldsymbol{v_1}$, $\boldsymbol{v_2}$, and $\boldsymbol{v_3}$. A linear combination, $a\boldsymbol{v_1} + b\boldsymbol{v_2} + c\boldsymbol{v_3}$ give the solution at the surface. The 3 constants are to be determined from the surface boundary conditions (the frequency dependence is implicit and dropped in the notation)

$$a\boldsymbol{v_1} + b\boldsymbol{v_2} + c\boldsymbol{v_3} = \begin{pmatrix} y_1 \\ 0 \\ y_3 \\ 0 \\ y_5 \\ 2l+1 \end{pmatrix} \tag{5.90}$$

The constants a, b, c, and the surface y_1,y_3, y_5 are then

$$\begin{pmatrix} a \\ b \\ c \\ y_1 \\ y_3 \\ y_5 \end{pmatrix} = \begin{pmatrix} v_{11} & v_{21} & v_{31} & -1 & 0 & 0 \\ v_{12} & v_{22} & v_{32} & 0 & 0 & 0 \\ v_{13} & v_{23} & v_{33} & 0 & -1 & 0 \\ v_{14} & v_{24} & v_{34} & 0 & 0 & 0 \\ v_{15} & v_{25} & v_{35} & 0 & 0 & -1 \\ v_{16} & v_{26} & v_{36} & 0 & 0 & 0 \end{pmatrix}^{-1} \begin{pmatrix} 0 \\ 0 \\ 0 \\ 0 \\ 0 \\ 2l+1 \end{pmatrix}, \tag{5.91}$$

where $v_{ij} = (\boldsymbol{v_i})_j$ stands for the j-th component of vector i. The Love Numbers at the surface are defined from

$$h_l = y_1 g_a \tag{5.92}$$
$$k_l = -1 + y_5 \tag{5.93}$$
$$l_l = y_3 g_a \tag{5.94}$$

To determine the functions y_i in each layer we use the previous introduced continuity conditions. The solution within layer i is, when solid:

$$\boldsymbol{y}^{s,i} = a\boldsymbol{v}_\mathbf{1}^i + b\boldsymbol{v}_\mathbf{2}^i + c\boldsymbol{v}_\mathbf{3}^i. \tag{5.95}$$

and the solution within layer $i-1$ is, when fluid

$$\boldsymbol{y}^{f,i-1} = a\boldsymbol{v}_\mathbf{1}^{i-1} + b\boldsymbol{v}_\mathbf{2}^{i-1}. \tag{5.96}$$

If layer $i-2$ is again solid the constant c is to be determined from the continuity of $[y_4]_-^+ = 0$ at the fluid solid interface.

$$c = -\frac{y_{14}^s}{y_{34}^s}a - \frac{y_{42}^s}{y_{34}^s}b \tag{5.97}$$

where the $y_{i,4}$ are taken at the top of the solid layer $i-1$.

5.3.5 Analytical solutions

For a spherically symmetric radially stratified initial configuration, made of homogeneous shells, in density and in elastic parameters, the equations describing small deformation about an initial configuration can be solved analytically if for the shell it is assumed that $g(r)/r = \text{const}$. The solutions are expressed as combination of radial Bessel and Neuman functions. The set of regular solutions can found in *Dahlen and Tromp* [1998] and a derivation of the analytical solutions of the differential equations describing spherical displacement in *Gilbert and Backus* [1968].

For an even more simplified setting (without assuming that $g(r)/r = \text{const}$), namely a homogeneous spherical incompressible planet of size r_a, density ρ, surface gravity g, and rigidity μ, the surface Love number, h_l, k_l, and l_l can be computed analytically.

$$h_l = \frac{2l+1}{2(l-1)}\frac{1}{1+\tilde{\mu}}, \quad k_l = \frac{3}{2l+1}h_l, \quad l_l = \frac{3}{l(2l+1)}h_l, \tag{5.98}$$

where

$$\tilde{\mu} = \frac{2l^2 + 4l + 3}{l} \frac{\mu}{\rho\, g\, r_a}, \tag{5.99}$$

and $l \geq 2$. Those expression are readily derived from the analytical solutions for the y_i's of an incompressible homogeneous sphere [e.g *Sabadini and Vermeersen*, 2004]. The Love numbers decrease from h to l and that for an incompressible planet they approximatively increase with the square of the planet size and the square of the average density and decrease inversely proportional to the shear modulus.

For a fluid incompressible sphere, the Love numbers h_l and k_l can be obtained from the above equations by setting $\mu = 0$. The Love number l_l cannot be determined since the tangential component of the deformation in a fluid is undetermined (see Sect.[5.3.3]). Note that for an incompressible fluid sphere the Love numbers do neither depend on the average density nor on the sphere' size. For $l = 2$ one obtains $h_2 = \frac{5}{2}$ and $k_2 = \frac{3}{2}$.

5.4 Phenomenology of deformation

In the previous section the equations describing deformations and external potential changes and associated surface Love numbers have been derived under the assumption that the planet behaves elastically. However, planets generally do not respond elastically to an external forcing and their response can be different depending on the period of the forcing. For instance, over very long timescales the Earth behave like Newtonian viscous fluids, i.e. the equilibrium figure of a planetary body determined through gravity observations is accordingly described by a rotating fluid. On intermediary timescales, those related to plate motions and mantle convection, planet materials involve plastic deformation. For frequencies associated to tides, it is observed that there is a delay between the forcing potential and the deformational response of the surface, the material behaves anelastically. For example in the Mars-Phobos system, the tidal dissipation inside Mars results in a tidal bulge on the surface of Mars which is delayed with respect to Phobos' direction. Since the orbital period of Phobos is smaller than the rotation period of Mars the tidal bulge results in a secular acceleration in Phobos' orbital motion. Consequently, determining this secular acceleration allows constraining the rheology of Mars. Finally, at time scales associated to seismic events the Earth's response is anelastic [3] in shear.

5.5 Non elastic rheology and dissipation

Rheology denotes the study of deformations, the flow of matter and the properties of the flow [*Ranalli*, 1987]. When the stress is linearly proportional to the strain and fully recoverable the material is defined to be elastic. The elastic behavior is described by Hook's law and by the material coefficients, e.g. κ and μ. Fluids or Newtonian bodies show steady-state flow under constant deviatoric stress. Their sole material parameter is the viscosity. In Newton bodies the strain rate is proportional to stress. The simplest non-elastic phenomenological rheology adequate for describing dissipation occurring during

[3] imperfect elasticity, part of the strain energy is dissipated as heat

tidal forcing is the viscoelastic *Maxwell* model. Its stress relaxation behavior is described in terms of the *Maxwell time*

$$\tau_M = \frac{\eta}{\mu}, \tag{5.100}$$

where μ is the elastic rigidity and η is the viscosity. For forcing periods $t < \tau_M$ the elastic response predominates; for $t > \tau_M$ the viscous response does. For instance. the Earth mantle with an average viscosity of $\eta = 10^{21}$Pa s and $\mu = 10^{11}$Pa has a Maxwell time of order of 10^3a.

5.5.1 From elasticity to viscoelasticity

For an isotropic material with hydrostatic initial stress, the elastic constitutive relation relating the incremental Lagrangian stress tensor $\boldsymbol{T}^{L1}$ to the strain $\boldsymbol{\varepsilon}$ is

$$\boldsymbol{T}^{L1}(t) = \kappa \nabla \cdot \boldsymbol{s}(t)\boldsymbol{I} + 2\mu \boldsymbol{d}(t), \tag{5.101}$$

where $\boldsymbol{d} = \boldsymbol{\varepsilon} - \frac{1}{3}\nabla \cdot \boldsymbol{s}\boldsymbol{I}$ is the deviatoric strain, and κ is the isentropic incompressibility and μ is the rigidity. This constitutive relation is only time dependent through the strain. It can be generalized to non-elastic materials by using the Boltzmann superposition principle: The stress experienced by a non-elastic material is assumed to depend linearly upon the entire past history of strain rate:

$$\boldsymbol{T}^{L1}(t) = \int_{-\infty}^{t} d\tau \; \kappa(t-\tau)\, \partial_\tau \nabla \cdot \boldsymbol{s}(\tau)\, \boldsymbol{I} + \int_{-\infty}^{t} d\tau \; 2\mu(t-\tau)\, \partial_\tau \boldsymbol{d}(\tau) \tag{5.102}$$

For causality reasons, there is of course no dependence upon deformation happening in the future. The Fourier transformation of (5.102) yields

$$\hat{\boldsymbol{T}}^{L1}(\omega) = \hat{\kappa}(\omega) \nabla \cdot \hat{\boldsymbol{s}}(\omega)\; \boldsymbol{I} + 2\hat{\mu}(\omega)\hat{\boldsymbol{d}}(\omega), \tag{5.103}$$

With the exception of the Fourier transformed and now frequency dependent incompressibility $\hat{\kappa}(\omega)$ and rigidity $\hat{\mu}(\omega)$ equation (5.103) is formally identical to the Fourier transformation of (5.101). Because the form of the constitutive relation for the non-elastic case in the Fourier domain is of the same form as the constitutive relation for a Hookean solid, dynamical problems for these solids may be solved by applying the *correspondence principle* [*Biot*, 1954]. The correspondence principle stipulates that for a linear viscoelastic setting the Fourier or the Laplace transformed deformation equations and boundary conditions are formally identical to the elastic equations and boundary conditions if the radial functions and material parameters are represented by complex functions.

Maxwell rheology

The simplest linear non-elastic constitutive relation for planetary materials is described by the viscoelastic Maxwell rheology. The correspondence principle states that if the tidal potential is harmonic in time the equations describing deformations are formally invariant if the elastic Lamé parameter μ and λ are transform as

$$\tilde{\mu}(\omega) = \quad \mu \left(\frac{\omega^2\eta^2}{\mu^2 + \omega^2\eta^2} + i \frac{\mu\eta\omega}{\mu^2 + \omega^2\eta^2} \right) \tag{5.104}$$

$$\tilde{\lambda}(\omega) = \quad \kappa - \frac{2}{3}\tilde{\mu}(\omega), \tag{5.105}$$

where μ and κ are the elastic rigidity and incompressibility and η is the viscosity. If the forcing period $T = 2\pi/\omega$ is significantly shorter than the relaxation time τ_M Eqs. (5.105) and (5.104) read $\tilde{\mu} \approx \mu$ and $\tilde{\lambda} \approx \lambda$. The material is approximatively elastic, dissipative effects are negligible. On the other hand, if the forcing period is significantly longer than the relaxation time the complex shear modulus $\tilde{\mu}$ is approximatively zero and the material behaves like a fluid. In other words, at very long periods the material can not support shear stress.

Burgers rheology

A more sophisticated model for the rheology of planetary material is the Burgers model. Compared to the Maxwell rheology it has a second viscosity and a second shear modulus. As it comprises two viscosities it has two associated relaxation frequencies. Consequently, it models for instance long period viscoelasticity together with intermediary period anelastic processes. The Lamé parameters for the simple Burger models are [*Peltier et al.*, 1981]:

$$\tilde{\mu}(\omega) = \left[\left(\frac{\mu_1}{\eta_1} + \frac{\mu_1+\mu_2}{\mu_2}\right)^2 \omega^2 + \left(\omega^2 - \frac{\mu_1}{\eta_1}\frac{\mu_2}{\eta_2}\right)^2\right]^{-1}$$
$$\left\{\mu_1\omega^2\left[\left(\frac{\mu_2}{\eta_1}\frac{\mu_1-\mu_2}{\eta_2} + \frac{\mu_1}{\eta_2}\frac{\mu_1+\mu_2}{\eta_2}\right) + \omega^2\right] + i\mu_1\left[\frac{\mu_1}{\eta_1}\frac{\mu_2}{\eta_2}\frac{\mu_1}{\eta_2}\omega + \omega^3\left(\frac{\mu_1}{\eta_1} + \frac{\mu_2}{\eta_2}\right)\right]\right\}$$
$$\tilde{\lambda}(\omega) = \left(\frac{\mu_1+\mu_2}{\eta_2} - \omega^2\right)^{-1}$$
$$\left[\left(\lambda_1 + \frac{2}{3}\mu_1\right)\frac{\mu_1}{\eta_1}\frac{\mu_2}{\eta_2} - \lambda_1\omega^2 + i\omega\left\{\left(\lambda_1 + \frac{2}{3}\mu_1\right)\frac{\mu_1}{\eta_1}\frac{\eta_1+\eta_2}{\eta_2} + \lambda_1\frac{\mu_2}{\eta_2}\right\}\right]$$

The elastic Lamé parameters are μ_1 and λ_1, and the long term viscosity is η_1. The Maxwell rheology is obtained by taking the limit $\eta_2 \to \infty$. For Earth, the long term viscosity η_1 is obtained by fitting the model to postglacial rebound data [*Lambeck et al.*, 1998], while the remaining variables μ_2 and η_2 are found by fitting the model to shorter time scale anelastic process like elastic gravitational free oscillation.

5.5.2 Global dissipation and Q

The quantity that characterizes the global dissipation resulting from the non-elastic rheology is the quality factor Q. It is defined as the ratio of the dissipated energy during one cycle of sinusoidal straining, the line integral over dE/dt, to the peak energy E^* stored in the system during the cycle [*Zschau*, 1978]

$$Q^{-1}(\omega) = \frac{1}{2\pi\ E^*}\oint dt\ \frac{d\,E}{dt}. \tag{5.106}$$

Q, or its inverse the global dissipation factor is related to the complex Love number k_2 [*Zschau*, 1978]

$$Q = -\frac{\mathrm{Re}k_2}{\mathrm{Im}(k_2)}. \tag{5.107}$$

Planets with low Q values have high dissipation rates and elastic non-dissipating bodies have $Q = \infty$.

Complex Love numbers follow from the complex non elastic rheology. For example from the Maxwell rheology ((5.104) and (5.105)) we have

$$\tilde{\mu}(\omega) = \tilde{\mu}(-\omega)^* \tag{5.108}$$

$$\tilde{\lambda}(\omega) = \tilde{\lambda}(-\omega)^*. \tag{5.109}$$

Form this properties we obtain for the equation of motion (5.28)

$$\boldsymbol{s}(\omega) = \boldsymbol{s}(-\omega)^* \tag{5.110}$$

and therefore $h_l(\omega) = h_l(-\omega)^*, l_l(\omega) = l_l(-\omega)^*$ and $k_l(\omega) = k_l(-\omega)^*$.

If we use the definition of Q ((5.107)), the shear modulus expression from the Maxwell rheology ((5.104)), and the analytical expression for k_2 ((5.98)) we obtain the following analytic expression for Q

$$Q(\omega) = \frac{\eta\omega}{\mu} + \frac{8\pi G r^2 \rho^2}{57\eta\omega}\left(1 + \frac{\eta^2\omega^2}{\mu^2}\right). \tag{5.111}$$

Q increases with the square of the planet size and with the square of the average planet density. For a liquid planet, $\mu \to 0$, $1/Q \to 0$. With increasing μ Q is decreasing and for $\mu \to \infty$ the quality factor is $\frac{4}{57} G r^2 \rho^2 \frac{\tau}{\eta}$.

For both the period $\tau = 2\pi/\omega$ and the viscosity, in the limits $\tau \to 0$ ($\eta \to 0$) and $\tau \to \infty$ ($\eta \to \infty$) the dissipation is zero. The period of maximal dissipation or the minimal Q value is

$$\tau = 2\pi\frac{\eta}{\mu}\sqrt{\frac{57}{8\pi G r^2 \rho^2} + 1} \tag{5.112}$$

and the viscosity of maximal dissipation is

$$\eta = \frac{\tau\mu}{2\pi\sqrt{\frac{57\mu}{8\pi G r^2 \rho^2} + 1}}. \tag{5.113}$$

5.6 Love number menagerie

In order to assess the dependence of the Love numbers on the interior structure of planets we have built simple spherically symmetric planetary models with homogeneous layers and calculated Love numbers and the quality factor Q for different planet sizes, number of layers, forcing frequencies, elastic properties, and viscosities. The fluid layers are considered inviscid, and the non-elastic behavior of the solid layers is only in shear as in viscoelastic Maxwell models. In what follows we call *Maxwell viscosity* the viscosity obtained as the product of average shear modulus of a layer and the chosen forcing period (see (5.100)).

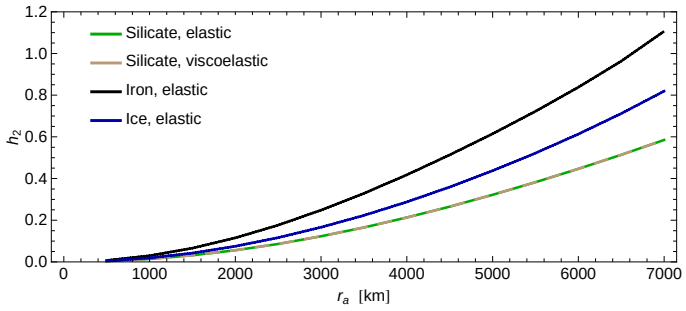
The values for the elastic parameters of the layers used in the calculations are given in Tab.[5.1]. To cover a meaningful range we consider the layers to consist of pure solid iron, a mixture of iron, and sulfur, silicate material, and solid water ice. Note that the values are mean values for a planet whose pressure and temperature range are compatible with those inside Mars (up to about $40GPa$). When a layer is liquid, the outer core here, the density and the bulk modulus are taken as for solids and the shear modulus is set to zero. We use a reference tidal period of 6.6h.

	ρ[kg/m^{-3}]	κ[GPa]	μ[GPa]	η[Pa s]	$\tau[d]$
Fe	8300	300	160	10^{25}	$7.2\ 10^{8}$
$Fe - 14wt\%S$	6100	260	150	0	
silicate	3500	190	70	$2\,10^{16}$	3.31
ice V	1260	15	6	10^{15}	1.93

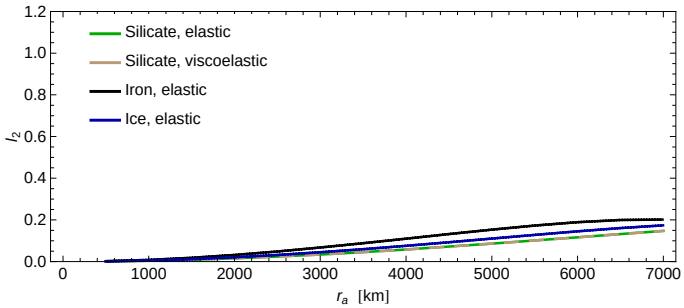
Table 5.1: Elastic parameters for reference models

5.6.1 Planet size and average composition

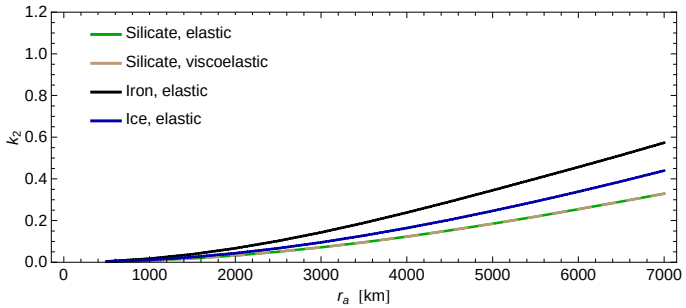
Fig.[5.1] shows the real part of the Love numbers (Figs [5.1a, 5.1b,5.1c]) and of the quality factor (Fig.[5.1d]) for homogeneous planets as a function of their size made of either solid iron, silicates, or solid water ice. The Love numbers increase with the planet size, and the rate of increase is strongest for the iron models, followed by solid ice, and last is silicate. The numerical calculations reproduce qualitatively the predictions of the analytic formulas (5.98) derived for an incompressible homogeneous planet ($\sim r^2\rho^2/\mu$). The real parts of the Love numbers for a Maxwell rheology are almost equal to the Love numbers of the corresponding elastic model. In accordance with the simple analytic model (5.111), Q increases with increasing planet size (see Fig.[5.1d]) and for a given material Q increases with increasing viscosity since the forcing period of 6.6h is significantly smaller than the Maxwell time.



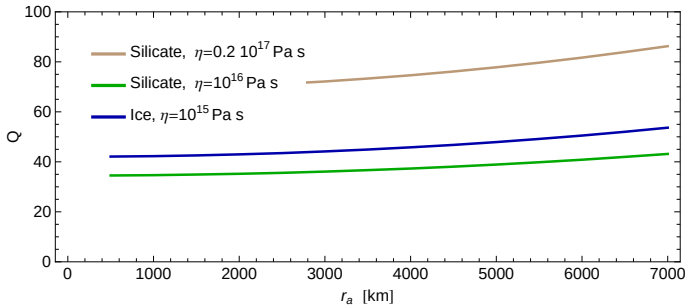
(a)



(b)



(c)



(d)

Figure 5.1: Love numbers, h_2 (a), l_2 (b), k_2 (c), and quality factor Q (d) as a function of planet size, for a homogeneous planet made of silicate, pure Fe, and ice.

5.6.2 Forcing period

Away from the fundamental eigenperiod, T_0, of the oscillating homogeneous sphere [*Dahlen and Tromp*, 1998, page 296], and for an elastic rheology, the Love numbers don't exhibit any appreciable dependence on the forcing period (results not shown here).

For non-elastic models the dependence is similarly weakly dependent on frequency if the period is larger than the fundamental eigenperiod and smaller than the Maxwell time (Fig.[5.3]). However, for periods larger than the Maxwell time the Love numbers increase sharply. This is a result of the strong decrease in of the shear modulus for periods larger than the Maxwell time (Fig.[5.2]) as the Love numbers are inversely proportional to the shear modulus. On a deformational level, the solid behaves like a fluid, and the numerical scheme established for calculating deformations of solids is no longer valid. For zero shear strength, i.e. for a fluid, the Love numbers calculated with the analytical formulas (5.98) are $h_2 = 5/2$, $l_2 = 3/4$, and $k_2 = 3/2$. For each model, the dissipation decreases to a minimum value at about the period of the fundamental eigenperiod (Fig.[5.3d]). Then the dissipation increases to reach a maximum for periods at about the Maxwell time.

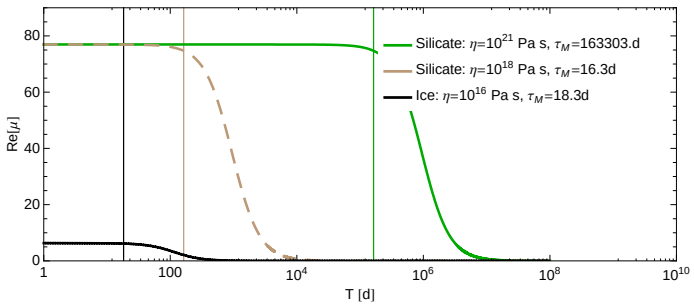
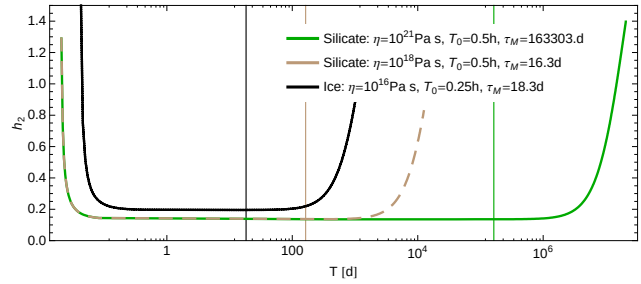
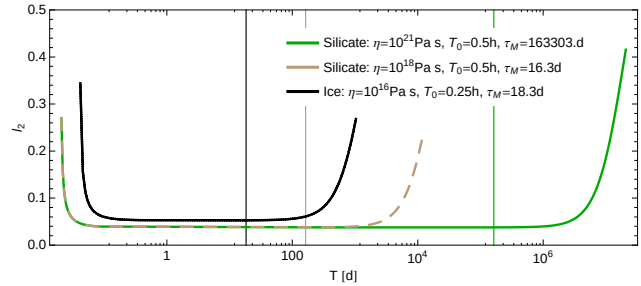


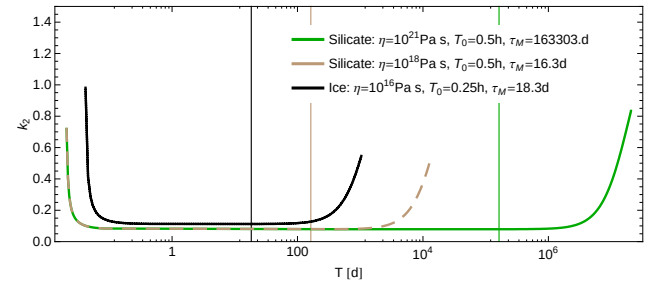
Figure 5.2: Real part of shear modulus as a function of forcing period. Where η is the viscosity and τ_M the Maxwell time. The vertical lines correspond to the respective Maxwell times.



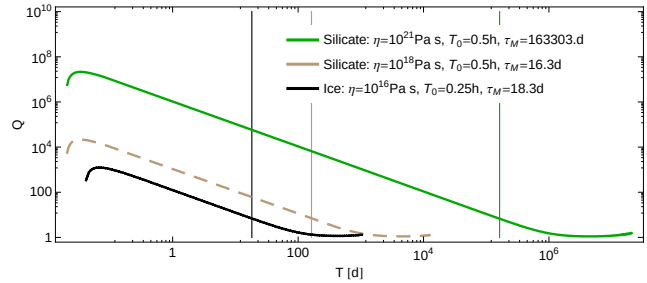
(a)



(b)



(c)

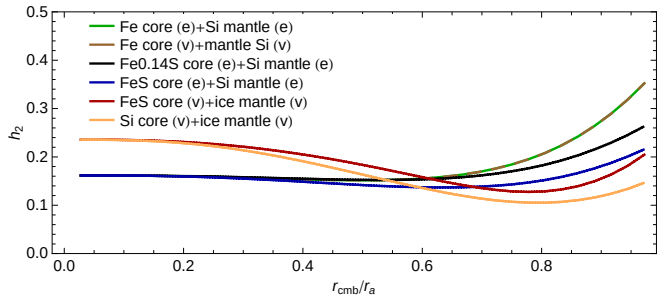


(d)

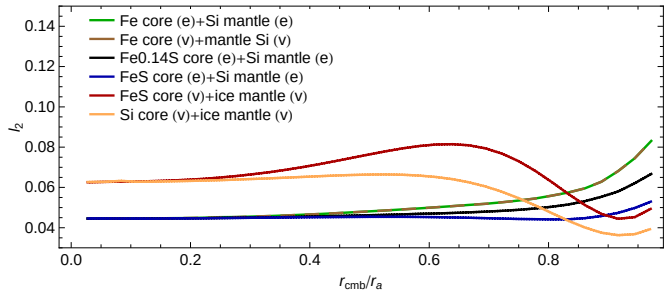
Figure 5.3: Love numbers, h_2 (a), l_2 (b), k_2 (c), and quality factor Q (d)as a function of excitation period, for a homogeneous non elastic planet made of silicates or ice. (Here η is the viscosity, τ_M the Maxwell time, and T_0 the period of the fundamental radial eigenperiod. The vertical lines correspond to the respective Maxwell times.

5.6.3 Solid core size

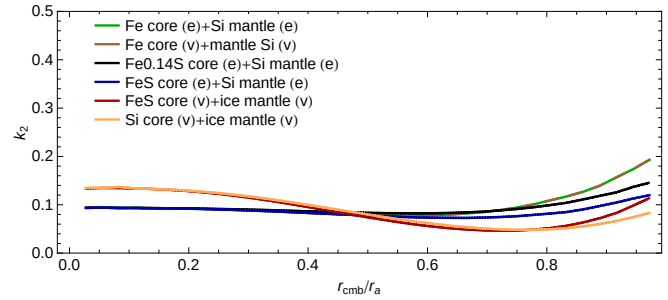
The variation of the Love numbers and of the quality factor Q as a function core size for a planet with a solid core and an overlaying solid mantle are shown in Fig.[5.4]. The considered cores are made of pure Fe, Fe − 16wt%S, FeS, and silicate and the mantles are silicate or water ice. Silicate shell models display a soft decrease in h_2 and k_2 numbers with increasing core size, reaching a minimum, and finally increasing with increasing core size. The planets with an ice mantle have larger Love number values when compared to those with silicate mantles for small cores. For h_2 and k_2 this trend is inverted when $r_{\rm core}/r_a$ is about 0.5. The Love number l_2 increases initially, attaining a maximum when the core is about half of the planet's size, after attaining a minimum it starts to increase when $r_{\rm core}/r_a$ is about 0.8. This behavior is somewhat more pronounced when the mantle is made of ice. The difference in Love numbers between elastic and viscous rheology is below 2% and decreases with core size. The Q values for models with viscoelastic models are initially constant and start to increase strongly at about $0.6r_{\rm core}/r_a$, when the mantle is made of ice, and at about $0.4r_{\rm core}/r_a$ when the mantle is made of silicates. The quality factor increases with relative core size since the contribution of the less dissipating core, compared to the mantle, increases.



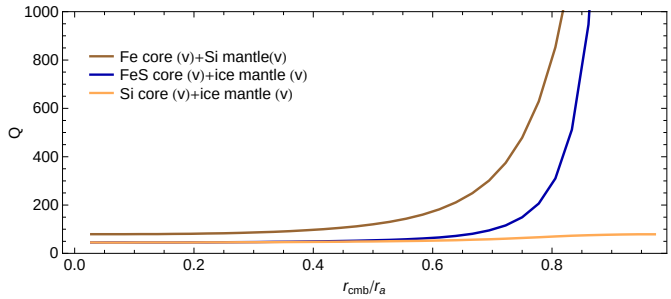
(a)



(b)



(c)



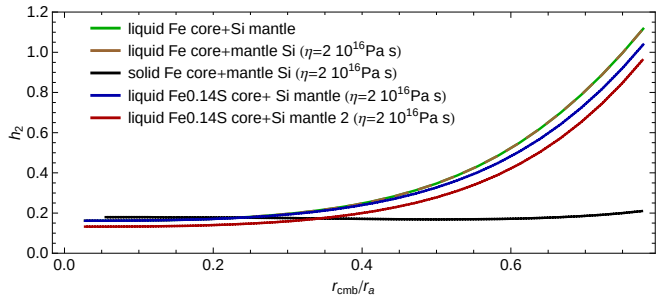
(d)

Figure 5.4: Love numbers, h_2 (a), l_2 (b), k_2 (c), and quality factor Q (d) as a function of solid core size. The homogeneous mantle is made of silicates (elastic and viscous $\eta = 2\,10^{16}$Pa s) or viscous ice ($\eta = 10^{15}$Pa s). The homogeneous core is made of Fe, Fe – xFeS, FeS, or silicates. The viscosity of the Fe core is $\eta = 10^{25}$Pa s. The label (e) stands for elastic and (v) for viscous.

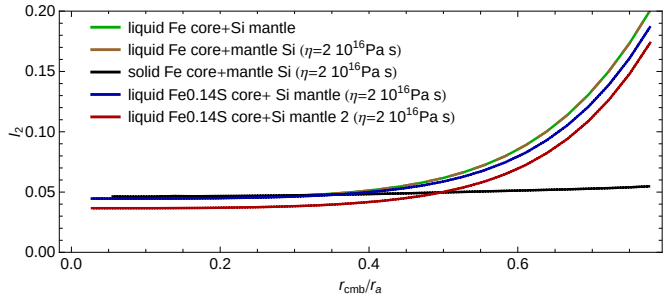
5.6.4 Liquid core size

Fig.[5.5] shows Love numbers and the quality factor for models with a liquid core and a solid overlying shell. The cores are made of pure Fe and Fe − 14wt%S. Two mantle models are considered; one made from the reference silicate model and a model with a 10% lower density than the silicate model. The results show that the Love numbers strongly increase with increasing core size. For comparison Fig.[5.5] also shows Love numbers for a model with a solid iron core. Note that for core sizes below about $0.3r_{\rm cmb}/ra$ the difference between solid core models and liquid core models is very small. The results also show that for fixed silicate shell, the Love number increase with increasing core density and that for a fixed core, the Love number increase with increasing mantle density. The influence of the mantle density is however, much stronger, a relative change in mantle density of about 10% leads to a change in Love numbers by more then 18%, whereas a change of core density by about 26% results in a Love number difference below 4%. The real parts of the Love numbers do not exhibit a significant dependence on viscosity of the mantle; the relative difference between an elastic and a viscous mantle model is on average below 0.01%.

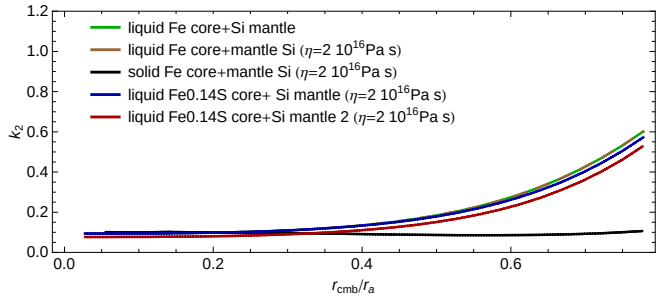
The quality factor Q increases with increasing core size Fig.[5.5], i.e. the dissipation decreases. The value of Q increases with the density of the core, just like k_2. However, Q is quasi not dependent on the density of the mantle, see Fig.[5.5]. The differences between the different models are only visible for core sizes larger than $0.4r_{\rm cmb}/r_a$. Note also that for $r_{\rm cmb} < 0.4r_{\rm cmb}/r_a$ the dissipation does not depend appreciably on the core state (solid or liquid), only for larger cores does Q increase significantly faster for solid core models than for liquid core models.



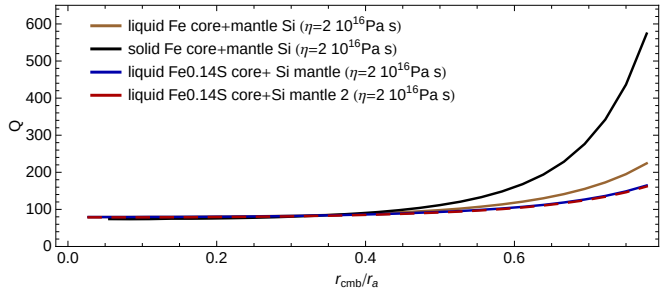
(a)



(b)



(c)



(d)

Figure 5.5: Love numbers, h_2 (a), l_2 (b), k_2 (c), and quality factor Q (d) as a function of liquid core size, for models with a silicate mantle (elastic or with $\eta = 2\,10^{16}$Pa s) and a liquid core made either of Fe or Fe $-$ 0.14S. For comparison purposes, the same results for a viscous solid planet with an Fe core is also given (black curve). Mantle 2 has a 10% lower density than the reference silicate shell.

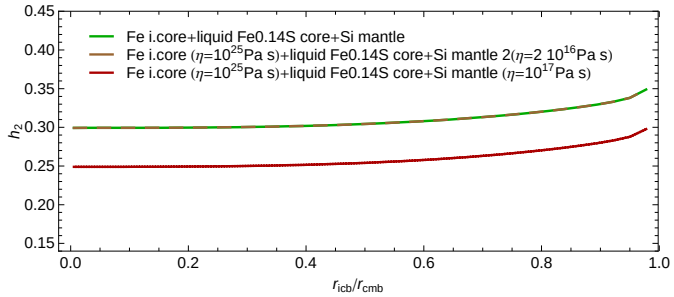
5.6.5 Inner core size

Fig.[5.6] shows the Love numbers and Q for 3 layer models made of a solid Fe inner, a liquid $Fe - 14wt\%S$ outer core, and a silicate shell mantle as a function of inner core size. The core size is $0.7r_a$. The silicate shell of mantle 2 is 0.9 times the density of the reference silicate shell. The signature of the growing inner-core is barely visible in the potential Love number k_2 and in the quality factor Q. However, the deformational Love numbers h_2 and l_2 increase with increasing inner-core size. Over the whole considered inner-core range, they increase by about 15%.

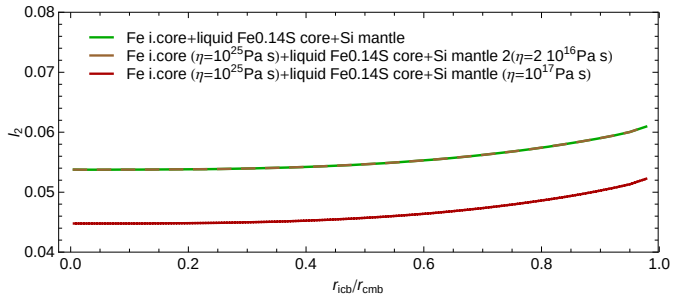
An appraisal of the influence of the inner core size on the Love number is best obtained by comparing models with inner cores to a reference model with a fully fluid core. Fig.[5.7] shows the relative difference in Love numbers between the reference model and models with different inner-core sizes. The results illustrate that inner cores already for inner cores of moderate size, compared to the planet size, lead to significant deviations in the displacement Love numbers. The deviation increases with increasing core size for fixed inner-core size and decreases with increasing inner-core size. Unlike to the Love numbers h_2 and l_2 the deviation in the k_2 value increases with increasing inner-core size since the k_2 increase with increasing core density and the density of the core increases with growing inner. The relative difference in k_2 increases with increasing core size if the inner cores size is fixed. Since for a given core size, models with an inner core have larger k_2 values, estimating the core size of interior structure models from k_2 and neglecting the presence of the inner core results in overestimated core sizes. This can however be avoided if the displacement Love numbers are considered together with k_2 as the former exhibit a strong dependence on the inner-core size.

Fig.[5.6d] shows that compared to the reference configuration, models with inner cores have smaller Q values and the deviation increases with increasing inner core size and increasing core size.

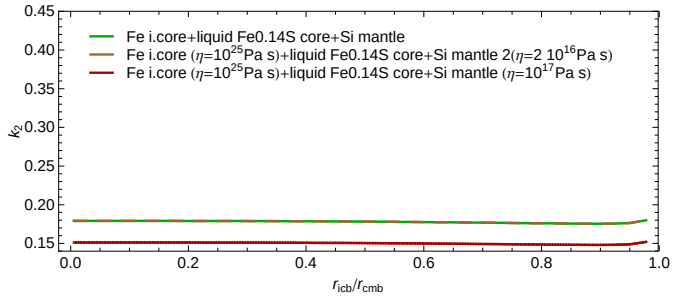
Love numbers and quality factors have also been calculated for models with a wide range of inner core viscosities, from Maxwell viscosity to $\eta = 10^{25}$Pa s (results not shown). However, the viscosity of the inner core has only a marginal effect on the values of Love numbers, they are about less than 1% lower than those calculated with an elastic inner core.



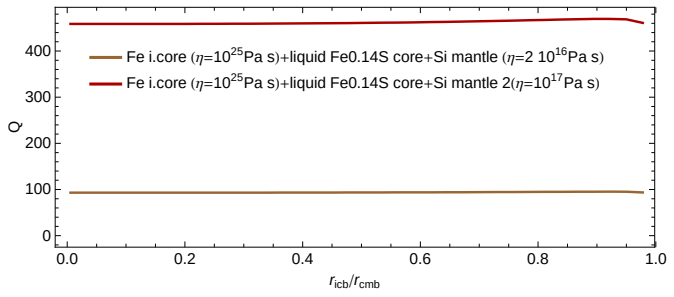
(a)



(b)

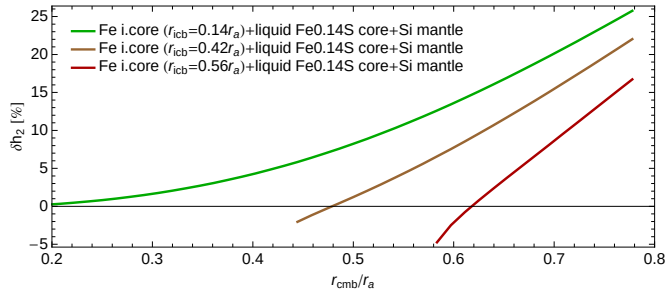


(c)

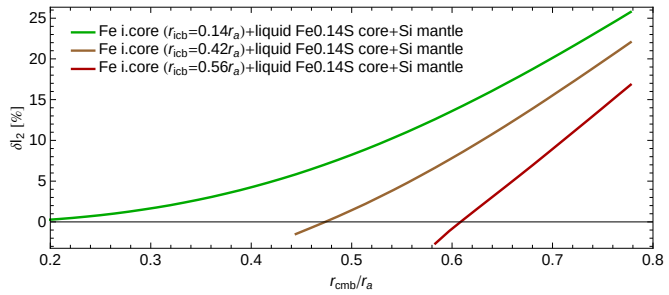


(d)

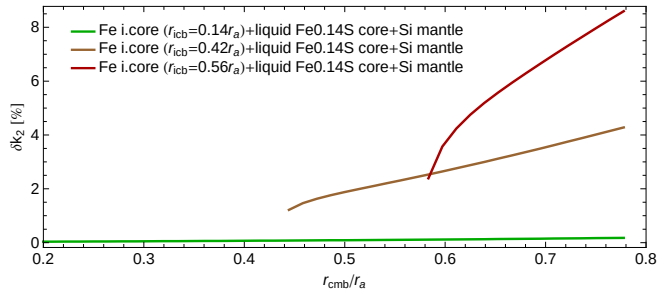
Figure 5.6: Love numbers, h_2 (a), l_2 (b), k_2 (c), and quality factor Q (d) as a function of relative inner core size. The planet has a solid Fe inner core (elastic or viscous, $\eta = 10^{25}$Pa s), a liquid outer core made of Fe − FeS, and a silicate mantle (elastic or viscous, $\eta = 2\,10^{16}$Pa s and $\eta = 10^{17}$Pa s).



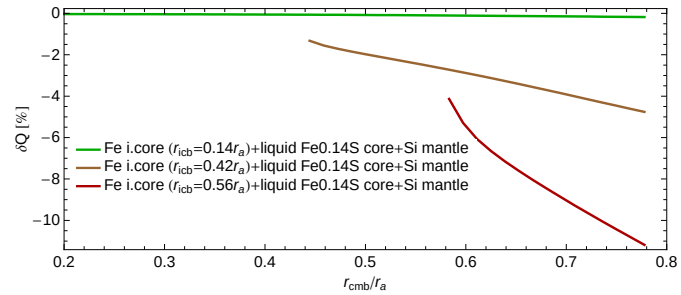
(a)



(b)



(c)



(d)

Figure 5.7: Relative difference of Love numbers, h_2 (a), l_2 (b), k_2 (c), and quality factor Q (d) compared to an inner core less planet as a function of relative core size for a planet with inner cores of $0.14r_a$, $0.42r_a$ and $0.56r_a$. The inner core is made of Fe ($\eta = 10^{25}$Pa s), the liquid core is made of FeS, and the the mantle is made of silicates ($\eta = 2\,10^{16}$Pa s).

5.6.6 Relative parameter influence

In order to assess the relative influence of the interior structure parameters on the Love numbers we have calculated relative deviations to a reference model by varying each interior parameter separately for solid cores and liquid cores. The studied parameters are: core size, mantle density, bulk and shear moduli, and core density and bulk modulus (and shear modulus if the core is solid). The reference model has a liquid core of 1400km, the densities and the moduli for the mantle and the core are: ($\rho = 3000\text{kgm}^{-3}$, $\kappa = 150\text{GPa}$, $\mu = 70\text{GPa}$) and ($\rho = 5000\text{kgm}^{-3}$, $\kappa = 150\text{GPa}$, $\mu = 80\text{GPa}$). The relative differences for liquid core models are shown in Fig.[5.8] those for solid core models are represented in Fig.[5.9].

The result show that for both solid and liquid cores in order of decreasing influence on Love numbers we have: mantle density, mantle shear modulus, mantle incompressibility, core density, core shear modulus (only for solid core models), and core incompressibility. For liquid core models mantle density and core size variations are of similar size if both parameter variation is below 50%. Above 50% the rate of variation due to core size is significantly more important. Doubling of the mantle density doubles approximatively the Love numbers whereby doubling the core size results in a 400% increase in h_2 and k_2 and about 300% in l_2. For solid core models the sensitivity of the Love numbers to core size variation is significantly lower as a doubling of the core size only increases the Love numbers by about 20%. For solid core models the sensitivity to the core size is approximatively the same as to the mantle shear moduli.

A doubling of the core elastic parameters results in relative Love number variations by less than 10%. The least influential parameter is the core incompressibility, a relative increase of 100% results in nearly no variation in Love numbers ($< 1\%$). Note that Love numbers decrease with increasing shear moduli of the mantle and the core and h_2 and k_2 increase with incompressibility but l_2 decreases with increasing incompressibility.

The order of sensitivity of the quality factor Q to variations of interior parameters is similar to the order of sensitivity of k_2 with the exception of the core size for solid core models. A doubling of the core size results in a relative increase of Q of about 80% for liquid core models whereas for solid cores the variation of Q is about 400%.

The previous results illustrate the dependence of the Love numbers on the composition, rheology, internal stratification and state, and excitation period. The real part of the Love number show only a relatively weak dependence to the rheology and to the excitation period when the later is away from the eigenperiods of the planet and below the Maxwell time. The Love numbers show a strong variation with core size when the planet has a liquid core and can therefore be used to estimate the core size. Similarly, if the core size is known the mantle density can be estimated. The Love number k_2 is only weakly dependent on the inner core size and can therefore be considered as a robust proxy for the core size, at least when the mantle is solid and made of silicates. The Love numbers h_2 and l_2 on the other hand, increase wit increasing inner core size. For equal core size, models with inner cores have lower l_2 and h_2 values than models without inner cores. The quality factor Q is quasi independent on the inner core size, and on the inner core's viscosity. It decreases with increasing excitation period and decreasing mantle viscosity. Among the other interior governing parameters, the most strongly constrainable parameter from the Love numbers is the density of the mantle, which exhibits a similar

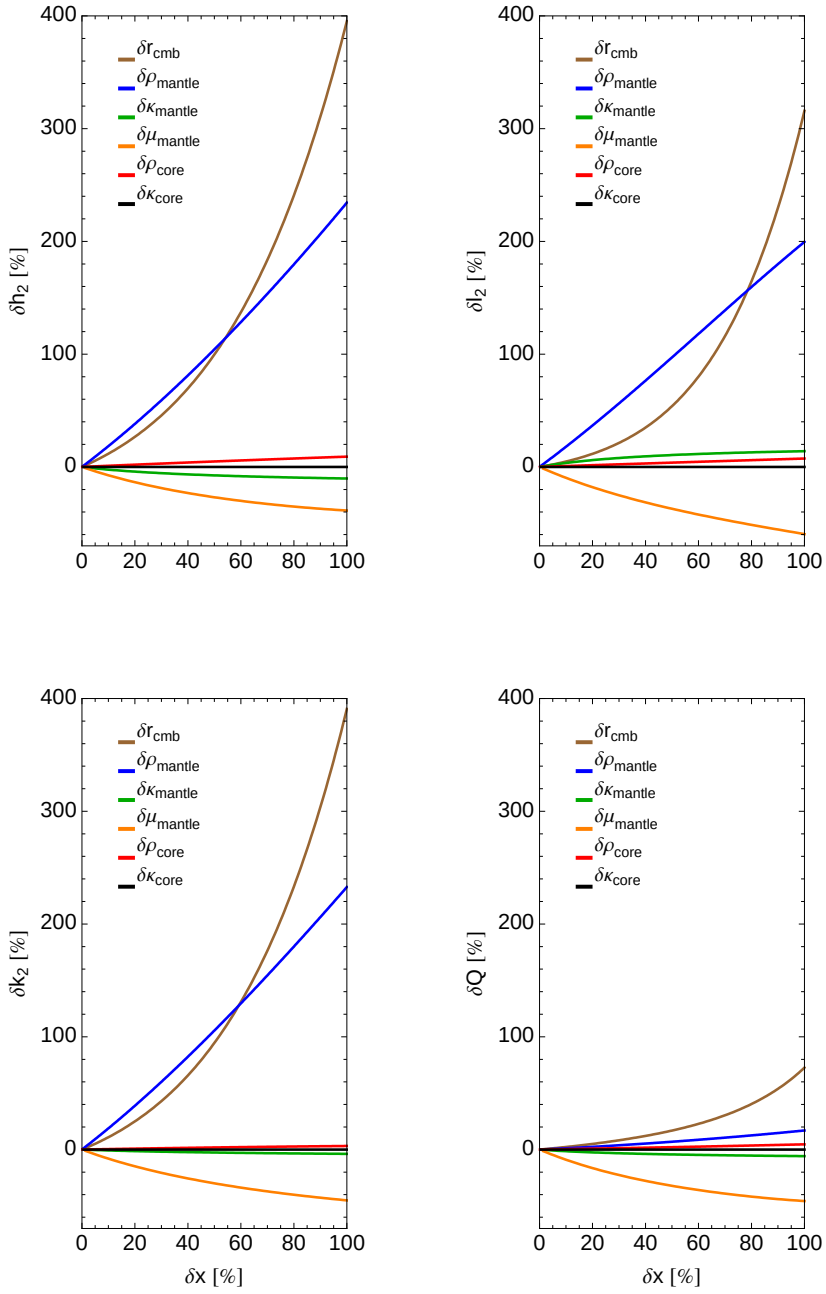


Figure 5.8: Relative change of Love numbers, h_2, l_2, k_2, and quality factor Q as a function of relative parameter change for models with a liquid core. The parameters are core size, for the mantle density, bulk, and shear moduli, and for the core density and bulk modulus.

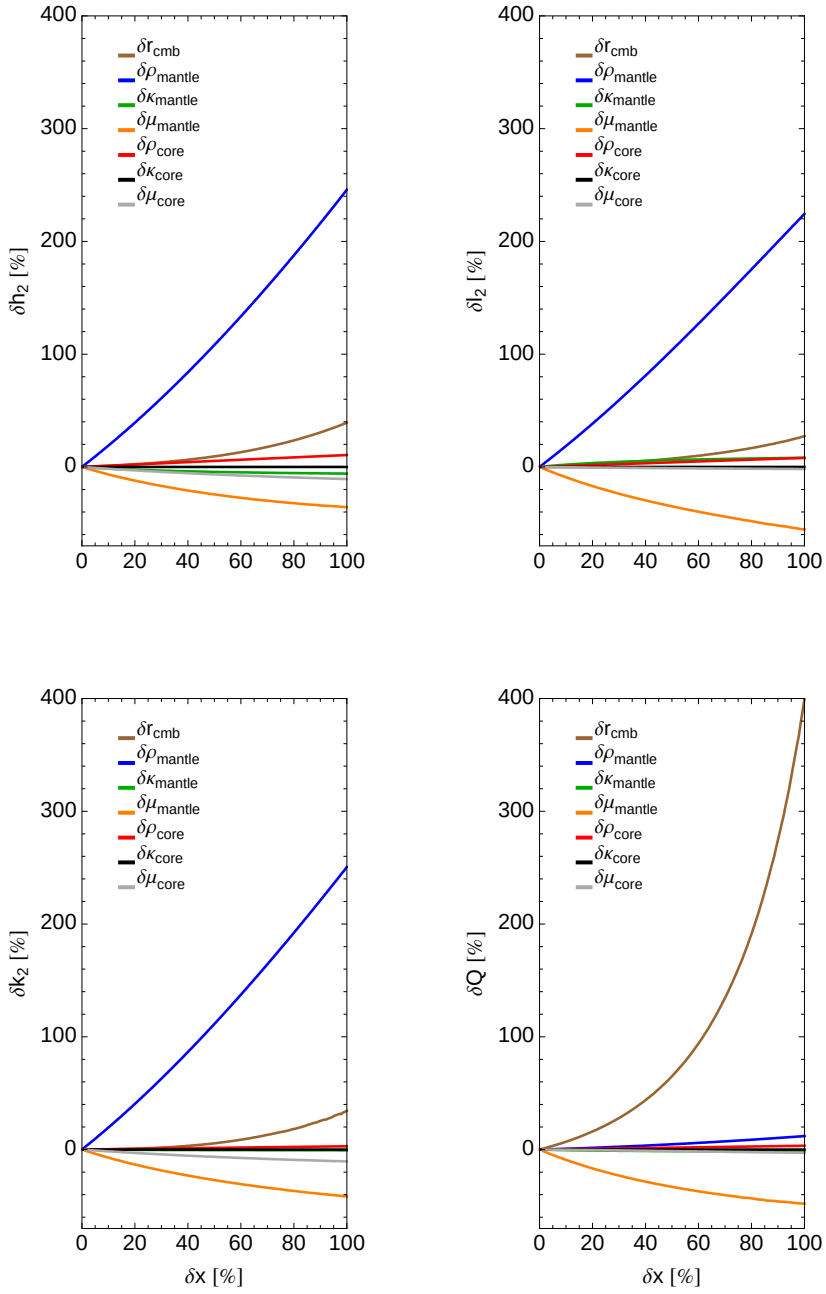


Figure 5.9: Relative change of Love numbers, h_2, l_2, k_2, and quality factor Q as a function of relative parameter change for models with a solid core. The parameters are core size, for the mantle density, bulk, and shear moduli, and for the core density and bulk modulus.

sensitivity of its variations as the core size.

Chapter 6

The interior structure of Mars

6.1 Introduction

After more than thirty years of space missions to Mars, our understanding of the planet Mars has dramatically increased, making it the best known planet of the solar system after the Earth. However, among the multiple observations, only a few give reliable constraints on the deep interior of the planet. The only data that provides reliable constraints to the interior of Mars are the mean density (from mass and radius), the moment of inertia [*Konopliv et al.*, 2006], and the tidal variations of the gravity field [*Konopliv et al.*, 2006; *Marty et al.*, 2009]. The average density of Mars is 3935kg/m^3. It is significantly lower than the average density of the Earth but very similar to that of a fully oxidized chondritic meteorite [*Anderson*, 2005]. Mars' density is, however not uniform as the moment of inertia requires a depth increasing density and the presence of a dense core.

Presently, the size, the state, and the composition of the core are only weakly constrained by the value of the moment of inertia. A stronger constraint is provided by the value of the tidal Love number k_2 [*Van Hoolst et al.*, 2003]. The most recent estimates indicate that the core of Mars is partially liquid and of substantial size [*Yoder et al.*, 2003; *Konopliv et al.*, 2006]. Further constraints on the interior structure of Mars are given by the crust density and thickness. The average thickness of the Martian crust is estimated to be 57 ± 24km if the crust average density is between $[2700, 3100]$kg/m^3 [*Neumann et al.*, 2004; *Wieczorek and Zuber*, 2004].

At the present no extensive rock samples, as for the Earth, and to a lesser extent for the Moon, are available for a direct chemical and isotopic analysis. The composition of Mars is inferred from cosmochemical considerations, meteorite analysis, and from a few meteorites that originate from Mars, the SNC meteorites [*McSween*, 1994]. The SNC meteorites are a set of igneous rocks that are not representative of Mars surface material [*Taylor et al.*, 2006] and therefore believed to be characteristic of the upper Martian mantle. Based on this hypothesis, it has been established that compared to the Earth, the mantle of Mars is richer in FeO (about 18wt% compared to 8wt%), that it has higher abundances of moderately volatile elements, and that siderophile elements that have chalcophile affinities are of lower abundances. If it is assumed that those elements are of chondritic abundance and that their depletion in the SNC's is the result of their migration into the core, then their abundance inside the core can be estimated [*McSween*,

1994]. Among the chalcophile elements, the most prominent is the light element FeS.

The recent bulk composition models are either based on chemical analysis of the SNC's, supplemented by assumptions relating the mantle composition to the bulk composition (like chondritic CI bulk Fe/Si ~ 1.7) [*Dreibus and Wänke*, 1985] or use ratios of specific isotopes found in the SNC's and match them via mass balance equations to mixtures of different chondritic material [*Lodders and Fegley*, 1997; *Sanloup et al.*, 1999; *Burbine and O'Brien*, 2004; *Mohapatra and Murty*, 2003]. In detail, the bulk mantle models are different, but the models agree more or less on a core whose mass ratio is about 20wt%, which is principally composed of iron, and whose most abundant light element is sulfur ($[10, 17]$wt%). If the core contains, such a high fraction of sulfur, its melting temperature is significantly lower [*Fei et al.*, 2000; *Stewart et al.*, 2007] than the melting temperature of pure iron [*Boehler et al.*, 1990; *Shen et al.*, 1998], suggesting that it is very unlikely that the core of Mars is solid.

Prior to the high precision determination of the moment of inertia by the Pathfinder mission to Mars, the most complete study on the interior structure of Mars is from *Sohl and Spohn* [1997]. They assumed a bulk composition of Mars based on the analysis of the SNC meteorites by *Dreibus and Wänke* [1985] and *Wänke and Dreibus* [1988]. One of their most notable findings is that, with a core sulfur composition of 14wt%, given the bulk composition model, they find that it is impossible to satisfy the moment of inertia constraint [*Esposito et al.*, 1992] and have a chondritic Fe/Si of 1.71.

Zharkov and Gudkova [2005] have used the moment of inertia and the tidal Love number k_2 estimate from *Yoder et al.* [2003] in order to constrain the interior structure of Mars. Their mantle mineralogy is based on the Dreibus and Wänke model, with the extension of a variable Fe#. They assume that the core is liquid, and made of iron, has 14wt% of sulfur, and a variable amount of hydrogen ($[0, 70]$mol%). In order for their models to agree simultaneously with the MOI and k_2 and have a Fe/Si ratio close to the chondritic value, the core size has to be in a range $[1625, 1816]$km, the Fe#in the mantle be in $[0.18, 0.22]$, and 50mol% of H is required in the core.

More recently *Khan and Connolly* [2008] have devised an interior model, relating the mantle chemical composition and its temperature profile to the geodetic observables k_2 [*Yoder et al.*, 2003] and MOI [*Sohl et al.*, 2005]. For this they assume a uniform crust parameterized by an average density and thickness, and a core parameterized by its size, average density, and by average seismic velocities. The model parameters are inferred by stochastic inversion of the geodetic observables with a strong prior assumption on the mantle temperature profile. The chemical composition parameters of the mantle are assumed to cover the range of compositions of the Earth, the Moon, and the chondritic meteorites. Their most probable model has a liquid core which is about 1680km, a sulfur concentration above 20wt%, and a core-mantle boundary temperature of about 2000K. Given there estimated very low Fe/Si ratio they conclude that Mars has a non-chondritic bulk composition.

In this work our goal is twofold, firstly construct detailed parameterized models of the interior of Mars, and secondly constrain the ranges of the parameter values such that the remaining models are within the uncertainty ranges of the most recent geodetic observations: mass, average moment of inertia, and tidal Love number k_2.

Compared to previous interior structure modeling attempts, with the exception of the recent work of *Khan and Connolly* [2008], five different mantle models are considered and

two mantle temperature profiles. The mantle temperature profiles are end-members that have been determined in studies on the thermal evolution of Mars. From the mineralogy and from the temperature profiles radial profiles, from the bottom of the crust to the core mantle boundary, of pressure, density and elastic properties are calculated. Analogously to previous studies it is assumed that the core of Mars is made of iron and of the light element sulfur. However, it is not assumed that the core sulfur concentration is known, but rather it is a free parameter of the interior model. In contrast to previous workers that have used thermoelastic properties of solid iron and solid iron-sulfide to model the liquid core, we here use the most recent laboratory data on liquid iron, liquid iron-sulfur, and their melting properties, together with a self-consistent thermodynamic description of liquid solutions to describe the fluid part of the core. Given the temperature and the pressure at the bottom of the mantle, the pressure, the temperature, the density, and the elastic properties of the core are calculated from the core mantle boundary towards the center of the planet. The presence of an inner core is determined from the melting data, the sulfur concentration inside the core, and from the pressure, and temperature conditions at the core mantle boundary. From the density and from the elastic properties of the whole planet, the mass, the moment of inertia, and the Love number k_2 are calculated.

This chapter is organized as follows. In Sect.[6.2] the five composition models of Mars are introduced and their relation to the SNC meteorites explained. Sect.[6.3] depicts the premises leading to the two mantle temperature end-members. From the chemical mantle models, for each mantle temperature profile, pressure, or depth dependent mineralogy profiles are constructed in Sect.[6.4] and their particularities in terms of density, seismic velocities, and electrical conductivity are discussed. Sect.[6.5] gives a summary of the equations and mathematical methods used to calculate the interior structure models. The resulting interior models are presented in Sect.[6.5]. A discussion and conclusions are presented in the final section.

Planetocentric constant	$G\,m_a$ [km^{3}s^{-2}]	$42828.37440 \pm 0.00028^a$
Mass	$m_a[10^{23}\text{kg}]$	6.41855 ± 0.0008^b
Equatorial radius	R_e[km]	3396.2 ± 0.1^c
Polar radius	R_p[km]	3376.2 ± 0.1^c
Volumetric mean radius	r_a[km]	3389.5 ± 0.2^c
Mean density	ρ_a[kg/m^3]	3934.97 ± 1.2
Normalized polar moment of inertia	$C/m_aR_e^2$	0.3654 ± 0.0008^a
Normalized mean moment of inertia (MOI)	$I/m_ar_a^2$	0.3655 ± 0.00096^d
Gravitational polar oblateness	$J_2 = -C_{20}$	$1.956607\,10^{-3}$

Table 6.1: Physical parameters of Mars. a: *Konopliv et al.* [2006], b: with $G = (6.67259 \pm 0.00085)\,10^{-11}\text{m}^3\text{s}^{-2}\text{kg}^{-1}$, c: *Seidelmann et al.* [2002], d: $I/m_ar_a^2 = C/M_ar_a^2 - \frac{2}{3}J_2$

6.2 Chemical composition

The meteorites formed together with our solar system, and their composition provides fundamental information for deducing the composition of planetary bodies. Among the

meteorites, carbonaceous chondrites appear to be the most primitive extra-planetary objects available to us. They are almost surely very close in composition, chemical and isotopic, to the fundamental building blocks of planetary bodies. Since planets formed under different temperature and pressure conditions, experienced losses of low-molecular-weight material, and acquired primitive material from different feeding zones inside the solar nebula, they have different compositions than primitive meteorites, however less altered ratios of refractory elements [1] provide useful constraints. Beside refractory elements fractions, oxygen isotope distribution inside primitive material together with in-situ rock samples provide key insight in deciphering the composition of planetary compositions as oxygen is the most abundant material in planetary bodies and meteorites.

For the planet Mars, most models for the chemical composition are deduced by either chemical or isotopic analysis of rock samples originating from Mars together with insight gained from carbonaceous chondrites. Here, prior to introducing Mars chemical composition models, we give a short introduction to notions related to meteorites.

6.2.1 Meteorites, chondrites, and SNC meteorites

There are three main types of meteorites: the iron meteorites, the stony-iron meteorites, and the stony meteorites. The metallic iron-meteorites are mainly made of iron and nickel. The stony meteorites are composed mostly of silicate minerals (stone-like), and of a significant part of iron-nickel alloy together with some iron sulfide. Meteorites are either virtually unaltered, dating back to the beginning of the solar system, or remains of differentiated bodies, such as the Moon or Mars. Finally, stony-iron meteorites are composed of nearly equal weight fractions of iron-nickel and silicate mineral.

Chondrites are a subclass of stony meteorites that formed nearly simultaneously with the Sun. They are almost undifferentiated, primordial matter that was nearly unaltered for the last 4.5 billion years. Chondrites may contain small glassy spheres that condensed out of the primordial solar nebula. Those chondrules are mainly made of olivine and pyroxene. The chemical composition of chondrites is very similar to the Sun without the most volatile elements like hydrogen and helium. However, the distribution of elements in the original solar nebula was not uniform, and the formation conditions of the chondritic parent bodies varied. The parent bodies were further subjected to different thermal and chemical processes as well as to impacts with other asteroids resulting in a variety of chondrites.

Among the different groups of chondrites, the meteorites that are of particular interest as precursor material for Mars are

- The oxidized carbonaceous chondrites, of type Ivuna (CI or C1) devoid of chondrules and of type Mighei (CM). They contain high abundances of volatile components such as water and contain heavier elements in nearly solar proportions. Indicating that they have not been altered by strong heating and compression (not been buried inside more massive objects like planets)

- Vigarano type (CV)

[1] Refractory elements vaporize at high temperatures. Refractory metals have melting temperatures about the melting temperature of iron.

- The less oxidized ordinary chondrites (H,L,LL)[2]
- The highly reduced enstatite chondrites (E)

The chondrites are not only different in there oxidation state, but they also differ in there isotopic signature, and their contents in volatile and refractory elements.

SNC [3] meteorites are achondrites[4] of igneous[5] origin [*McSween*, 2003]. They are thought to originate from the planet Mars, since they contain trapped rare-gas and nitrogen different from those inside meteorites but closely matching the Martian atmosphere. The SNC meteorites are different from other meteorites, lunar samples, and terrestrial rocks according to their oxygen isotope ratios.

6.2.2 Mars bulk models

Basically, the proposed models for the bulk composition of Mars can be separated in two groups that are both related to the SNC meteorites. In the first group are those models that are based on the assumptions that the SNC meteorites are chemically representative for the Martian mantle. Within the models of the second group, the chemical composition of Mars is deduced under the assumption that Mars accreted from an unknown mixture of chondritic material. The amount of each chondritic precursor material is then constrained from the premise that specific isotope fractions of the resulting model should match those of the SNC's.

Dreibus and Wänke [1985] and *Wänke and Dreibus* [1988] estimated the composition of Mars by assuming that refractory elements are present in CI-chondritic abundances and that volatile element abundances are provided by SNC meteorites. We will here refer to this model as the DW-model. *Dreibus and Wänke* [1985] and *Wänke and Dreibus* [1988] found that the martian mantle contains about 18wt% of FeO compared to the 8wt% of Earth's upper mantle [*McDonough and Sun*, 1995] and associated the depletion of the chalcophile element sulfur, compared to the SNC's, to its incorporation inside the core. They estimated the core sulfur weight fraction to about 14.2wt%.

Within the second group, the bulk composition of Mars is deduced by comparing oxygen isotopes in SNC meteorites with those of different fractions of chondritic precursor material. Following this approach *Sanloup et al.* [1999] derived a bulk composition model based on a mixture of H ordinary and EH enstatite chondrites. We will refer to this model as the EH45- model. Based on the same approach *Lodders and Fegley* [1997] found that they can match the oxygen isotopes with an assemblage of H, CV, and CI meteoritic material. With the estimated mantle composition, they estimate the abundances of siderophile and chalcophile elements is calculated from metal-sulfide/silicate partition coefficients. We will refer to this model as the LF97-model.

[2]The acronyms are related to the iron abundance of the meteorite. HL: high iron, low metal; LL: low iron, low metal; L: low iron or hypersthene(belonging to the group of orthorhombic pyroxenes)-olivine

[3]Shergottites get their name from the Indian village of Shergotty (Shergahti) in Bihar state, where a dark boulder fell from space on the morning of August 25, 1865. They consist mostly of olivine, the pyroxene mineral pigeonite, and plagioclase feldspar. The first found nakhalite is a piece of a meteorite that fell near El-Nakhla, in northern Egypt, in 1911. The nakhalites are clinopyroxenites. Finally the Chassigny meteorite, a dunite, has been discovered in 1815 in the village of Chassigny in France.

[4]Achondrites are stony meteorites that consists of material similar to terrestrial basalts.

[5]Igneous rocks are formed by solidification of cooled magma.

wt%	LF97	DW84	MM03	MA79	EH45	EH70	Pyrolite
CaO	2.35	2.4	1.9	2.69	2.00	2.00	3.5
FeO	17.22	17.9	16.9	15.85	17.7	11.4	8.36
MgO	29.71	30.1	29.1	32.68	27.30	27.30	37.97
Al_2O_3	2.89	2.9	2.5	6.39	2.50	2.5	4.31
SiO_2	45.39	44.4	47.1	41.6	47.50	51.00	44.5
Mg#	76	75	76	77	72	80	88

Table 6.2: Bulk mantle composition in major oxides. LF97 *Lodders and Fegley* [1997], DW84 *Dreibus and Wänke* [1985], MM03 *Mohapatra and Murty* [2003], MA79 *Morgan and Anders* [1979], EH45 and EH70 *Sanloup et al.* [1999]

vol%	LF97	DW84	MM03	MA79	EH45	EH70	Pyrolite
olivine	42.53	58.7	33.40	60.	25.5	4.1	62.5
orthopyroxene	42.87	20.6	54.53	4.1	61.2	81.4	8.2
clinopryroxene	3.09	11.4	2.13	24.9	3.1	2.1	16.3
garnet-majorite	11.51	9.3	9.94	10.9	10.2	12.4	13.

Table 6.3: Low pressure mantle mineral volume fractions.

Mohapatra and Murty [2003] (model MM03) use oxygen isotope ratios together with nitrogen isotope ratios to infer the composition of Mars. They conclude that both isotope ratios can be matched if Mars accreted from a mixture of enstatite and ordinary chondrites. Their model results in a mantle with only 6wt% FeO. In order to increase the low FeO fraction in the mantle they postulate that about 8wt% of silicon has migrated inside the core.

For comparison we also consider a second model of *Sanloup et al.* [1999] (EH70) obtained from similar assumptions as model EH45, the pyrolite model for the mantle of the Earth, and a mantle mineralogy model that has been established prior to associating the SNC meteorites to Mars. The model of *Morgan and Anders* [1979] is based on the cosmochemical model of *Ganapathy and Anders* [1974] and uses supplementary petrological and geophysical constraints. We will refer to this model as the MA-model.

The mantle mineral composition of the above models in terms of principal low pressure minerals is given in Tab.[6.3]. Note that with the exception of the pyrolite model, the Mars mantle model's main oxide weight fractions differ only by a few wt%. By neglecting the weight fraction of Al_2O_3 and with the chemical formulas for low pressure minerals (see Tab.[3.1]), the fractions of each mineral can be calculated. The results are shown in Tab.[6.3].

All the above Mars bulk models provide beside the composition of the mantle also a composition for the core. The proposed core compositions are mainly made of iron, with a chondritic fraction of nickel (about 8wt%), and of the principal light element sulfur. The proposed sulfur weight fractions are between about $10 - 17$wt%. Here, we neglect the contribution of nickel inside the core, firstly because its thermoelastic properties are very similar to those of iron and secondly because there is nearly do data available on

$Fe - Ni$ rich liquid solution relevant to the core conditions of Mars. Further, we only consider sulfur as a light element together with iron inside the core, see Sect.[4.2] for a discussion.

To summarize, in the subsequent interior modeling of Mars we will use the mantle models DW84, LF97, EH45, and MM03, with a core made of iron with a variable amount of sulfur.

6.3 Thermal state

We consider two different temperature profiles for the mantle of Mars, a hot $T_h(r)$ and a cold $T_c(r)$ profile, see Fig.[6.1]. They are plausible end members suggested by present-day results of models designed for Mars' thermal evolution [*Breuer and Spohn*, 2003].

The premises for constructing the thermal profiles were an early episode of geomagnetic activity (during the first 500 million years) and a crust growth history in agreement with a present day average crustal thickness of $50 - 120$km. *Breuer and Spohn* [2003] studied both early epoch plate tectonics followed by single-plate tectonics with stagnant lid convection and single plate stagnant lid cooling through the whole history of Mars. One of their conclusions is that an early episode of plate tectonics is difficult to reconcile a plausible history of crust formation and an early magnetic field.

Following their conclusions we here use temperature profiles resulting from thermal evolution modeling based on single plate stagnant lid cooling. The hot and cold temperature profiles can be considered upper and lower bounds of their calculation results.

The cold temperature profile is characterized by a thermal gradient of 2.7K/km in the first 450km (conductive lid). Between 450km and 550km depth, this gradient is decreased to 2.3K/km corresponding to the boundary between the conductive stagnant lid and the thermal boundary layer. At greater depth, the temperature increases adiabatically (0.12K/km) down to the core-mantle boundary. Compared to the cold profile the hot profile has a steeper thermal gradient in the upper part of the mantle. This profile has been obtained with a thermal conductivity of $2\mathrm{Wm}^{-1}\mathrm{K}^{-1}$ in the crustal basaltic layer, whereas the for the cold profile $4\mathrm{Wm}^{-1}\mathrm{K}^{-1}$ have been used. The resulting conductive lid is about 150km thinner than in T_c. The temperature increases in three steps with three distinct gradients: 6.4K/km and 3.4K/km in the crust and the conductive mantle, and by 0.12K/km in the adiabatic part of the mantle. Both temperatures incorporate also a small conductive boundary at the bottom of the mantle. Note that using the results of *Takahashi* [1990] on the liquidus and solidus of anhydrous peridotite [6] the cold temperature profile never crosses the solidus and that the hot temperature profile would allow for a small fraction of partial melt at the bottom of the lithosphere. This small fraction of melt will however be neglected here since the mount is too small to significantly alter the deformational properties of the mantle.

Both temperature profiles have been established for a specific interior structure (e.g. core size), but we will use them for all the interior structure models. In practice, the temperature profiles are adapted to a given mantle depth by shortening or lengthening their adiabatic part and leaving the other parts unchanged.

[6] Peridotite is the dominant rock of the upper part of the Earth's mantle, consisting mostly of the minerals olivine and pyroxene.

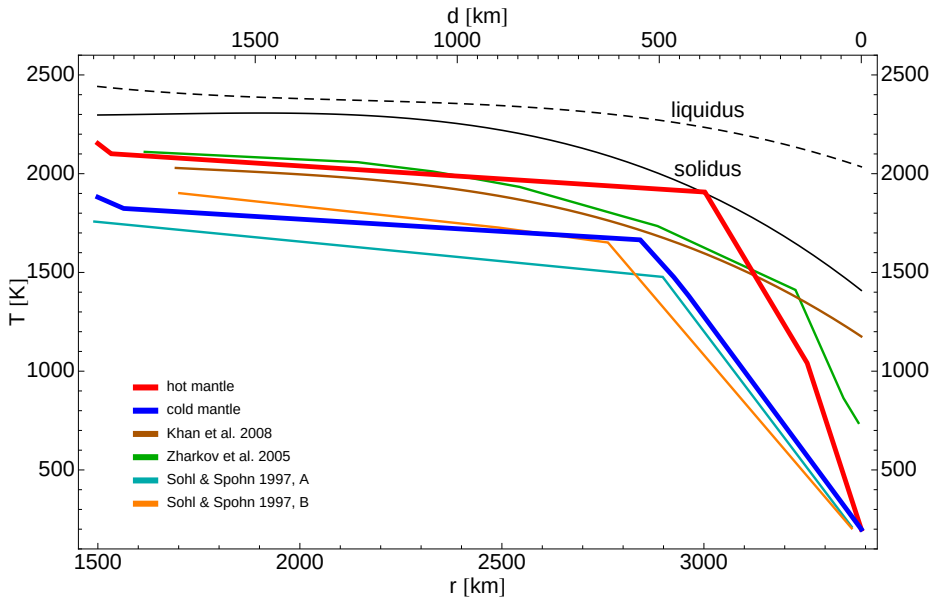


Figure 6.1: Mars mantle temperature profiles. Mantle modeling end-members, T_h (hot, red curve) and T_c (cold, blue curve) from *Schumacher and Breuer* [personal communication]. The solidus and liquidus are from *Takahashi* [1990]. The other temperature profiles are from *Sohl and Spohn* [1997], *Zharkov and Gudkova* [2005], and *Khan and Connolly* [2008] (most probable estimate).

Fig.[6.1] also shows mantle temperature profiles of other workers. The temperature profiles of *Sohl and Spohn* [1997] and *Zharkov and Gudkova* [2005] have been obtained by assuming a specific distribution of heat-producing radioactive elements inside the mantle and by assuming either a core-mantle heat flow or a surface heat flow. In contrast to those profiles the temperature profile of *Khan and Connolly* [2008] is the most probable temperature profile estimated by inferring the probability distribution of the mantle temperature and mantle composition, in terms of principal oxides, from the measured moment of inertia, mass, and tidal Love number k_2. Interestingly, the inferred temperature distribution inside the Martian mantle of *Khan and Connolly* [2008] is nearly indistinguishable from their assumed prior temperature distribution and the temperature distribution close to the surface allows for temperature larger than 1000K. Note that the temperature profiles of *Zharkov and Gudkova* [2005] and *Khan and Connolly* [2008] are very similar. With the exception of the upper part of the mantle associated to the lithosphere where the temperature profile of *Khan and Connolly* [2008] does not exhibit the characteristic discontinuous change in slope, associated to the transition from convective to conductive heat transport.

With the exception of the temperature profile associated with model A of *Sohl and Spohn* [1997], which is slightly cooler in the lower part of the mantle than the cold end-member (about 100K), the other temperature profiles are approximatively warmer than the cold end-member and colder than the hot end-member. The temperature profile of model B of *Sohl and Spohn* [1997] is very similar to the cold end-member and the other two temperature profiles, *Zharkov and Gudkova* [2005] and *Khan and Connolly* [2008], have about the same temperature in the lower mantle than the hot end-member.

6.4 The mineralogy of the mantle

Given the mantle mineralogy models introduced in Sect.[6.2] and the two end-member temperature profiles (see Sect.[6.3]) the mineral composition for the mantle of Mars can be calculated as function of pressure or depth from the fractions of low pressure mineral phases and their Fe#(see Tab.[6.3]) [*Verhoeven et al.*, 2005]. Phase transitions of the low pressure mineral phases olivine, pyroxene, and garnet are included using laboratory determined phase diagrams. The depth dependent mineral and phase fractions resulting from the two temperature end-members are shown in Figs. [6.2, 6.3, 6.4, 6.5, 6.6, 6.7, and 6.8]. For all models a core size of 1300km is taken, the crust density is 2900kg/m^3, and the crust thickness is 100km. The depth dependent pressure profiles and density profiles have been obtained by integrating differential equations (2.1) and (2.2) from the surface to the core mantle boundary (see Chapt.[2]). For all models, the pressure profile is almost linear with pressure gradient of about (0.0122 ± 0.00006)GPa/km.

The results show that an increasing in the mantle temperature has two main effects on mineralogy profile. Firstly the phase transition from low pressure clinopyroxene to orthopyroxene migrates to higher depths or higher pressures with increasing temperature. Secondly at the low temperature end-member olivine can change first to ringwoodite before changing to wadsleyite with depth in contrast to the hot end-member and the Earth where the transition is olivine-wadsleyite-ringwoodite (Figs. [6.2, 6.3, 6.5, 6.6, 6.7]). For all Mars mantle models, the phase transition olivine-wadsleyite-ringwoodite occurs over a depth range of about 70km starting at a depth of about 1000km ($\sim$ 12GPa). In the pyrolite model these phase transitions occur at higher pressures and larger depths since the model has a lower Fe#and this transition migrates to higher pressures with decreasing Fe#(see Sect.[6.4]). For all models, the transformation of all pyroxenes to majorite is completed at a depth of approximatively 1390km ($\sim$ 17GPa). At pressures of about 23GPa for hot mantle models and about 22GPa for cold models, ringwoodite transforms to perovskite and magnesio-wüstite. The phase transition majorite-perovskite occurs at similar pressures.

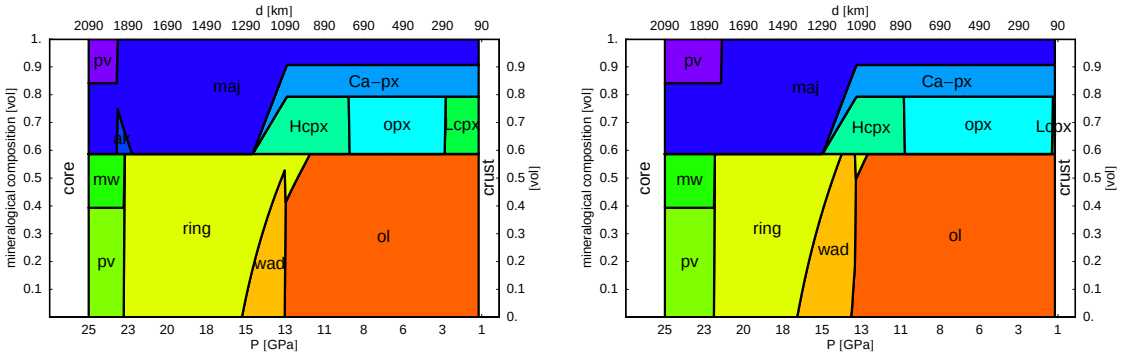


Figure 6.2: DW mineral composition as a function of radius in vol% for the hot (right) and cold (left) mantle. The letters ol, wad, ring, opx, Lcpx, Hcpx, Ca-px, maj, mw, and pv represent olivine, wadselyite, ringwoodite, orthopyroxene, low-pressure clinopyroxene, high-pressure clinopyroxene, Ca-pyroxene, majorite, Mg-wüstite, and perovskite.

Figs. [6.9] show the density profiles corresponding to the mantle mineralogy models as

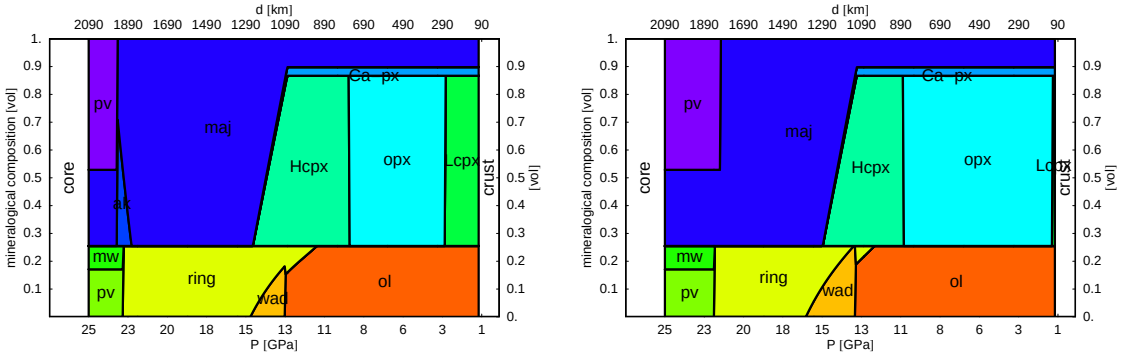


Figure 6.3: EH45 mineral composition as a function of radius in vol% for the hot (right) and cold (left) mantle. The letters ol, wad, ring, opx, Lcpx, Hcpx, Ca-px, maj, mw, and pv represent olivine, wadselyite, ringwoodite, orthopyroxene, low-pressure clinopyroxene, high-pressure clinopyroxene, Ca-pyroxene, majorite, Mg-wüstite, and perovskite.

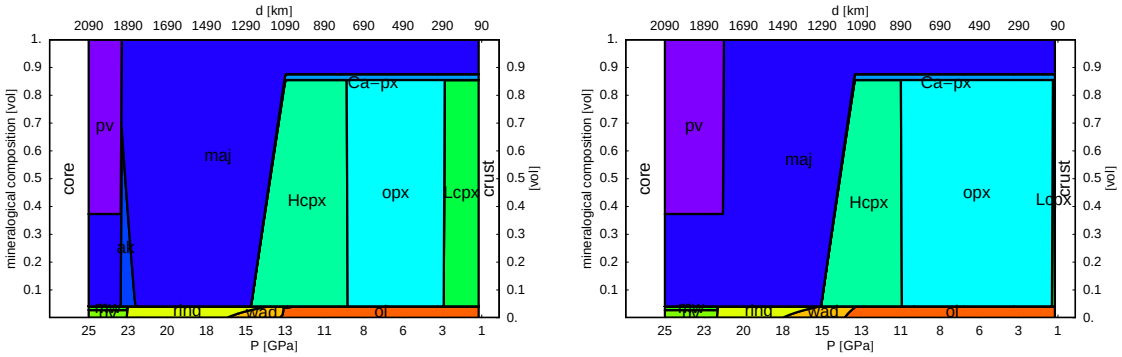


Figure 6.4: EH70 mineral composition as a function of radius in vol% for the hot (right) and cold (left) mantle. The letters ol, wad, ring, opx, Lcpx, Hcpx, Ca-px, maj, mw, and pv represent olivine, wadselyite, ringwoodite, orthopyroxene, low-pressure clinopyroxene, high-pressure clinopyroxene, Ca-pyroxene, majorite, Mg-wüstite, and perovskite.

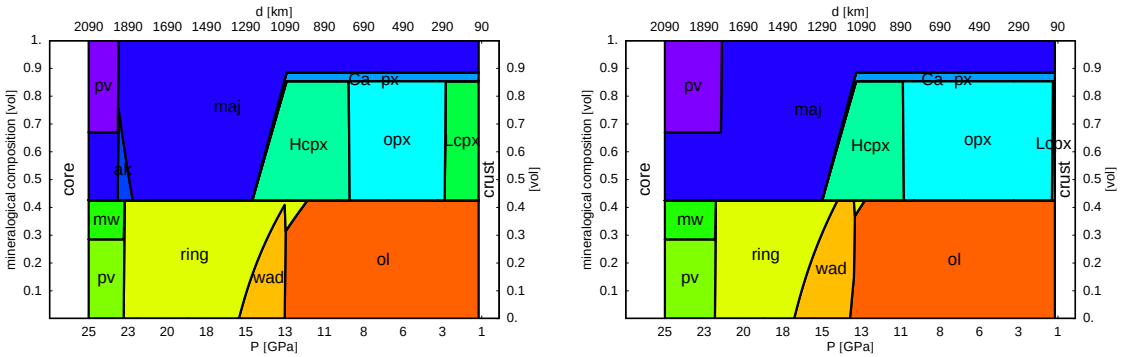


Figure 6.5: LF97 mineral composition as a function of radius in vol% for the hot (right) and cold (left) mantle. The letters ol, wad, ring, opx, Lcpx, Hcpx, Ca-px, maj, mw, and pv represent olivine, wadselyite, ringwoodite, orthopyroxene, low-pressure clinopyroxene, high-pressure clinopyroxene, Ca-pyroxene, majorite, Mg-wüstite, and perovskite.

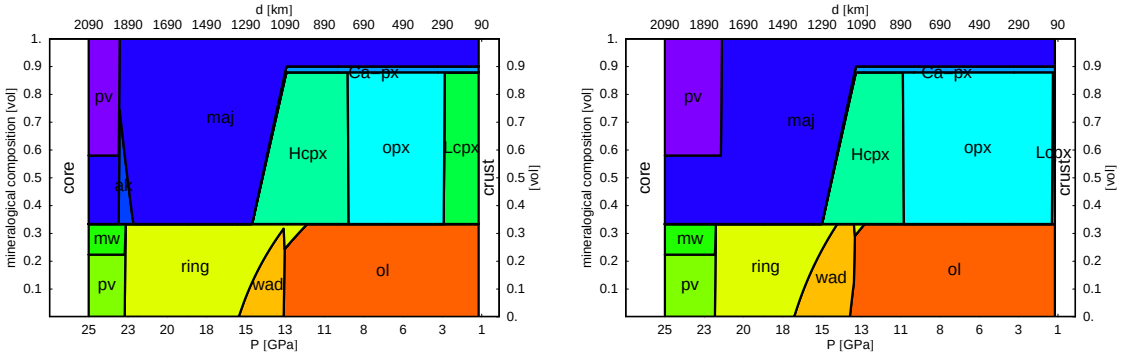


Figure 6.6: MM03 mineral composition as a function of radius in vol% for the hot (right) and cold (left) mantle. The letters ol, wad, ring, opx, Lcpx, Hcpx, Ca-px, maj, mw, and pv represent olivine, wadselyite, ringwoodite, orthopyroxene, low-pressure clinopyroxene, high-pressure clinopyroxene, Ca-pyroxene, majorite, Mg-wüstite, and perovskite.

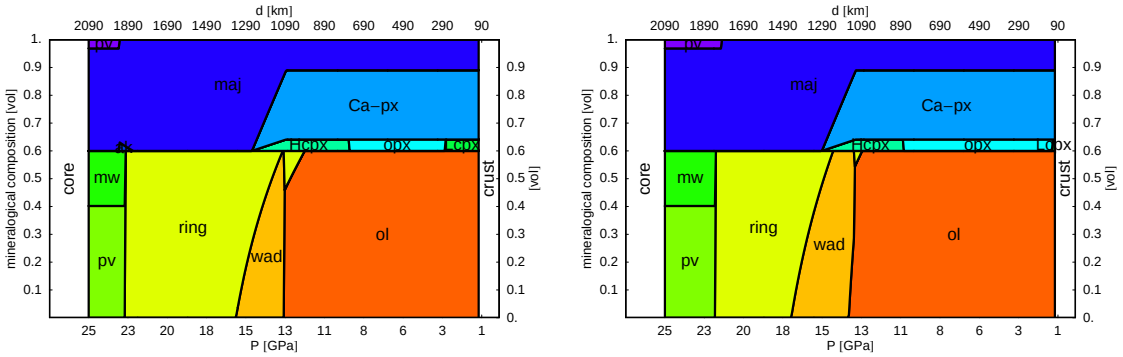


Figure 6.7: MA79 mineral composition as a function of radius in vol% for the hot (right) and cold (left) mantle. The letters ol, wad, ring, opx, Lcpx, Hcpx, Ca-px, maj, mw, and pv represent olivine, wadselyite, ringwoodite, orthopyroxene, low-pressure clinopyroxene, high-pressure clinopyroxene, Ca-pyroxene, majorite, Mg-wüstite, and perovskite.

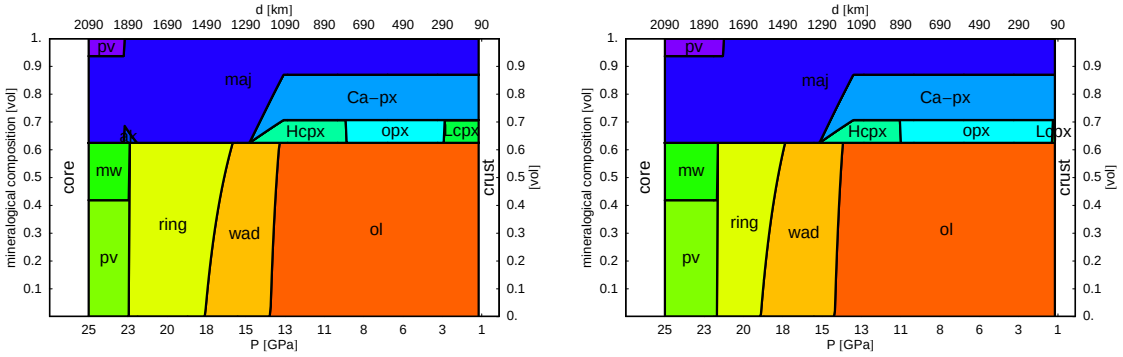


Figure 6.8: PY mineral composition as a function of radius in vol% for the hot (right) and cold (left) mantle. The letters ol, wad, ring, opx, Lcpx, Hcpx, Ca-px, maj, mw, and pv represent olivine, wadselyite, ringwoodite, orthopyroxene, low-pressure clinopyroxene, high-pressure clinopyroxene, Ca-pyroxene, majorite, Mg-wüstite, and perovskite.

a function of depth for the cold and hot temperature end-member for a core of 1600km[7]. In all the curves, the locations of discontinuous changes in the slopes can be identified with the occurrence of the phase transitions. The five models MA79, DW84, LF97 and EH45 which have approximatively the same Fe#have very similar density profiles. Differences in mantle densities result in different mantle mass, moment of inertia, and mantle $m_{\mathrm{Fe}}/m_{\mathrm{Si}}$ ratio (see Tab.[6.4]). The cold, less dense models have a mantle mass and moment of inertia that is about 1.4% larger than for their hotter counter parts. The DW mantle, which has the largest Fe#, has the highest mass and the E70 mantle, which has the lowest Fe#, has the lowest mass. The relative difference in mass is below 3%.

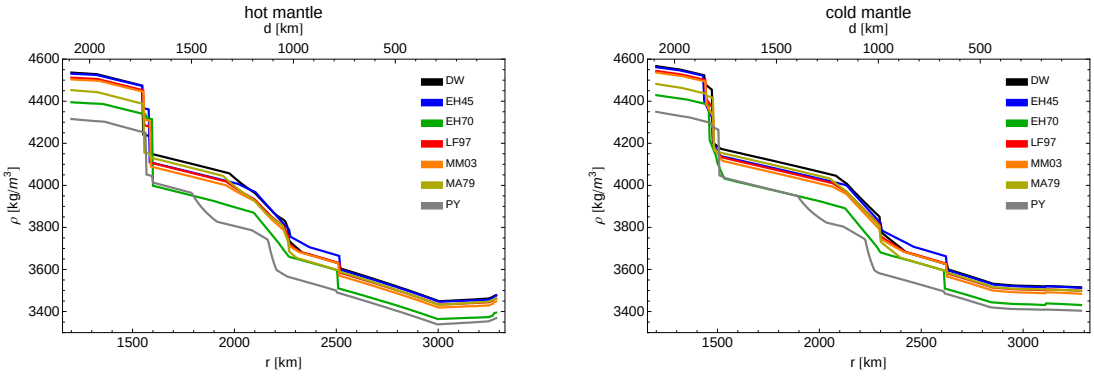


Figure 6.9: Mantle density as a function of radius for the hot (right) and cold (left) mantle temperature profiles and the DW84, EHxx, LF97, MM03, MA79, and PY mineralogy.

The mantle p-wave and s-wave velocity profiles are given in Fig.[6.10] and Fig.[6.11]. The MA79 model has significantly lower seismic velocity in the upper mantle than all the other models because of the comparatively high abundance of slow Ca-pyroxene compared to the faster orthopyroxene, LC-pyroxene, and HC-pyroxene in the upper part of the mantle of this model, see Fig.[6.7] and Tab.[3.2].

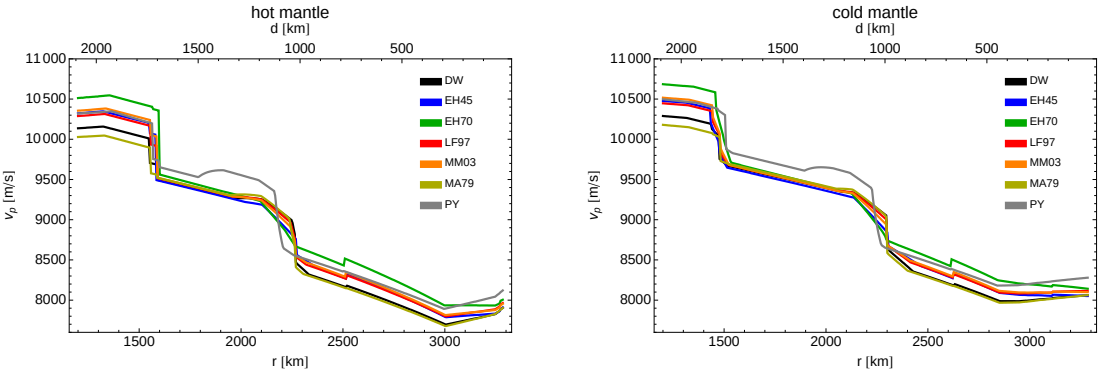


Figure 6.10: Mantle v_p as a function of radius for the hot (right) and cold (left) mantle temperature profiles and the DW84, EHxx, LF97, MM03, MA79, and PY mineralogies.

[7]About the radius of the core that agrees best with MOI and k_2, see Sect.[6.5].

	P_{cmb}	m_m/m_a	$m_{\mathrm{Fe}}/m_{\mathrm{Si}}$	I_m/I_a
LF97 T_1	21.92	0.744	0.63	0.828
LF97 T_2	21.77	0.755	0.63	0.840
DW84 T_1	21.91	0.749	0.72	0.833
DW84 T_2	21.75	0.759	0.72	0.844
MMO3 T_1	21.96	0.741	0.60	0.825
MMO3 T_2	21.80	0.751	0.60	0.837
MA79 T_1	21.95	0.744	0.64	0.828
MA79 T_2	21.79	0.754	0.64	0.840
EH45 T_1	21.88	0.748	0.66	0.832
EH45 T_2	21.71	0.758	0.66	0.845
EH70 T_1	22.03	0.729	0.40	0.814
EH70 T_2	21.88	0.739	0.40	0.824
PY T_1	22.07	0.721	0.35	0.803
PT T_2	21.96	0.730	0.35	0.814

Table 6.4: Pressure at the core mantle boundary, relative mantle mass m_m/m_a and moment of inertia I_m/I_a, and bulk Fe/Si ratio for an iron core with 14.2wt% of sulfur for the hot (T_1) and cold (T_2) temperature profile.

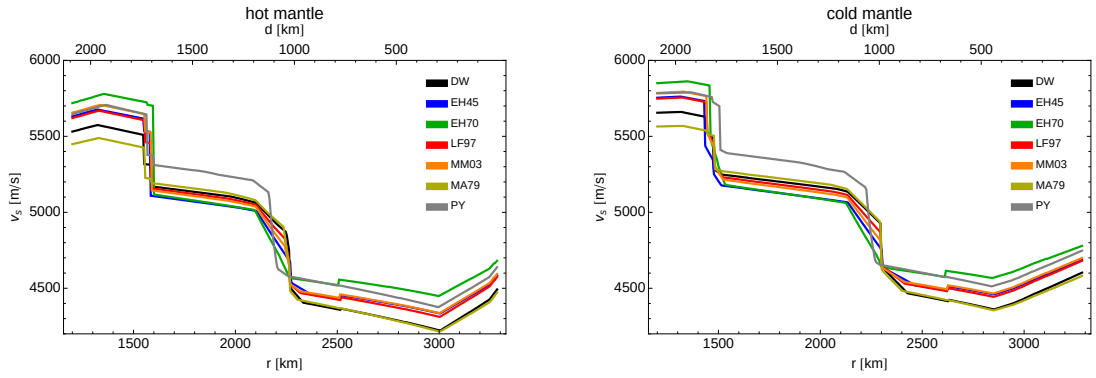


Figure 6.11: Mantle v_s as a function of radius for the hot (right) and cold (left) mantle temperature profiles and the DW84, EHxx, LF97, MM03, MA79, and PY mineralogies.

Finally, the electrical conductivity of the mantle and the associated real and imaginary part of the surface impedances are shown in Figs. [6.12, 6.13, and 6.14]. The low Fe#models have the lowest electrical conductivity and consequently the highest real part surface impedance.

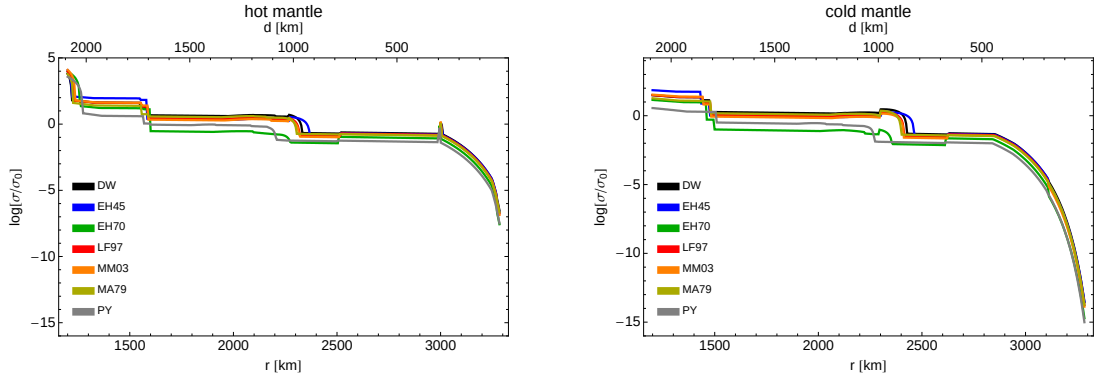


Figure 6.12: Logarithm of mantle electrical conductivity (σ) as a function of radius for the hot (right) and cold (left) mantle temperature profiles and the DW84, EHxx, LF97, MM03, MA79, and PY mineralogies. $\sigma_0 = 1$Sm

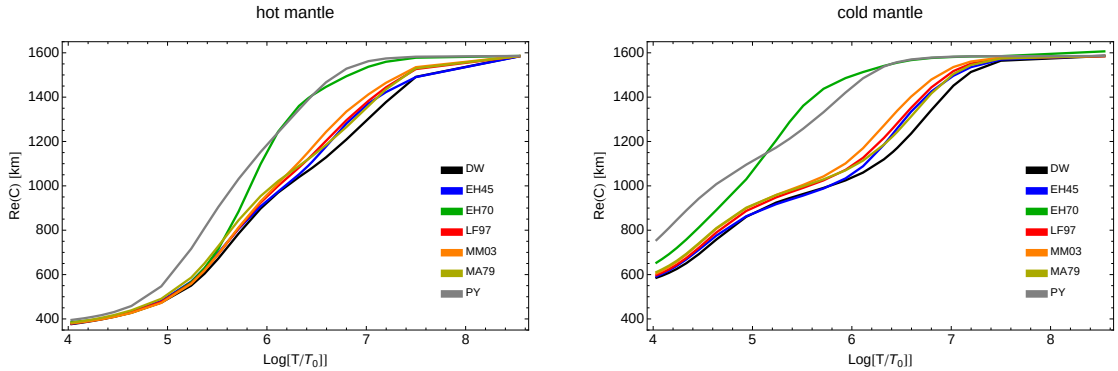


Figure 6.13: Real part of C-function of the mantle as a function of the logarithm of the period for the hot (right) and cold (left) mantle temperature profiles and the DW84, EHxx, LF97, MM03, MA79, and PY mineralogies. $T_0 = 1$s

The locations of the different temperature regimes are clearly visible in the profiles of the different models. The conductive temperature profile in the upper mantle leads to a stagnation or even a decrease in density (Fig.[6.9]) and seismic velocities with depth (Fig.[6.11]). The electrical conductivity on the other hand, increases by several orders in magnitude (Fig.[6.12]) in that region. In the convective part of the mantle, where adiabatic conditions prevail, the density and acoustic wave velocity increase monotonically between the jumps of the phase transitions. The phase transitions between radius coordinates 2000 and 2250km, corresponding to the phase transition of olivine to wadsleyite to ringwoodite lead to a significant increase in σ, v_p, and v_s. The locations of the jumps resulting from the phase transitions are determined by the intersection of the thermal

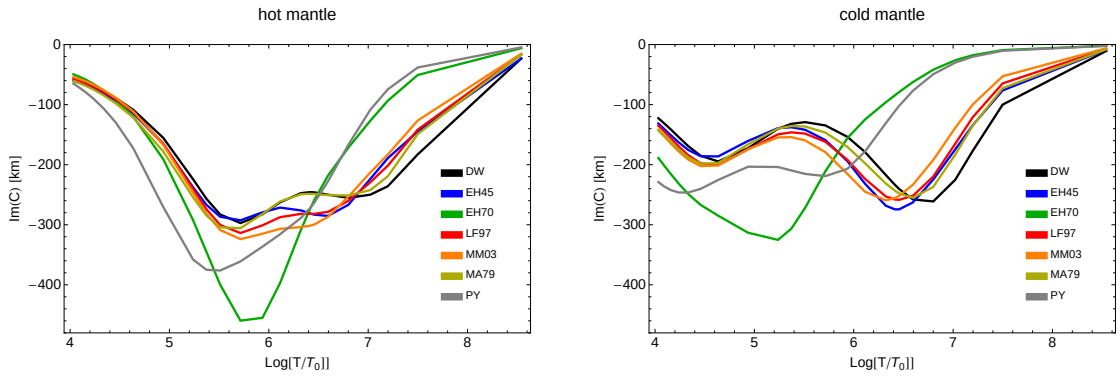


Figure 6.14: Imaginary part of C-function of the mantle as a function of the logarithm of the period for the hot (right) and cold (left) mantle temperature profiles and the DW84, EHxx, LF97, MM03, MA79, and PY mineralogies. $T_0 = 1$s

profile with the various phase boundaries in a temperature pressure phase diagram. The magnitude of the jumps at the phase transition depends on the abundance of the phase undergoing the phase transition. Moreover, since phase diagrams as well as the thermoelastic properties of the minerals and phases depend on Fe#, the depth (c.f. Fig.[3.2]) and the amplitude of the jumps vary accordingly.

The real and imaginary part of the time dependent C-response functions resulting from the electrical conductivity profiles are shown in Figs. [6.13] and [6.14]. The modulus of the $C-$response functions is related to the penetration depth of the frequency dependent magnetic field (c.f. Sect.[3.6]). The cold models with the lower conductivity profiles have lower Re(C) values at high magnetic wave frequencies. The difference is however, decreasing with increasing period. Note also that the low Fe#number low conducting EH70 and PY model exhibit the highest Re(C) values. Starting from a period of about 10^7s (183days) the slope of the real part of the C-functions of all models decreases strongly and remains nearly constant up to the highest periods. The corresponding modulus of the C-function is about 1700km, close to the depth of the core mantle boundary. As a consequence, the flattening of Re(C) at periods above 10^7s is a signature of the very high conducting core ($\sigma_{\text{core}} = 10^6$Sm). A sounding period of a Martian year would allow thoroughly sounding of the mantle down to the core.

6.5 Models for the interior structure of Mars

We now calculate models of the whole interior of Mars, from the center to the surface. For a given mantle temperature and mantle mineralogy, each model of the interior depends on three parameters: the density of the crust, the thickness of the crust, and the size of the core. The a priori range for the core size is between $[1200 - 2300]$km and the step size is 1km. The crust thickness is in the range $[20 - 100]$km with a step size of 5km and the crust density in the range $[2900, 3200]$kg/m^3 with a step size of 25kg/m^3. For each set of values of core size, crust thickness, and density, and for each mantle mineral model and mantle temperature the structure differential equations (see Chapt.[2]) are solved under the constraints of surface pressure and gravity. Of all the resulting models only those are

retained that agree with the moment of inertia value (MOI), see Tab.[6.1]. Note that by MOI we here mean the whole range of values within a 2σ interval. The bounds for the core size range are chosen such that the smallest possible pure iron solid core and the largest possible fluid core, given the constraints of global mass and moment of inertia, are included.

In the following figures no distinction is made between the mineralogies of the different models. For each mantle temperature profile a surface is drawn whose boundary is determined by those models that fit the global mass and MOI constraints. The considered mantle models are DW84, LF97, MA79, SJ99.EH45, and MM03.

We first discuss the constraints on the interior parameters, core size and crust thickness and density, by only using the mass and the moment of inertia of Mars. Fig.[6.15] shows that the core radius r_{cmb} increases with increasing core sulfur content. Since the core density decreases with increasing sulfur content the core size must increase to conserve the mass of Mars. For an analogous reason, hot models have a larger core than cold models for a given sulfur concentration in the core: since a temperature increase leads to a less dense interior, the most dense part of the interior, the core, needs to be larger to conserve the total mass. For the mass and moment of inertia constraints, the core sizes is between about 1250km and 2009km (see Tab.[6.5]), or 1666 ± 419km. Models with the smallest cores are made of pure solid iron, and the models with the largest possible cores are liquid and have about 23wt% of sulfur in the core (see Tab.[6.5]), or 11.5 ± 11.5wt%. Note that the MM03 models can only have a solid pure iron core if the temperature in the mantle is below the the temperature of the hot end-member.

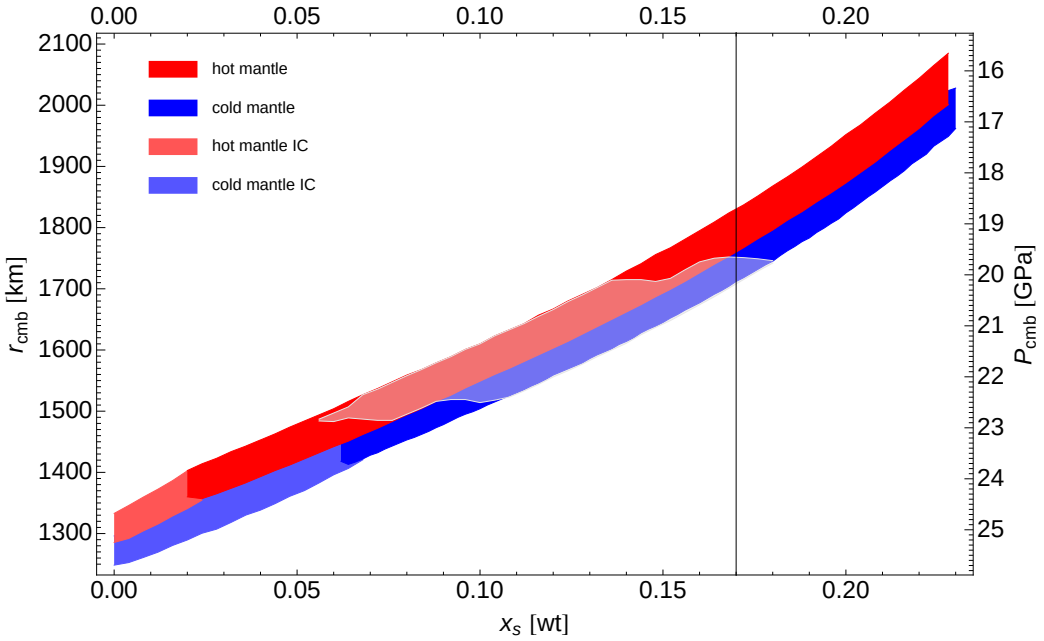


Figure 6.15: Core size as a function of core sulfur concentration. The blue shaded area corresponds to the cold mantle models and the red shaded area to the hot mantle models. The lighter blue and red areas correspond to models with inner cores.

For both hot and cold temperature profiles, a solid inner core is possible (Fig.[6.15]) but requires a low core sulfur content. As Fig.[6.16] shows, for the hot mantle tempera-

ture the core bulk sulfur concentration has to be below 2.5wt% and for the cold mantle temperature below 7wt%.

For all mantle models, and for both temperature profiles, the inner core results from iron solidifying at the upper part of the core and snowing towards the center, see Sect.[4.5]. In this scenario, the sulfur concentration of the outer core of models with an inner core has an outer core sulfur concentration such that the melting temperature is equal to the temperature at the core mantle boundary. The ranges of pressure and temperatures at the CMB are shown in Fig.[6.20]. For the cold mantle models the core sulfur fraction is just below 7wt%, for the hot mantle models it is below 2.5wt% (Fig.[6.16]). For hot and cold mantle models, the core sulfur concentrations decreases with increasing inner core size. In order to conserve the global mass, and since the inner core is denser than the outer core, the core sulfur concentration has to decrease with increasing inner core size. With decreasing core size, the pressure at the CMB increases, and more sulfur is needed for the outer core to melt. However, as the pressure variations at the CMB are small (< 3GPa), and since the temperature at the CMB depends only weakly on pressure (about 1.3K/GPa), the outer core sulfur fraction variation is less than 0.2wt% for the cold mantle models and even smaller for the hot mantle models.

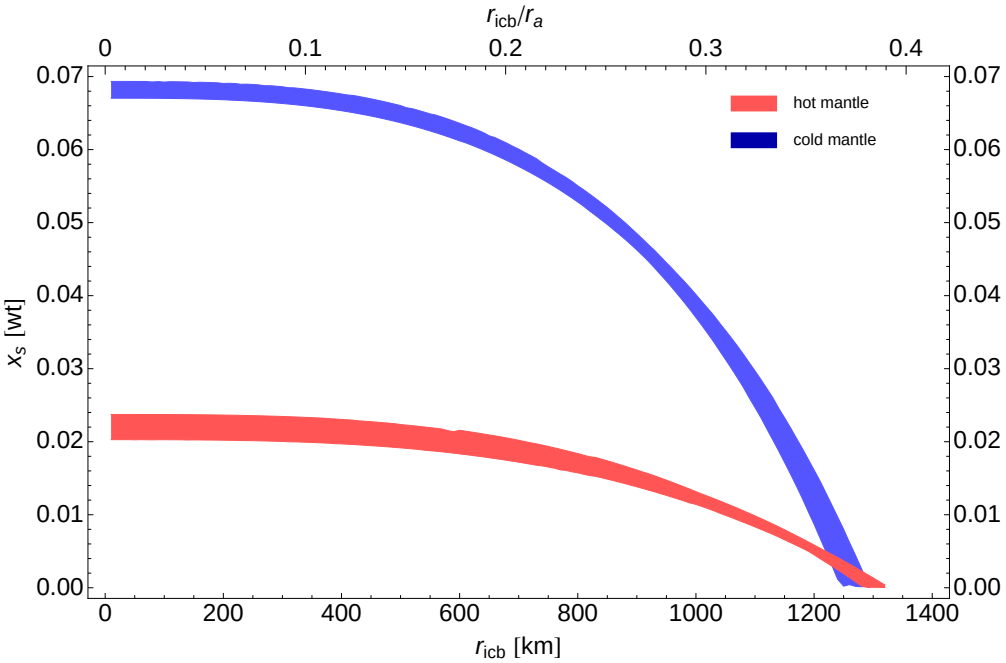


Figure 6.16: Inner core size as a function of core sulfur weight fraction. Cold models are drawn in blue and hot models in red.

The allowed ranges for the interior parameters, $r_{\rm cmb}$, $d_{\rm crust}$, and $\rho_{\rm crust}$, specific to each mantle mineralogy resulting from the global mass and MOI are given in Tab.[6.5]. The results show that the assumed range for crust density and thickness cannot be constrained by global mass and moment of inertia alone. The core bulk sulfur concentration for all models is in the range $[0, 23]$wt% and the Fe/Si ratio within $[1.2, 2.6]$. The ranges for the possible core sizes are very similar. The difference in cores size between the models having the densest mantle (DW84) and those having the least dense mantle (LF97 and

MA79) is only about 30km. Note that even by improving the precision on MOI by a factor 4, the uncertainty on the core size estimate is only reduced by about 10km.

	r_{cmb} [km]	d_{crust} [km]	ρ_{crust} [kg/m^3]	x_{S} [wt]	Fe/Si
LF97	[1265, 2075]	[20, 100]	[2700, 3200]	[0, 0.23]	[1.2, 2.4]
DW84	[1246, 2062]	[20, 100]	[2700, 3200]	[0, 0.23]	[1.3, 2.6]
MM03	[1275, 2085]	[20, 100]	[2700, 3200]	[0, 0.23]	[1.2, 2.4]
MA79	[1268, 2084]	[20, 100]	[2700, 3200]	[0, 0.23]	[1.3, 2.6]
SJ99	[1252, 2057]	[20, 100]	[2700, 3200]	[0, 0.23]	[1.2, 2.3]

Table 6.5: Model parameter values constrained by global mass and MOI.

The bulk Fe/Si ratio for each individual mineralogy as a function of core size, without distinguishing between the mantle temperature, is shown in Fig.[6.17]. For a fixed core size, the DW84 model has the highest Fe/Si value and the MM03 the lowest.

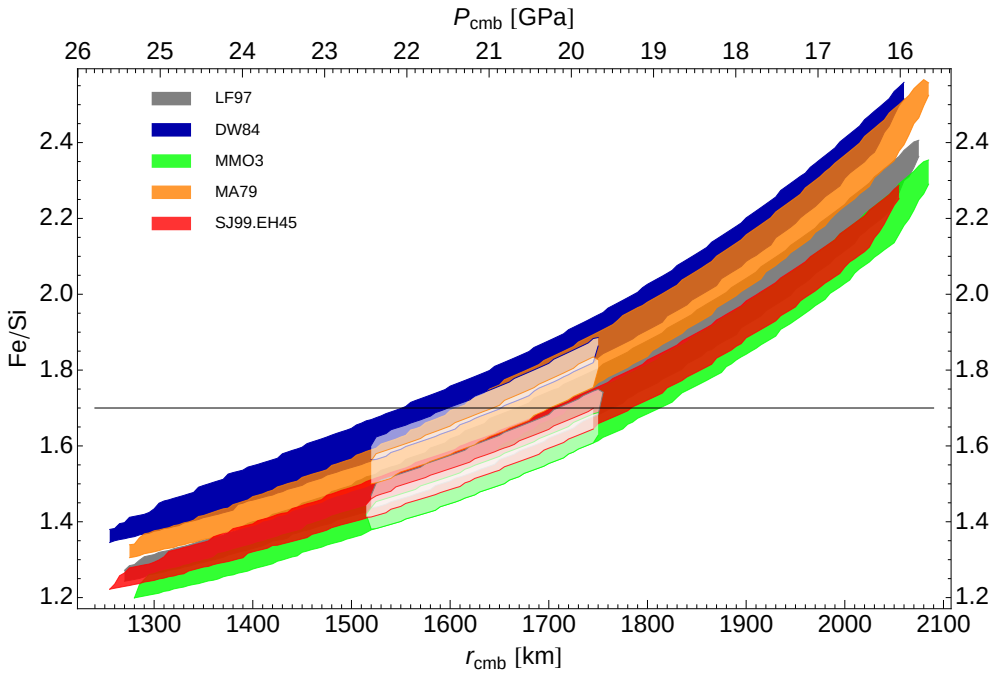


Figure 6.17: Bulk Fe/Si as function of core size. The models within the gray shaded area are within the measured k_2 interval of *Marty et al.* [2009] and *Konopliv et al.* [2006].

The two volcanic centers Tharsis and Elysium on the surface of Mars have often been interpreted as resulting from hot upwellings from the Martian core-mantle boundary [e.g. *Zuber*, 2001]. The presence of an endothermic phase transition at the bottom of the mantle has been invoked as a possible mechanism responsible for the formation of these two major volcanic centers [e.g. *van Thienen et al.*, 2006]. Since the phase transition to perovskite is endothermic it is interesting to investigate whether the phase transition to perovskite can occur. Fig.[6.20] shows the recent laboratory results on the determination of the location, in pressure, and temperature, for the transition to perovskite [*Irifune et al.*, 1998; *Ito and Takahashi*, 1989; *Helffrich and Wood*, 2001; *Hirose*, 2002; *Katsura*

et al., 2003]. Laboratory results show that the temperature of the phase boundary to perovskite decreases with increasing pressure. Depending on the study, the phase transition can occur at pressures as low as 20GPa, if the mantle is hot, or as high as 24GPa, if the mantle is cold.

Fig.[6.20] shows the pressure and temperature at the core mantle boundary. The highest pressures, about 26GPa, results from the cold mantle models with the smallest cores. The lowest pressure is about below 16GPa and corresponds to hot mantle models that have a core size about 2100km. For those models the pressure is too low for the phase transition to ringwoodite to occur, see Figs. [6.2, 6.3, 6.5, 6.6, and 6.7]. For both cold and hot models, the pressure and temperature conditions at the core mantle boundary allow for the phase transition to perovskite to occur if the core size of cold models is smaller than 1620km (cold mantles) and smaller than 1680km for hot mantles.

The precision of core size estimates can be increased slightly if the crust parameters are constrained more tightly. Most recent estimates of the average Martian crust thickness obtained from geoid-to-topography ratios constrain the crust thickness to a range of $[38, 62]$km if the crust density is between$[2700, 3100]$ kg/m^3 [*Wieczorek and Zuber*, 2004]. As a result of these narrower ranges the upper value of the uncertainty range on the core size is reduced by about 24km for the models LF97 to about about 70km for the DW84 models. As a consequence, the upper bound on the bulk mass fraction of iron in the planet decreases and with it the upper value in the Fe/Si ratio range. In order to compensate for the loss in global moment of inertia, resulting from the thinner and less dense crust, the mantle thickness has to increase. Since the mantle is denser than the crust, the core size of those models is smaller in order to conserve the global mass. For the models that experience a phase transition to the denser phases ringwoodite and majorite the decrease in core size is more prominent.

	$r_{\rm cmb}$ [km]	$d_{\rm crust}$ [km]	$\rho_{\rm crust}$ [kg/m^3]	$x_{\rm S}$ [wt]	Fe/Si
LF97	$[1265, 2051]$	$[40, 60]$	$[2700, 3100]$	$[0, 0.23]$	$[1.2, 2.3]$
DW84	$[1246, 1994]$	$[40, 60]$	$[2700, 3100]$	$[0, 0.22]$	$[1.3, 2.3]$
MM03	$[1276, 2070]$	$[40, 60]$	$[2700, 3100]$	$[0, 0.23]$	$[1.2, 2.2]$
MA79	$[1268, 2059]$	$[40, 60]$	$[2700, 3100]$	$[0, 0.23]$	$[1.3, 2.4]$
SJ99	$[1252, 1993]$	$[40, 60]$	$[2700, 3100]$	$[0, 0.23]$	$[1.2, 2.1]$

Table 6.6: Model parameter values constrained by global mass, MOI, 40km $\leq d_{\rm crust} \leq$ 60km, and 2700kg/m^3 $\leq \rho_{\rm crust} \leq$ 3100kg/m^3.

Beside global mass and moment of inertia, the Love number k_2 provides an important constraint on the interior structure of a planet (see Chapt.[5]). The Love number k_2 increases with both increasing core size and sulfur concentration, Fig.[6.18] and Fig.[6.19]. They range from about 0.065, for solid pure iron core models of size 1250km, to about 0.24, for models that have a core of about 2090km and a sulfur concentration of about 23wt%. With increasing core size, the more easily deformable fluid layer inside the planet facilitates global deformations and therefore leads to larger Love numbers. Love numbers are also sensitive to the density and seismic velocities of the mantle. For a given core size, the relative variation in k_2 resulting from the different mantle mineralogies is about

10% and a change in the mantle temperature end-member leads to a variation of about 20%.

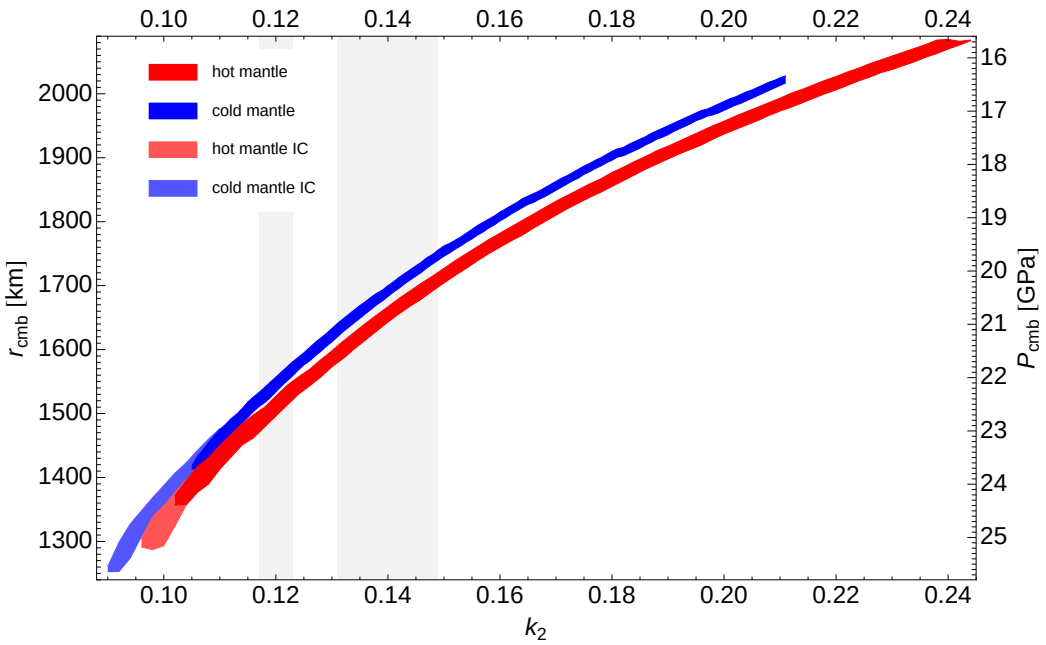


Figure 6.18: Core size as a function of Love number k_2. Cold models are drawn in blue and hot models in red. Models that allow for inner cores are drawn in lighter red and lighter blue. The left gray shaded area corresponds to the k_2 estimate of *Marty et al.* [2009] and the right gray shaded area to the k_2 value determined by *Konopliv et al.* [2006].

The two most recent estimates of the Love number k_2 are: $k_2 = 0.14 \pm 0.009$ [*Konopliv et al.*, 2006] and $k_2 = 0.12 \pm 0.003$ [*Marty et al.*, 2009]. A conservative range for k_2 is then $[0.117, 0.149]$. With this value of k_2 the core of Mars is fully liquid (see Fig.[6.18]) and the core size is within the range $[1479, 1753]$ or 1616 ± 137km. The associated core bulk sulfur concentration is in the range $[6, 18]$wt%, or 12 ± 6wt% (see Fig.[6.19]). If the uncertainty on k_2 is 0.003 then the core size can be estimated with an error of about 50km and the core sulfur concentration with an error of 3wt%.

The obtained values of the interior structure parameters resulting from the three constraints mass, MOI, and k_2 are given in Tab.[6.7]. The addition of the Love number constraint has moved the Fe/Si ratio closer to the chondritic value of 1.7, (Fig.[6.17]). On the other hand, the crust parameters values are not constrained by k_2.

Without further assumption on the bulk composition of Mars the above estimates cannot be improved. The two most constraining compositional parameters are the core sulfur concentration and the bulk Fe/Si ratio. If it is assumed that Mars has a chondritic Fe/Si ratio of 1.7 ± 0.1, together with the mass and moment of inertia constraint, the core size can be estimated with an error of 140km. The associated error on the core sulfur concentration is 5wt%. On the other hand, if the core sulfur concentration is assumed to be $x_S = 14 \pm 0.2$, the core size can be estimated with an error of 100km. If both constraints are assumed the estimated error on the core size reduces to 90km.

Finally, if one uses all measured constraints, m_a, MOI, k_2, and the tighter crust, with the more speculative bulk compositional constraints Fe/Si and x_S, the core size error

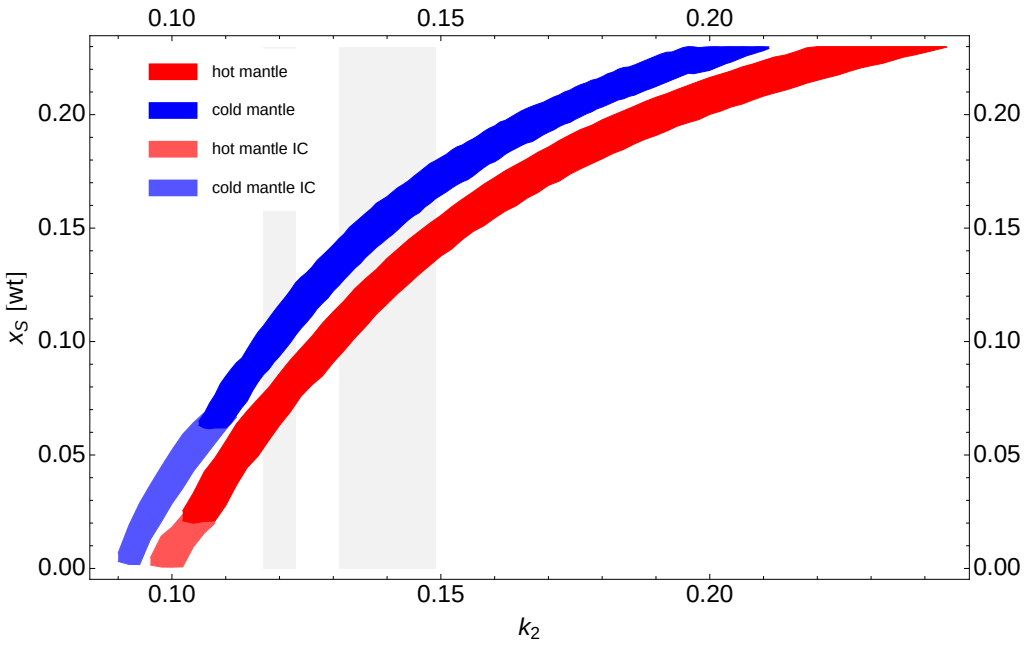


Figure 6.19: Core sulfur concentration as a function of Love number k_2. Cold models are drawn in blue and hot models in red. Models that allow for inner cores are drawn in lighter red and lighter blue. The left gray shaded area corresponds to the k_2 estimate of *Marty et al.* [2009] and the right gray shaded area to the k_2 value determined by *Konopliv et al.* [2006].

	r_{cmb} [km]	d_{crust} [km]	ρ_{crust} [kg/m^3]	x_{S} [wt]	Fe/Si
LF97	$[1487, 1753]$	$[20, 100]$	$[2700, 3200]$	$[0.06, 0.17]$	$[1.4, 1.8]$
DW84	$[1485, 1749]$	$[25, 100]$	$[2700, 3200]$	$[0.07, 0.18]$	$[1.5, 1.9]$
MM03	$[1490, 1750]$	$[20, 100]$	$[2700, 3200]$	$[0.06, 0.17]$	$[1.4, 1.7]$
MA79	$[1479, 1749]$	$[20, 100]$	$[2700, 3200]$	$[0.06, 0.17]$	$[1.5, 1.8]$
SJ99	$[1488, 1746]$	$[20, 100]$	$[2700, 3200]$	$[0.07, 0.18]$	$[1.4, 1.7]$

Table 6.7: Model parameter values constrained by global mass, MOI and k_2.

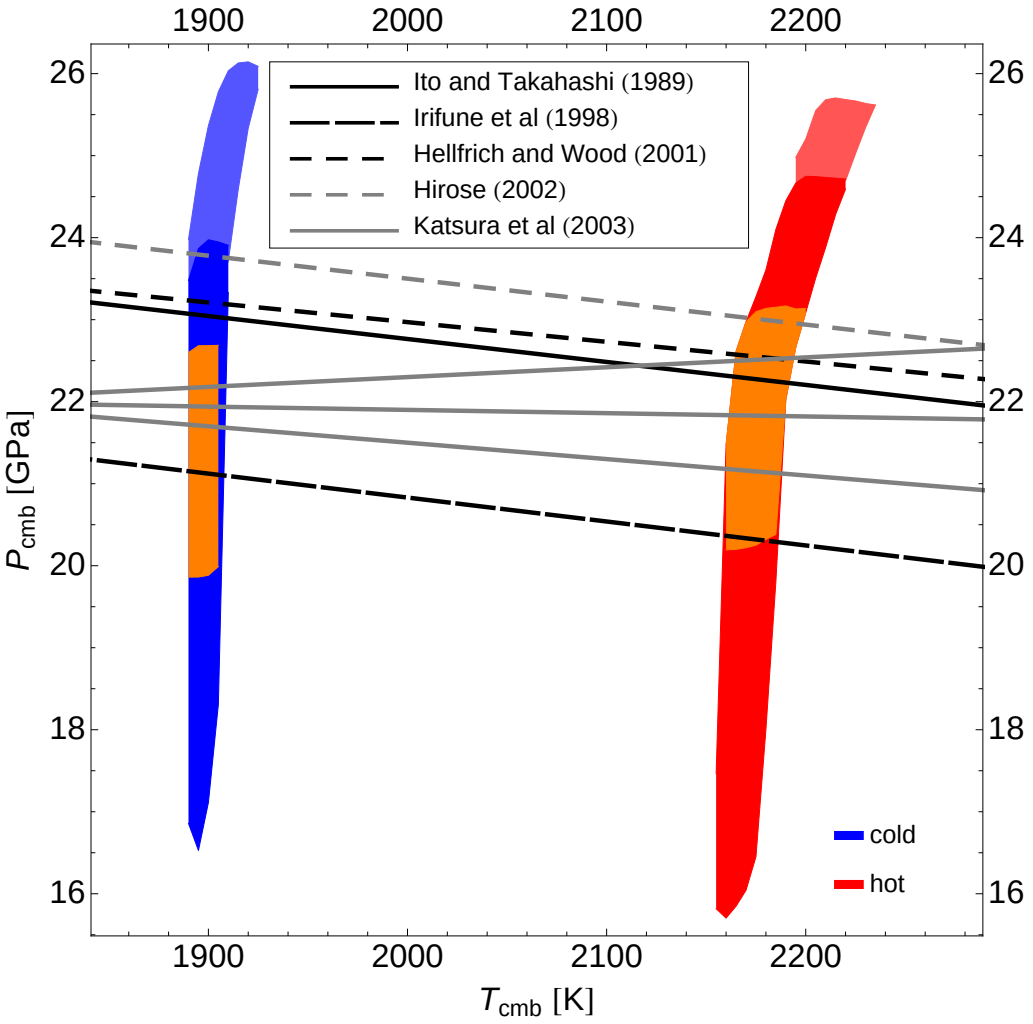


Figure 6.20: Pressure and temperature range at the core mantle boundary. Cold models are drawn in blue and hot models in red. Models that allow for inner cores are drawn in lighter red and lighter blue. Models within the orange shaded area are within the measured k_2 interval of *Marty et al.* [2009] and *Konopliv et al.* [2006]. The black lines are phase boundaries for transition to perovskite. Perovskite occurs above the lines.

reduces to 55km. The interior structure parameters for the individual mantle mineralogies are given in Tab.[6.8]. The result shows, that with this ultimate constraints, the crust density for all mineralogies, expect MM03, has to be below 3100kg/m^3.

	$r_{\rm cmb}$ [km]	$d_{\rm crust}$ [km]	$\rho_{\rm crust}$ [kg/m^3]	$x_{\rm S}$ [wt]	Fe/Si
LF97	$[1639, 1715]$	$[40, 60]$	$[2700, 3000]$	$[0.12, 0.16]$	$[1.6, 1.7]$
DW84	$[1609, 1705]$	$[40, 60]$	$[2700, 2900]$	$[0.12, 0.15]$	$[1.7, 1.8]$
MM03	$[1671, 1723]$	$[40, 60]$	$[2700, 3100]$	$[0.12, 0.16]$	$[1.6, 1.7]$
MA79	$[1598, 1708]$	$[40, 60]$	$[2700, 3025]$	$[0.12, 0.16]$	$[1.6, 1.8]$
SJ99	$[1653, 1711]$	$[40, 60]$	$[2700, 2900]$	$[0.13, 0.15]$	$[1.6, 1.7]$

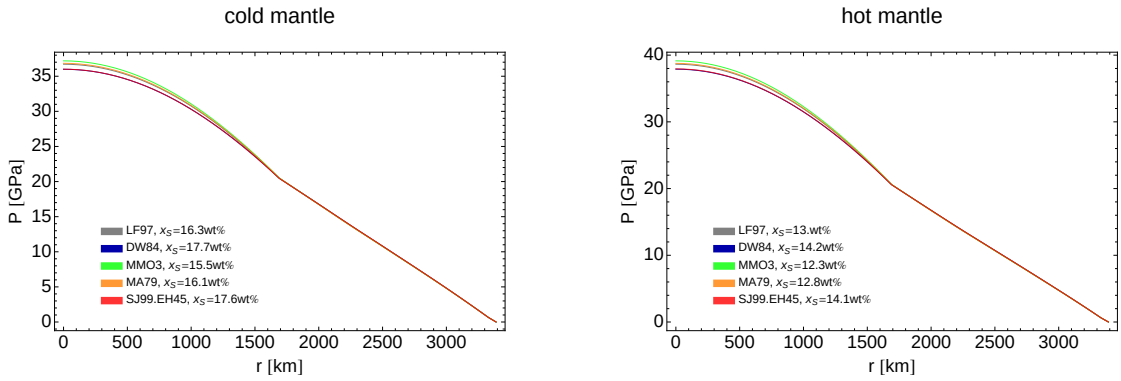
Table 6.8: Model parameter values constrained by global mass, MOI, k_2, Fe/Si $= 1.7 \pm 0.1$, $x_{\rm S} = 14 \pm 2$wt%, 40km $\leq d_{\rm crust} \leq$ 60km, and 2700kg/m^3 $\leq \rho_{\rm crust} \leq$ 3100kg/m^3.

We close the section by giving a selection of profiles for pressure, temperature, density, and seismic velocities, see Fig.[6.21]] to Fig.[6.25]. The chosen values for the structure parameters are: core size is $r_{\rm cmb} = 1690$km, crust density $\rho_{\rm crust} = 2900$kg/m^3, and crust thickness $d_{\rm crust} = 60$km. For this particular choice of parameter values, the hot mantle temperature end-member model with the DW84 mineralogy has a core sulfur weight fraction of 14.2wt%, the mass fraction of core sulfur that has been estimated for the bulk model of *Dreibus and Wänke* [1985] and is often assumed in other studies [e.g. *Sohl and Spohn*, 1997; *Bertka and Fei*, 1998; *Zharkov and Gudkova*, 2005]. The crust thickness is also within the range of the latest estimates, but significantly smaller than those used in the models of the above cited references. The models obtained from the cold mantle temperature end-member have denser mantles than those obtained from the hot mantle temperature end-member, incorporate about 3wt% more sulfur in the core in order to comply to the global mass constraint, see Tab.[6.9]. The difference in core sulfur between the model with the densest mantle, DW84, and the model with the lightest mantle, MM03, is about 1wt%. Fig.[6.21] shows that the pressure at the center of the core is about 36GPa for cold mantle temperature end-members and about 38GPa for the hot mantle temperature end-members that have a denser core, see Fig.[6.23]. Note that for both hot and cold models the pressure at the core mantle boundary is about 20GPa.

The temperature profile for all the models is shown in Fig.[6.22]. The figures show that the temperature inside the core is nearly identical for all models associated to a specific mantle temperature. The temperature at the center of the planet is about 2050K for cold mantle models and about 2400K for hot mantle models. The density profiles and the seismic velocity profiles for the hot and cold end-member mantle temperature end-member are given in Fig.[6.23], Fig.[6.24], and Fig.[6.25]. The result show that the variations in mantle density, resulting from the different mantle mineralogies, are significantly lower than the variations inside the core, resulting from small changes in core sulfur weight fractions. On the other hand, small variations in core sulfur concentration produce significantly smaller variations in the core v_p velocity than the different mantle mineralogies produce on the v_p velocity of the mantle.

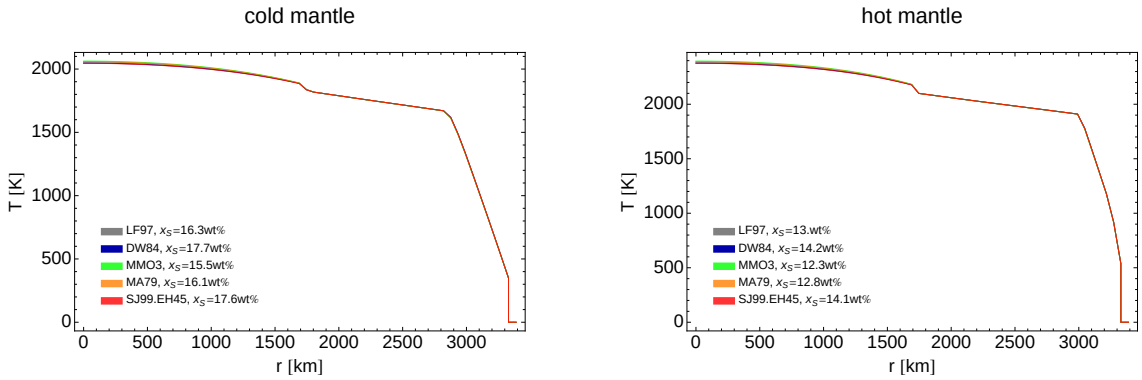
	LF97	DW84	MM03	MA79	SJ99
x_S [wt%], hot	0.13	0.142	0.123	0.128	0.141
x_S [wt%], cold	0.163	0.177	0.155	0.161	0.176

Table 6.9: Calculate core sulfur weight fraction for hot and cold mantle models with a core of 1690km, a crust thickness of 60km, and a crust density of 2900kg/m^3.



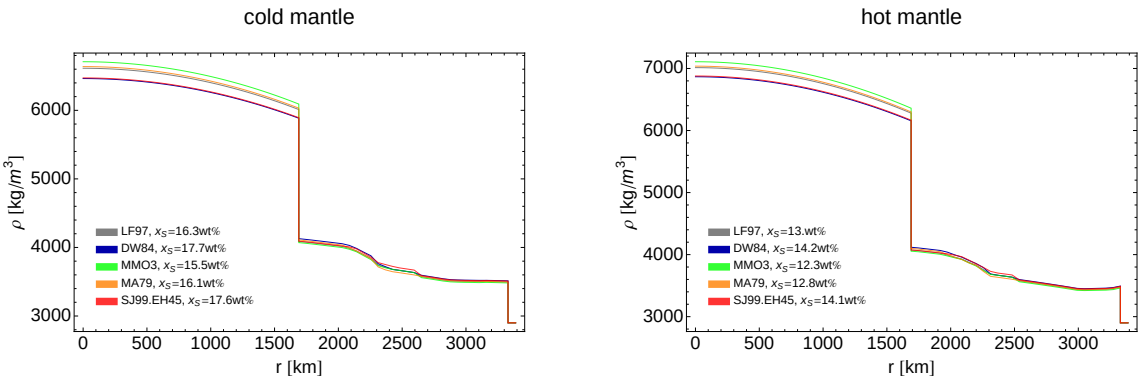
(a) **(b)**

Figure 6.21: Pressure profiles as a function of radius for the cold Fig.[6.21a] and hot Fig.[6.21a] mantle temperature. Core size is $r_{\rm cmb} = 1690$km, crust density $\rho_{\rm crust} = 2900$kg/m^3, and crust thickness $d_{\rm crust} = 60$km.



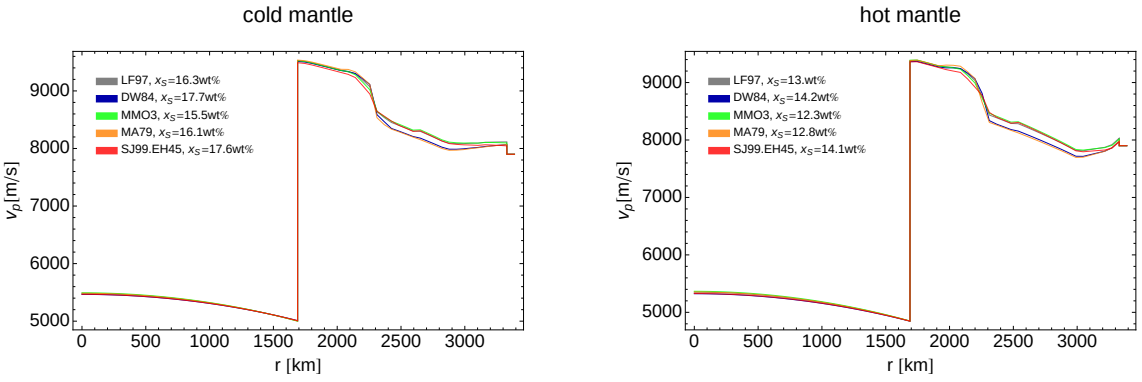
(a) **(b)**

Figure 6.22: Temperature profiles as a function of radius for the cold Fig.[6.22a] and hot Fig.[6.22a] mantle temperature. Core size is $r_{\rm cmb} = 1690$km, crust density $\rho_{\rm crust} = 2900$kg/m^3, and crust thickness $d_{\rm crust} = 60$km.



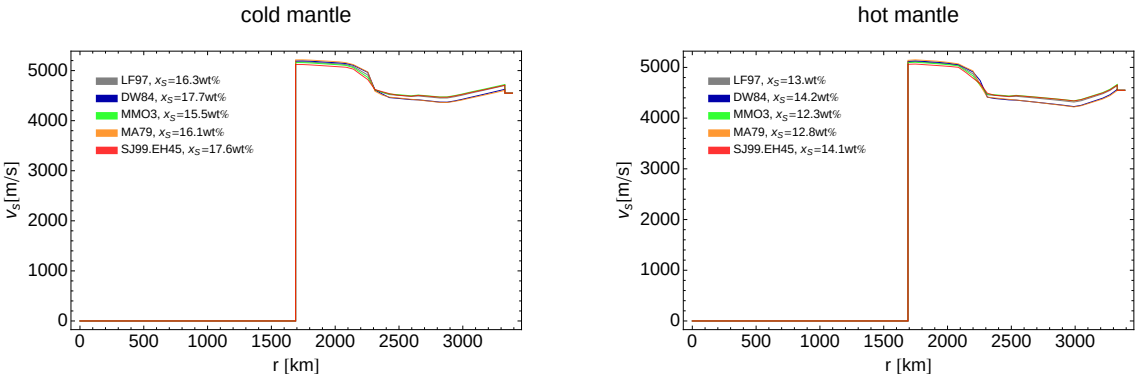
(a) **(b)**

Figure 6.23: Density profiles as a function of radius for the cold Fig.[6.23a] and hot Fig.[6.23a] mantle temperature. Core size is $r_{\text{cmb}} = 1690\text{km}$, crust density $\rho_{\text{crust}} = 2900\text{kg/m}^3$, and crust thickness $d_{\text{crust}} = 60\text{km}$.



(a) **(b)**

Figure 6.24: v_p profiles as a function of radius for the cold Fig.[6.24a] and hot Fig.[6.24a] mantle temperature. Core size is $r_{\text{cmb}} = 1690\text{km}$, crust density $\rho_{\text{crust}} = 2900\text{kg/m}^3$, and crust thickness $d_{\text{crust}} = 60\text{km}$.



(a) **(b)**

Figure 6.25: v_s profiles as a function of radius for the cold Fig.[6.25a] and hot Fig.[6.25a] mantle temperature. Core size is $r_{\text{cmb}} = 1690\text{km}$, crust density $\rho_{\text{crust}} = 2900\text{kg/m}^3$, and crust thickness $d_{\text{crust}} = 60\text{km}$.

6.6 Discussion and conclusions

Despite the limited set of data related to the interior structure of Mars, it is possible, given reasonable assumptions, to make robust estimates about the state of the core, about the presence or not of an inner core, and about the size of the core. Further improvements on the interior structure are expected once the value of k_2 is known with less uncertainty. On the other hand, even if k_2 is perfectly known, important uncertainties on the interior structure parameters remain as long as more precise knowledge on the composition of the mantle, on the crust, and on the temperature inside Mars is not available. Experiences on future space missions toward Mars will be dedicated to the study of the deep interior. Among the possible experiences, seismic soundings, induction studies dedicated to the measurement of the conductivity of the mantle, planetary rotation studies, and surface heat flux measurement, will give the most valuable information about the interior. From the seismic measurements the locations of the most important phase transitions inside the mantle, the core size, and the crust thickness can be determined. Eventually even a radial density profile of the planet could be obtained. Electromagnetic sounding data will provide a radial electrical conductivity profile, that will allow to constrain temperature and composition. Finally, rotation measurements, especially nutation, will bring forth independent estimates on the moment of inertia of the core In part II of this thesis we will discuss a strategy on how seismic data together with electromagnetic sounding data can be used to infer knowledge about the temperature and on the mineral composition of the mantle.

Part II

Mantle models from combined geophysical data sets

Chapter 7

Introduction

The first part of this work was dedicated to the modeling of the global interior structure of terrestrial planets. More precisely, the goal was to constrain the size, state, and composition of the core from the data, planet size, global mass, average moment of inertia, and tidal Love number k_2. In the constructed models, the temperature inside the mantle and the composition of the mantle have been assumed. In our approach, we have used temperature profiles that are end-member results of studies dedicated to the thermal evolution of terrestrial planets. Similarly, we have used mantle mineralogies that have been inferred from the acquired knowledge about in-situ planet surface analyses, meteoritic samples originating from the planetary body of interest, primitive primordial meteoritic material, and planetary accretion scenarios. In principle, the above data could be used to constrain the core size and composition, the mineralogy and temperature of the mantle, and the density and thickness of the crust. However, especially the tradeoff between mantle temperature and composition is too strong and the data too weak to provide more than weak constraining insights to the mantle temperature and composition. Nevertheless, this approach has been followed by *Khan and Connolly* [2008]. From their results, it appears that the temperature of the mantle cannot be constrained together with the other parameters of the model. Since, the inferred mantle temperature does not display any obvious increase in knowledge if compared to the assumed prior mantle temperature. Meaning either that the assumed mantle temperature distribution is strongly informative and is representative of the real temperature, which is doubtful since it displays only a weak temperature gradient in the conductive upper part of the mantle and temperatures close to the surface that are as high as about 1000K (see Fig.[6.1]). Or that the data do not allow to simultaneously constrain mantle temperature and composition without assuming a strong informative temperature prior. In other words, different temperature priors will result in different strongly prior dependent inversion results.

Form the above considerations, it is obvious that in order to get relevant knowledge about the temperature and composition of the mantle we need supplemental geophysical data. Furthermore, in order to infer local quantities like the local temperature we also have to use depth dependent data sets and not only information provided by integrated quantities like mass, moment of inertia, and Love number k_2. All three quantities depend on the internal structure, the temperature, and the composition, however, only indirectly since their values are representative for the whole planet.

In this second part we focus only on the silicate shell of the planet, i.e. the crust

and the mantle. The objective is to assess if the temperature and the mineralogy of the mantle can be inferred by combining the depth profile of the electrical conductivity, the profile of the seismic sound velocity, and the moment of inertia of the silicate shell. Obviously, all those data are sensitive to the materials comprising the mantle. At a given depth, the density, the elastic properties, and the electrical conductivity of a chunk of mantle material depend on the local temperature and pressure and on the chemical and mineralogical composition. The electrical conductivity of a mineral depends mainly on its iron concentration and on the temperature (see Eq. 3.32). The seismic sound velocity of a mineral is primarily related the compressibility and the density (see Eq. 3.31), and both quantities depend on temperature and pressure. Finally, the moment of inertia is sensitive to the mass distribution inside the mantle (see Eq. 2.12). Note that we tacitly assume that the thickness of the crust and the size of the core are precisely determined from the seismic data.

The motivation for using the bulk sound velocity profile instead of the profiles of pressure and shear waves is twofold. First, the uncertainties on laboratory determined compressional properties are smaller than those related to shear deformation (see Tabs. [3.2] and [3.3]). And second, shear waves are significantly more altered than sound waves while propagating through a non elastic media. Therefore, in order to compare model calculated elastic shear wave velocities with observational determined shear velocities a mantle attenuation model has to be taken into account [e.g. *Cammarano et al.*, 2003], whereas for the bulk sound waves the attenuation can be neglected and calculated and measured velocity can be compared directly.

The data for this study are not raw data but rather the result of independent inversions. The electrical conductivity profile is computed by inverting surface induction data. The ionospheric electromagnetic field due to the interaction of the solar wind with the magnetosphere of the planet induces currents inside the planet, which produce electromagnetic field variations at the surface of the planet. The surface field variations depend on the entire conductivity of the planet. Therefore, by measuring the electromagnetic field variations at the surface the inductive structure in depth can be determined (see Sect.[3.6]). The seismic velocities are obtained by inverting measured arrival times of seismic events by using a model of seismic wave propagation inside the planet. Finally, the moment of inertia of the silicate shell is the difference of the moment of inertia of the planet and the moment of inertia of the core. The moment of inertia of the planet is obtained from precession rate measurements and measurements of the gravity field. The moment of inertia of the core can be determined by measuring nutations. Both the gravity field and the variations in rotation are determined by measuring the Doppler frequency shift an electromagnetic signal experiences when transmitted from the Earth to a satellite in orbit around a planet or to a lander on the surface of the planet and retransmitted coherently back to Earth.

Initially, our approach has been motivated by the late NetLander mission [*Harri et al.*, 1999] to Mars. The proposal of the mission included an orbiter and four identical landers. Each lander ought to be equipped with a seismometer [*Lognonné et al.*, 2000] and a magnetometer [*Menvielle et al.*, 2000]. Moreover, the position of each lander with respect to the Earth and with respect to the orbiter ought to be measured by two-way Doppler tracking [*Barriot et al.*, 2001]. The three experiments were expected to provide depth dependent seismic velocity profiles, a precise determination of the thickness of the

crust and of the size of the core, a depth dependent electrical conductivity profile, an improved estimate of the polar moment of inertia, and an estimate of the moment of inertia of the core.

In Chapt.[3] we have explained in detail how for a given bulk mantle composition, a depth dependent, i.e., pressure and temperature dependent, mineralogical composition is derived, and how from the obtained phase diagram depth dependent bulk sound velocity, density, and electrical conductivity are calculated from the reference values of the thermo-elastic and electrical conductivity parameters of each mineral. Since the functional relation mapping the interior structure parameters, composition, pressure, and temperature to the data of bulk sound velocity, density, and electrical conductivity is inherently strongly non-linear we have opted for an inversion method based on Bayesian inference (Chapt.[8]). Bayesian inversion is well suited for non-linear problems since it only requires us to be able to calculate or make a prediction of the data from a given set of parameter values. Moreover, within the Bayesian framework the predictions of the model do not have to be deterministic but rather can be of probabilistic nature. For instance, if the uncertainties on thermo-elastic parameters are included in the model, the predictions of the model become stochastic, i.e. for a given set of parameter values we do not obtain one definite set of data values but rather a distribution of data values that are described by a probability density function. Additionally, the Bayesian method allows to take into account information about the parameters that is known independently of the data, like for example, the restriction of the values of a parameter to a specific range or even it allows to formalize statements like: parameter x is to be larger than y for all values of x and y.

Chapt.[8] is organized as follows: Since the Bayesian inversion method is intrinsically probabilistic, we start with a short reminder on some useful notions related to probability theory. We then introduce the fundamental concept of the Bayesian paradigm (Sect.[8.2]): the inference of knowledge about model parameters, also known as the posterior probability density function by combining assumed prior information with the the information provided by the data (conjunction of knowledge). We detail how the posterior density function is constructed from the model predictions and from the prior knowledge. Once the posterior probability density function is established, we know the solution of the inverse problem. However, for most nontrivial settings we usually know the posterior probability density function proportional to a normalization constant only. In principle the proportionality constant can be calculated, however in practice it is rarely the case. We therefore explain how to implement different iterative schemes that allow to simulate the posterior proportional density function even if the proportionality constant is unknown (Sect.[8.3]).

In Chapt.[9], we explicitly specify the model relating the interior structure parameters to the data and construct the posterior density function. To reduce the number of parameters we apply different approximations. In particular we assume an empirical relation between the volume fractions of the upper mantle mineralogies and a linear pressure profile in the mantle (Sect.[9.2]). We validate our approach in Sect.[9.5] by inverting the model for different scenarios of simulated data sets relative to the planet Mars. We test the robustness of our method by discussing settings where the data are not available for the whole depth of ther mantle (Sect.[9.5.2]), where data sets are missing (Sect.[9.5.3]), and settings with larger uncertainties (Sect.[9.5.4]). In Sect.[9.6] we show

how the inferences change if the empirical relation between upper mantle mineral volume fractions is discarded and the pressure inside of the mantle is computed at each depth from the parameter values. The conclusions are presented in Sect.[9.7].

Chapter 8

Bayesian Inversion

8.1 Introduction

Most of our understanding of planet interiors comes from analyzing data at the surface or exterior to the planet. Therefore, observations are almost always of an indirect nature, and an *inverse problem* relating external observations to interior information must be solved. Major structural zones within the Earth, and to a lesser extent within other planets, such as the crust, mantle, core, and inner core, have been detected and characterized by indirect measurements made at the surface. In part two we will show that seismic sounding data, supplemented with electromagnetic depth sounding data, gravity field data, planet rotation data, and high pressure and high temperature mineralogy data give tight constraints about composition and thermal state. The key question that will be addressed in this chapter is "How do we extract reliable information from the multi-faceted and complex geophysical data sets?".

The relationship between the sought information, also called model parameters x, and the observed data data y is formally written as

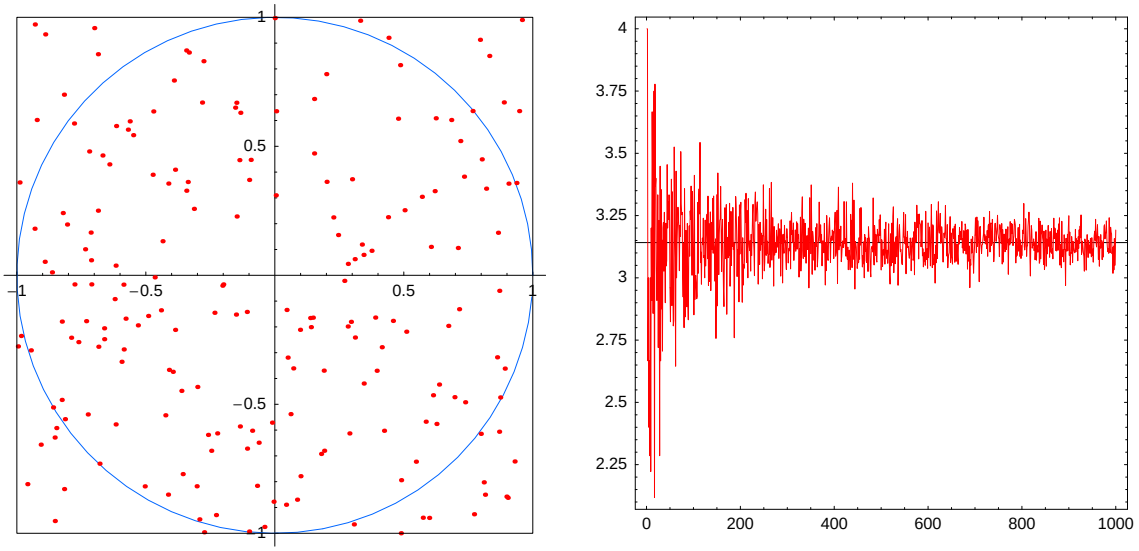
$$y = \mathrm{F}(x), \tag{8.1}$$

where the operator F is called the *forward operator* or model. F incorporates our physical understanding of the relation between parameters and data. The prediction or the calculation of data y given the parameter values x, also called the *forward problem*, might be as diverse as solving differential equations, finding roots of a function, calculating integrals, or applying an algorithm when F cannot be expressed as an analytical expression. Solving the inverse problem consists in using the observational data and the model predictions to infer the values of the parameters characterizing the model. In practice solving an inverse problem is difficult for two main reasons: non-uniqueness, i.e., different parameter values may lead to the same predictions and finding the parameter values that reproduce the data may require exploring a vast parameter space. The non-uniqueness and the inherent presence of measurement uncertainties make that inverse problems are often ill posed, and therefore regularization procedures need to be applied prior to seeking for the solutions.

A particular versatile tool for solving ill-posed inverse problems is Bayesian inversion. In the Bayesian formalism the information provided by the data and the predictions of the forward problem are expressed as a probability density function (pdf) that is conditional

on the parameter values (the data *likelihood*) and data independent knowledge, acting as a regularization, (the *prior* information) can be introduced and be expressed as a pdf. From the conjunction of the prior knowledge and the likelihood the pdf on the parameters, the *posterior* pdf, can be inferred. In practice, the full expression for the posterior pdf is often numerically intractable, and one has to resort to Monte Carlo methods that generate samples that are distributed according to the posterior pdf. From those samples, the empirical posterior pdf can be estimated and other estimates like mean values or variances can be calculated.

Hammersley and Handscomb [1964] define Monte Carlo as "the branch of experimental mathematics that is concerned with experiments on random numbers", or said differently, the use of random numbers to solve probabilistic or deterministic problems. The phrase "Monte Carlo methods" was introduced by *Metropolis and Ulam* [1949]. A simple example to illustrate the principle behind the Monte Carlo method is the computation of π by throwing coins onto a square delimiting a disk of unit radius. The ratio of the number of coins inside the disk to the number of coins inside the square converges to $\pi/4$, the ratio of both surfaces, for large numbers of coins thrown.



(a) **(b)**

Figure 8.1: Disk inscribed in a square with 200 randomly thrown coins and value of π as a function of drops ($\pi = 3.144447154$)

The Monte Carlo method is a versatile tool for computing integrals over high dimensional spaces. We consider the integral

$$I = \int_{\Omega} dx\ g(x)\ p(x) \tag{8.2}$$

where $g(x)$ and $p(x)$ are functions, $g(x)\ p(x)$ is integrable over the domain Ω, and $p(x)$ is a non-negative valued, integrable function such that

$$\int_{\Omega} dx\ p(x) = 1. \tag{8.3}$$

Evaluating the integral (8.2) or equivalently calculating the estimate of g can be done by generating N random samples x_i from the probability density function $p(x)$

$$I \approx \frac{1}{N} \sum_{i=1}^{N} g(x_i) \tag{8.4}$$

As long as the dimension of x is low, the Monte Carlo method is particularly inefficient, compared to more direct numerical evaluations of (8.2). For high dimensions, however, Monte Carlo is often the only feasible method. Numerical approximations in a D dimensional Ω space, usually have an absolute error decreasing not faster then $N^{-\frac{1}{D}}$, whereas the absolute error of the MC method decreases like $N^{-\frac{1}{2}}$ that is independent of the dimension of the space and only dependent on the number of random samples.

Monte Carlo methods depend on effective algorithms that can generate random samples of a given probability density function. However, before we discuss the sampling algorithms we use within the framework of the Bayesian inversion we have to introduce the mathematical formalism.

8.2 Bayesian inference

In Bayesian inference, we calculate the conditional probability density of a variable X given the value a variable Y assumes from the conjunction of the **known** conditional probability density on Y given X with the prior probability density on X. Basically, Bayesian inference is about inverting conditional probability densities. In practice, X stands for parameter values, Y for data, and the prior probability for the knowledge we have on the parameters independent of the data. If we know how to calculate or predict data from parameter values we can construct a conditional probability density for the data given the parameter values. We will denote this conditional probability density by the likelihood function and the solution to the inverse problem, the conditional probability for the parameters given the data, as the posterior probability density.

8.2.1 The basics

The fundamental concept in probability theory, the groundwork on which Bayesian interference is based, is the *random variable*. A random variable is a real number that is assigned to a random event. Random variables are a useful concept when dealing with quantities whose values are not known with certainty. For example, the result of a measurement is conveniently described by a random variable, since each time the measurement is performed a slightly different value is obtained. If the measurement is repeated multiple times we acquire information on the distribution of the possible measured values.

An example illustrating the concept of a random variable is a coin toss. The two possible events are head and tail. The random variable X describing the outcome of the coin toss takes the values

$$X = \begin{cases} 0, & \text{for tail} \\ 1, & \text{for head} \end{cases} \tag{8.5}$$

If the coin is fair we can associate the following probability distribution to the random variable X

$$\mathbf{Pr}(X = x) = \begin{cases} \frac{1}{2}, & \text{if} \quad x = 0 \\ \frac{1}{2}, & \text{if} \quad x = 1 \\ 0, & \text{otherwise} \end{cases} \tag{8.6}$$

where we write the random variable X in upper case, and a realization of the same random variable in lower case x, i.e. $X = x$ means that X has the value of x. The function associating a probability to a given event is represented by the symbol $\mathbf{Pr}(.)$. The probability for $X = x$ is written as $\mathbf{Pr}(X = x)$, or more conveniently $\mathbf{Pr}(x)$. For example, the probability for the random variable X to lie in the interval $a \leq X < b$ is

$$\mathbf{Pr}(a \leq X < b) = \int_a^b dx\ \mathbf{p}(x), \tag{8.7}$$

where $\mathbf{p}(x)$ is called the probability density function associated to random variable X. The probability density function is real, non-negative and normalized such that

$$\int_{-\infty}^{\infty} dx\ \mathbf{p}(x) = 1. \tag{8.8}$$

This simply states that the probability for X to occur in $(-\infty, \infty)$ is one. For a normal distribution of mean μ and variance σ^2, the probability density function can be written as

$$\mathbf{N}(x|\mu, \sigma) = \frac{1}{\sqrt{2\pi\sigma^2}} e^{-\frac{(x-\mu)^2}{2\sigma^2}} \tag{8.9}$$

and the probability for $a \leq x < b$ is

$$\mathbf{Pr}(a \leq X < b) = \frac{1}{2}\left[\mathrm{Erf}(\frac{b-\mu}{\sqrt{2\sigma^2}}) - \mathrm{Erf}(\frac{a-\mu}{\sqrt{2\sigma^2}})\right], \tag{8.10}$$

where $\mathrm{Erf}(x)$ is the error function.

A probability density function depending on n variables is called a n-variate joint probability density and is written as $\mathbf{p}(x_1, x_2, \ldots, x_{n-1}, x_n)$. If the random variables X_i are independent then the joint probability density can be expressed as

$$\mathbf{p}(x_1, x_2, \ldots, x_{n-1}, x_n) = \mathbf{p}(x_1)\mathbf{p}(x_2)\ldots\mathbf{p}(x_n). \tag{8.11}$$

The generalization of (8.7) and (8.8) to *n-variates* is straightforward. The $n-1$-variate joint probability density is related to the a n-variate joint probability density by

$$\mathbf{p}(x_1, x_2, \cdots, x_{n-1}) = \int_{-\infty}^{-\infty} dx_n\ \mathbf{p}(x_1, x_2, \ldots, x_{n-1}, x_n). \tag{8.12}$$

The process of integrating over all possible values of a random variable is called *marginalization*, and $\mathbf{p}(x_1, x_2, \cdots, x_{n-1})$ is the called *marginal probability density* of $\mathbf{p}(x_1, x_2, \ldots, x_{n-1}, x_n)$.

Within the framework of Bayesian inference both the parameter and the data variables are expressed as random variables.

8.2.2 Inverting conditional probabilities

In order to make statements about a random variable X (parameter) conditional on the values of Y (data) we must first provide a relation between X and Y. Formally it is expressed by a joint probability density depending on X and Y. The joint probability density is written as the conjunction of two probability densities

$$\mathbf{p}(x, y) = \mathbf{p}(y|x)\boldsymbol{\pi}(x), \tag{8.13}$$

where $\boldsymbol{\pi}$ is the probability density function for X, and $\mathbf{p}(y|x)$ is the conditional probability density function for Y given $X = x$. In the framework of Bayesian inversion, $\boldsymbol{\pi}(x)$ is called the *prior* pdf for the parameter X and the conditional probability density function $\mathbf{p}(y|x)$ is called the *likelihood function* for the data given that the parameter $X = x$.

By using Bayes' rule

$$\mathbf{p}(x|y) = \frac{\mathbf{p}(x, y)}{\mathbf{p}(y)} \tag{8.14}$$

we obtain from (8.13) the rule for inverting conditional probabilities

$$\mathbf{p}(x|y) = \frac{\mathbf{p}(x, y)}{\mathbf{p}(y)} = \frac{\mathbf{p}(y|x)\boldsymbol{\pi}(x)}{\mathbf{p}(y)}, \tag{8.15}$$

where the denominator of (8.15)

$$\mathbf{p}(y) = \int dx\ \mathbf{p}(x, y) = \int dx\ \mathbf{p}(y|x)\boldsymbol{\pi}(x) \tag{8.16}$$

is also called the *evidence*. The conditional probability $\mathbf{p}(x|y)$ for X given that $Y = y$ is called the *posterior probability distribution function* for the variable X. It is the solution to the Bayesian inference method. We will see below how to construct the model $\mathbf{p}(x, y)$ and the prior $\boldsymbol{\pi}(x)$ by formalizing everything we know about X prior to acquiring the data Y.

With Bayes' rule we can factorize joint probabilities as conditional probabilities. A n variate joint pdf reads

$$\begin{aligned}\mathbf{p}(\{x_k\}) &= \mathbf{p}(\{x_k\}_{-n}, |x_n)\mathbf{p}(x_n) \\ &= \mathbf{p}(x_1|\{x_k\}_{-1})\mathbf{p}(x_2|\{x_k\}_{-1,-2}) \dots \mathbf{p}(x_{n-1}|x_n)\mathbf{p}(x_n),\end{aligned} \tag{8.17}$$

where

$$\{x_k\} = (x_1, x_2, \dots, x_k, \dots, x_{n-1}, x_n)$$

and

$$\{x_k\}_{-i} = (x_1, x_2, \dots, x_{i-1}, x_{i+1}, \dots, x_{n-1}, x_n).$$

If two random variables X and Y are *conditionally independent* then

$$\mathbf{p}(x|y) = \mathbf{p}(x) \text{ and } \mathbf{p}(y|x) = \mathbf{p}(y). \tag{8.18}$$

The conditional independence follows from the statistical independence, i.e. if X and Y are independent then

$$\mathbf{p}(x|y) = \frac{\mathbf{p}(x, y)}{\mathbf{p}(y)} = \frac{\mathbf{p}(x)\mathbf{p}(y)}{\mathbf{p}(y)} = \mathbf{p}(x). \tag{8.19}$$

The usefulness of conditional probabilities and Bayes' rule for inverting conditional probabilities is illustrated in the following example.

Example:
Meteorite samples found on Earth can sometimes be assigned to a specific parent body after a precise isotopic analysis has been performed. Here we want to assess the probability that a sample found in Antarctica is of Martian origin if an isotopic analysis provides a positive result. We assume that if the meteorite were of Martian origin an isotopic analysis would return a positive result with a probability of $\mathbf{p}(\text{pos.}|\text{Mars}) = 0.99$ and a false positive result with a probability of $\mathbf{p}(\text{pos.}|\text{not Mars}) = 0.05$. The prior probability that a Martian meteorite hits Antarctica can be roughly estimated from the total number of Martian meteorites found, the total number of meteorites hitting Earth, the relative continental area, and the relative area of Antarctica. In the last 20 years 12 Martian meteorites have been found. During one year the Earth is hit by about 5000 meteorites. The relative continental surface is 29% and the relative surface of Antarctica is about 3%. The number of meteorites hitting Antarctica during one year is therefore 150 and the number of Martian meteorites hitting Antarctica during one year is about 0.06. Hence, the prior probability $\boldsymbol{\pi}(\text{Mars})$ that a meteorite from Mars hits Antarctica is about $0.4\,10^{-3}$. Then the probability that a meteorite is from Mars given that the isotopic analysis is positive is

$$\begin{aligned}\mathbf{p}(\text{Mars}|\text{pos.}) &= \frac{\mathbf{p}(\text{pos.}|\text{Mars})\boldsymbol{\pi}(\text{Mars})}{\mathbf{p}(\text{pos.}|\text{Mars})\boldsymbol{\pi}(\text{Mars}) + \mathbf{p}(\text{pos.}|\text{not Mars})\boldsymbol{\pi}(\text{not Mars})} \\ &= 0.0078.\end{aligned}$$

Therefore, the probability that a positive result is a false positive is about 0.99. So in spite of the apparent high accuracy of the analysis the probability for obtaining a false positive result is very large. The reason for this is that meteorites from Mars hit Earth only very occasionally. The more infrequent the events the larger the probability for a false positive result. The only way to reduce the number of false positive results is to significantly increase the accuracy of the analysis so that the probability of positive test results for non-Martian meteorites is significantly smaller. For example, if $\mathbf{p}(\text{pos.}|\text{not Mars}) = 0.001$ then the probability for a false positive decreases to about 0.72. We can also calculate the probability that a meteorite is from Mars if the isotopic analysis concludes that it is not

$$\begin{aligned}\mathbf{p}(\text{Mars}|\text{neg.}) &= \frac{\mathbf{p}(\text{neg.}|\text{Mars})\boldsymbol{\pi}(\text{Mars})}{\mathbf{p}(\text{neg.}|\text{Mars})\boldsymbol{\pi}(\text{Mars}) + \mathbf{p}(\text{neg.}|\text{not Mars})\boldsymbol{\pi}(\text{not Mars})} \\ &= 0.000020.\end{aligned}$$

The probability for a negative false result is significantly smaller than the probability for a positive false result. The number of false negative results would be larger if the number of Martian meteorites hitting the Earth were larger.

8.2.3 Expectations

The information provided by a probability density function can often be *summarized* by calculating expectation values. The expectation value of a function f of a random

variable X is the pdf weighted integral over f,

$$\mathbf{E}f(X) = \int_{-\infty}^{\infty} dx\ f(x)\ \mathbf{p}(x). \tag{8.20}$$

If $f(x) = x^n$, the expectation values are called raw moments [e.g. *Papoulis*, 2002]. The n-th raw moment is

$$\mu'_n = \mathbf{E}X^n = \int_{-\infty}^{\infty} dx\ x^n\ \mathbf{p}(x). \tag{8.21}$$

From the definition of the probability density (8.8) it follows that the zeroth raw moment is equal to 1. The first raw moment is the *mean* denoted by μ.

More useful in practice than raw moments are the central moments. They are defined as

$$\mu_n = \mathbf{E}(X-\mu)^n = \int_{-\infty}^{\infty} dx\ (x-\mu)^n\ \mathbf{p}(x). \tag{8.22}$$

The second central moment is called the *variance*. The variance is related to the second raw moment and to the mean

$$\mathbf{var}X = \mathbf{E}(X-\mu)^2 = \mathbf{E}X^2 - \mu^2. \tag{8.23}$$

If random variables X_i are mutually independent the expectation of their product is the product of their individual expectation:

$$\mathbf{E}(X_1 X_2 \cdots X_n) = \mathbf{E}X_1\ \mathbf{E}X_2 \ldots \mathbf{E}X_n \tag{8.24}$$

Two random variables X and Y are said *uncorrelated* if

$$\mathbf{E}(XY) = \mathbf{E}X\ \mathbf{E}Y. \tag{8.25}$$

Independent random variables are uncorrelated **but** the converse is generally not true, see [*Papoulis*, 2002, page 212] for an example.

Expectation values represent relevant information of pdf's. For example, all the information described by a normal distribution can be summarized by its first and second moment. In general, if pdf's are symmetric and mono-modal the first and second moments provide useful information about the maximum of probability and the spread of the pdf. However, for non-symmetric or multi-modal probability density functions the first and second moments do not provide any useful insight. There is, no general rule for deciding which expectations best represent the information of a pdf. Moreover, some probability density functions do not have any finite moment (see lighthouse problem of Sect.[8.2.8]). The choice of expectation values that best represents the information depends on the problem at hand.

8.2.4 Functions of random variables

In practice, one is often confronted with the problem of finding the probability density function of a random variable Y that is related to another random variable X by a function f. Let $\mathbf{p}_X(x)$ be the pdf for X, and $y = f(x)$. If $\mathbf{p}_X$ is continuous and f one to one, then the probability density function for Y, $\mathbf{p}_Y(y)$, is [*Papoulis*, 2002]

$$\mathbf{p}_Y(y) = |\mathrm{J}|\ \mathbf{p}_X(f^{-1}(y)), \tag{8.26}$$

where $|\mathrm{J}|$ is the determinant of the *Jacobian* matrix of the transformation $x = f^{-1}(y)$ and the components of the Jacobian matrix are

$$\mathrm{J}_{i,j} = \frac{\partial x_i}{\partial y_j}. \tag{8.27}$$

For example, let the random variable θ have a uniform probability density function on $[0, \pi]$, then the probability density function for θ is

$$\mathbf{p}_\theta(\theta) = \frac{1}{\pi} \tag{8.28}$$

and let

$$x = f(\theta) = b - \frac{a}{\tan\theta}, \tag{8.29}$$

with $a \geq 0$ and $b \geq 0$. The Jacobian matrix of the transformation is then

$$\mathrm{J} = \frac{\partial \theta}{\partial x} = \frac{a}{a^2 + (b-x)^2} \tag{8.30}$$

and the probability density on X

$$\mathbf{p}_X(x) = |\mathrm{J}|\ \mathbf{p}_\theta(f^{-1}(x)) = \frac{1}{\pi}\frac{a}{a^2 + (b-x)^2}. \tag{8.31}$$

8.2.5 The Likelihood function

Central to the Bayesian paradigm is the likelihood function. The likelihood function assigns a probability, a likelihood, to the data for a fixed set of parameter values. It is constructed from the observed data and from data predicted from the mathematical model for given parameter values. The model prediction is either deterministic or probabilistic. A model is deterministic if the relation between the parameters and the model prediction is certain otherwise the model is probabilistic. We discuss two kinds of probabilistic models. In the first case, the model is probabilistic because some aspects of the physical relation between parameters and data cannot be described by the deterministic mathematical model, and we choose to model those omissions by introducing supplemental random variables of presumed probability density function. The parameters describing those pdf's are then estimated together with the parameters of the mathematical model.

In the second case, the model prediction is probabilistic because other quantities that are used for calculating data values from parameter values are not known precisely but are characterized by probability density functions. This case occurs for example, while calculating the density of a mineral at a given pressure and temperature. Typically, the equation of state relating the density to the pressure and the temperature depends on thermoelastic quantities that are described by pdf's.

The likelihood is the conditional probability density for obtaining the data Y given the parameter values X and can be written as $\mathbf{p}(y|x)$. Y stands for the collection of data random variables $(Y_1, Y_2, \ldots, Y_m)$, $X = (X_1, X_2, \ldots, X_n)$ stands for the set of parameters, and $Z = (Z_1, Z_2, \ldots, Z_m)$ for the predictions of the model, i.e., the data predicted by the model for a given set of parameter values X. We describe the model predictions with

a conditional pdf, $\mathbf{p}_Z(z|x)$, since we want to consider the general setting of a stochastic model. If the data are acquired or measured with a given uncertainty, characterized by the pdf $\mathbf{p}_E$, then the i-th datum is the sum of the i-th model prediction with the measurement noise e_i:

$$y_i = z_i(x) + e_i. \tag{8.32}$$

The relation between the measured data, the model predictions, and the measurement noise are described by the joint probability density $\mathbf{p}(y_i, z_i, e_i|x)$. The conditional probability for the i-th datum given the parameter values $\mathbf{p}(y_i|x)$ can be calculated from the joint conditional probability $\mathbf{p}(y_i, z_i, e_i|x)$ by marginalization

$$\mathbf{p}(y_i|x) = \int dz_i \; de_i \; \mathbf{p}(y_i, z_i, e_i|x). \tag{8.33}$$

If the measurement noise E_i and the model prediction Z_i are independent and if E_i is independent of X then the joint pdf can be factorized by applying Baye's rule:

$$\mathbf{p}(y_i|x) = \int dz_i \; de_i \; \mathbf{p}(y_i|z_i, e_i, x)\mathbf{p}(z_i|x)\mathbf{p}(e_i), \tag{8.34}$$

Since it follows from (8.32) that $\mathbf{p}(y_i|z_i, e_i, x) = \delta(y_i - z_i - e_i)$, equation (8.34) yields

$$\mathbf{p}(y_i|x) = \int dz_i \; \mathbf{p}_Z(z_i|x)\mathbf{p}_E(y_i - z_i). \tag{8.35}$$

With (8.35) we can now consider deterministic or stochastic prediction models.

Deterministic model

In a deterministic model there is no uncertainty in the predicted value z_i. If we denote $z_i = f_i(x)$, where f is our deterministic mathematical model, then $\mathbf{p}_Z(z_i|x) = \delta(z_i - f_i(x_i))$ and (8.35) yields

$$\mathbf{p}(y_i|x) = \mathbf{p}_E(y_i - f_i(x)). \tag{8.36}$$

In other words the distribution of the difference of i-th datum with the i-th prediction is equal to the distribution of the i-th error term, $Y_i \sim E_i$. If all errors are independent, then the likelihood is

$$\mathbf{p}(y|x) = \prod_{i=1}^{m} \mathbf{p}_E(y_i - f_i(x)). \tag{8.37}$$

If all data points have an associated Gaussian uncertainty with standard deviation σ_i then likelihood is written as

$$\mathbf{p}(y|x) = (2\pi)^{-\frac{m}{2}} \left(\prod_{i=1}^{m} \sigma_i^{-1} \right) \exp\{-\sum_{i=1}^{m} \frac{(y_i - f(x))^2}{2\sigma_i^2}\}. \tag{8.38}$$

Probabilistic model

We discuss two settings that are relevant for the geophysical setting we elaborate in the next chapter. In the first, the model prediction z_i includes an additive statistical noise component ξ_i that is independent of the model parameters X

$$z_i = f_i(x) + \xi_i. \tag{8.39}$$

If the random variable $\Xi_i \sim \mathbf{p}_\Xi(\xi_i)$ it follows that the random variable $Z_I \sim \mathbf{p}_\Xi(z_i - f_i(x))$ or

$$\mathbf{p}_Z(z_i|x) = \mathbf{p}_\Xi(z_i - f_i(x)). \tag{8.40}$$

In the second case we consider random auxiliary parameters $W = (W_1, \ldots, W_K)$:

$$z_i = f_i(x, w). \tag{8.41}$$

If the pdf $\mathbf{p}_W$ on W is known then the pdf on Z_i can in principle be calculated from (8.26). For this we have to express W as a function of Z and X. Formally we can write

$$w_i = f_i^{-1}(x, z). \tag{8.42}$$

By using (8.26) the conditional probability density function on Z given x and w can be expressed as

$$\mathbf{p}_Z(z|w, x) = |\mathrm{J}(z, w)|\ \mathbf{p}_W(f^{-1}(x, z)), \tag{8.43}$$

where the determinant of the Jacobian is

$$|\mathrm{J}(z, w)| = \left|\frac{\partial\, w_i}{\partial z_j}\right| = \left|\frac{\partial\, f_i^{-1}(x, z)}{\partial z_j}\right|. \tag{8.44}$$

Since, for both settings we now know $\mathbf{p}_Z$ (see (8.40) and (8.43)) the conditional probability density for Y_i given X can in principle be calculated from (8.35).

If we assume for example, in the first setting that $Z_i \sim \mathrm{N}(f_i(x), \sigma_{m,i})$ and $E_i \sim \mathrm{N}(z_i - y_i, \sigma_i)$, the convolution integral from (8.35) yields

$$\mathbf{p}(y_i|x) = (2\pi)^{-\frac{1}{2}} \left(\sigma_i^2 + \sigma_{m,i}^2\right)^{-\frac{1}{2}} \exp\left\{-\frac{(y_i - f(x))^2}{2(\sigma_i^2 + \sigma_{m,i}^2)}\right\}. \tag{8.45}$$

If the model uncertainty and the data uncertainty have a normal distribution, then the conditional pdf for Y_i is also a normal distribution with a variance equal to the sum of the model and the measurement variance. If the data points are independent the likelihood is

$$\mathbf{p}(y|x) = (2\pi)^{-\frac{m}{2}} \left(\prod_{i=1}^{m} \left(\sigma_i^2 + \sigma_{m,i}^2\right)^{-\frac{1}{2}}\right) \exp\left\{-\sum_{i=1}^{m} \frac{(y_i - f(x))^2}{2(\sigma_i^2 + \sigma_{m,i}^2)}\right\} \tag{8.46}$$

For the second setting, we assume that the model relating X to Z can be written as

$$z_i = x_1 w_i + x_2 \tag{8.47}$$

with $W_i \sim \mathrm{N}(w_{0,i}, \sigma_{m,i})$. By using (8.43) and $w_{0,i} = (z_{0,i} - x_2)/x_1$ the pdf on Z_i can be written as

$$\mathbf{p}_Z(z_i|x_1, x_2) = \frac{1}{\sqrt{2\pi x_1^2 \sigma_{m,i}^2}} \exp\left\{-\frac{(z_i - z_{0,i})^2}{2\sigma_{m,i}^2 x_1^2}\right\} \tag{8.48}$$

since $|\mathrm{J}| = x_1^{-1}$. The convolution integral (8.35) then yields

$$\mathbf{p}(y_i|x_1, x_2) = (2\pi)^{-\frac{1}{2}} \left(\sigma_i^2 + x_1^2 \sigma_{m,i}^2\right)^{-\frac{1}{2}} \exp\left\{-\sum_{i=1}^{m} \frac{(y_i - x_1 w_{i,0} - x_2)^2}{2(\sigma_i^2 + x_1^2 \sigma_{m,i}^2)}\right\}, \tag{8.49}$$

and the likelihood can be expressed as

$$\mathbf{p}(y|x_1,x_2) = \frac{1}{(2\pi)^{\frac{m}{2}}}\left(\prod_{i=1}^{m}\left(\sigma_i^2 + x_1^2\sigma_{m,i}^2\right)^{-\frac{1}{2}}\right)\exp\left\{-\sum_{i=1}^{m}\frac{(y_i - x_1 w_{i,0} - x_2)^2}{2(\sigma_i^2 + x_1^2\sigma_{m,i}^2)}\right\}. \quad (8.50)$$

Examples relating to both settings are given below (in particular, see the epicenter example in Sect.[8.2.8]). For an application of the first setting see for instance *Koot et al.* [2008]. In *Koot et al.* [2008] Earth interior parameters are inferred from VLBI data by Bayesian inversion of an Earth rotation model.

In practice for real geophysical problems, there are two major caveats. First, the convolution integral (8.35) can often not be calculated analytically and second the inverse of the function f, (8.42), can often not be determined.

8.2.6 Priors

The prior probability formalizes whatever additional information we have beyond what we have chosen to call data [*Jaynes*, 2003, chapt. 4]. It should allow for all possible values of the parameter but doesn't need to be realistically concentrated around the true value, in a certain sense it represents our subjective state of knowledge. For instance, we don't know the exact temperature in the core of the Earth, but we know for certain that it is positive and limited from above. Practically, the prior acts as a regularization as it reduces the configuration space.

One distinguishes between *informative* and *noninformative* priors [*Gelman et al.*, 2003, chapt. 2]. We have an informative prior on our parameter of interest if, for example, the parameter can only take certain values and the prior assigns probabilities to their occurrences. Another example is when we know that the parameter $X \sim \mathrm{N}(\mu,\tau)$, i.e. that it is normally distributed about μ with standard deviation τ. The parameters μ and τ of the prior distribution are called *hyperparameters*.

Noninformative prior distributions, on the other hand, are constructed in such a way that their influence on posterior inferences is as weak as possible. They are also called vague, diffuse, or *noninformative*. The idea is to let the data speak for themselves so that the inferences are unaffected by information external to the data. Commonly used noninformative priors are the flat prior, $\mathbf{p}(x) \propto k$, for $x \in (-\infty,\infty)$, or $\mathbf{p}(\sigma^2) \propto \frac{1}{\sigma^2}$ for $\sigma^2 \in (0,\infty)$. Such distributions are strictly speaking not allowed as their integral sums up to infinity. They are called *improper* priors. A prior density is called *proper* if it does not depend on the data and the integral is a constant $< \infty$. An improper prior $\mathbf{p}(x)$ combined with the likelihood $\mathbf{p}(y|x)$ results in an improper joint density $\mathbf{p}(x,y)$. However, improper priors may lead to a proper unnormalized posterior density $\mathbf{p}(x|y) \propto \mathbf{p}(y|x)\mathbf{p}(x)$ if $\int dx\ \mathbf{p}(x|y)\,\mathbf{p}(x)$ is finite for all y. For example, if the prior on X is flat and the likelihood for $\mathbf{p}(y|x)$ is a Gaussian with mean x and standard deviation σ the resulting posterior is proper. In practice, when dealing with improper priors, the finiteness of the integral over the posterior has to be assured.

Generally, it is not an easy task to construct priors that have an effect as small as possible on the posterior distributions. A systematic scheme for constructing such priors has been proposed by Jeffreys, see [*Gelman et al.*, 2003, chapt. 2]. Jeffreys considered a one-to-one transformation of the parameter: $z = h(x)$. The prior density on z is then

according to (8.26)

$$\mathbf{p}_X(x) = \mathbf{p}_Z(z) \left| \frac{d\, h(x)}{dx} \right|. \tag{8.51}$$

Jeffreys' principle then states that any rule for determining the prior density $\mathbf{p}_X(x)$ should yield an equivalent result if applied to the transformed parameter. This can be obtained with the requirement that $\mathbf{p}_X(x)$ is form invariant under the transformation h, $\mathbf{p}_X(x) = \mathbf{p}_Z(h(x))$. Within this framework *Baker and Christakos* [2007] consider the transformation group representing the change in dimensional units. Accordingly, the "state of prior information" should have the same representation regardless of the physical units employed. The transformation of change of origin and scale, $g(x) = ax+b$, with the imposed invariance condition of the prior function leads to the following two solutions

$$\mathbf{p}_X(x) = \begin{cases} c_X |x - x_1|^{-1} \\ c_0 \end{cases} \tag{8.52}$$

where c_X, c_0 are normalization constants, $x_0 \leq x \leq x_f$, and x_1 a particular value in the X range. Both solutions are improper priors, the first resulting from the singularity in x_1 and the second when $x_0 \to -\infty$ and $x_f \to \infty$. The arbitrariness of x_1 can be resolved if identified with natural reference point, e.g. like the lowest possible temperature cannot be below $0K$. The natural reference points of non-dimensional variables can be found if they are defined as ratios of dimensional variables. Examples of the above principle are also found in *Tarantola* [2005]. Finally, *Baker and Christakos* [2007] argue against the flat prior since one is usually not "enough ignorant" to motivate its usage.

8.2.7 The posterior distribution

The posterior distribution is the conditional probability distribution of the unobserved parameters of ultimate interest, given the observed data. In order to derive a probability statement about the unobserved parameters x given the data y we first have to provide a relation providing a joint probability density function between the parameters and the data, $\mathbf{p}(x, y)$. This joint pdf can be written as the product of the prior probability on the parameters $\boldsymbol{\pi}(x)$ and the likelihood function $\mathbf{p}(y|x)$:

$$\mathbf{p}(x, y) = \boldsymbol{\pi}(x)\mathbf{p}(y|x). \tag{8.53}$$

By using Baye's rule we obtain the posterior probability density function

$$\mathbf{p}(x|y) = c\, \mathbf{p}(y|x)\boldsymbol{\pi}(x), \tag{8.54}$$

where the proportionally constant c is independent on the parameters x and defined as

$$c = \int dx\, \mathbf{p}(y|x)\boldsymbol{\pi}(x). \tag{8.55}$$

Generally, the direct calculation of the proportionality constant c, even for a modest number of parameters, is a non trivial task. Fortunately, it is sufficient for most applications to know the posterior proportionality density function proportional up to a constant. In Sect.[8.3] we introduce different methods for simulating the posterior probability density function that do not rely on the proportionality constant c.

8.2.8 Examples

In the two following examples, we illustrate the conjunction of prior knowledge and data likelihood and show how the number of data points influence the shape of the posterior probability density function. In the first example, we also discuss the different likelihood functions resulting from different kinds of probabilistic parameter-data relations. In the second example the model at hand together with the uncertainty on the data leads to a posterior proportionality density that does not have any moments other than the zeroth. As a consequence, the uncertainty on the estimated average of a position random variable does not decrease with increasing number of data points.

Epicenter

The probability density for the location of the epicenter of an earthquake can to be inferred from measured arrival times at n seismic stations. We assume a flat two dimensional setting where the epicenter is in $\boldsymbol{\alpha} = (0, 0)$. The event occurrence of the earthquake is in τ_0 and we assume that seismic velocity v_0 is constant and known (example adapted from *Tarantola* [2005]).

If the epicenter of an earthquake is in $\boldsymbol{\alpha}$ then the arrival time at a station located in $\boldsymbol{x_i}$ is

$$\tau_i(\boldsymbol{\alpha}, \boldsymbol{x_i}) = \tau_0 + \frac{|\boldsymbol{\alpha} - \boldsymbol{x_i}|}{v_0}. \tag{8.56}$$

At each station the arrival times are determined with an uncertainty ϵ (noise). Consequently at each station i the measured arrival time t_i is

$$t_i(\boldsymbol{\alpha}, \boldsymbol{x_i}) = \tau_i(\boldsymbol{\alpha}, \boldsymbol{x_i}) + \epsilon_i. \tag{8.57}$$

For simplification, we assume that the measurement uncertainties are equal in each station and that they can be represented by a normal distribution with zero mean and variance σ^2

$$\epsilon \sim \mathbf{N}(0, \sigma). \tag{8.58}$$

We assume that v_0 and τ_0 are precisely known. The the probability density for the arrival time in station i given that the epicenter is in $\boldsymbol{\alpha}$ is then

$$\mathbf{p}(t_i|\boldsymbol{\alpha}) \propto \mathrm{e}^{-\frac{(\tau_i(\boldsymbol{\alpha}, \boldsymbol{x_i}) - t_i)^2}{2\sigma^2}}. \tag{8.59}$$

Since the determination of the arrival times at each station is independent of the determination at the other stations the likelihood is the product of the individual pdf's for the arrival times at each individual station

$$\mathbf{p}(\{t_i\}|\boldsymbol{\alpha}) = \prod_{i=1}^{n} \mathbf{p}(t_i|\boldsymbol{\alpha}) \propto \mathrm{e}^{-\sum_{i=1}^{n} \frac{(\tau_i(\boldsymbol{\alpha}, \boldsymbol{x_i}) - t_i)^2}{2\sigma^2}}. \tag{8.60}$$

The posterior pdf is proportional to the product of the likelihood and prior pdf

$$\mathbf{p}(\boldsymbol{\alpha}|\{t_i\}) \propto \mathbf{p}(\{t_i\}|\boldsymbol{\alpha})\boldsymbol{\pi}(\boldsymbol{\alpha}), \tag{8.61}$$

where $\boldsymbol{\pi}(\boldsymbol{\alpha})$ is the prior pdf on the parameter $\boldsymbol{\alpha}$ (and the proportionality constant is independent of the parameter).

Fig.[8.2a] shows the posterior pdf for the earthquake epicenter and Fig.[8.3a] the posterior pdf for the distance of the epicenter to the station if only the data from one seismic station is considered and if the prior probability for $\boldsymbol{\alpha}$ is uniform, i.e. $\boldsymbol{\alpha} \sim 1$. Since it is impossible to acquire any information about the angular position with one station, the posterior pdf is ring-shaped with an origin located in $\boldsymbol{x_i}$. The thickness of the ring increases with σ. The result shows that the epicenter is within the 0.67 probability domain of posterior pdf.

The only way to improve our knowledge about the epicenter with only one datum is to increase our prior knowledge. Assume that we know from a geological survey, that a fault is approximatively orientated along the $y - x = 10$ line. It is then reasonable to assume that there is a significant probability for an earthquake to occur in close vicinity to the fault. We formalize this knowledge by proposing the following 'fault' prior pdf on $\boldsymbol{\alpha}$

$$\boldsymbol{\alpha} = (\alpha_x, \alpha_y) \sim \mathbf{N}(10 + \alpha_x - \alpha_y, \lambda) \tag{8.62}$$

where λ represents the width of the fault. We associate to each point on the $y - x = 10$ line a normal distribution of zero mean and standard deviation λ. Note that in order for this prior pdf and the previous uniform prior pdf to be proper, i.e., normalizable, we additionally require $\mathbf{p}(|\boldsymbol{\alpha}| > 1000) = 0$.

Fig.[8.2b] represents the posterior pdf for the epicenter obtained by using the prior from (8.62). The results show that there are two locations that have an associated high probability for the epicenter. They are located at the intersection of the surfaces that represent the 0.997 domains of the likelihood function and of the prior pdf. Compared to the result obtained with the uniform and non-informative prior, Fig.[8.2a], this informative prior pdf allows for a significant better localization of the epicenter. The inferred pdf is heavily biased toward the prior and the posterior probability for the epicenter to be located in $\boldsymbol{\alpha}$ is negligibly small. We will see below how the bias of the prior is reduced if the number of data points is increased.

Assume a second earthquake has occurred and that another station has measured the arrival time. If we assume that the epicenter of this new earthquake is located close to the epicenter of the previous quake we can use the posterior pdf for the epicenter inferred from the first earthquake, Fig.[8.2a], as a prior pdf for inferring the epicenter of the second earthquake. Fig.[8.2c] shows the inferred posterior pdf. The domain of significant probability is drastically reduced, however there still isn't enough information to locate the epicenter univocally.

Fig.[8.2d] shows the posterior pdf obtained by using the arrival times measured at four seismic stations, resulting from the same earthquake, and by using the fault prior information. The spread of the 0.997 probability surface is significantly reduced, and it appears that the epicenter can be located with a high confidence. The bias introduced by the fault prior is still present, although it is reduced. If we infer the posterior pdf from the same data in conjunction with the uniform prior we find with a very high confidence (within the 0.67 probability domain) that the epicenter is located in $\boldsymbol{\alpha}$. see Fig.[8.4a].

The result shows that a strong informative prior has a strong influence on posterior inferences, especially if the number of data values are small. If the prior assumptions are wrong the posterior inferences will be biased. Moreover, specific prior settings will not allow the bias to decrease appreciably if the amount of data is increased significantly.

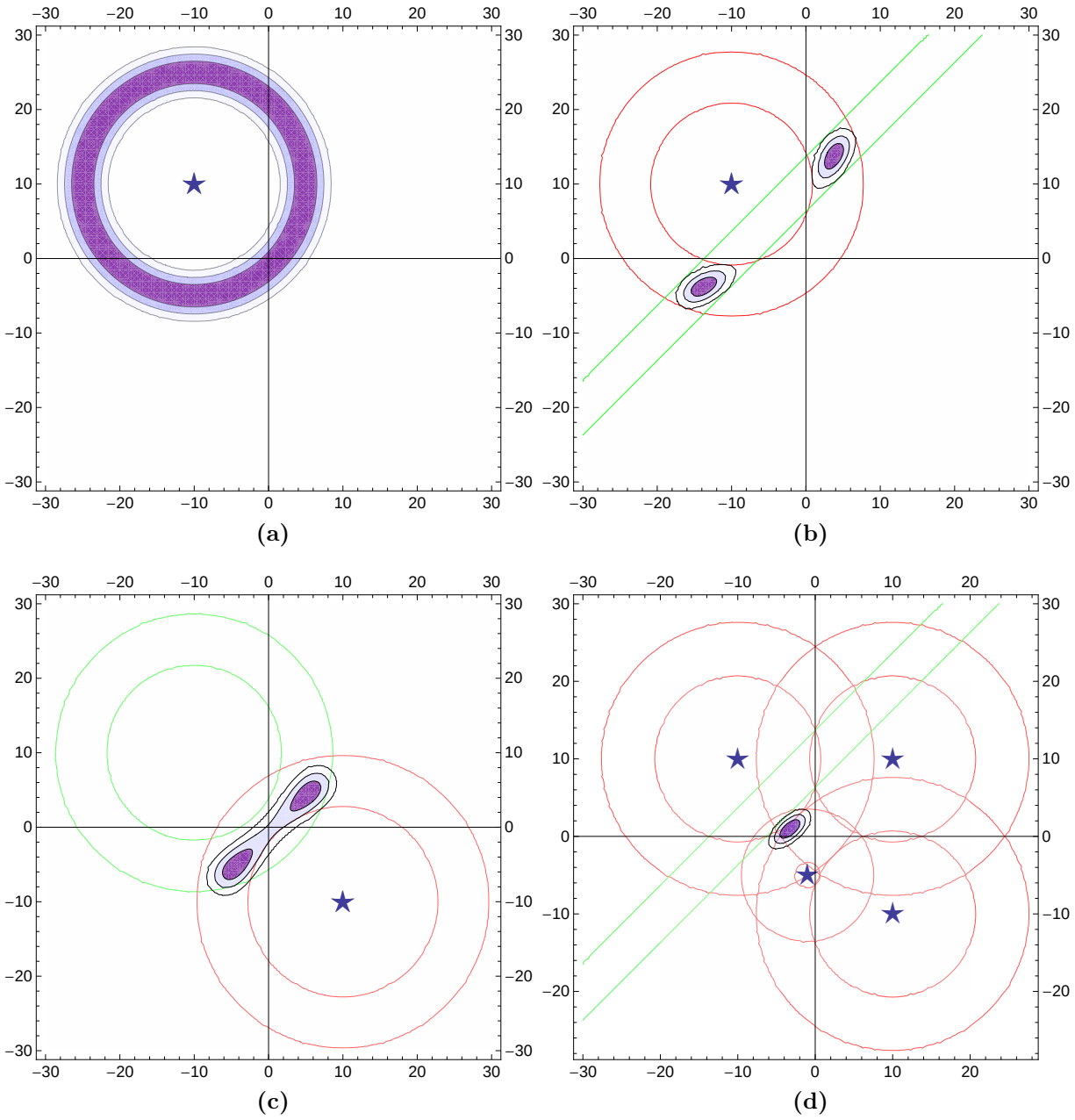


Figure 8.2: Posterior probability density for earthquake epicenter inferred from arrival times of seismic stations. The stars correspond to the location of the seismic stations and the earthquake epicenter is in $(0, 0)$. Contour shadings are drawn for posterior probability density for 0.67, 0.95, and 0.997 probabilities. Prior pdf's (green) and likelihood functions (red) are represented by 0.997 probability contours. (a) is the inferred posterior pdf from one station with uniform prior pdf. (b) is the inferred posterior pdf from one station with a prior pdf represented by normal distributions of mean zero along the $y - x = 10$ line. (c) is the inferred posterior pdf from one station with a prior pdf equal to the posterior pdf obtained from (a). (d) is the inferred posterior pdf from four stations with a prior pdf represented by a normal distributions of mean zero along the line $y - x = 10$.

We now discuss how the posterior pdf changes if the model predicting the arrival times at the seismic stations is stochastic. First, we assume that the earthquake occurrence time τ_0 is not known precisely (see the first case of the probabilistic model setting in Sect.[8.2.5]), but that it is characterized by a normal distribution with standard deviation σ_m and centered about τ_{00}:

$$\tau_0 \sim \mathrm{N}(\tau_{00}, \sigma_m). \tag{8.63}$$

The likelihood function is then given in (8.46). And the posterior density function is

$$\mathbf{p}(\boldsymbol{\alpha}|\{\boldsymbol{\tau_i}\}) \propto \left(\prod_{i=1}^{n}\left(\sigma_i^2+\sigma_{m,i}^2\right)^{-\frac{1}{2}}\right)\mathrm{e}^{-\sum_{i=1}^{n}\frac{(\tau_0(\boldsymbol{\alpha},\boldsymbol{x_i})-\tau_i)^2}{2(\sigma^2+\sigma_m^2)}} \tag{8.64}$$

From the above likelihood we calculate the posterior pdf with (8.61) under the assumption that the prior pdf on $\boldsymbol{\alpha}$ is uniform within the square $[-30,30]\otimes[-30,30]$.

Fig.[8.3c] shows the posterior pdf for the distance between the earthquake epicenter and one station, and Fig.[8.4b] represents the posterior pdf for the epicenter given the data from the four stations. Because of the uncertainty on the earthquake occurrence time, the posterior pdf's have a wider spread. If compared to the posterior pdf of the exact model setting, Fig.[8.4a], the region delimited by the 0.67 probability contour is about four times larger.

Secondly, we assume that τ_0 is well known but that v_0 is only known approximatively. This is the second setting we have discussed in the probabilistic model case of Sect.[8.2.5]. To apply (8.43) we first have to calculate the Jacobian of the function relating v_0 to τ_i. From (8.56) v_0 reads

$$v_0 = \frac{|\boldsymbol{\alpha}-\boldsymbol{x_i}|}{\tau_i-\tau_0} \tag{8.65}$$

and the Jacobian is

$$J = \frac{\partial\, v_0}{\partial \tau_i} = -\frac{|\boldsymbol{\alpha}-\boldsymbol{x_i}|}{(\tau_i-\tau_0)^2} \equiv -\frac{\Delta_i}{(\tau_i-\tau_0)^2}. \tag{8.66}$$

We discuss three examples for plausible prior probability density functions on v_0:

$$v_0 \sim \begin{cases} \text{Unifom: 1 in } [v_{\min}, v_{\max}] \\ \text{Jeffreys: } 1/v_0 \text{ in } [v_{\min}, v_{\max}] \\ \text{LogNormal}(\log v_0, \sigma_m) \end{cases} \tag{8.67}$$

For each pdf of v_0 the induced probability density function on τ_i is then calculated from (8.43). The conditional pdf's at each station i (see (8.35)) then yield

$$\mathbf{p}_{\mathrm{U}}(t_i|\boldsymbol{\alpha}) \propto \int_{\frac{\Delta_i}{v_{\min}}}^{\frac{\Delta_i}{v_{\max}}} d\tau_i\ \frac{\Delta_i}{(\tau_i-\tau_0)^2}\mathrm{e}^{-\frac{(\tau_i-t_i)^2}{2\sigma^2}} \tag{8.68}$$

$$\mathbf{p}_{\mathrm{J}}(t_i|\boldsymbol{\alpha}) \propto \int_{\frac{\Delta_i}{v_{\min}}}^{\frac{\Delta_i}{v_{\max}}} d\tau_i\ \frac{\Delta_i}{(\tau_i-\tau_0)}\mathrm{e}^{-\frac{(\tau_i-t_i)^2}{2\sigma^2}} \tag{8.69}$$

$$\mathbf{p}_{\mathrm{LN}}(t_i|\boldsymbol{\alpha}) \propto \int_0^{\infty} d\tau_i\ \frac{1}{(\tau_i-\tau_0)}\mathrm{e}^{-\frac{\left(\log\frac{\Delta_i}{(\tau_i-\tau_0)}-\log v_0\right)^2}{2\sigma_m^2}}\mathrm{e}^{-\frac{(\tau_i-t_i)^2}{2\sigma^2}}, \tag{8.70}$$

where $\mathbf{p}_{\mathrm{U}}$, $\mathbf{p}_{\mathrm{J}}$, and $\mathbf{p}_{\mathrm{LN}}$ stand for the conditional pdf's obtained with the uniform, Jeffreys, and lognormal pdf on v_0. Note that the probability constants have been dropped in order to simplify the notation and that of the three above integrals only the first two have an analytical solution.

We again assume that the prior pdf on $\boldsymbol{\alpha}$ is uniform within the square $[-30, 30] \otimes [-30, 30]$. The posterior pdf's for the epicenter distance obtained from the data of only one station for the uniform, Jeffreys, and lognormal pdf on v_0 are shown in Figs [8.3c,8.3d,8.3e]. The corresponding posterior pdf's for the epicenter location are given in Figs. [8.4c,8.4d,8.4e].

The results also show that the shapes of the main probability contours of the posterior pdf's are highly non trivial making it very difficult to summarize the information by classical estimators.

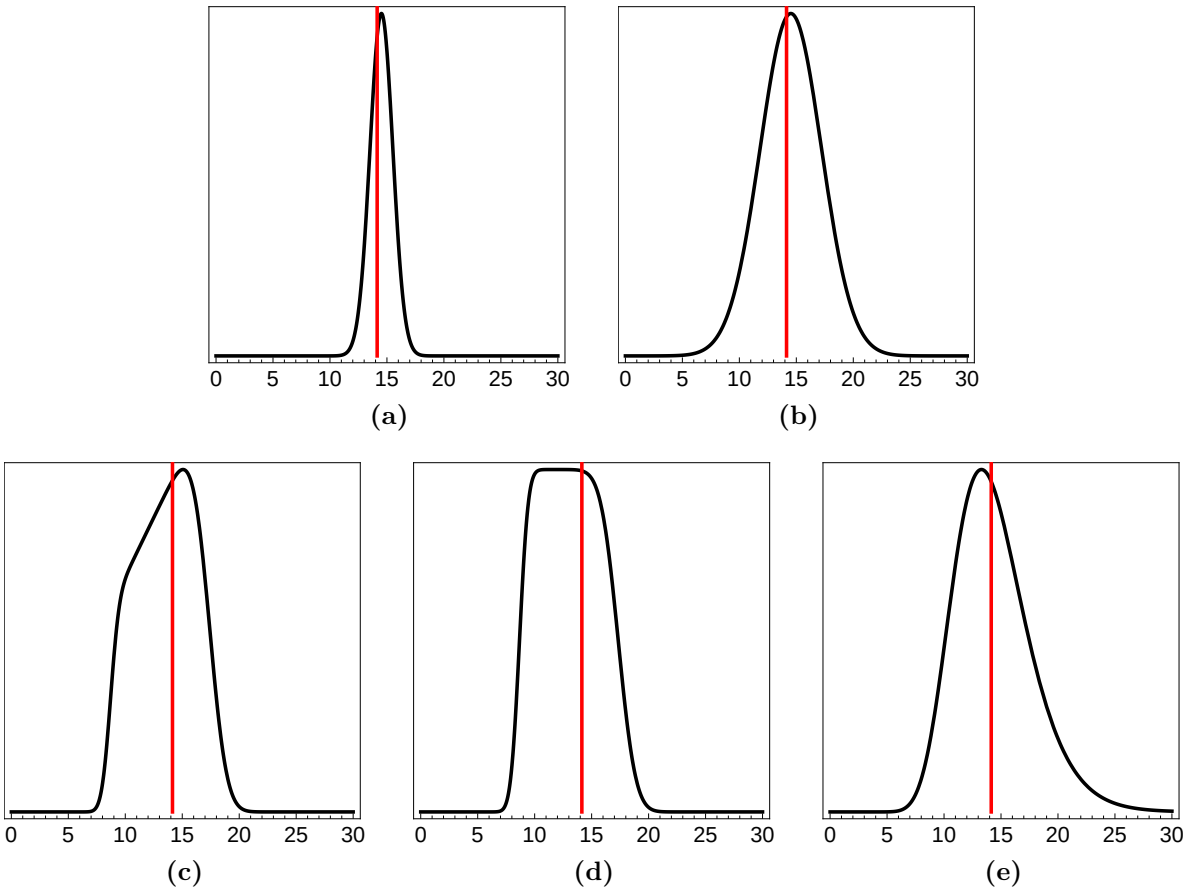


Figure 8.3: Posterior probability density functions for epicenter distance. For non-stochastic model (a), model with arrival time uncertainty (b) (normal), and for models with seismic velocity uncertainty (uniform (c), Jeffreys (d), and lognormal (e)). The vertical red line corresponds to the epicenter distance.

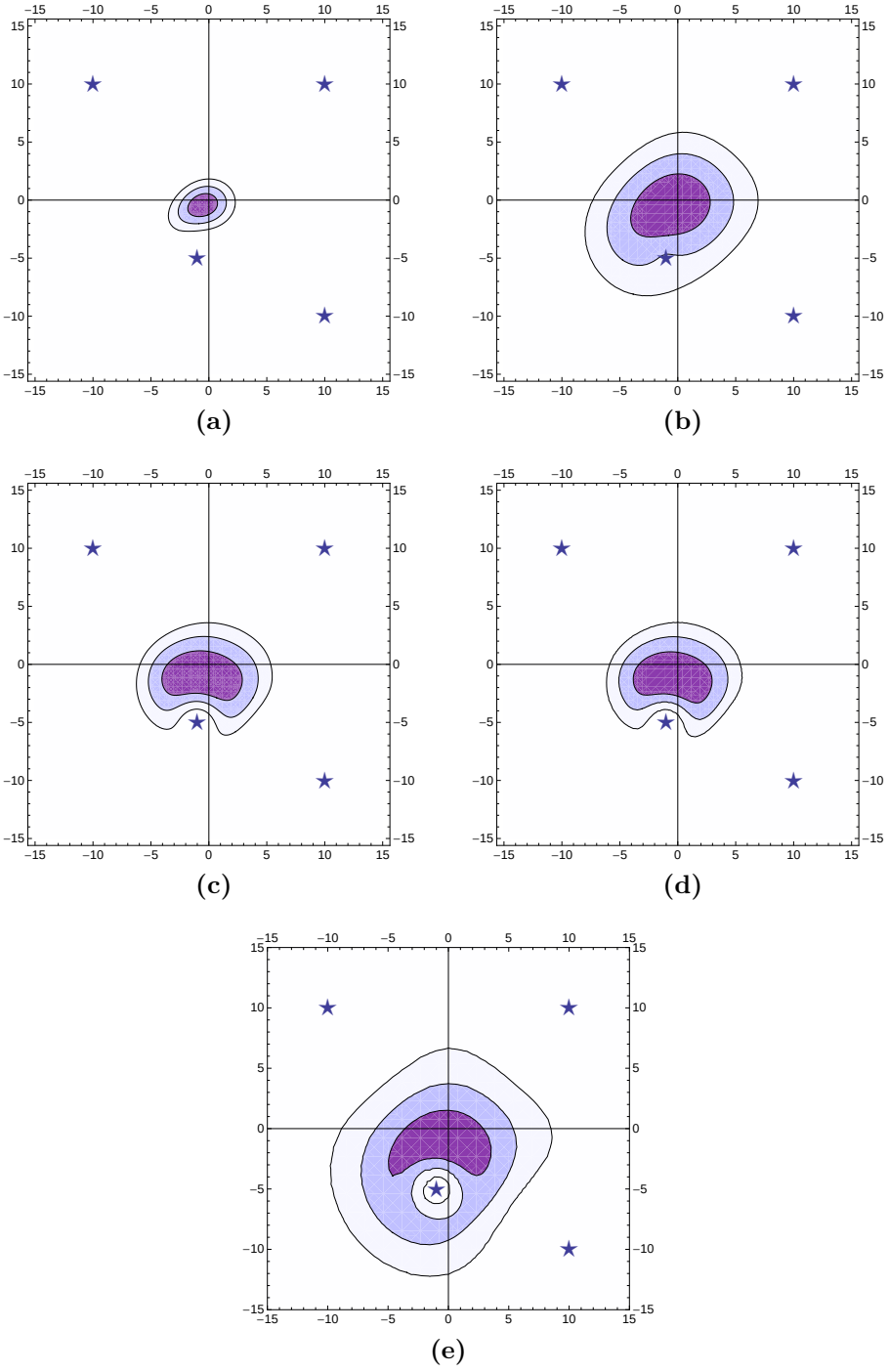


Figure 8.4: Posterior probability density functions for epicenter location. For non-stochastic model (a), model with arrival time uncertainty (b) (normal), and for models with seismic velocity uncertainty (uniform (c), Jeffreys (d), and lognormal (e)). The stars correspond to the location of the seismic stations and the earthquake epicenter is in $(0, 0)$. Contour shadings are drawn for posterior probability density for 0.67, 0.95, and 0.997 probabilities.

The Lighthouse problem

We consider a lighthouse positioned somewhere out at sea in position (x, y) with respect to the coast, see Fig.[8.5] (adapted from *Sivia and Skilling* [2006]). The lighthouse emits light flashes at random intervals and therefore random azimuths θ_k. Along the coast, in the locations x_k, the incoming light impulses are recorded by photodetectors that do not provide angular information. A number N of flashes are recorded in different positions along the coast. Where is the lighthouse?

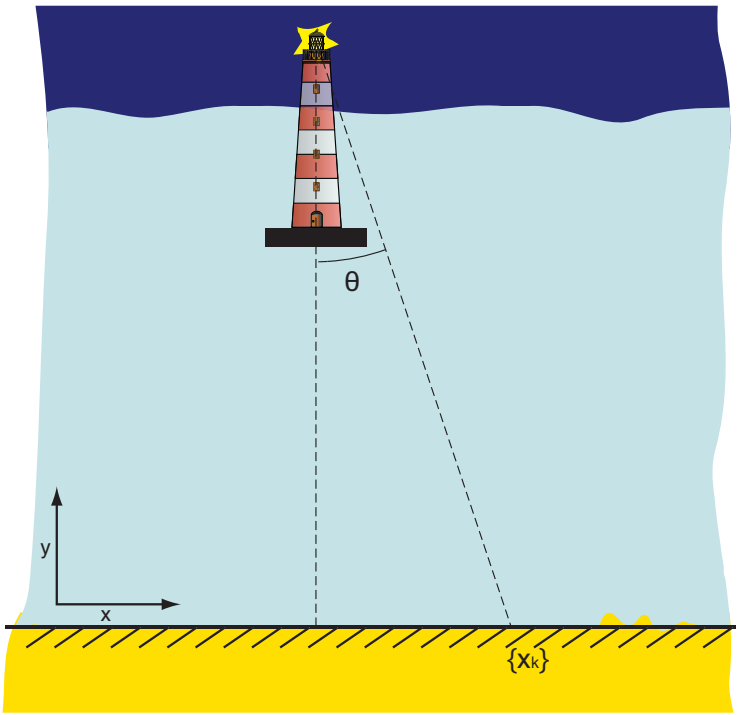


Figure 8.5: Geometry of the lighthouse problem

In order to infer the position of the lighthouse given the data we have to determine the posterior density function. The posterior probability is proportional to the product of the likelihood function with the prior distribution (8.54). Following Sect.[8.2.5] we first construct the likelihood function. Since the light flashes are emitted at random intervals it is reasonable to assume that the probability for a flash occurring at a given azimuth, θ_k, is equally probable, i.e., uniform. The likelihood function then is

$$\mathbf{p}(\theta_k|x, y) = \frac{1}{\pi} \tag{8.71}$$

The photodetectors do however not measure θ_k but x_k, therefore we have to reparameterize the likelihood (8.71) to the variable x_k. From the Fig.[8.5] we see that

$$\tan\theta_k = \frac{y}{x_k - x}. \tag{8.72}$$

Given this relation between θ_k and x_k and given the probability distribution for θ_k we can calculate the probability distribution for x_k by means of (8.26). The likelihood function

for x_k, i.e. the probability for measuring a flash in x_k given that the lighthouse location is (x, y), then reads

$$\mathbf{p}(x_k|x,y) = \frac{1}{\pi}\frac{y}{y^2+(x-x_k)^2}. \tag{8.73}$$

This particular probability density function is called the *Cauchy distribution*[1] [e.g *Papoulis*, 2002]. The Cauchy distribution is symmetric about the location parameter x_k, the position of its maximum and median. The scale parameter y specifies the half-width at half-maximum height. The Cauchy distribution has properties that make it a remarkable counterexample to many standard results. Since it is heavy tailed, all its moments, except the zeroth moment, are undefined (i.e. infinite). With the first and second moment undefined one cannot apply the law of large numbers to estimate the expected value from a set of samples of a Cauchy distribution. Since the distribution of the average value of a set of independent samples of Cauchy distribution with given location and scale parameter is also a Cauchy distribution with the *same* location and scale parameters. Therefore, if the measurement error of a certain process has a Cauchy distribution then the average of any large number of measurements will not be more precise than any other individual measurement. This counterintuitive example is in sharp contrast to the more familiar finite variance normal distribution, for which, according to the law of large numbers, the sample average deviates from the average by less than a real number ϵ with probability one.

If we have N location observations and if we assume that each recording is independent of any previous recording then the likelihood for N data points is the product of the individual likelihoods

$$\mathbf{p}(\{x_k\}|x,y) = \prod_{k=1}^{N}\frac{1}{\pi}\frac{y}{y^2+(x-x_k)^2}. \tag{8.74}$$

For the prior distribution, we will simply assume that the prior probability for a flash of light to be detected at a particular spot along the coastline of length L to be of uniform probability and of zero probability elsewhere

$$\boldsymbol{\pi}(x_k) = \begin{cases} L^{-1}, -L/2 \leq x_k \leq L/2 \\ 0, \quad \text{else} \end{cases} \tag{8.75}$$

With likelihood and prior pdf the posterior probability density function then reads

$$\mathbf{p}(x,y|\{x_k\}) \propto \prod_{k=1}^{N}\frac{y}{y^2+(x-x_k)^2}. \tag{8.76}$$

To find the most likely or most probable location for the lighthouse we have to seek for the maxima of (8.76). This is, however, analytically intractable for reasonably large values of N. In the next section, we will explain how this can be done by simulating the posterior pdf. Here, we will use a graphical and numerical approach to find the location of maximal probability.

Fig.[8.6] shows how the posterior probability (depicted by contour lines for $(0.68, 0.95, 0.997)$ probability) evolves with increasing number of data points. Fig.[8.7] shows the corresponding marginal distributions. The posterior pdf shrinks with increasing number of

[1] Also called the Lorentz or Breit-Wigner distribution.

data points. Additionally, from about 50 data points on the most probable position of the lighthouse converges. For less data points the pdf can even be multimodal. The uncertainty, here represented by the 0.68 probability contour is, however, still relatively large since it is about 50 length units in both x and y direction about the maximum. Fig.[8.6] and Fig.[8.7] also indicate the sample mean μ of position x calculated from the recorded positions on the coast.

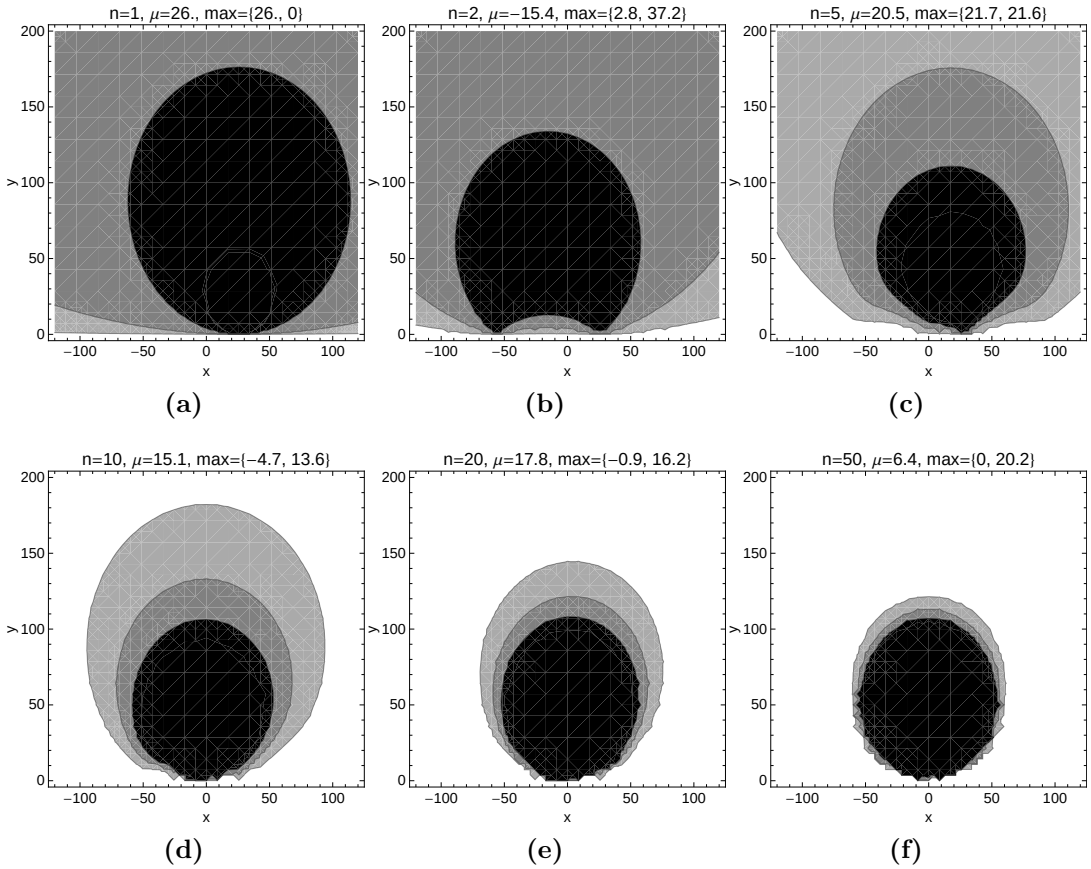


Figure 8.6: Posterior probability density for position of the lighthouse for different number of data (n) given that the lighthouse is positioned in $(0, 20)$km out to sea. The shaded areas, gray, darker gray, and black delimit the domains with $(0.68, 0.95, 0.997)$ probability. μ denotes the sample mean position in x and max denotes the most probable location.

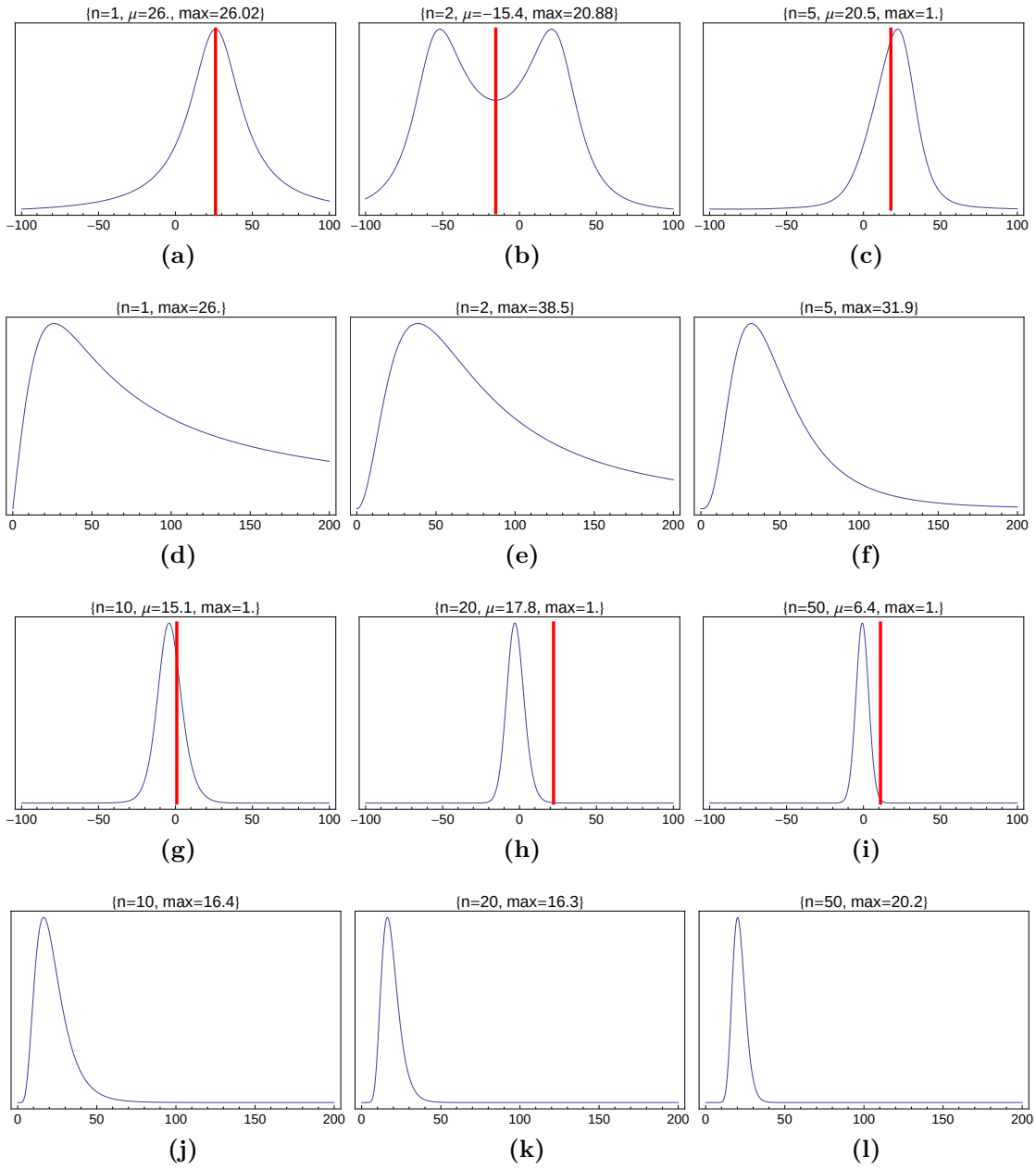


Figure 8.7: Marginal posterior pdf for x (8.7a,8.7b,8.7c,8.7g,8.7h,8.7i) and y (8.7d,8.7e,8.7f,8.7j,8.7k,8.7l) location of the lighthouse for different number of data (n) given that the lighthouse is positioned in $(0, 20)$km out to sea. The red lines correspond to the sample mean position in x. max denotes the most probable location in x and y.

8.3 Sampling probability distributions

In practice, it is often impossible to directly generate samples from a probability density function $\mathbf{p}(x)$. The notable exceptions are the uniform distribution and those distributions that can be derived from the uniform distribution by ingenious mathematical transformations. Like for example, the Box-Muller [*Box and Muller*, 1958] and the Ziggurat [*Marsaglia and Tsang*, 2000] methods for generating samples from a normal distribution. Moreover, as we have seen in Sect.[8.2.7], some pdf's like the posterior probability density function are often only known up to a normalization constant. Here, we introduce two sampling algorithm's that can generate samples from about any pdf $\mathbf{p}(x)$ even if it is only known up to a constant. The *Metropolis-Hasting* sampler [*Hastings*, 1970; *Metropolis et al.*, 1953] and the *Gibbs* sampler [*Geman and Geman*, 1984]. Both methods simulate a *Markov process* to sample $\mathbf{p}(x)$ and are known as *Markov Chain Monte Carlo (MCMC)* methods.

Before introducing the MCMC samplers we briefly discuss computer generated uniform random samples and introduce two conceptually simpler methods, the inverse sampler and the independence sampler, that use uniformly distributed random numbers to generate random samples of more complicated pdf's.

8.3.1 Pseudo-random-numbers

Computers cannot generate real random number sequences, only pseudo-random numbers (*PRN*) sequences. PRN sequences approximate some of the properties of real random numbers. As they are generated from a deterministic algorithm they are periodic; a property real random sequences don't have. Given the limited amount of computer memory and sufficient time, a PRN algorithm will inevitably reproduce the same sequence forever. A PRN generator can be started from an arbitrary starting point, the *random seed*. It will reproduce the same sequence when reinitialized with this number.

To overcome the periodicity problem, computer PRN generators are designed with periods exceeding the expected age of the universe, which is sufficient for most applications. The *Mersenne-Twister* algorithm designed by *Matsumoto and Nishimura* [1998] has a period of $2^{19937} - 1$ iterations, and it is proven to produce PRN's that are uniformly distributed within an Euclidean space of up to 623 dimensions. Although, the pseudo-random character of the Mersenne-Twister can be detected from analyzing its output [*Berlekamp*, 1968; *Massey*, 1969], this has no negative operational effect for most applications. Since the Mersenne-Twister has a very long period and since is very fast, we use it as our PRN generator.

8.3.2 The inverse sampler

Inverse sampling is conceptually the simplest method for generating samples of a given probability density function from random samples that are uniformly distributed over $[0, 1]$. Inverse sampling is based on the fact that the cumulative distribution function $\mathbf{Pr}$, which is the integral over a probability density function $\mathbf{p}$

$$\mathbf{Pr}(x) = \int_{-\infty}^{x} dz\ \mathbf{p}(z) \tag{8.77}$$

is uniformly distributed over $[0, 1]$. If a number r is drawn uniformly in $[0, 1]$, then the random number x calculated through formula

$$x = \mathbf{Pr}^{-1}(r) \tag{8.78}$$

is a sample of the probability density function $\mathbf{p}$. This method will only work if the analytical expression of $\mathbf{p}(x)$ is known and $\mathbf{p}(x)$ is easily integrable. Even if those conditions are fulfilled, $\mathbf{Pr}(x)$ is almost never analytically invertible, and the method cannot be applied in multivariate settings.

8.3.3 The rejection sampler

The rejection sampler works in multivariate settings, does neither require the invertible condition on $\mathbf{Pr}(x)$ (8.78), nor does $\mathbf{p}(x)$ need to have an analytic form: it suffices that one can evaluate the probability density $\mathbf{p}$ for each x up to an unknown multiplicative constant c. If one can find a sampling distribution $\mathbf{p}_2(x)$, i.e., a distribution from which we know how to generate samples, and an associated "covering constant" M such that $M\ \mathbf{p}_2(x) \geq \mathbf{p}(x), \forall x$, then the following algorithm will produce samples of $\mathbf{p}$:

1. *draw* x from $\mathbf{p}_2(.)$, i.e. generate a random sample from $\mathbf{p}_2(.)$, and compute the ratio

$$r = \frac{\mathbf{p}(x)}{M\ \mathbf{p}_2(x)}$$

2. *accept* x with probability r, i.e. draw a sample u from the uniform distribution on $[0, 1]$ and accept x if $u \leq r$

To reduce computation time and increase the acceptance rate it is essential that the envelope $M\ \mathbf{p}_2(x)$ (see Fig.[8.8]) is as close to $\mathbf{p}$ as possible. This is, however, a difficult problem in high dimensional settings and therefore this simple approach is bound to fail.

8.3.4 MCMC samplers

Markov Chains

To understand how MCMC samplers produce samples from a given target distribution some concepts from the theory of Markov chains need to be introduced. Consider the random sequence $X^{(0)}, X^{(1)}, \ldots$ defined on a finite state space $\Omega = \{x_1, \ldots, x_k\}$. A Markov chain (MC) is a sequence that satisfies the *Markov property*, that the value of $X^{(t+1)}$ only depends on its history through its most recent past:

$$\begin{aligned}&\mathbf{p}(X^{(t+1)} = x_j | X^{(0)} = x_{i_0}, X^{(1)} = x_{i_1}, \ldots, X^{(t-1)} = x_{i_{t-1}}, X^{(t)} = x_i) \\ &= \mathbf{p}(X^{(t+1)} = x_j | X^{(t)} = x_i)\end{aligned} \tag{8.79}$$

Given an initial distribution $\mathbf{p}(X^{(0)} = x_{i_0})$, the transition probability for $X^{(t)}$ to $X^{(t+1)}$ determines the Markov chain. If the transition probability $\mathbf{p}(X^{(t+1)} = x_j | X^{(t)} = x_i)$ is time independent it is called homogeneous and commonly written by a *transition matrix* $P_{i,j}$. The $k \times k$ elements of $P_{i,j}$ are called transition probabilities. $P_{i,j}$ is the conditional probability for moving to state x_j if we are in state x_i.

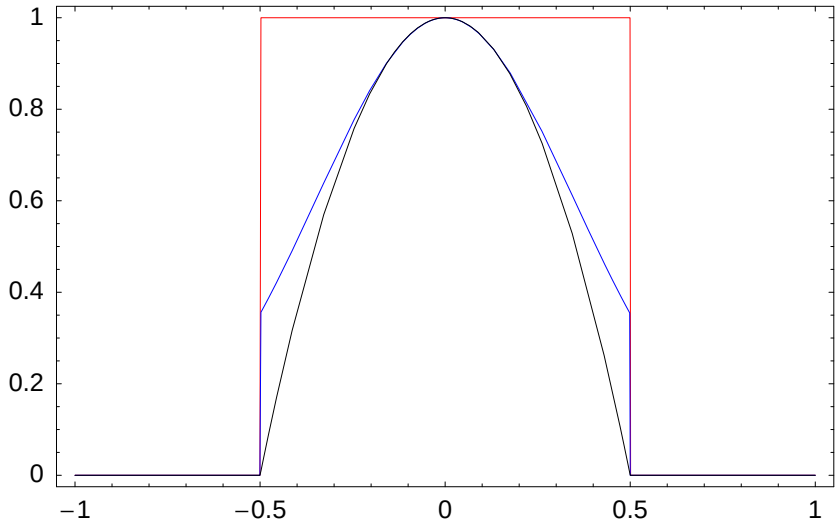


Figure 8.8: Truncated gaussian distribution (blue) and uniform distribution (red) as covering envelopes to a truncated parabola distribution (black). The more tightly enveloping gaussian produces acceptance rates about 90% and the unit distribution about 75% when sampled with the rejection algorithm.

From the probability definition of $\mathbf{p}$ it follows that

$$\sum_{j\in\Omega} P_{i,j} = 1 \text{ for all } i. \tag{8.80}$$

Suppose that in $t = 0$ the initial configuration is represented by a row vector $\boldsymbol{\pi}^0$. The k elements of $\boldsymbol{\pi}^0$ are

$$\boldsymbol{\pi}^0 = \left(\pi_1^0, \ldots, \pi_k^0\right) = \left(\mathbf{p}(X^0 = x_1), \ldots, \mathbf{p}(X^0 = x_k)\right). \tag{8.81}$$

Then $\mathbf{p}(X^{(1)} = x_j) = \pi_j^{(1)}$ is related to $\pi_i^{(0)}$ by

$$\begin{aligned} \pi_j^{(1)} &= \sum_{i\in\Omega} \pi_i^{(0)} P_{i,j} \\ &= \sum_{i\in\Omega} \mathbf{p}(X^0 = x_i)\mathbf{p}(X^{(1)} = x_j | X^{(0)} = x_i) \\ &= \sum_{i\in\Omega} \mathbf{p}(X^{(0)} = x_i, X^{(1)} = x_j) \\ &= \mathbf{p}(X^1 = x_j) \end{aligned} \tag{8.82}$$

If for some $\boldsymbol{\pi}$

$$\boldsymbol{\pi} = \boldsymbol{\pi} P, \tag{8.83}$$

$\boldsymbol{\pi}$ is a left eigenvalue of P with eigenvalue 1, then $\boldsymbol{\pi}$ is a *stationary distribution* of P, since if $\boldsymbol{\pi}^{(t)} = \boldsymbol{\pi}$, then $\boldsymbol{\pi}^{(t+1)} = \boldsymbol{\pi}^{(t)} P = \boldsymbol{\pi} P = \boldsymbol{\pi}$.

A Markov chain $\mathcal{M}$ is said *ergodic* with equilibrium distribution $\boldsymbol{\pi}$ if for any $\boldsymbol{\pi}^{(0)}$, $\boldsymbol{\pi}^{(t)} \to \boldsymbol{\pi}$ as $t \to \infty$. In other words, for sufficient large t the system is in equilibrium

and the states of $\mathcal{M}$ are distributed like $\boldsymbol{\pi}$. The ergodic condition on the MC guarantee that the empirical average

$$\lim_{N\to\infty} \frac{1}{N} \sum_{i=1}^{N} f(X_i) = \sum_{i\in\Omega} f(i)\pi(i) \tag{8.84}$$

converges to the probabilistic average $\mathbf{E}f$ [e.g. *Brémaud*, 1999, chap. 4].

Obviously not every MC is ergodic. The sufficient conditions for ergodicity are *irreducibility* and *reversibility*. An MC is said irreducible under P if for any two states x_i and x_j in Ω there is a path with non-zero probability linking x_i to x_j. A homogeneous MC is reversible if there is a $\boldsymbol{\pi}$ such that

$$\pi_i P_{i,j} = \pi_j P_{j,i} \text{ for all } i,\, j \in \Omega. \tag{8.85}$$

The reversibility condition is also known as the *detailed balance condition*. Since

$$\sum_i \pi_i P_{i,j} = \pi_j \tag{8.86}$$

$\boldsymbol{\pi}$ is always the stationary distribution for reversibility MC's.

The conditions for the distribution $\boldsymbol{\pi}$ to be the unique stationary distribution are formulated in the following theorem:

Theorem 1. *For an irreducible, aperiodic Markov chain $\mathcal{M}$ on a countable space with transition matrix P, if there exists a $\boldsymbol{\pi}$ such that $0 \le \pi_i \le 1$, $\sum_i \pi_i = 1$ and*

$$\pi_i P_{i,j} = \pi_j P_{j,i} \textit{ for all } i,\, j \in \Omega \tag{8.87}$$

then $\mathcal{M}$ is reversible and ergodic with unique equilibrium distribution π.

For more details about Markov chains, and demonstrations of the theorems the reader may consult e.g. *Häggström* [2002], *Brémaud* [1999], and *Meyn and Tweedie* [1993].

The Metropolis-Hasting sampler

The Metropolis-Hastings sampler is a generalization by [*Hastings*, 1970] of the Metropolis sampler [*Metropolis et al.*, 1953] which is based on the idea of simulating a *Markov Chain* in the state space so that the limiting/stationary/equilibrium (see [*Liu*, 2001, appendix] for a discussion) distribution of the chain is the target distribution $\pi(\mathbf{x})$, e.g., the distribution we want to sample. The Metropolis-Hasting algorithm initiates a Markov chain that has the stationary distribution of the target distribution. The Markov chain transition matrix is constructed in the following way. Given the current state $\mathbf{x}^{(t)}$:

1. draw $\mathbf{y}$ from the proposal distribution $T(\mathbf{x}^{(t)}, \mathbf{y})$
2. draw $U \sim \text{Uniform}[0, 1]$, and update

$$\mathbf{x}^{(t+1)} = \begin{cases} \text{y}, & \text{if} \quad U \le r(\mathbf{x}^{(t)}, \mathbf{y}) \\ \mathbf{x}^{(t)} & \text{otherwise} \end{cases}$$

where *Hastings* [1970] suggests

$$r(\mathbf{x},\mathbf{y}) = \min\left\{1, \frac{\pi(\mathbf{y})\ T(\mathbf{y},\mathbf{x})}{\pi(\mathbf{x})\ T(\mathbf{x},\mathbf{y})}\right\} \tag{8.88}$$

for the acceptance function. The algorithm simplifies to the original Metropolis algorithm when $T(\mathbf{x},\mathbf{y}) = T(\mathbf{y},\mathbf{x})$. Other expressions for the acceptance have been developed [*Liu*, 2001, chap 5]. It is generally not possible to privilege one expression over another on theoretical grounds, but *Peskun* [1973] was able to show that the original choice of $r(\mathbf{x},\mathbf{y})$ is optimal in terms of statistical efficiency for discrete spaces.

The proposal distributions most often encountered in practice are the independent and the random walk Metropolis sampler. In the independence sampler, the proposal density $T(\mathbf{x},\mathbf{y})$ is an independent distribution $g(\mathbf{y})$, i.e., the new proposed state $\mathbf{y}$ is generated from g independently of the current state $\mathbf{x}^{(t)}$. The resulting acceptance function is then

$$r(\mathbf{x},\mathbf{y}) = \min\left\{1, \frac{\pi(\mathbf{y})\ g(\mathbf{x})}{\pi(\mathbf{x})\ g(\mathbf{y})}\right\}. \tag{8.89}$$

The efficiency, that is the rate at which new propositions are accepted, depends, as for the rejection sampler, on how close the $g(\mathbf{y})$ is to the target $\pi(\mathbf{y})$. The often encountered choice of the uniform distribution for the proposal function simplifies the acceptance function to the original one proposed by Metropolis, but results most of the time in poor acceptance rates.

The random-walk Metropolis sampler samples the target distribution $\pi(\mathbf{x})$ by initiating a random walk in the configuration space. The current configuration $\mathbf{x}^{(t)}$ is "perturbed" through the addition of a random error: the new candidate is proposed as $\mathbf{y} = \mathbf{x}^{(t)} + \epsilon_t$. The $\epsilon_t \sim g_\sigma(.)$ are independent and identically distributed for each t. σ represents the step size, or range of the perturbation and it is tuned to the problem at hand by the user. The most commonly used proposal density g_σ, when no specific information on the target distribution is available, are spherically symmetric. Like for example, a spherical Gaussian distribution $N(0,\sigma^2 I)$ (I is the identity matrix), or the uniform distribution in a ball of radius σ. The random-walk Metropolis sampler then iterates the following steps:

from the current state $\mathbf{x}^{(t)}$,

1. draw $\epsilon \sim g_\sigma$ and set $\mathbf{y} = \mathbf{x}^{(t)} + \epsilon$, where g_σ is spherical symmetric and tuned by the user

2. draw $U \sim$ Uniform$[0,1]$, and update

$$\mathbf{x}^{(t+1)} = \begin{cases} \mathbf{y}, & \text{if} \quad U \leq r(\mathbf{x}^{(t)},\mathbf{y}) \\ \\ \mathbf{x}^{(t)} & \text{otherwise} \end{cases}$$

where

$$r(\mathbf{x},\mathbf{y}) = \min\left\{1, \frac{\pi(\mathbf{y})}{\pi(\mathbf{x})}\right\} \tag{8.90}$$

Random walks on finite intervals

In practice one often has to deal with parameters whose pdf is nonzero only on a finite interval. Those can either be reparameterized and mapped to $(-\infty, \infty)$ or one initiates a random walk on the finite interval. If from the current state $\mathbf{x}^{(t)}$ the new proposed state $\mathbf{y}$ is outside of the interval then the proposal is rejected and $\mathbf{x}^{(t+1)} = \mathbf{x}^{(t)}$. Alternatively one can have the random walk reflect on the interval borders. The only import point to consider, when doing Metropolis random walks, is to respect the symmetry of the proposal distribution: $T(\mathbf{x}, \mathbf{y}) = T(\mathbf{y}, \mathbf{x})$.

The Gibbs sampler

The Gibbs sampler [*Geman and Geman*, 1984] is an MCMC sampler that can be interpreted as a componentwise Metropolis Hastings algorithm where the proposals are made from the full conditionals. If the current state is $\mathbf{x}$ then at each time only one component is updated. Assume that component i is to be updated, i.e., $x_j = y_j \vee j \neq i$,

$$T_i(\mathbf{x}, \mathbf{y}) = \mathbf{p}(y_i|x_{-i}) = \mathbf{p}(y_i|x_1, x_2, \ldots, x_{i-1}, x_{i+1}, \ldots, x_n). \tag{8.91}$$

The notation x_{-i} means all values of $\boldsymbol{x}$ but the $i-$th, i.e.

$$x_{-i} = (x_1, x_2, \ldots, x_{i-1}, x_{i+1}, \ldots, x_n).$$

So the ratio in (8.88) is one and the proposals are always accepted.

$$\frac{\mathbf{p}(y_i, x_{-i})\ \mathbf{p}(x_i|x_{-i})}{\mathbf{p}(x_i, x_{-i})\ \mathbf{p}(y_i|x_{-i})} = \frac{\mathbf{p}(y_i|x_{-i})\ \mathbf{p}(x_{-i})\ \mathbf{p}(x_i|x_{-i})}{\mathbf{p}(x_i|x_{-i})\ \mathbf{p}(x_{-i})\ \mathbf{p}(y_i|x_{-i})} = 1. \tag{8.92}$$

There are two variants of the Gibbs sampler, either at iteration step t the ith component is chosen randomly in $(1, n)$ or all n components are systematically updated one after the other.

For the random scan Gibbs sampler we iterate the following steps: Let $\mathbf{x}^{(t)} = (x_1^{(t)}, x_2^{(t)}, \ldots, x_n^{(t)})$ at iteration t, then at iteration $t + 1$ do

1. randomly select i in $(1, \ldots, n)$, e.g. uniformly with probability $1/n$
2. draw $x_i^{(t+1)}$ from $\mathbf{p}(.|x_{-i})$, leaving all other components unchanged and set $\mathbf{x}^{(t+1)} = (x_1^{(t)}, x_2^{(t)}, \ldots, x_{i-1}^{(t)}, x_i^{(t+1)}, x_{i+1}^{(t)}, \ldots, x_n^{(t)})$

Why do MCMC samplers work?

The Metropolis-Hastings algorithm prescribes a transition rule $P(\mathbf{x}, \mathbf{y})$ under which the target distribution $\pi(\mathbf{x})$ is invariant [*Liu*, 2001] if the detailed balance condition holds:

$$\int_\Omega d\mathbf{x}\ \pi(\mathbf{x}) P(\mathbf{x}, \mathbf{y}) = \int_{\in\Omega} d\mathbf{y}\ \pi(\mathbf{y}) P(\mathbf{y}, \mathbf{x}) = \pi(\mathbf{y}). \tag{8.93}$$

The transition matrix for the Metropolis algorithm, c.f. 8.3.4, when $\mathbf{x} \neq \mathbf{y}$ corresponds to the probability to move from $\mathbf{x} \to \mathbf{y}$. It is the product of the proposal probability $T(\mathbf{x}, \mathbf{y})$ with the acceptance probability

$$P(\mathbf{x}, \mathbf{y}) = T(\mathbf{x}, \mathbf{y})\ \min\left\{1, \frac{\pi(\mathbf{y})\, T(\mathbf{y}, \mathbf{x})}{\pi(\mathbf{x})\, T(\mathbf{x}, \mathbf{y})}\right\} \tag{8.94}$$

for $\mathbf{x} \neq \mathbf{y}$. Then the detailed balance condition follows from:

$$\begin{aligned} \pi(\mathbf{x})P(\mathbf{x},\mathbf{y}) &= T(\mathbf{x},\mathbf{y})\ \min\left\{1, \frac{\pi(\mathbf{y})\,T(\mathbf{y},\mathbf{x})}{\pi(\mathbf{x})\,T(\mathbf{x},\mathbf{y})}\right\} \\ &= \min\left\{\pi(\mathbf{x})\,T(\mathbf{x},\mathbf{y}), \pi(\mathbf{y})\,T(\mathbf{y},\mathbf{x})\right\} \\ &= \pi(\mathbf{y})P(\mathbf{y},\mathbf{x}). \end{aligned} \tag{8.95}$$

Since the function in the second line of (8.95) is symmetric in $\mathbf{x}$ and $\mathbf{y}$. For $\mathbf{x} = \mathbf{y}$ the detailed balance condition holds trivially.

Summarizing simulated posterior inference

Once the posterior probability density function has been simulated and before we decide on how to summarize the information we recommend to plot the estimated empirical posterior probability density, i.e., the histogram. Of course, this can only be done for single and bivariate probability density functions. For $n-$variate pdf's one can plot one and two dimensional empirical marginals. Depending on the shape of the empirical probability density function we can choose appropriate summaries.

For example, if the empirical pdf is mono-modal and symmetric then the sample mean provides information about the location of the maximum and the average value. Additionally, the spread of the empirical pdf can be characterized by the sample standard deviation. If the empirical pdf's are skewed or heavy tailed the spread of the empirical pdf is often best summarized by the intervals, or surfaces in two dimension, delineating the $(0.68, 0.95, 0.997)$ probability regions. For a normal distribution this is equivalent to 1,2, and 3 standard deviations.

Under what conditions do the empirical summaries provide valid estimators? Suppose we want to estimate

$$\mathbf{E}\, g = \int_\Omega dx\ g(x)\boldsymbol{\pi}(x), \tag{8.96}$$

where Ω is the state space of the Markov chain $X = \{X_1, X_2, X_3, ...\}$ with invariant distribution $\boldsymbol{\pi}$. Then it can be shown, if X is *Harris ergodic*[2] and if $\mathbf{E}|g| < \infty$ [*Meyn and Tweedie*, 1993] that

$$\bar{g}_N = \frac{1}{N}\sum_{i=1}^{N} g(X_i) \to \mathbf{E}\, g \text{ as } N \to \infty \tag{8.97}$$

with probability 1. This is a consequence of the strong law of large numbers (SLLN)[3] [*Meyn and Tweedie*, 1993, Theorem 17.1.7] and the Harris recurrence condition assures that the SSLN holds for any starting distribution if it holds for one starting position.

Since the above introduced MCMC samplers induce a Markov chain satisfying the above regularity conditions, $\bar{g}_N$ estimates $\mathbf{E}\, g$ if we simulate X for a finite number of steps N. Obviously, it is now legitimate to ask about the run length of the simulation. How large should N be in order for $\bar{g}_N$ to be a good estimate of $\mathbf{E}\, g$? There is no general solution to this problem. However, a method called *exact sampling* introduced recently

[2]If finite state space Markov chains are generalized to uncountable state spaces, the "equivalent" finite state space ergodicity condition is the Harris ergodic condition.

[3]The strong law of large numbers states that the sample average converges almost surely to the expected value, i.e., with probability one.

by *Propp and Wilson* [1996], offers a complete solution since it produces an output whose distributions is exactly the equilibrium distributions and, it determines automatically how large N has to be. For the problems of our concern, we introduce two empirical methods for deciding on the run length of the simulation in the following section.

Convergence and other difficulties

When doing iterative simulations the first question that naturally arises is about the number of iterations N. The number should be large enough such that the obtained sample sequence is representative of the target distribution and such that the Monte Carlo approximation of our estimator, say $\bar{g}_N$, lies within a given tolerance. Indeed, $\bar{g}_N$ is not the exact value of the integral we want to approximate, but it is off by the amount $\bar{g}_N - \mathbf{E}\, g$, the *Monte Carlo error*. Of course, we don't know the Monte Carlo error since we don't know $\mathbf{E}\, g$, the quantity we want to estimate. Nevertheless, given certain regularity conditions, the Markov chain X and the function g will admit a *central limit theorem (CLT)*

$$\sqrt{N}(\bar{g}_N - \mathbf{E}\, g) \xrightarrow{d} \mathrm{N}(0, \sigma_g^2) \text{ as } N \to \infty \tag{8.98}$$

where $\mathrm{N}(0, \sigma_g^2)$ is the normal distribution with mean zero and variance σ_g^2,

$$\sigma_g^2 = \operatorname{var} g(X) + 2 \sum_{i=2}^{\infty} \operatorname{cov}(g(X_1), g(X_i)). \tag{8.99}$$

Note that "$\xrightarrow{d}$" means that the distribution of the random variable on the left side tends to the distribution on the right. For a discussion about when the CLT holds and on the different techniques to estimate σ_g^2 see for instance *Flegal et al.* [2007]. From all the proposed techniques the one based on the *batch means* is in our view the most easy to implement. In non-overlapping batch means the simulated output of length N is split into a blocks of length b. The batch means estimate of σ_g^2 is defined as

$$\hat{\sigma}_g^2 = \frac{b}{a-1} \sum_{i=1}^{a} (\bar{y}_i - \bar{g}_N)^2, \tag{8.100}$$

where $\bar{y}_i$ is

$$\bar{y}_i = \frac{1}{b} \sum_{j=(i-1)b+1}^{ib} g(x_j) \text{ for } i = 1, \ldots, a \tag{8.101}$$

(8.100) is, however, not a consistent estimator of σ_g^2 when used with fixed batch length and number. *Jones et al.* [2006] have shown that if the batch size and number of batches increases with the simulation length N, or more generally are a function of N, then $\hat{\sigma}_g^2 \to \sigma_g^2$ with probability 1. A convenient choice that works well with all applications is $b_N = \lfloor \sqrt{N} \rfloor$ and $a_N = \lfloor b_N / N \rfloor$ [*Flegal et al.*, 2007]. The run length dependent batch means, also called consistent batch means (CBM) to distinguish it from the version with fixed number of batches, the Monte Carlo standard error (MCSE) of $\bar{g}_N$ is estimated to be $\hat{\sigma}_g / \sqrt{N}$. The half-width of an asymptotically valid confidence interval for $E\, g$ is then

$$t_{a_N - 1} \frac{\hat{\sigma}_g}{\sqrt{N}} \tag{8.102}$$

where t_{a_N-1} is an appropriate quantile from the Student's t distribution with $a_N - 1$ degrees of freedom. The z-quantile of a pdf corresponds to the location x where

$$\int_{-\infty}^{x} dy\ \mathbf{p}(y) = \mathbf{Pr}(y < x) = z. \tag{8.103}$$

For a normal distribution of standard deviation σ the 0.84 quantile is 1σ, the 0.16 quantile is -1σ, therefore for $X \sim \mathrm{N}(\mu, \sigma)$ there is about 0.68 probability for the value of X to be in a 1σ interval about μ. As the Student t distribution asymptotically approaches a normal distribution for an infinite number of degrees of freedom [*Papoulis*, 2002, page 2007], the 1σ confidence interval for $\bar{g}_N$ is about $\frac{\hat{\sigma}_g}{\sqrt{N}}$.

For an overview about proposed convergence diagnostic techniques and simulation run length see *Cowles and Carlin* [1996].

In practice, none of the diagnostic methods will produce any useful output if the Markov Chains are not ergodic. According to our experience, it is best to repeat the simulations with different starting values, and visually assure that the Markov Chains are stationary by plotting the draws or the estimates of interest as a function of the iteration steps (also called trace plots), and discard the initial draws (burn in). Finally, we suggest to simulate until the MCSE is below the requested significant figures of the estimates. As seen in (8.100) and (8.102) the MCSE error decreases as $\sqrt{N}$ and is proportional to σ_g^2. It can be shown that the later can also be written as $\sigma_g^2 = \mathrm{var}\, g(X)\tau$, where τ is the *integrated autocorrelation time* (IACT) or *autocovariance time* [*Sokal*, 1996]

$$\tau = 1 + 2\sum_{i=2}^{\infty} \mathrm{cov}(g(X_1), g(X_i))/\mathrm{var}\ g(X). \tag{8.104}$$

In summary, to reduce the MCSE error one has to simulate as long as possible and decrease the autocorrelation as fast as possible. The latter, at least for the Metropolis sampler is related to the choice of the random walk jumping rule. Indeed, if the jumps size is too small each update will change the state by only a small amount, so many updates will be required to move a substantial distance. As the state is only altered slightly, most proposal will be accepted, and the acceptance rate is high. On the other hand, if the jump size is too large, the proposals are almost always rejected, the acceptance rate is also low. Both cases lead to highly correlated chains and large values for τ. Note that the correlation length can to some extent be reduced if only each $k-$th sample is retained during simulation, this procedure is known as *thinning*.

It is hard to give a general advice on choosing efficient jumping rules, but theoretical results on sampling a normal distribution with a random walk Metropolis sampler using a normal proposal density can be used as a guideline. For normal distributions an optimal jumping rule produces an acceptance rate of about 44% in one dimension and decreases to about 23% for multidimensional problems (> 5) [*Gelman et al.*, 2003, chap. 11.9]. In practice, for other distributions, acceptance rates of about $20 - 30\%$ for multidimensional problems, with one parameter updating schemes produce acceptable MCSE values. A problem is that we often do not know enough about the distribution π to choose suitable values for the step sizes w. A common approach is to perform preliminary runs using different values for w until the acceptance rate results in acceptable MCSEs. However, this can be quite a tedious task if the number of parameters is large (> 10). Different automatically adapting step-size procedures have been proposed, but seem only to converge to the correct estimates under certain conditions [*Neal*, 2005].

8.4 An illustrative example

To further illustrate and clarify the above concepts we give an example of MCMC inversion. In this example, we want to infer the core state and the three principal moments of inertia of the planet Mercury from its gravity field, its obliquity, and from its 88 *day* libration amplitude. For a detailed discussion about the hypotheses leading to the forward model see for instance *Van Hoolst* [2007].

The parameters of the model are the three principal moments of inertia and the ratio of the polar moment of inertia of the planet to that of the silicate shell comprising mantle and crust. If Mercury is solid this ratio is equal to one, if Mercury's core is partially liquid it is smaller than one. Since the data, the gravity field, the obliquity, and the 88 day libration amplitude are known up to a given uncertainty, we describe them by probability density functions. We establish the expression for the posterior probability density function up to a constant from the probability density functions describing the data, the model relating the parameters to the data, and the prior knowledge we attribute to the parameters. We simulate draws from the a posterior density with the Metropolis random walk sampler. From the set of samples, we estimate the empirical marginal posterior distribution of the individual moments of inertia.

8.4.1 Forward problem

The forward problem describes the mathematical relation between the three principal moments of inertia of A, B, C and the ratio $c = C_m/C$ of the polar moment of inertia C_m of the shell to that of the planet C, to the Stokes coefficients C_{20} and C_{22}, to the obliquity θ, and to the amplitude γ_1 of the 88 day libration. The forward problem can be expressed as

$$C_{20} = \frac{\frac{1}{2}(A+B) - C}{m_a r_a^2} \tag{8.105}$$

$$C_{22} = \frac{B-A}{4 m_a r_a^2} \tag{8.106}$$

$$\theta = -\frac{\mu C \sin\iota}{\mu C \cos\iota + 2n\left(\frac{7}{2}e - \frac{123}{16}e^3\right) - n\left(1-e^2\right)^{-3/2} C_{20}} \tag{8.107}$$

$$\gamma_1 = \frac{3}{2}\frac{B-A}{C}\frac{1}{C_m/C}\left(1 - 11e^2 + \frac{959}{48}e^4\right), \tag{8.108}$$

where $e = 0.206$ is the eccentricity, $\mu = -6.07019\ 10^{-13}\mathrm{s}^{-1}$ is the orbital precession rate, $n = \sqrt{G(M_\odot + m_a)/a^3}$ is the mean motion, and $\iota = 8.6°$ is the inclination of the orbital plane. Finally, $m_a = 3.302 \cdot 10^{23}$kg and $r_a = 2440$km are the mass and the average radius of Mercury, $M_\odot = 1.98911 \cdot 10^{30}$kg is the mass of the Sun, and $a = 5.79061 \cdot 10^{10}$m is Mercury's the semimajor axis. We assume that the uncertainties on those auxiliary variables are negligible.

The data and the associated uncertainties of the gravity coefficients and of the obliquity and of the libration amplitude available are given in table [8.1].

C_{20}	C_{22}	θ	γ_1
$(-6 \pm 2)10^{-6}$	$(1 \pm 0.5)10^{-5}$	$(6.1378 \pm 0.2909)10^{-4}$	$(1.736 \pm 0.097)10^{-4}$

Table 8.1: The Stokes coefficients C_{20} and the C_{22} are from *Anderson et al.* [1987] and the obliquity θ and libration amplitude γ_1 are from *Margot et al.* [2007].

8.4.2 Direct inversion

The equations forming the forward problem can be solved algebraically for the parameters A, B, C, and C_m/C. The resulting parameter values calculated from the mean data values (Tab.[8.1]) are

$$A = 0.427208,\ B = 0.427248,\ C = 0.427288,\ \text{and}\ C_m/C = 0.467017. \tag{8.109}$$

The normalized principal moments of inertia are increasing from A to C but are larger than 0.4, indicating that the planet is denser in the mantle than in the core. Such a configuration is impossible since it would be gravitationally unstable. Since $C_m/C < 1$, the data are in favor of a planet with a core that is not fully solid. To take into account the uncertainties associated with the data we also perform a Monte Carlo error propagation on the algebraic equations relating the parameters to the data. The resulting histograms are shown in figure [8.9]. The resulting principal moments of inertia have their average value at about 0.427 with standard deviation of about 0.13, see Tab.[8.2]. The histogram for the C_m/C parameter shows that there is a small probability for negative values and a somewhat larger probability for values larger than one.

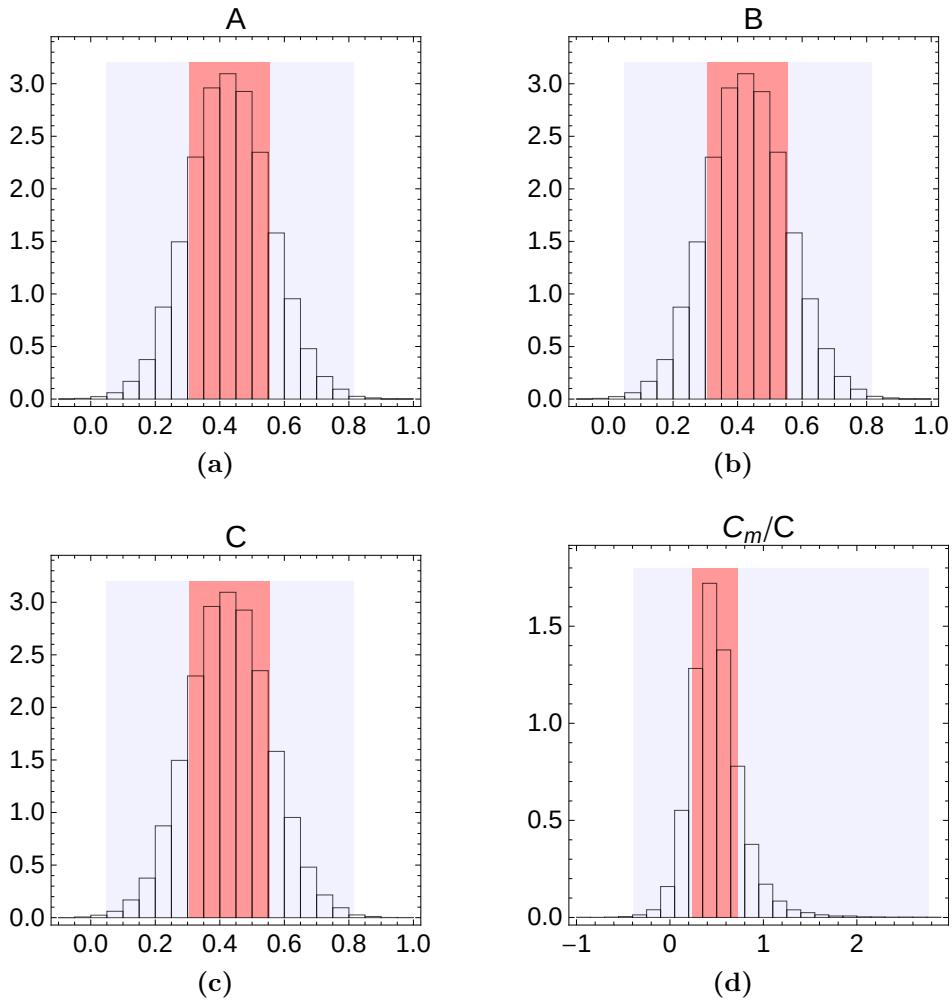


Figure 8.9: Empirical marginal probability density functions for the parameters A, B, C, and C_m/C. The blue surface represents the 0.997 probability domain the and red surface the 0.68 probability domain.

8.4.3 Bayesian inversion

We suppose that the random data variables are independent and choose each datum random variable to have a normal distribution. The associated mean values and standard deviations are given in Tab.[8.1]. Since the data random variables are independent and the model predictions are deterministic the likelihood is the product of the four individual conditional probabilities describing the data. The likelihood for the data given the parameters can be obtained from Eq. (8.38) as

$$\mathbf{p}(C_{20}, C_{22}, \theta, \gamma_1 | A, B, C, c) = \frac{1}{4\pi^2 \sigma_{C_{20}} \sigma_{C_{22}} \sigma_\theta \sigma_\lambda} \tag{8.110}$$

$$\exp - \left\{ \frac{(C_{20}^* - C_{20}(A,B,C))^2}{2\sigma_{C_{20}}^2} + \frac{(C_{22}^* - C_{22}(A,B))^2}{2\sigma_{C_{22}}^2} + \right.$$
$$\left. \frac{(\theta^* - \theta(A,B,C))^2}{2\sigma_\theta^2} + \frac{(\gamma_1^* - \gamma_1(A,B,C,c))^2}{2\sigma_{\gamma_1}^2} \right\}, \tag{8.111}$$

where the "*" superscripted quantities are the measured data found in Tab.[8.1]. The posterior probability density function is then

$$\mathbf{p}(A, B, C, c | C_{20}, C_{22}, \theta, \gamma_1) \propto \mathbf{p}(C_{20}, C_{22}, \theta, \gamma_1 | A, B, C, c)\, \boldsymbol{\pi}(A, B, C, c), \tag{8.112}$$

where $\boldsymbol{\pi}(A, B, C, c)$ is the joint prior of the parameters. We take the prior pdf on parameter c independent on that of A, B, and C:

$$\boldsymbol{\pi}(A, B, C, c) = \boldsymbol{\pi}(A, B, C)\, \boldsymbol{\pi}(c). \tag{8.113}$$

To illustrate the influence of the prior knowledge on the inferred probability density functions of the parameters and on their summaries we consider different joint priors for the parameters A, B, and C. From here on, the symbols designating the moments of inertia are normalized by $m_a r_a^2$.

1. flat non-informative prior[4] on c and A, B, and C

2. weak prior constraining the moments of inertia to be positive, enforcing that as per definition that $A < B < C$, and that the shell's moment of inertia is smaller or equal the planet's moment of inertia:

$$\boldsymbol{\pi}(c) = 1 \quad \text{if } 0 < c \leq 1 \tag{8.114}$$

$$\boldsymbol{\pi}(A, B, C) = \begin{cases} k & \text{if } 0 < A < B < C, \\ 0 & \text{otherwise.} \end{cases} \tag{8.115}$$

[4]By flat prior is meant that the a priori value of the parameter is constant over $\mathbb{R}$. Note that this prior is not normalizable and therefore it is not a probability density function. Those priors are also called improper. Since the likelihood is a Gaussian the posterior probability density function is well defined. The choice of the improper prior is for pure convenience. An equivalent proper prior is $\boldsymbol{\pi}(x) = 1/1000$ for $0 \leq x \leq 1000$ and $\boldsymbol{\pi}(x) = 0$ otherwise.

3. weak geophysical prior similar to prior 2 with the supplemental constraint that in order for the planet to be stably stratified the normalized moment of inertia are less or equal 0.4:

$$\boldsymbol{\pi}(c) = 1 \quad \text{if } 0 < c \leq 1 \tag{8.116}$$

$$\boldsymbol{\pi}(A,B,C) = \begin{cases} k & \text{if } 0 < A < B < C \leq 0.4, \\ 0 & \text{otherwise.} \end{cases} \tag{8.117}$$

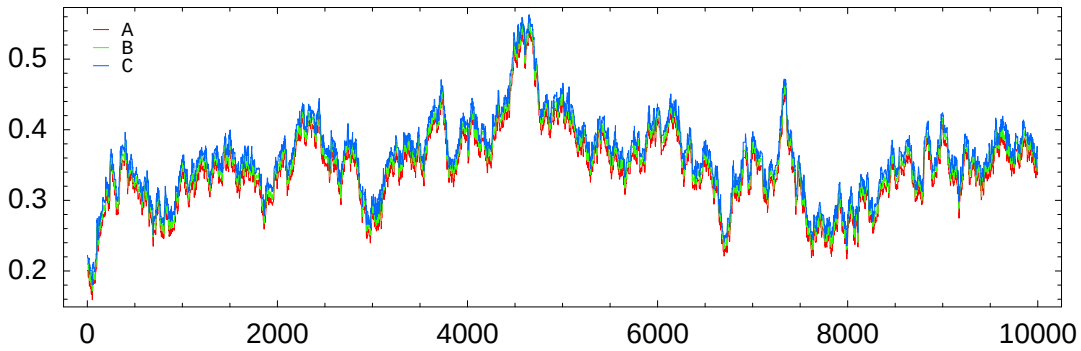
where k is a constant defined such that

$$\int dA\, dB\, dC\; \boldsymbol{\pi}(A,B,C) \equiv 1. \tag{8.118}$$

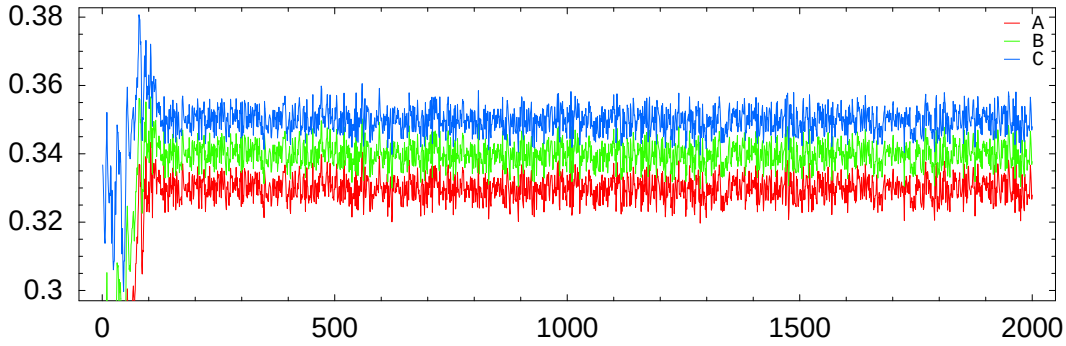
8.4.4 Sampling and other practical considerations

In principle, the proportionality constant appearing in the posterior pdf (8.112) could be calculated by numerical integration. Once the proportionality constant is known, other estimates like the mean values of the different moments of inertia or the marginal histograms could also be calculated by numerical integration. However, it is unlikely that simple integration schemes will succeed. Here, we therefore simulate realizations of the posterior probability density function and from the generated samples estimate for all parameters marginal histograms, mean values and probability intervals. To simulate realizations of the posterior pdf we use the Metropolis random walk sampler introduced in Sect.[8.3.4].

As a starting configuration for the Metropolis sampler we use a draw from the parameter joint prior probability density function. In each step of the iteration, we update all parameters simultaneously by drawing a new proposal from a quadri-variate normal distribution that has the present configuration as a mean vector. We initially chose a diagonal covariance matrix for the normal distribution, and by trial, and error selected step sizes for the individual parameters in order to obtain acceptance rates not too low ($< 10\%$) and not to high ($> 40\%$). Even with step widths of about 10^{-6} the acceptance rate was still below 2%. From the trace plot of the parameters A, B, and C (Fig.[8.10a]) it can be seen that the individual chains are not in a stationary regime. When analyzing the volume in configuration space for A, B, and C where their marginal posterior pdf is significantly different from zero (Fig.[8.11a]) this is not really surprising. Empirically, we found that a better choice for the covariance matrix is obtained by aligning the principal axis of the variance ellipsoid of the normal distribution to those of the posterior distribution. This is done by computing the sample covariance matrix from the samples of the run with the diagonal covariance matrix and iterated until an acceptance rate of about 20% is obtained. The trace plots of this much improved configuration are shown in Fig.[8.10b]. The individual chains are visually stationary after about 200 iterations. In order to further decrease the correlation between successive samples only each 10th sample is retained (thinning). With this thinning choice the correlation length drops below 10 (see Fig.[8.12]). We run the sampler until the Monte Carlo standard errors (8.104) on the estimated sample means of the parameters are below 0.1% (after about $6 \cdot 10^6$ generated samples). Finally, to diminish the effect of the starting configuration, we discard the first 10% of the samples (burn-in).

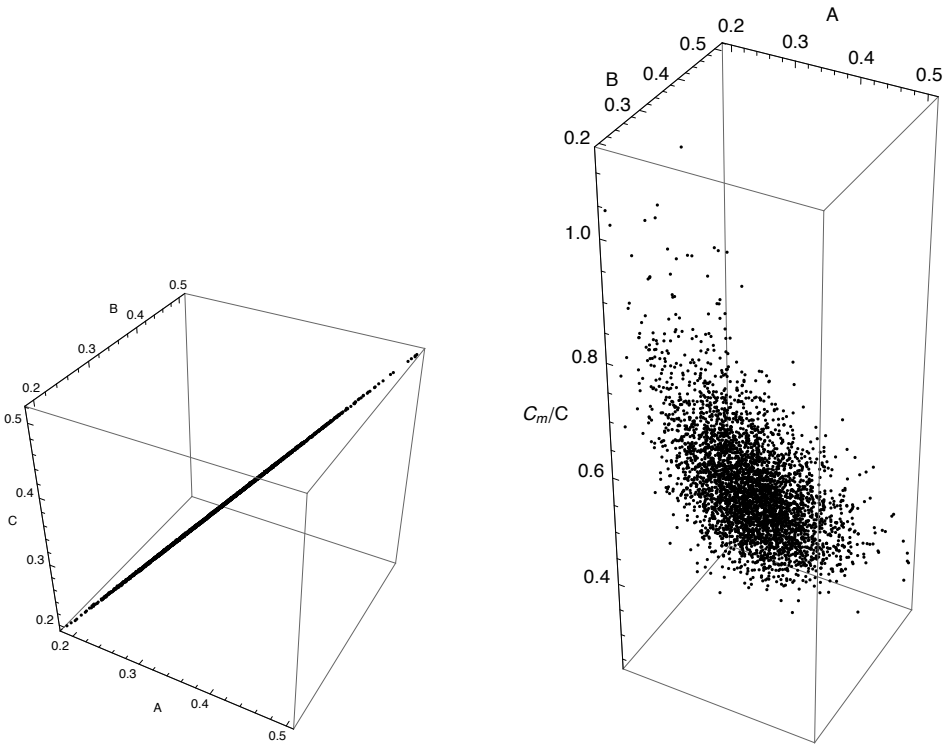


(a)



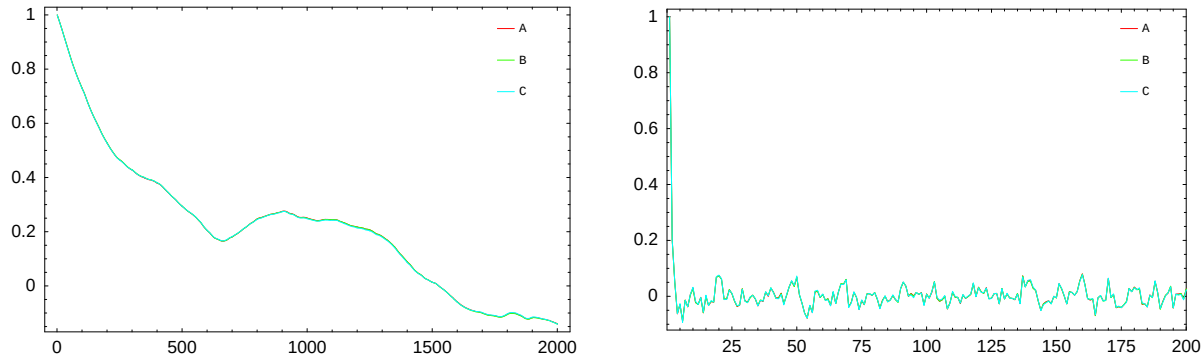
(b)

Figure 8.10: Trace plots for A, B, and C for the naive step size selection (top) and for the problem adapted step size (bottom).



(a) **(b)**

Figure 8.11: Loci in parameter space where the marginal pdf's of A, B, C and $C_m/C, B, C$ are significantly different from zero.



(a) **(b)**

Figure 8.12: Autocorrelation function for A, B, and C for the naive step size selection (left) and for the problem adapted step size (right).

8.4.5 Results

MCMC inversion with flat priors

The estimated values of the moments of inertia and the C_m/C ratio are somewhat higher and the estimated standard deviations are similar to those obtained through the direct inversion, see Tab.[8.2]. Again, the data allows for $C_m/C > 1$ and has a small negligible probability for $C_m/C < 0$. The estimated marginal pdf's are shown in Fig.[8.13]. Note that with the exception of the marginal pdf for C_m/C, the estimated pdf's of A, B, and C are somewhat broader than those obtained from the direct inversion method.

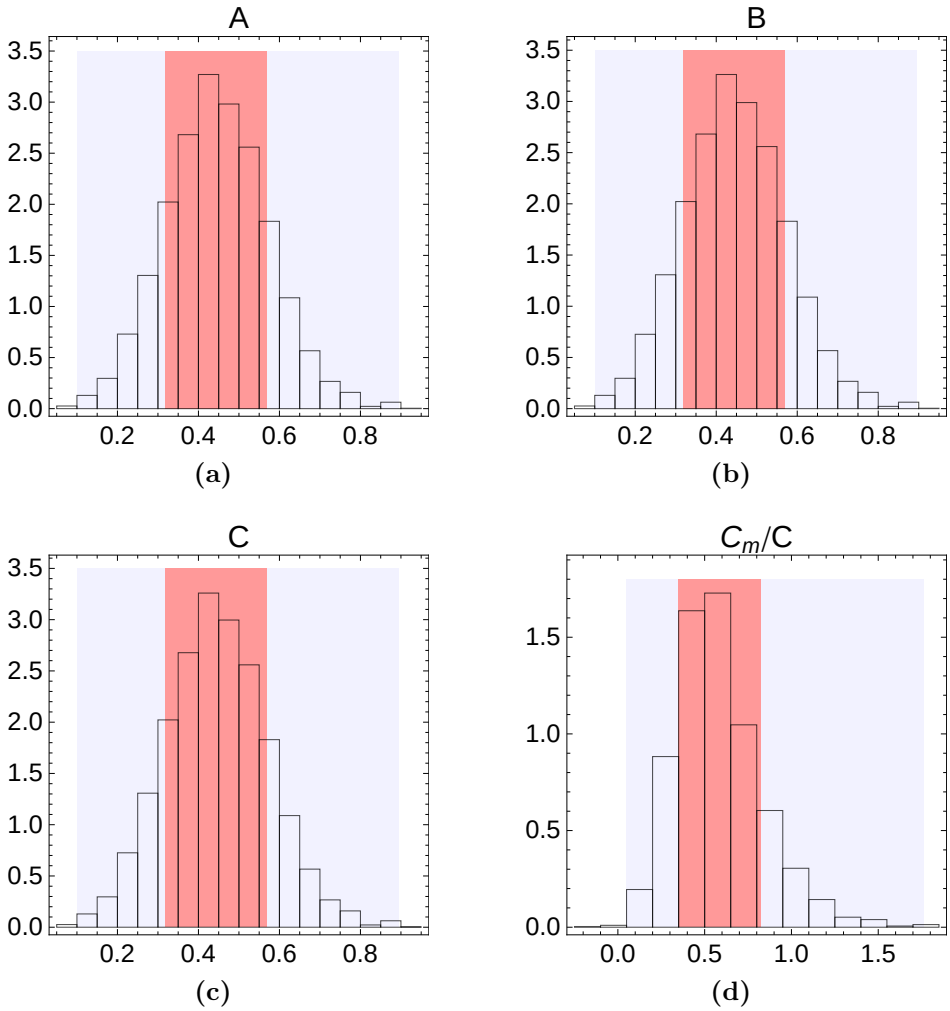


Figure 8.13: Empirical marginal probability density functions for the parameters A, B, C, and C_m/C. The blue surface represents the 0.997 probability domain the and red surface the 0.68 probability domain.

MCMC inversion with prior setting 2

For this inversion the prior constraints are: $0 \leq A \leq B \leq C$ and $0 < C_m/C \leq 1$. Compared to the flat prior case the estimated average moments of inertia are somewhat larger, see Tab.[8.2]. The estimated marginal pdf's are shown in Fig.[8.14].

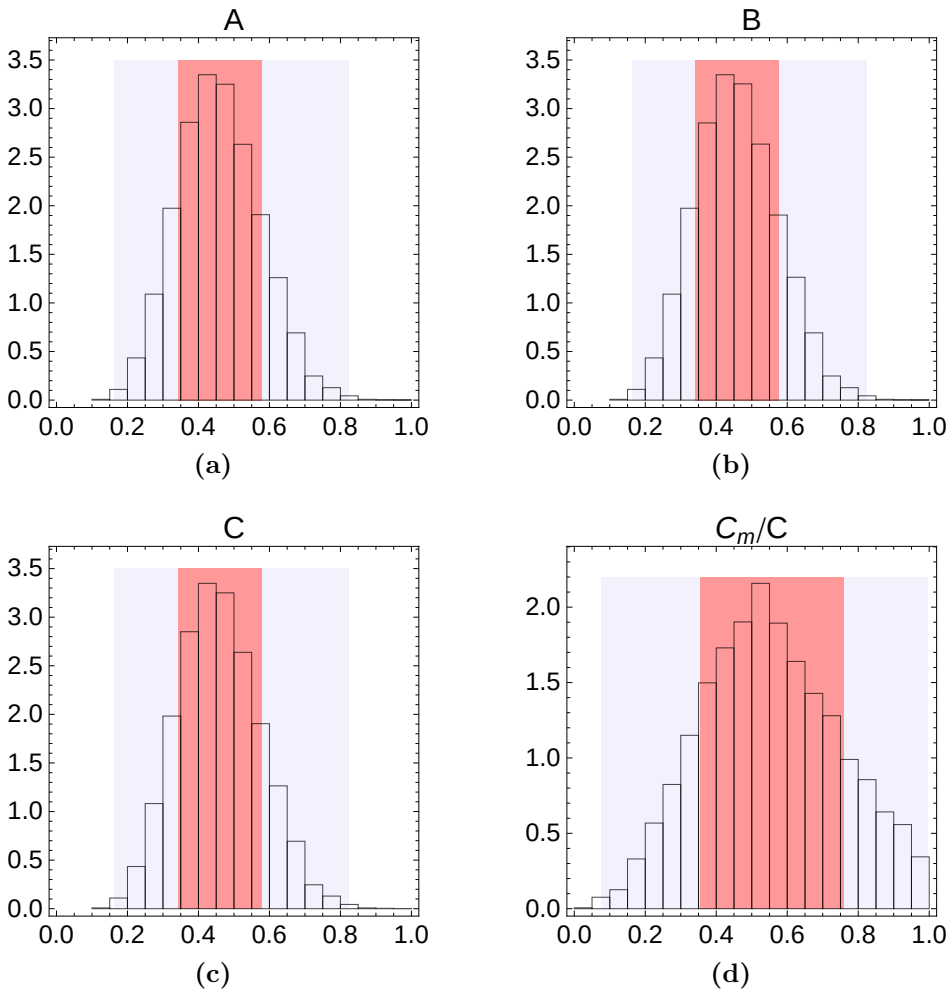


Figure 8.14: Empirical marginal probability density functions for the parameters A, B, C, and C_m/C for prior setting 2. $0 \leq A \leq B \leq C$ and $0 < C_m/C \leq 1$. The blue surface represents the 0.997 probability domain the and red surface the 0.68 probability domain.

MCMC inversion with prior setting 3

Compared to the previous setting we have the supplementary constraint that $C \leq 0.4$. The resulting pdf's have their tails clipped on the right side (Fig.[8.15]). Because of the restricted value range of A, B, and C the estimated average values and standard deviations are lower than those of the previous settings (Tab.[8.2]). Note that the histograms for A, B, and C are highly unsymmetrical, therefore, the estimated mean and median are strictly speaking not representative summaries of the probability densities functions.

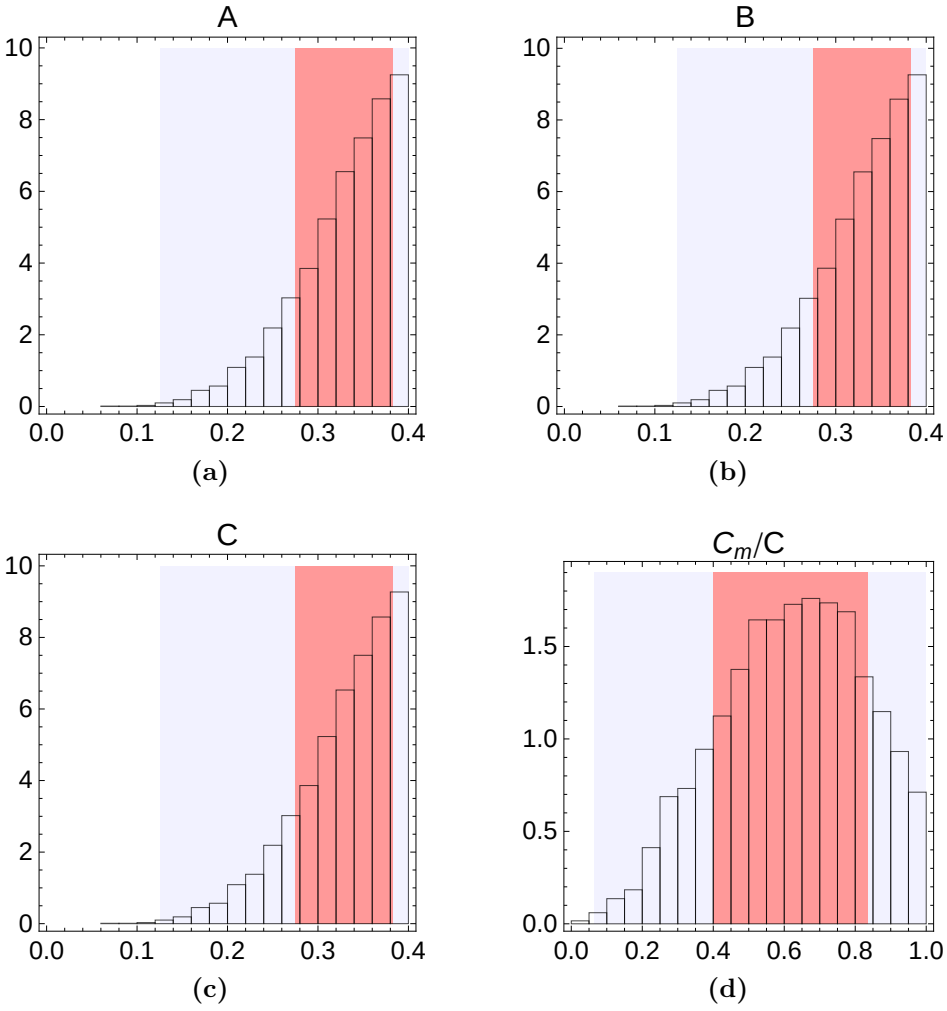


Figure 8.15: Empirical marginal probability density functions for the parameters A, B, C, and C_m/C for prior setting 3. $0 \leq A \leq B \leq C \leq 0.4$ and $0 < c \leq 1$. The blue surface represents the 0.997 probability domain the and red surface the 0.68 probability domain.

8.4.6 Wrap up

The above results clearly illustrate the influence and importance of the different priors on the estimated parameter values. The measured values of the Stokes coefficients C_{20} and C_{22} and their relatively large associated uncertainties lead to inferred pdf's on the

parameters that show non-negligible probabilities for unphysical parameters values if the parameters are not constrained by informative priors. There is a low probability for small C_m/C values, indicating that a large core for Mercury is less probable than a small core. There is a probability of about 0.95 that $C_m/C < 0.86$ for prior setting 1 and $C_m/C < 0.91$ for prior setting 2 (Fig.[8.16]). For prior setting 3, the most probable value for C_m/C is about 0.7 ± 0.1. Within a reasonable set of assumptions about the composition and thermal state of Mercury, *Rivoldini et al.* [2009] have shown that this would imply that Mercury has a core radius of less than 1850km, about the smallest core radius possible within the model assumptions. Because of the poor quality of the data, nothing informative about the principal moments of inertia can be inferred. With the exception of the relatively confident affirmation that they are larger than 0.2. In order for the data to allow for an estimate of the moment of inertia of Mercury with about the same precision we presently have on the moment of inertia of Mars, the uncertainties on the data have to be reduced by more than a factor of 100.

	mean	median	68%	95%	99.7%
Direct inversion					
A	0.4288	0.4279	$[0.3031, 0.5541]$	$[0.184, 0.67940]$	$[0.1594, 0.8079$
B	0.4289	0.4279	$[0.3032, 0.5542]$	$[0.1841, 0.6795]$	$[0.1594, 0.8080$
C	0.4289	0.4280	$[0.3032, 0.5542]$	$[0.1841, 0.6796]$	$[0.1594, 0.8081$
C_m/C	0.4910	0.4594	$[0.2395, 0.7267]$	$[0.0094, 1.1370]$	$[-0.0473, 2.4335]$
Flat priors					
A	0.4457	0.4438	$[0.3201, 0.5727]$	$[0.1968, 0.6948]$	$[0.1595, 0.8277]$
B	0.4457	0.4438	$[0.3201, 0.5728]$	$[0.1968, 0.6948]$	$[0.1596, 0.8278]$
C	0.4457	0.4439	$[0.3202, 0.5728]$	$[0.1969, 0.6949]$	$[0.1595, 0.8279]$
C_m/C	0.5918	0.5480	$[0.3444, 0.8108]$	$[0.1793, 1.3131]$	$[0.1535, 2.5986]$
Prior: $0 \leq A \leq B \leq C$ and $0 < C_m/C \leq 1$					
A	0.4637	0.4568	$[0.3446, 0.5835]$	$[0.2477, 0.7084]$	$[0.2266, 0.8237]$
B	0.4637	0.4569	$[0.3447, 0.5835]$	$[0.2477, 0.7084]$	$[0.2266, 0.8238]$
C	0.4637	0.4569	$[0.3447, 0.5836]$	$[0.2477, 0.7085]$	$[0.2266, 0.8239]$
C_m/C	0.5364	0.5244	$[0.3404, 0.7423]$	$[0.1837, 0.9299]$	$[0.1702, 0.9965]$
Prior: $0 \leq A \leq B \leq C \leq 0.4$ and $0 < C_m/C \leq 1$					
A	0.3301	0.3411	$[0.275, 0.38280]$	$[0.2049, 0.3969]$	$[0.1789, 0.3999]$
B	0.3301	0.3412	$[0.2751, 0.3828]$	$[0.2049, 0.3969]$	$[0.1789, 0.3999]$
C	0.3301	0.3412	$[0.2751, 0.3829]$	$[0.2050, 0.3970]$	$[0.1789, 0.3999]$
C_m/C	0.6206	0.6304	$[0.4056, 0.8412]$	$[0.2116, 0.9644]$	$[0.1722, 0.9972]$

Table 8.2: Estimated mean, median, standard deviation, and probability intervals $(0.68, 0.95, 0.997)$ for the direct inversion with Monte Carlo error propagation and for the MCMC inversion with the 3 different prior settings.

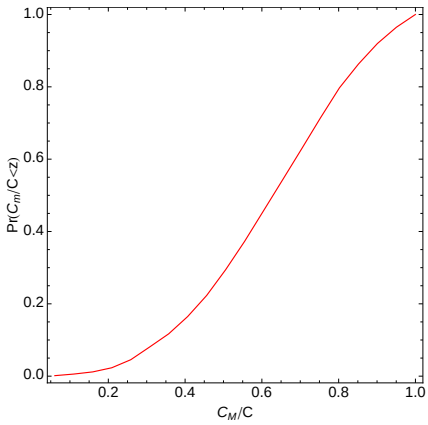


Figure 8.16: Probability for C_m/C for prior setting 3 ($0 \leq A \leq B \leq C \leq 0.4$ and $0 < c \leq 1$).

Chapter 9

Joint inversion of electromagnetic, geodetic, and seismic data

9.1 Introduction

In this chapter we show how electromagnetic, seismic, and geodetic data can jointly be used to infer knowledge about the interior structure of the silicate shell of terrestrial planets. As stated previously (see Chapt.[7]) we will not use raw data but rather the following geophysical quantities that have been derived from the raw data: the electrical conductivity and the bulk sound velocity of the mantle, and the moment of inertia of planet's silicate shell. We will, however, refer to these quantities as data. The electrical conductivity of each mineral inside the mantle has a particular strong dependence on temperature and iron content (see Sect.[3.5]). The bulk sound velocity of each mineral depends on the compressibility and density and both quantities depend on pressure and temperature (see Sect.[3.3]). Finally, the moment of inertia of the silicate shell depends on the repartition of masses inside the shell. It is then natural to parameterize an interior model that maps the temperature and the mineralogy of the mantle, and the density of the crust to the data. Since the functional expressions relating the parameters to the data are highly non-linear in the parameters (see Sect.[3.3] and Sect.[3.5]) we use the Bayesian inversion method introduced in the previous chapter to gain knowledge about the parameters from the data.

The chapter is organized as follows: We first explain the forward problem and describe in detail the model parameters. We then discuss the simulated data sets that we use to validate our approach and motivate the data associated uncertainties. In the next section, we construct the posterior probability density function. We introduce two types of likelihood functions, one based on a deterministic model and the second one based on a stochastic model. We finish the section by giving practical details about our implementation for simulating the posterior distribution. We then invert the model on the simulated data sets and discuss the ramification related to the prior knowledge, likelihood function, and different scenarios about the quality of the data. By quality we mean not only the measurement uncertainties, but also the data availability due to short data assimilation periods, instrument failure, or sheer absence because of unmet initial experimental hypothesizes. The quality of the data of the seismic, electromagnetic, and geodesy experiment could decrease due to, e.g., too weak and too shallow seismic activ-

ity resulting in a partially sampled planet, a layer of substantial electrical conductivity in the shallow mantle that impedes the diffusion of the magnetic waves to the deeper mantle, a solid core for which the moment of inertia cannot be determined from geodesy measurements.

9.2 The forward problem and the model parameters

Similarly to Chapt.[1] we assume a spherically symmetric, isotropic, and non-rotating planet of radius r_a in hydrostatic equilibrium. The interior is subdivided into three chemically homogeneous reservoirs: the crust, the mantle, and the core. In comparison to the interior model described in Chapt.[1] we introduce four simplifying approximations. We consider the thickness of the crust and the size of the core to be known. In addition, we do not detail the structure of the core but rather characterize it by its average density, and we assume that the pressure gradient inside the mantle of Mars is a constant[*Mocquet et al.*, 1996][1]. We further assume that the bulk sound velocity and the electrical conductivity have been determined at n equidistant depths within the mantle and therefore subdivide the mantle into n layers of equal thickness. The mean depth of the layers correspond to the depths for which the bulk sound velocity and the electrical conductivity have been determined. Within each layer, the bulk sound velocity, and the electrical conductivity are constant.

The parameters of the interior model are the density of the crust and the pressure gradient, the temperature profile, and the mineralogy of the mantle. For a given set of parameter values, the bulk sound velocity, the density, and the electrical conductivity can be calculated from the forward model, which we explain below. From the density in each layer of the mantle and from the density of the crust the moment of inertia of the silicate shell of the planet is calculated.

For the assumed linear pressure increase in the mantle, the pressure in the i-th layer is

$$P(z_i) = P_c + \nabla P(z_i - d_c), \tag{9.1}$$

where d_c is the thickness of the crust, ∇P the pressure gradient in the mantle, and z_i the depth of the bottom of layer i. The pressure at the top of the mantle P_c is obtained by integrating the hydrostatic pressure equation (2.1) and the Poisson equation (2.2) from the surface to the bottom of the crust

$$P_c = \frac{\rho_c d_c}{r_a - d_c}\left[g_a r_a - \frac{2}{3}\pi G \rho_c d_c (3r_a - d_c)\right], \tag{9.2}$$

where ρ_c is the density of the crust, r_a the mean radius of the planet, and $g_a = g(r_a)$ the surface gravity. We neglected the very small contribution of the surface pressure.

As explained in Chapt.[3] the bulk sound velocity, density, and electrical conductivity inside that mantle at given pressure and temperature can be calculated if the mantle mineralogy is specified. In our model the mantle mineralogy is specified through the volume

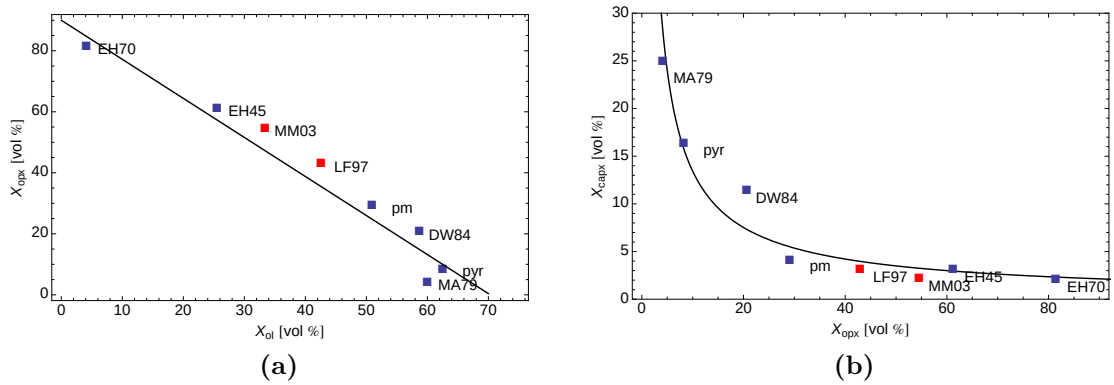
[1] It can be shown empirically that for the interior models we consider below this assumption is approximatively valid. Here, we make this assumption for practical reason since calculating the pressure inside the mantle from the hydrostatic pressure equation (2.1) and Poisson (2.2) equations result in a significantly longer computer runtime.

fractions of the low pressure minerals olivine ($X_{\rm ol}$), orthopyroxene ($X_{\rm opx}$), clinopyroxene ($X_{\rm capx}$), and garnet ($X_{\rm gt}$) and by the iron number (Fe#) which specifies the bulk mantle atomic fraction of iron. Note that in this chapter we denote the bulk atomic fraction of iron by $x_{\rm Fe}$,

We will also consider a simplified mantle mineralogy model by *Verhoeven et al.* [2005]:

$$\begin{aligned} X_{\rm opx} &= -1.28 X_{\rm ol} + 90 \\ X_{\rm capx} &= 92.3 X_{\rm opx}^{-0.837} \\ X_{\rm gt} &= 100 - X_{\rm ol} - X_{\rm opx} - X_{\rm capx}, \end{aligned} \tag{9.3}$$

where the volume fractions are in vol%. Note that the above relations are only valid if $X_{\rm ol} < 70.3$vol%. With these relations the volume fractions of orthopyroxene, Ca-pyroxene, and garnet can be calculated from the volume fraction of olivine so that the mantle mineralogy is described by only two parameters: $X_{\rm ol}$ and $x_{\rm Fe}$. The numerical values in (9.3) have been obtained by fitting the volume fractions of the bulk mantle models DW84, EH45, EH70, PM, pyr, and MA79 models, see Sect.[6.2.2]. Fig.[9.1] shows the empirical relations (9.3) together with the volume fractions of the minerals used for the fit and the mantle mineralogy models LF97 and MM03 (see Sect.[6.2.2]).



(a) **(b)**

Figure 9.1: Volume fractions of olivine ($X_{\rm ol}$) versus orthopyroxne ($X_{\rm opx}$) and volume fractions of orthopyroxne versus clinopyroxene ($X_{\rm capx}$) of the mantle mineralogy models pm, pyr, MA79, DW84, LF97, EH45, EH70, MM03. The black curves are functional fits true data points of models pm, pyr, MA79, DW84, EH45 and EH70.

For all the models, with the exception of MA79, the calculated fractions of $X_{\rm opx}$ and $X_{\rm capx}$ deviate by less than about 6vol% from the model volume fractions. For model MA79 the deviations are about 10vol%. Since the pyroxenes transform to garnet at high pressure, see Sect.[3.2], the differences between calculated and model volume fraction lead only to differences in the calculated density, bulk sound velocity, and electrical conductivity in the upper part of the mantle, i.e. above the depth of the phase transition. For the density and, the bulk sound velocity the relative deviations are about 1% and significantly lower than 1% for the electrical conductivity.

Once the pressure, temperature, and mineralogy are known, the bulk sound velocity, density, and electrical conductivity can be computed in each layer. The details of the different involved steps are explained in Chapt.[3]. From the densities of the crust and

of each mantle layer, the moment of inertia of the silicate shell is calculated as

$$I_s = \frac{8}{15}\rho_c \left[r_a^5 - (r_a - d_c)^5\right] + \frac{8}{15}\sum_{i=1}^{n-1} \rho_i \left(z_{i+1}^5 - z_i^5\right), \tag{9.4}$$

where ρ_i the density of mantle layer i, $z_1 = d_c$, and $z_n = r_a - r_{\text{cmb}}$.

To summarize the forward model depends on the following parameters

- the temperature inside each of the n mantle layers: T_i
- the bulk mantle atomic fraction of iron: x_{Fe}
- the volume fraction of olivine: X_{ol}
- the pressure gradient of the mantle: ∇P
- the density of the crust: ρ_c.

Additionally to the parameters, the model depends on the following auxiliary variables

- the number of layers in the mantle: n
- the planet mass: m_a
- the planet moment of inertia: I_a
- the crust thickness: d_c
- the size of the core: r_{cmb}
- the depth of the bottom of each of the n mantle layers: z_i
- the equation of state parameters of the minerals and phases comprising the mantle, see Tab.[3.2] and Tab.[3.4]: Ξ.

Formally we can write for the forward problem as

$$\begin{pmatrix} \boldsymbol{v}_\phi \\ \boldsymbol{\sigma} \\ I_s \end{pmatrix} = \begin{pmatrix} \boldsymbol{v}_\phi(x_{\text{Fe}}, X_{\text{ol}}, \nabla P, \boldsymbol{T}, \Xi) \\ \boldsymbol{\sigma}(x_{\text{Fe}}, X_{\text{ol}}, \boldsymbol{T}, \Xi) \\ I_s(x_{\text{Fe}}, X_{\text{ol}}, \nabla P, \boldsymbol{T}, \rho_c, \Xi) \end{pmatrix}, \tag{9.5}$$

where the dependence on each parameter is given explicitly and where $\boldsymbol{v}_\phi = \{v_\phi(r_i)\}_{i=1}^n \equiv \{v_{\phi,i}\}_{i=1}^n$, $\boldsymbol{\sigma} = \{\sigma(r_i)\}_{i=1}^n \equiv \{\sigma_i\}_{i=1}^n$, and $\boldsymbol{T} = \{T(r_i)\}_{i=1}^n \equiv \{T_i\}_{i=1}^n$. For convenience we denote $\boldsymbol{x} = \{X_{\text{ol}}, x_{\text{Fe}}\}$, and $\sigma_i = \log \bar{\sigma}_i/\sigma_0$, where $\sigma_0 = 1\text{Sm}$ and $\bar{\sigma}_i$ is the electrical conductivity in layer i.

9.3 The data

For Mars, we have simulated 8 different sets of data corresponding to 8 different sets of model parameters from the mantle mineralogy models DW84, EH45, EH70, and PM, for the hot and cold mantle temperature end-members. For all models we have subdivided the mantle in $n = 50$ layers of equal thickness, chosen a crust of 100km thickness, and a mantle pressure gradient of 0.012GPa/km [*Verhoeven et al.*, 2005]. The core size and the crust density of each model have been selected such that for a given mantle temperature and mineralogy, the resulting mass and moment of inertia of the planet are as close as possible to the measured values, see Tab.[6.1], and the values of the average crust density and average core density are within plausible ranges. Tab.[9.1] summarizes the parameter values of each model and Fig.[9.2] shows the two mantle temperature end-members, which are the same temperature profiles as have been used in Chapt.[6]

	PM_c	DW_c	$EH45_c$	$EH70_c$	PM_h	DW_h	$EH45_h$	$EH70_h$
d_c [km]	100	100	100	100	100	100	100	100
$r_{\rm cmb}$ [km]	1800	1570	1570	1850	1900	1600	1600	1850
∇P [GPa/km]	0.012	0.012	0.012	0.012	0.012	0.012	0.012	0.012
Temp. profile	T_c	T_c	T_c	T_c	T_h	T_h	T_h	T_h
$x_{\rm Fe}$ [at]	0.09	0.25	0.28	0.2	0.09	0.25	0.28	0.2
$X_{\rm ol}$ [vol]	0.51	0.59	0.26	0.04	0.51	0.59	0.26	0.04
ρ_c [kg/m^3]	3199	2496	2549	2879	3203	2753	2814	3091
I_s [10^{36} kgm^2]	2.4610	2.5571	2.5565	2.4423	2.3944	2.5461	2.5455	2.4327

Table 9.1: Model parameters for interior structure models and resulting moment of inertia of silicate shell.

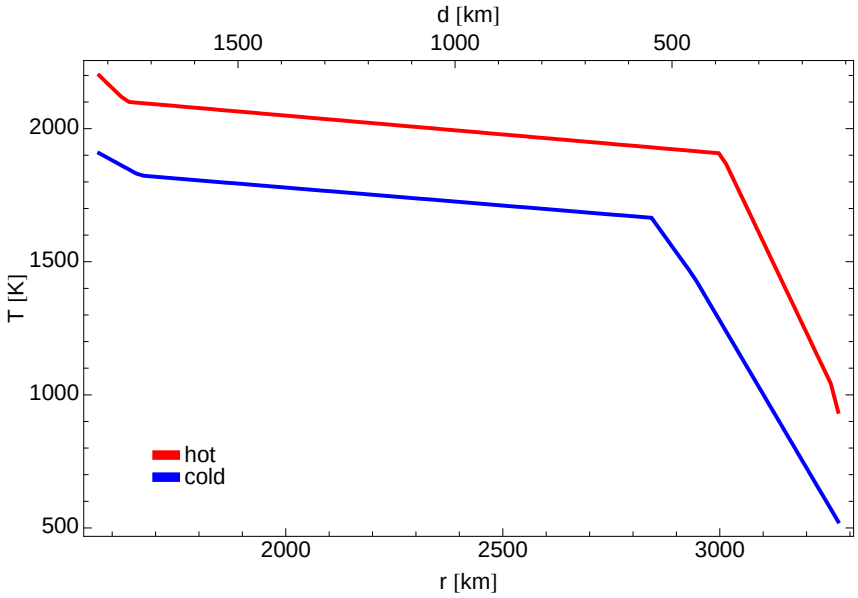


Figure 9.2: Temperature profiles for the mantle as functions of the radius r or depth d.

The profiles of density, bulk sound velocity, and electrical conductivity corresponding to the 8 models are shown in Fig.[9.3].

The uncertainties we take on the data sets are given in Tab.[9.2]. The uncertainty on the v_ϕ profile is 2%. It is about twenty times larger than the corresponding uncertainty given by Earth reference models, see *Dziewonski and Anderson* [1981] for the PREM model and *Kennett et al.* [1995] for the ak135 model, and of about the same order of magnitude as that for the Moon, the only terrestrial body beside the Earth for which seismic data exist. The most recent estimated seismic lunar velocity profiles give an uncertainty range of about $[2, 6]$% (see *Verhoeven et al.* [2005] for a discussion and for references). An uncertainty of about 2% on v_ϕ corresponds to about $\pm$130m/s, which is somewhat larger than the largest uncertainty expected on v_ϕ resulting from uncertainties on thermoelastic constants at reference conditions, see Sect.[3.7.2].

The complexities encountered in the assessment of the uncertainties on the σ profile are discussed in *Verhoeven et al.* [2005]. Since no value for an expected uncertainty on the electrical conductivity profile is given and since for the Earth's mantle we have estimated that the uncertainty on the logarithm of σ is about 0.6 (see Sect.[3.6.4]) we here use an average depth independent uncertainty of 1 for the logarithm of the electrical conductivity. This is significantly larger than the estimated uncertainty on the logarithm of σ (about 0.3%) due to uncertain electrical conductivity constants at reference conditions, see Sect.[3.7.2].

The uncertainty on the moment of inertia of the silicate shell, σ_{I_s}, can be estimated from the uncertainties of the moment of inertia of the planet, σ_{I_a}, and from the uncertainty on the moment of inertia of the core, σ_{I_c}. If we assume that the moments of inertia of the core and the planet are normal random variables, with known mean value and standard deviation, then the relative uncertainty on I_s can be written as

$$\frac{\sigma_{I_s}}{I_s} = \left(1 - \frac{I_c}{I_a}\right)^{-1} \sqrt{\left(\frac{\sigma_{I_a}}{I_a}\right)^2 + \left(\frac{\sigma_{I_c}}{I_a}\right)^2}. \tag{9.6}$$

According to Tab.[6.1] $\sigma_{I_a}/I_a = 0.0023$. In Sect.[6.5], we have used the moment of inertia and k_2 in order to seek compatible interior structure models of Mars. We have found that the core moments of inertia of those models are within $[0.035, 0.065]I_a$. If we then associate an uncertainty of 20% to the moment of inertia of the core, we obtain about 0.01 for the relative uncertainty on the moment of inertia of the mantle.

The spread of the 1σ uncertainty domain on v_ϕ and $\log(\sigma/\sigma_0)$ can be appreciated for mantle model EH45 with the hot temperature profile in Fig.[9.3b] and Fig.[9.3c]. For a given temperature profile the uncertainties associated with the different mantle models have significant overlaps. This makes it difficult, at the 1σ level, to distinguish between models having similar x_{Fe} values and notable different X_{ol} values, like the DW and EH45 model (see Tab.[9.1]).

v_ϕ	$\log(\sigma/\sigma_0)$	I_s
2%	1	1%

Table 9.2: Assumed data uncertainties. With $\sigma_0 = 1$Sm

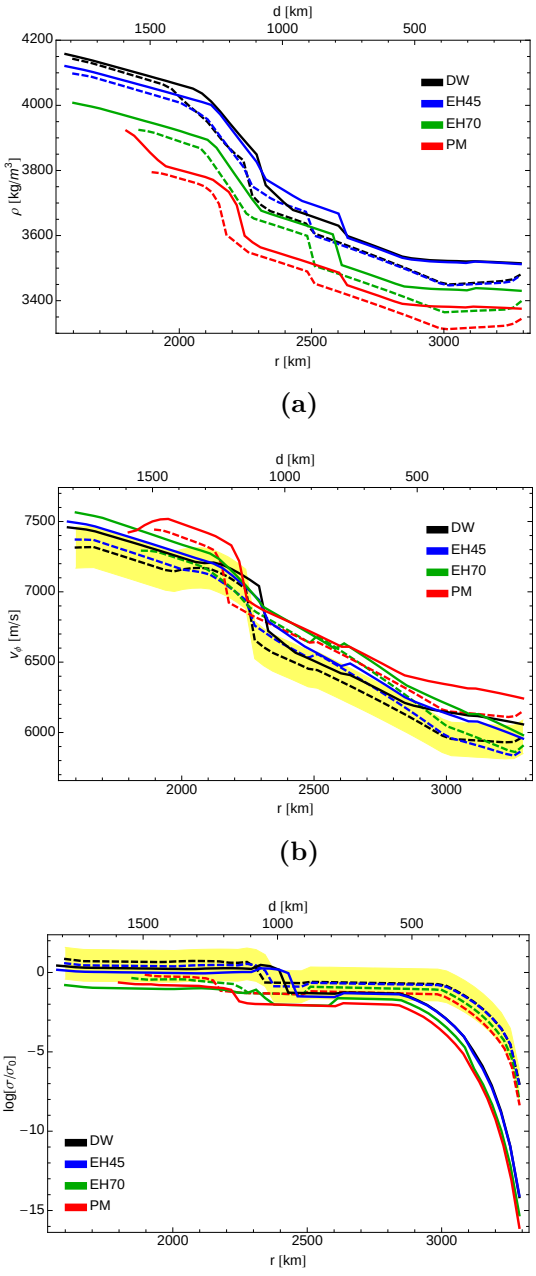


Figure 9.3: Synthetic data sets for all mantle mineralogies. Density (a), acoustic wave speed (b), and electrical conductivity (c) profiles as a function of radius r and depth d. The solid and dashed curves correspond to the cold and hot temperature profiles. The yellow shaded area delimits the 1σ interval of the hot EH45 model. $\sigma_0 = 1\mathrm{Sm}$

9.4 The posterior probability density function

9.4.1 The likelihood

The measurement of travel times of seismic waves, the measurement of induced electromagnetic waves at the surface of the planet, and the determination of the planet's rotation are independent. Therefore, and since the processing of the raw measurements are independent, the data, bulk sound velocity, electrical conductivity, and moment of inertia of the core are also statistically independent. The likelihood is then (see (8.37))

$$\begin{aligned}\mathbf{p}(\boldsymbol{v}_\phi, \boldsymbol{\sigma}, I_s|\nabla P, \boldsymbol{T}, \boldsymbol{x}, \rho_c, \Xi) =& \mathbf{p}(\boldsymbol{v}_\phi|\nabla P, \boldsymbol{T}, \boldsymbol{x}, \Xi)\ \mathbf{p}(\boldsymbol{\sigma}|\boldsymbol{T}, \boldsymbol{x}, \Xi) \\ & \mathbf{p}(I_s|\nabla P, \boldsymbol{T}, \boldsymbol{x}, \rho_c, \Xi). \end{aligned} \tag{9.7}$$

For convenience we here assume that the uncertainties on each set of raw measurements induce uncertainties on the data that have a normal distribution with known mean vectors and covariance matrices. We write for the random variables representing the data

$$\boldsymbol{v}_\phi \sim \left\{\mathrm{N}(\boldsymbol{v}_\phi^*, \boldsymbol{\lambda}_v)\right\}_{i=1}^n \tag{9.8}$$

$$\boldsymbol{\sigma} \sim \left\{\mathrm{N}(\boldsymbol{\sigma}^*, \boldsymbol{\lambda}_\sigma)\right\}_{i=1}^n \tag{9.9}$$

$$I_s \sim \mathrm{N}(I_s^*, \lambda_I), \tag{9.10}$$

where $\boldsymbol{v}_\phi^*$, $\boldsymbol{\sigma}^*$, and I_s^* are the mean data vectors and $\boldsymbol{\lambda}_v$, $\boldsymbol{\lambda}_\sigma$, and λ_I are the covariance matrixes. For convenience, we assume that the data points at each depth are uncorrelated, i.e. that the covariance matrixes $\boldsymbol{\lambda}_v$ and $\boldsymbol{\lambda}_\sigma$ are diagonal.

If the model predictions are deterministic (see (8.36)), i.e. for a set of parameter values only one set of data values are predicted, and the data random variables have a normal distribution then the three terms of the likelihood function (9.7) are

$$\mathbf{p}(\boldsymbol{v}_\phi|\nabla P, \boldsymbol{T}, \boldsymbol{x}, \rho_c, \Xi) = \exp\left\{-\sum_{i=1}^n \frac{(v_{\phi,i}^* - v_{\phi,i})^2}{2\lambda_{v,i}^2} - \frac{n}{2}\log 2\pi - \sum_{i=1}^n \log \lambda_{v,i}\right\} \tag{9.11}$$

$$\mathbf{p}(\boldsymbol{\sigma}|\boldsymbol{T}, \boldsymbol{x}, \rho_c, \Xi) = \exp\left\{-\sum_{i=1}^n \frac{(\sigma_i^* - \sigma_i)^2}{2\lambda_{\sigma,i}^2} - \frac{n}{2}\log 2\pi - \sum_{i=1}^n \log \lambda_{\sigma,i}\right\} \tag{9.12}$$

$$\mathbf{p}(I_s|\nabla P, \boldsymbol{T}, \boldsymbol{x}, \rho_c, \Xi) = \exp\left\{-\frac{(I_s^* - I_s)^2}{2\lambda_I^2} - \frac{1}{2}\log 2\pi - \log \lambda_I\right\}. \tag{9.13}$$

The predictions of the model, (9.5), become probabilistic if we allow the auxiliary parameters to have uncertainties. Here, we discuss only the case for uncertain EoS parameters. We have seen in Sect.[8.2.5] that in order to determine the induced model prediction pdf from the pdf's of the auxiliary parameters we need to determine the analytic function mapping model predictions and model parameters to auxiliary parameters. For the forward problem at hand this is, however, impossible. Therefore, we resort to the setting where the model predictions are probabilistic because of an additive noise component that is independent of the parameter values. This choice can be motivated as follows. In Sect.[3.7] we have assessed how EoS parameter uncertainties propagate to calculated bulk sound velocities and electrical conductivities. We have assumed uncorrelated pdf's for each EoS parameter and have empirically determined pdf's on the bulk sound velocity, electrical conductivity, and mantle moment of inertia. The estimated mean values

from the noisy data deviate only marginally from the original data (obtained without EoS noise) and the spreads of the empirical pdf's are quasi symmetric about their mean values. Further, as far as we could judge from our empirical tests the estimated pdf's are only weakly dependent on the values of the model parameters. The average estimated standard deviation on the bulk sound velocity profile, resulting from EoS uncertainties, is about ten times larger than the above assumed uncertainty on the bulk sound velocity data, see Tab.[9.2], the uncertainties on the electrical conductivity and moment of inertia of the mantle are appreciably smaller the values given in Tab.[9.2].

We therefore use parameter-value-independent, additive, zero-mean, normal distributions to describe model prediction uncertainties. For the standard deviations of the normal distributions we use the estimated values for the standard deviations estimated in Sect.[3.7] at each depth. We have seen in Sect.[8.2.5] that if both data uncertainty and additive model prediction uncertainties have a normal distribution then the resulting conditional pdf's also have a normal distribution (see (8.45)). The mean value of this normal distribution is the mean value of the normal distribution describing the data uncertainty and the variance is the sum of the variances of the data uncertainty and model uncertainty.

9.4.2 The prior information

In our setting we use a weak but geophysical sound prior knowledge on the parameters. We start by assuming that the prior knowledge on each parameter group is independent on the others. The probability density function for the joint prior then factorizes to

$$\boldsymbol{\pi}(\boldsymbol{T}, \nabla P, X_{\mathrm{ol}}, x_{\mathrm{Fe}}, \rho_c) = \boldsymbol{\pi}(\boldsymbol{T})\ \boldsymbol{\pi}(\nabla P)\ \boldsymbol{\pi}(X_{\mathrm{ol}})\ \boldsymbol{\pi}(x_{\mathrm{Fe}})\ \boldsymbol{\pi}(\rho_c). \tag{9.14}$$

Individually, each parameter is supposed to be of uniform distribution within a given interval. The parameter ranges are given in table Tab.[9.3]. The lower value of the temperature range is conservative and the upper value is limited by the melting temperature of plausible mantle material at the core mantle interface depth. The crust density range is broader than the recent estimated range of $[2700, 3100]\mathrm{kg/m^3}$ [*Wieczorek and Zuber*, 2004]. For a crust that is 100km thick the crust density range allows for a bottom crust pressure in the $[0.84, 1.25]$GPa range. From this pressure range and with the range of possible values for ∇P the pressure at the bottom of the mantle is in the interval $[13, 30]$GPa if the core size is within $[1500, 1900]$km. Finally the X_{ol} and x_{Fe} prior ranges comprise previous published values [*Verhoeven et al.*, 2005].

	min	max
T [K]	300	3000
ρ_c [kg/m^3]	2300	3300
∇P [GPa/km]	0.008	0.015
X_{ol} [vol]	0.01	0.66
x_{Fe} [at]	0.09	0.4

Table 9.3: Prior ranges of parameters.

Besides the assumed ranges on the parameters we require the temperature profile of an isotropic model to have a certain level of smoothness. This condition can be met by a local quadratic Gaussian prior that penalizes sharp local temperature variations. We consider two such priors. A 2-point neighbor prior, censuring variations of the local temperature with respect to the nearest left or right temperature value, and a 3-point smoother, censuring strong local variations in the derivative of the temperature [*Besag et al.*, 1995]. The 2-point smoother is given by

$$\boldsymbol{\pi}(\boldsymbol{T}|\lambda) = k\lambda^{\frac{n}{2}} \exp\left\{-\frac{1}{2}\lambda \sum_{i=1}^{n-1}(T_i - T_{i+1})^2\right\} \ , \lambda > 0, \tag{9.15}$$

and the 3-point smoother is

$$\boldsymbol{\pi}(\boldsymbol{T}|\lambda) = k\lambda^{\frac{n}{2}} \exp\left\{-\frac{1}{2}\lambda \sum_{i=2}^{n-1}(T_{i-1} - 2T_i + T_{i+1})^2\right\} \ , \lambda > 0 \tag{9.16}$$

where k is a constant independent of λ and $\boldsymbol{T}$, defined such that

$$\int_{T_{min}}^{T_{max}} \prod_{i=1}^{n} dT_i \ \boldsymbol{\pi}(T_1, \ldots, T_n|\lambda) = 1. \tag{9.17}$$

Both smoothers can also be written in the following compact form

$$\boldsymbol{\pi}(\boldsymbol{T}|\lambda) = k\lambda^{\frac{n}{2}} e^{-\frac{1}{2}\lambda \boldsymbol{T}^T W \boldsymbol{T}} \ , \lambda > 0, \tag{9.18}$$

where W is a $n \times n$ matrix easily constructed from the definitions of (9.15) and (9.16).

The *hyperparameter* λ controls the strength of the smoothing on the temperature profile. The higher its value the stronger local temperature variations are penalized and the stronger the influence of the prior compared to the likelihood. In other words, λ does not only control the smoothness of the temperature profile but also the relative importance of the prior and the likelihood function in the posterior density function and therefore introduces bias on posterior estimates.

We use two different strategies to choose the value of λ. First, we do pilot runs on synthetic noisy data sets and choose a value for λ which leads to an acceptable tradeoff between bias on estimates and smoothness of the temperature profile. For this setting we write for the joint prior probability density function conditioned on the value of λ

$$\begin{aligned}\boldsymbol{\pi}_1(\boldsymbol{T}, \nabla P, X_{\mathrm{ol}}, x_{\mathrm{Fe}}, \rho_c|\lambda) =& \frac{k\lambda^{\frac{n}{2}} e^{-\frac{1}{2}\lambda T^T W T}}{(T_{\max} - T_{\min})^n} \frac{1}{\nabla P_{\max} - \nabla P_{\min}} \\ & \frac{1}{\rho_{c,\max} - \rho_{c,\min}} \frac{1}{X_{\mathrm{ol,max}} - X_{\mathrm{ol,min}}} \frac{1}{x_{\mathrm{Fe,max}} - x_{\mathrm{Fe,min}}} \qquad (9.19) \\ & \propto \lambda^{\frac{n}{2}} e^{-\frac{1}{2}\lambda \boldsymbol{T}^T W \boldsymbol{T}}. \qquad (9.20)\end{aligned}$$

Second, we promote the variable λ to a random variable and infer its probability density function together with the other parameters from the data (*data-driven* smoothing). Similarly to the other parameters we have to introduce a prior probability density function on λ. We express our ignorance on the value of λ by ascribing a non-informative

vague prior to it. Commonly used prior probability density functions for precision parameters are the gamma pdf, improper Jeffrey's prior, and uniform larger than zero improper prior[2][*Gelman et al.*, 2003]:

$$\boldsymbol{\pi}(\lambda) = 1,\ \lambda > 0 \quad \text{Uniform prior,} \tag{9.21}$$

$$\boldsymbol{\pi}(\lambda) = \frac{1}{\lambda},\ \lambda > 0 \quad \text{Jeffrey's prior,} \tag{9.22}$$

$$\boldsymbol{\pi}(\lambda) = \mathrm{G}(\lambda|a,b) = \frac{\lambda^{a-1}}{\Gamma(a)b^a} e^{-\frac{\lambda}{b}},\ \text{Gamma distribution,} \tag{9.23}$$

where a is the location parameter, b the scale parameter, and $\Gamma(a)$ is the gamma function. For this extended setting the joint prior probability density function is

$$\boldsymbol{\pi}_2(\boldsymbol{T}, \nabla P, X_{\mathrm{ol}}, x_{\mathrm{Fe}}, \rho_c, \lambda) = \boldsymbol{\pi}(\boldsymbol{T}, \nabla P, X_{\mathrm{ol}}, x_{\mathrm{Fe}}, \rho_c|\lambda)\boldsymbol{\pi}(\lambda) \tag{9.24}$$

$$\propto \mathrm{G}(\lambda|a', b'), \tag{9.25}$$

where

$$a' = \frac{n}{2} + 1,\ b'^{-1} = \frac{1}{2}\boldsymbol{T}^T W \boldsymbol{T} \quad \text{for the uniform prior} \tag{9.26}$$

$$a' = \frac{n}{2},\ b'^{-1} = \frac{1}{2}\boldsymbol{T}^T W \boldsymbol{T} \quad \text{for the Jeffrey's prior} \tag{9.27}$$

$$a' = \frac{n}{2} + a,\ b'^{-1} = \frac{1}{2}\boldsymbol{T}^T W \boldsymbol{T} + b^{-1} \quad \text{for the Gamma prior} \tag{9.28}$$

9.4.3 The posterior

The posterior probability density functions for hand-set values of the smoothing parameters for deterministic models and models with additive Gaussian noise is

$$\mathbf{p}_1(\nabla P, \boldsymbol{T}, \boldsymbol{x}, \rho_c|\boldsymbol{v}_\phi, \boldsymbol{\sigma}, I_s, \lambda) = \mathbf{p}(\boldsymbol{v}_\phi, \boldsymbol{\sigma}, I_s|\nabla P, \boldsymbol{T}, \boldsymbol{x}, \rho_c)\ \boldsymbol{\pi}_1(\boldsymbol{T}, \nabla P, \boldsymbol{x}, \rho_c|\lambda), \tag{9.29}$$

and for data-driven smoothing parameter

$$\mathbf{p}_2(\nabla P, \boldsymbol{T}, \boldsymbol{x}, \rho_c, \lambda|\boldsymbol{v}_\phi, \boldsymbol{\sigma}, I_s) = \mathbf{p}(\boldsymbol{v}_\phi, \boldsymbol{\sigma}, I_s|\nabla P, \boldsymbol{T}, \boldsymbol{x}, \rho_c)\ \boldsymbol{\pi}_2(\boldsymbol{T}, \nabla P, \boldsymbol{x}, \rho_c, \lambda). \tag{9.30}$$

9.4.4 Simulating the posterior probability density

To simulate the posterior probability we use a single site random walk Metropolis algorithm, i.e. at each iteration only one parameter value is updated, and a Gibbs step to update the hyperparmeter λ, see Sect.[8.3.4] and Sect.[8.3.4]. We streamline the notation by denoting all the parameters by

$$\boldsymbol{\chi} = \{\nabla P, \boldsymbol{T}, \boldsymbol{x}, \rho_c\}, \tag{9.31}$$

where $\boldsymbol{\chi}$ has $n + 4$ components and we denote all the data sets by

$$\boldsymbol{d} = \{\boldsymbol{v}_\phi, \boldsymbol{\sigma}, I_s\}. \tag{9.32}$$

[2]Since uniform prior on $(0, \infty]$ is not normalizable it is called improper or a measure. Note that the product of this improper prior with the likelihood results in a proper posterior probability density function.

In this compact notation the posterior pdf is

$$\mathbf{p}(\boldsymbol{\chi}, \lambda|\boldsymbol{d}) = \mathbf{p}(\boldsymbol{d}|\boldsymbol{\chi})\ \boldsymbol{\pi}(\boldsymbol{\chi}|\lambda)\ \boldsymbol{\pi}(\lambda) \tag{9.33}$$

During each iteration we first draw a new value for the hyperparameter λ with a Gibbs step. The full conditional probability for λ, i.e. the conditional pdf for λ if all other parameters are constant, is proportional to (see (9.25) and (9.33))

$$\mathbf{p}(\lambda|\chi, \boldsymbol{d}) \propto \mathrm{G}(\lambda|a', b') \tag{9.34}$$

Therefore a new value for λ is simulated by drawing a sample from a Gamma distribution with position parameter a' and scale parameter b'.

For the last step, one of the $n+4$ parameters is randomly selected, say χ_i. A new value χ_i^* is proposed according to the symmetric proposal density $T(\chi_i^*, \chi_i)$ (see Sect.[8.3.4]). The proposition χ_i^* is accepted with probability

$$r_i = \min\left\{1, \frac{\mathbf{p}(\chi_i^*|\chi_{-i}, \boldsymbol{d}, \lambda)}{\mathbf{p}(\chi_i|\chi_{-i}, \boldsymbol{d}, \lambda)}\right\}. \tag{9.35}$$

We use normal distributions centered about χ_i for the proposal density functions T. The step-sizes σ_i have been tuned during pilot runs such that the acceptance rates were about $20-30\%$. The algorithm is then iterated until the MCSE's decrease to acceptable values. The first 10% of the samples are discarded (burn-in) and only each 100-th sample is retained to decrease The autocorrelation length.

9.5 Inversion results

We have performed inversions on all the eight models of synthetic data sets (Sect.[9.3]). Since the obtained results are very similar, we only display and discuss the results obtained from the hot EH45 synthetic data set. In Sect.[9.5.1] we give the results for different values of the smoothing parameter λ and discuss how the results change if the value of λ is data-driven. Next we show how the two introduced temperature smoothers (Eqs. (9.15) and (9.16)) influence the inferences. In Sect.[9.5.2] and Sect.[9.5.3] we assess to what degree the outcome of the inversion depends on the availability of the different data sets and on the depth where the data has been sampled. Then, in Sect.[9.5.4], we study how model parameters (the uncertainties on the EoS parameters) induce a supplemental parameter and how different assumed uncertainties on the simulated data sets influence the estimates. Finally, in Sect.[9.6], we give the results for the extended forward model (the model that does not use the empirical relations (9.3)).

9.5.1 Smoother bias

In order to motivate the necessity of the temperature smoothing prior we first give the inversion results for the setting without of smoothing.

For simulated data sets, we can obviously compare the input parameter values to whatever convenient estimate of the parameters and decide upon the success of the inversion if those estimates are close enough to the input values. However, in practice when

using real data, the success of the inversion can only be assessed though the comparison of the data with the posterior data, i.e., the data calculated from realizations of the posterior probability density. If the posterior data samples are "plausible" compared to the data then the inversion is ascribed to have been successful. How posterior data estimates are compared to the data depends on the problem at hand. Here, since the data random variables have been assumed independent normal distributions, characterized by mean and standard deviation, we compare estimated mean posterior data to data mean and assess the spread of the posterior data density (from estimated 0.997, 0.95, and 0.68 probability intervals) to the data standard deviation.

The data sets and the estimated posterior data sets are compared in Fig.[9.4], Fig.[9.5b], and Fig.[9.5c]. We also give the inassessible density profile and estimated posterior density profile in Fig.[9.5a]. The result show that the estimated 0.68 interval of v_ϕ is within and smaller than the 1σ interval of the data. The estimated mean profile of v_ϕ is very close the input profile (the relative differences are below 0.5%) for depths shallower than 750km and deeper than 1250km. For the depth range $[750, 1250]$km the relative deviation is about 1%. In that depth range major phase transitions occur, like the transitions olivine-ringwoodite and olivine- wadsleyite-ringwoodite and the transition pyroxenes to majorite (see Fig.[6.3]). Similarly, for $\log(\sigma/\sigma_0)$ the deviations between the estimates and the data are relatively small (below about 5%) outside of the major phase transition domain and the estimated 0.68 probability domain is commensurable to the 1σ data interval. Within the phase transition domain the deviations between the estimates and the data are larger. The relative differences can reach up to 40% and the 0.68 probability domain is shifted to higher values compared to the 1σ data interval. Finally, the estimated posterior pdf for the silicate shell moment of inertia is shown in Fig.[9.4]. The posterior 0.68 interval corresponds to the 1σ data interval (about 0.25 10^{36}kgm^2.)

To summarize, the estimated posterior data sets are plausible when compared to the input data sets, since the estimated 0.68 intervals are commensurable to the 1σ data intervals and the average estimated profiles are, with the exception of the phase transition zone, very close to the input profiles.

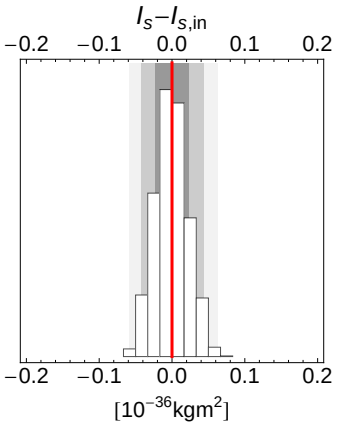


Figure 9.4: Histograms of the posterior silicate shell moment of inertia. The red line is the input value. The gray surfaces (lighter to darker) delimit the 0.997, 0.95, and 0.68 probability intervals.

Prior to comparing the input parameters to the parameter estimates we first have

to assess if the estimated parameter pdf's increase our knowledge compared to the input prior pdf's and second we have to decide if the estimates and realizations are in accordance with our understanding of the interior structure. If the estimated configurations deviate significantly from our perception of the interior, we have to increase or refine our prior knowledge, i.e. penalize the offending configurations.

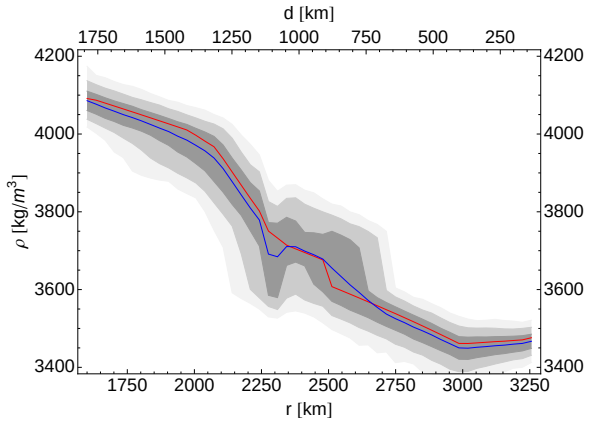
The estimated parameter pdf's for all the parameters, Fig.[9.6] and Fig.[9.7], show that, with the exception of ρ_{crust}, the data significantly increase our knowledge on the parameters compared to the assumed prior knowledge (see Sect.[9.4.2]). Note that for all parameters the axes ranges in the figures correspond to the prior ranges (see Tab.[9.3]). The numerical values of the parameter estimates are given in Tab.[9.4].

	in	mean	median	0.68	0.95	0.997
X_{ol} [vol]	0.26	0.22	0.21	$[0.15, 0.28]$	$[0.10, 0.36]$	$[0.06, 0.47]$
x_{Fe} [at]	0.28	0.28	0.28	$[0.26, 0.3]$	$[0.24, 0.33]$	$[0.21, 0.35]$
∇P [GPa/km]	0.012	0.0120	0.0120	$[0.0118, 0.0123]$	$[0.0115, 0.0125]$	$[0.0112, 0.0126]$
ρ_{crust} [kg/m^3]	2814	2874	2882	$[2647, 3099]$	$[2436, 3252]$	$[2314, 3298]$

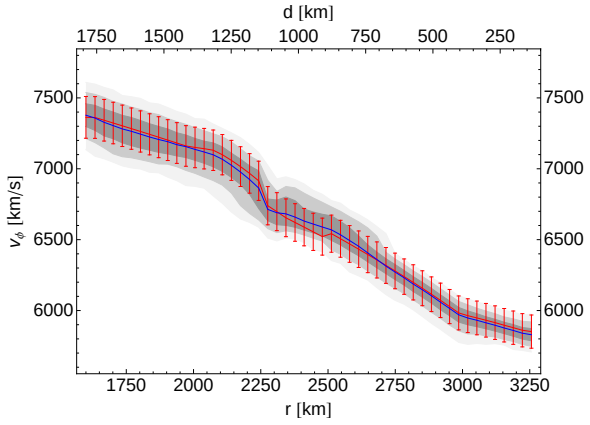
Table 9.4: Initial parameter values versus estimated mean, median, and probability intervals for 0.68, 0.95, and 0.997.

For all parameters the estimated 0.68 probability interval contains the input parameter value. The temperature in the shallow mantle, the bulk iron fraction, and the mantle pressure gradient are the most constrained by the data and their estimated mean values are extremely close to the input value. The estimated mean value of the olivine fraction is, however, about 4vol% lower than the input value. The estimated average temperature profile in the convective part of the mantle is on average about 100K higher than the input temperature in that part of the mantle. As can be seen in the correlation plot Fig.[9.9] the olivine fraction and the temperature in the convective part of the mantle are anti-correlated.

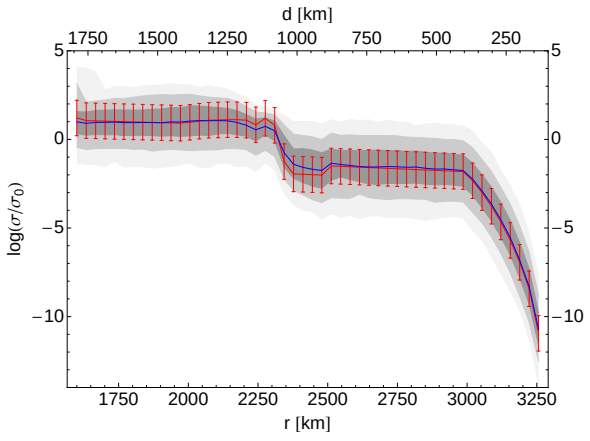
The 0.68 probability domain of the temperature estimate increases with increasing depth. In the conductive part of the mantle the width of the 0.68 interval increases from about 100K to about $400K$ and in the convective part of the mantle, it is on average about 400K. The estimated mean temperature profile shows a sharp kink at a depth of about 1100km and a relative broader spread pdf over the depth range $[600, 1200]$km if compared to the other depths, roughly corresponding to the depths of the occurrence of the major phase transitions and to the locations where data and estimated posterior data deviate strongest. Over the phase transition depth interval the temperature profile pdf shows a bimodal behavior (see Fig.[9.8]).



(a)



(b)



(c)

Figure 9.5: Histograms of posterior density (a), v_ϕ (b), and $\log(\sigma/\sigma_0)$ (c). The red curves are the input values and the blue curves are the estimated mean values. The error-bars on v_ϕ and $\log(\sigma/\sigma_0)$ represent the data uncertainties. The contours of the gray surfaces (lighter to darker) are the 0.997, 0.95, and 0.68 probability domains.

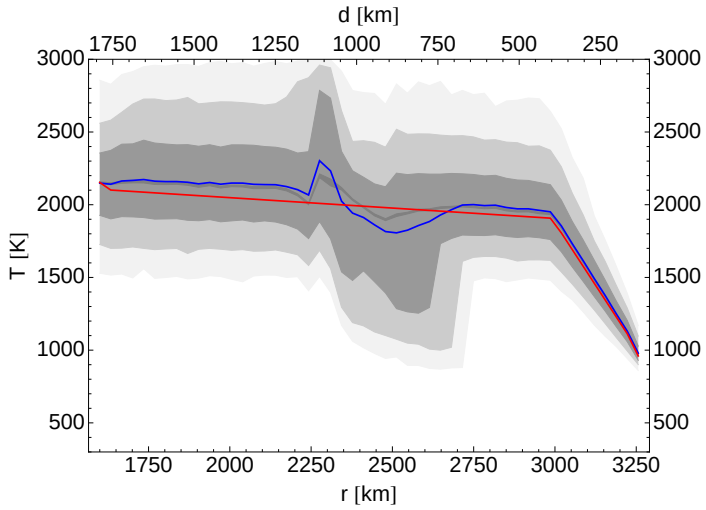


Figure 9.6: Mantle temperature histogram. The red curve is the input temperature and the blue curve is the estimated mean temperature profile. The contours of the gray surfaces (lighter to darker) are the 0.997, 0.95, and 0.68 probability domains.

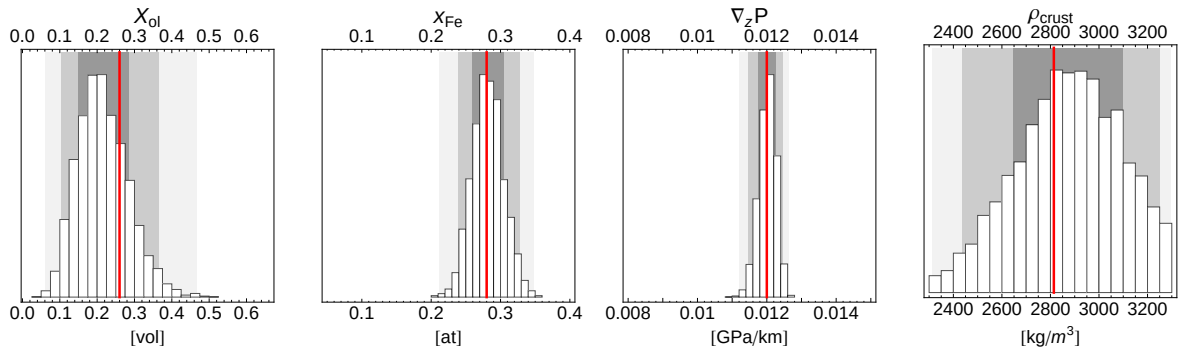
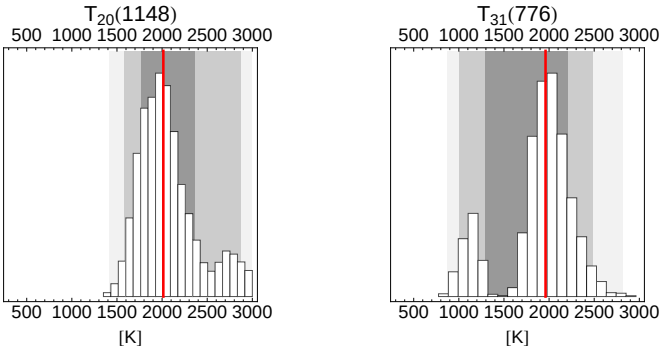


Figure 9.7: Histograms for X_{ol} (a), x_{Fe} (b), ∇P (c), and ρ_{crust} (d). The red lines represent parameter input values. The gray surfaces (lighter to darker) delimit the 0.997, 0.95, and 0.68 probability intervals.



(a) **(b)**

Figure 9.8: Mantle temperature histogram of layers 20 and 31, corresponding to depths of 1148km and 776km. The red lines represent parameter input values. The gray surfaces (lighter to darker) delimit the 0.997, 0.95, and 0.68 probability intervals.

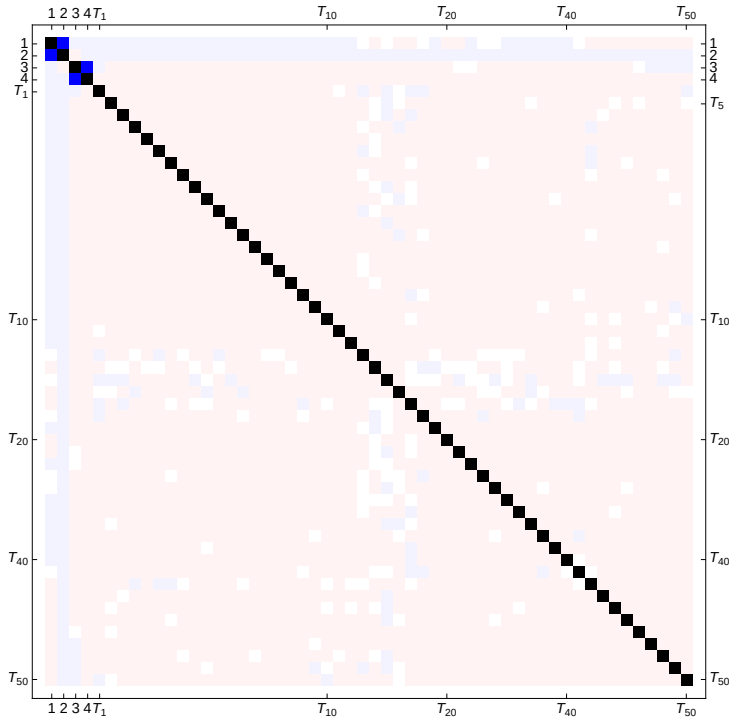


Figure 9.9: Estimated parameter correlation matrix. Black squares have correlation 1, blue squares have negative correlation and red squares have positive correlation. Darker blue or red squares have absolute correlation larger than 0.25. Indices 1,2,3, and 4 stand for X_{ol}, x_{Fe}, ∇P, and ρ_{crust}.

The temperature at a given depth is only constrained by the local value of v_ϕ, $\log(\sigma/\sigma_0)$, and ρ (see Fig.[9.5]) and to a lesser extent by the moment of inertia of the mantle. The other parameters depend on all the data. Therefore, local temperature fluctuations are least constrained. Moreover, since the locations of the phase transitions depend on the local pressure and temperature conditions, and since the pressure in the mantle is tightly constrained by the data, the locations of the phase transitions fluctuate as a consequence of the local temperature variations. This leads to fluctuations in local v_ϕ and $\log(\sigma/\sigma_0)$ values. The induced variations in the data are, however, compatible with the 1σ uncertainty interval of the data and therefore allowed.

Basically, there are two solutions for suppressing the local temperature fluctuations. Acquire data with significantly lower uncertainties or introduce a prior knowledge on the mantle temperature that penalizes strong local temperature variations.

We have found empirically that if we reduce the uncertainty on v_ϕ by a factor of 20 and the uncertainties on $\log(\sigma/\sigma_0)$ and I_s by a factor 10 we can strongly reduce the local temperature variations. The estimated temperature pdf and the estimated pdf's on the scalar parameter are shown in Fig.[9.10] and Fig.[9.11]. The estimated average temperature profile is quasi-indistinguishable from the input temperature profile, and the 0.68 probability domain is only about 50K wide. There remains, however, a small cusp with an amplitude of about $100K$ in the temperature profile at a depth of about 1000K. Compared to the previous setting the 0.68 interval widths decrease, depending on depth, by a factor 2 to 8, see Fig.[9.6]. The estimates of the scalar parameters are given in Tab.[9.5].

	in	mean	median	0.68	0.95	0.997
$X_{\rm ol}$ [vol]	0.26	0.25	0.25	$[0.24, 0.27]$	$[0.22, 0.28]$	$[0.21, 0.3]$
$x_{\rm Fe}$ [at]	0.28	0.28	0.28	$[0.28, 0.28]$	$[0.27, 0.29]$	$[0.27, 0.29]$
∇P [GPa/km]	0.012	0.0121	0.0122	$[0.0112, 0.0121]$	$[0.0119, 0.0122]$	$[0.0118, 0.0122]$
$\rho_{\rm crust}$ [kg/m^3]	2814	2830	2832	$[2726, 2934]$	$[2624, 3035]$	$[2534, 3154]$

Table 9.5: Initial parameter values versus estimated mean, median, and probability intervals for 0.68, 0.95, and 0.997.

Compared to the estimates in Tab.[9.4] the 0.68 intervals decrease by about a factor of 4 for $X_{\rm ol}$, a factor 10 for $x_{\rm Fe}$, a factor 5 for ∇P, and a factor of 2 for $\rho_{\rm crust}$.

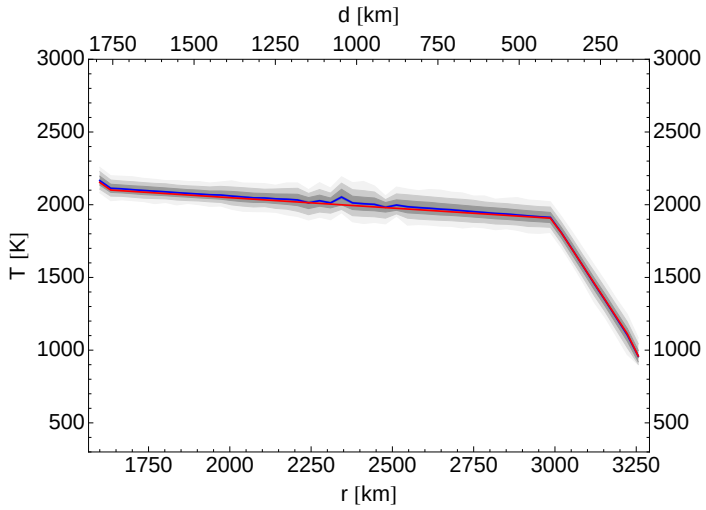


Figure 9.10: Mantle temperature histogram. The red curve is the input temperature and the blue curve is the estimated mean temperature profile. The contours of the gray surfaces (lighter to darker) are the 0.997, 0.95, and 0.68 probability domains.

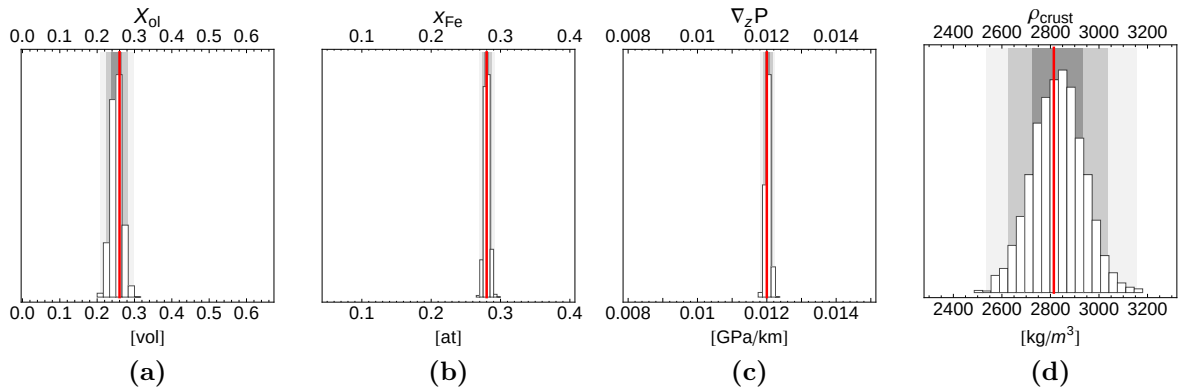


Figure 9.11: Histograms for X_{ol} (a), x_{Fe} (b), ∇P (c), and ρ_{crust} (d). The red lines represent parameter input values. The gray surfaces (lighter to darker) delimit the 0.997, 0.95, and 0.68 probability intervals.

We now study the other solution for suppressing strong local temperature variations, namely the introduction of a prior that penalizes those configurations. In Sect.[9.4.2] we have introduce two prior probability density functions on the temperature parameters of the mantle that result in smoothed mantle temperature profiles. Both prior pdf's depend on a smoothing parameter λ_T (see (9.15) and (9.16)). The value of λ_T is either set by hand or driven by the data. In the first case, we decided on the value of λ_T from pilot runs. An acceptable value for λ_T is a compromise between a smooth enough temperature profile and posterior data estimates that reproduce as close as possible the features of the input data. For the 2 point prior (9.15) we have chosen a value of 0.008 for λ_T and 0.014 for the 3 point prior (9.16). In the second case, we have assigned a vague non-informative prior to the hyperparameter λ_T, see (9.21), (9.22), and (9.23). All three priors lead to very similar inversion results. Here, we only give the results for the 2 point prior with the Gamma distribution (see (9.23)) for the hyperparameter λ_T. The estimated posterior pdf for λ_T is shown in Fig.[9.12]. The pdf on λ_T has its mode at a value of about 0.011, slightly larger than our hand-picked value of 0.008. However, the spread of the posterior pdf for λ_T shows that notably smaller and larger values for λ_T are also possible.

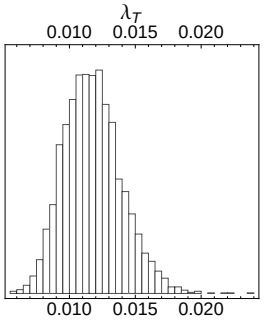


Figure 9.12: Estimated posterior pdf of λ_T for the Gamma prior distribution.

Since the posterior data estimates are very similar for each of the above discussed prior setting we only give the results for the 2 point smoother with the hand-picked value of λ_T (Fig.[9.13] and Fig.[9.14]). Compared to the non smoothed setting of the v_ϕ profile Fig.[9.5b] the spread of the probability domains are strongly reduced, the 0.997 is narrower than the 1σ domain of the input data and the estimated average profile reproduces to a very high degree the input profile. Similarly, the estimated average $\log(\sigma/\sigma_0)$ profile reproduces most of the features of the input profile. Moreover, the 0.95 interval is narrower than the data 1σ interval. Note that in the non-smoothed setting the 0.68 domain of the estimate is as narrow as the 1σ data interval, see Fig.[9.5c].

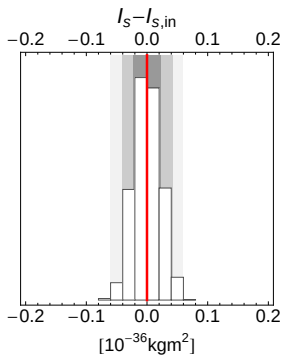
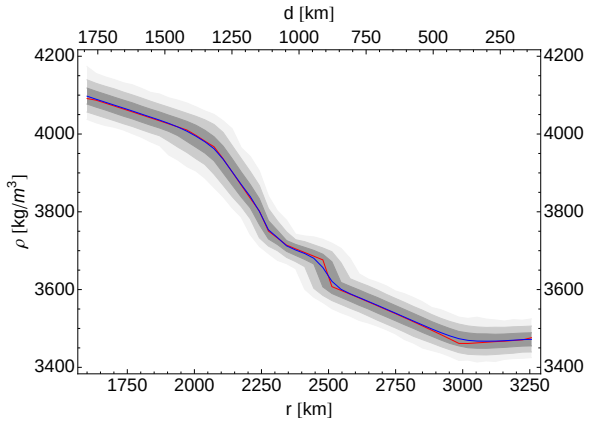
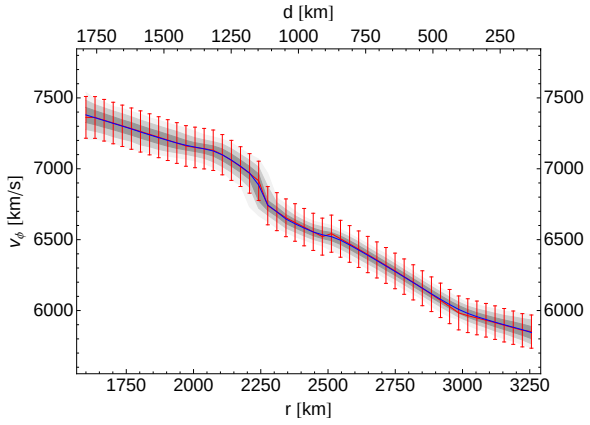


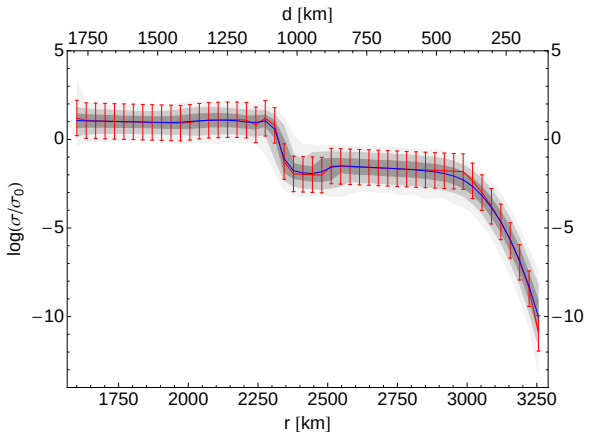
Figure 9.13: Histograms of the posterior silicate shell moment of inertia. The red lines is the input value. The gray surfaces (lighter to darker) delimit the 0.997, 0.95, and 0.68 probability intervals.



(a)



(b)



(c)

Figure 9.14: Histograms of posterior density (a), v_ϕ (b), and $\log(\sigma/\sigma_0)$ (c). The red curves are the input values and the blue curves are the estimated mean values. The error-bars on v_ϕ and $\log(\sigma/\sigma_0)$ represent the data uncertainties. The contours of the gray surfaces (lighter to darker) are the 0.997, 0.95, and 0.68 probability domains.

The influence of the smoothing prior on the temperature is best visualized when realizations of the temperature posterior pdf with and without smoother are compared. Fig.[9.15a] shows two realization of the temperature pdf when no smoothing prior is applied. The figure shows that especially in the $[7050, 1250]$km depth range the data allowed temperature fluctuations are very important, i.e. the amplitude can be as high as 1000K. Conversely, if a prior that penalizes local temperature variations is introduced the amplitudes of local temperature variations are only about 100K, see Fig.[9.15b].

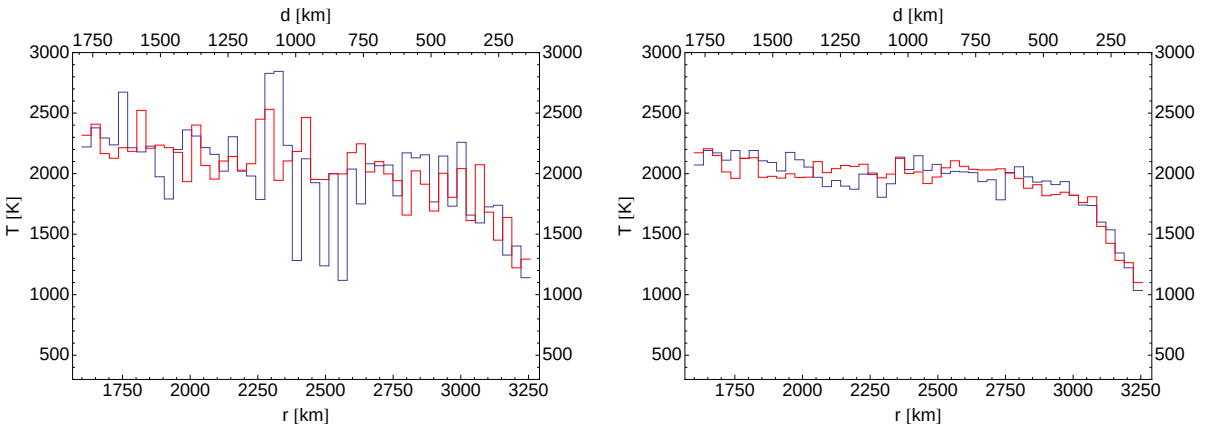


Figure 9.15: Two posterior realizations of the mantle temperature (blue and red curves) without smoother (a) and with the 2 point temperature smoother (b).

The estimated 2 point smoothed temperature profile is shown in Fig.[9.16], the 3 point smoothed profile in Fig.[9.17], and the 2 point smoothed temperature with the Gamma distributed hyperparameter λ_T in Fig.[9.18]. Compared to the non-smoothed setting in Fig.[9.6] in all the three temperature profiles the cusp in the estimated mean temperature profile is strongly suppressed. Moreover, the 0.68 probability intervals in the lower mantle are by about 100K narrower. For the majority of the mantle depths, the 2 point smoother recovers the input temperatures. The notable differences are the small conductive layer at the very bottom of the mantle, the remaining small oscillation between the depths $[800, 1200]$km, and the over-smoothing of the sharp edge between the lower conductive and upper adiabatic part of the mantle. A more faithful reproduction of the edge is obtained with the 3 point smoothing Fig.[9.17]. However, the estimated mean temperature in the adiabatic part of the mantle is slightly overestimated and has a moderate wobbly appearance. Compared to the 2 point smoother the slightly overestimated temperature in the adiabatic part of the mantle leads to a shifting to the left of the 0.68 intervals of X_{ol} by about 1vol%.

Fig.[9.19] shows the estimated correlation matrix for the 2 point smoother setting. Unlike the non-smoothed setting, (Fig.[9.9]), the temperatures in each layer show a depth increasing correlation strength. Moreover, the temperature variables in the first twenty layers show a significant in between correlation over most of the neighbors. For layers larger than twenty the in between correlation length decreases to about five neighbors. Note also, that compared to the non-smoothed setting the correlation between olivine and the other scalar parameters and the temperature of the first twenty layers is larger.

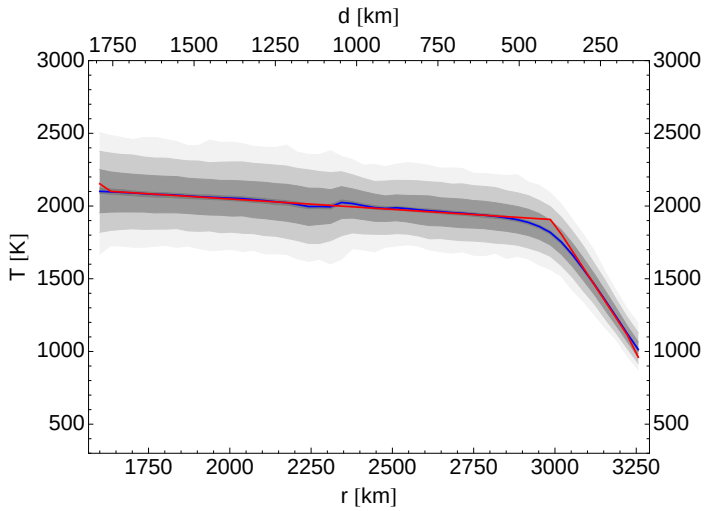


Figure 9.16: Posterior mantle temperature histogram from 2 point smoother. The red curve is the input temperature and the blue curve is the estimated mean temperature profile. The contours of the gray surfaces (lighter to darker) are the 0.997, 0.95, and 0.68 probability domains.

In conclusion, given the assumed data uncertainties (see Tab.[9.2]) it is mandatory to employ a temperature prior suppressing temperature fluctuations in the middle of the adiabatic part of the mantle. Here, we have chosen priors that suppress strong local temperature variations. Other temperature priors are possible. For instance given the shape of the temperature profile a parameterization of the temperature profile in 3 or more domains of unknown span with linearly increasing temperatures with depth could be considered. An additional advantage of the smoothers is that the central estimates of all the parameters are recovered very close to the input parameters values.

Both the 2 point and the 3 point smoother lead to smooth temperature profiles that are in line with our perception of possible mantle temperature profiles. The 3 point smoother does a better job reconstituting local slope variations and the 2 point smoother gives better results in the relatively flat adiabatic part of the temperature profile. Consequently, if we expect the temperature profile to have geophysically relevant strong slope variations the 3 point smoother prior is probably the better choice.

Our results have shown that independent of the three introduced priors on λ_T, that the inferred temperature pdf is very comparable to the result obtained with the hand-set value of λ_T. On the other hand, if the data uncertainties are larger, i.e., the influence of the data is diminished compared to the prior, then the data driven smoothing has a tendency to produce too smooth temperature profiles (figure not shown here). Therefore, we do not recommend to resort blindly to the data driven smoothing procedure.

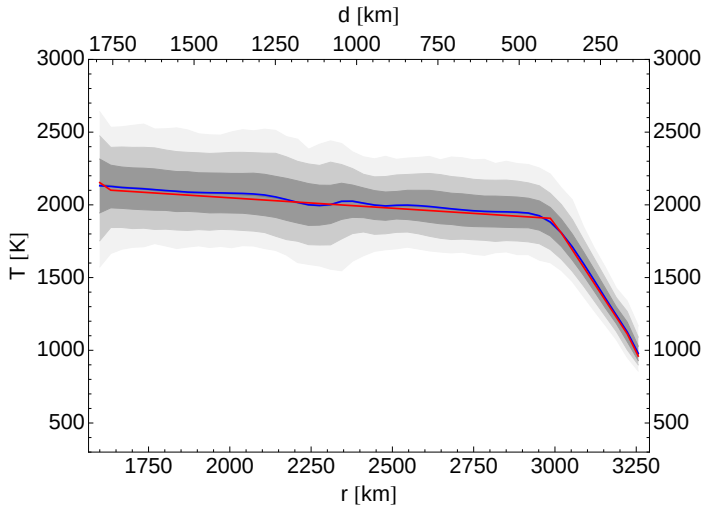


Figure 9.17: Posterior mantle temperature histogram from 3 point smoother. The red curve is the input temperature and the blue curve is the estimated mean temperature profile. The contours of the gray surfaces (lighter to darker) are the 0.997, 0.95, and 0.68 probability domains.

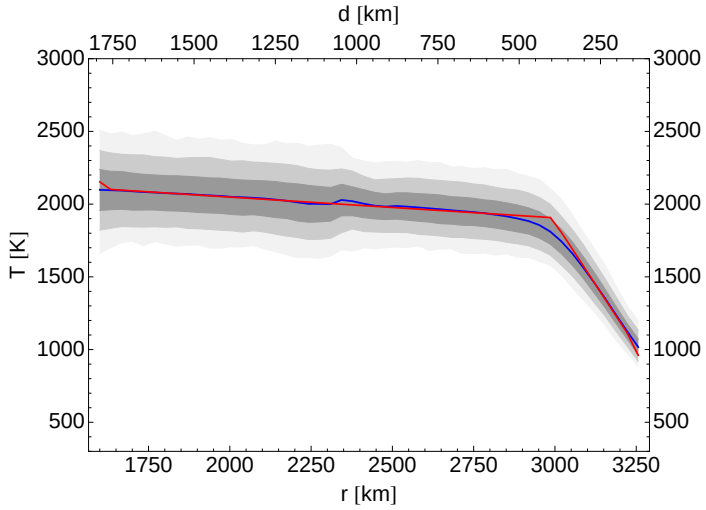


Figure 9.18: Posterior mantle temperature histogram from 2 point smoother and data driven λ_T. The red curve is the input temperature and the blue curve is the estimated mean temperature profile. The contours of the gray surfaces (lighter to darker) are the 0.997, 0.95, and 0.68 probability domains.

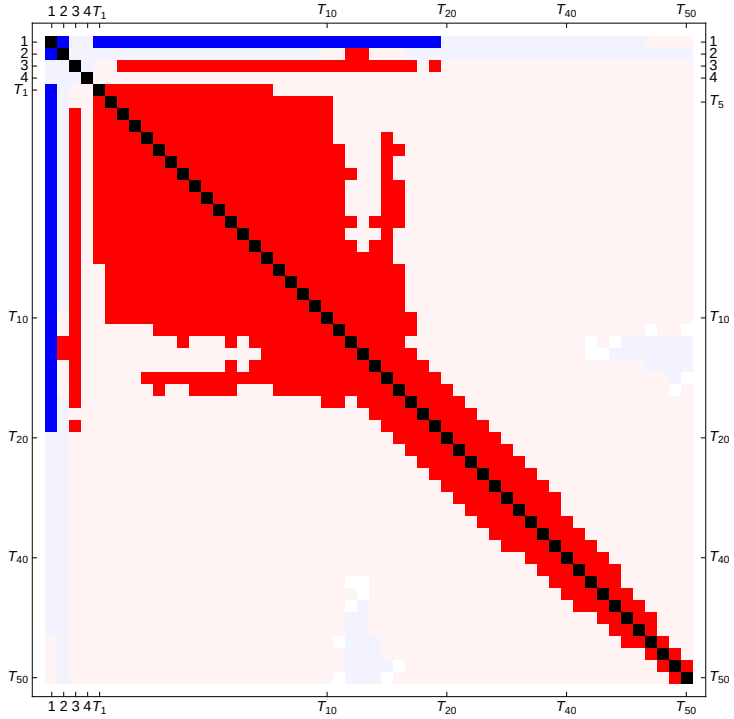


Figure 9.19: Estimated parameter correlation matrix. Black squares have correlation 1, blue squares have negative correlation and red squares have positive correlation. Darker blue or red squares have absolute correlation larger than 0.25. Indices 1,2,3, and 4 stand for X_{ol}, x_{Fe}, ∇P, and ρ_{crust}.

The estimates of the scalar parameters and the posterior marginal histograms obtained with the 2 point smoother with hand-set λ_T values are shown in Tab.[9.6] and Fig.[9.20]. Note that the results for the 3 point smoother and those obtained with the different prior pdf's on λ_T are very similar, and therefore they are not shown here. Unlike the results from the non-smoothed setting, Fig.[9.7] and Tab.[9.4], the 0.68 domains of the $X_{\rm ol}$ and $\rho_{\rm crust}$ estimates are now centered about their input values. Consequently, the input values of the scalar parameters are recovered with very high confidence. Moreover, with the exception of $X_{\rm ol}$, the spread of the 0.68 probability domains do not change in an appreciable way. The spread of the 0.68 interval of $X_{\rm ol}$ is however, larger by about 3vol%.

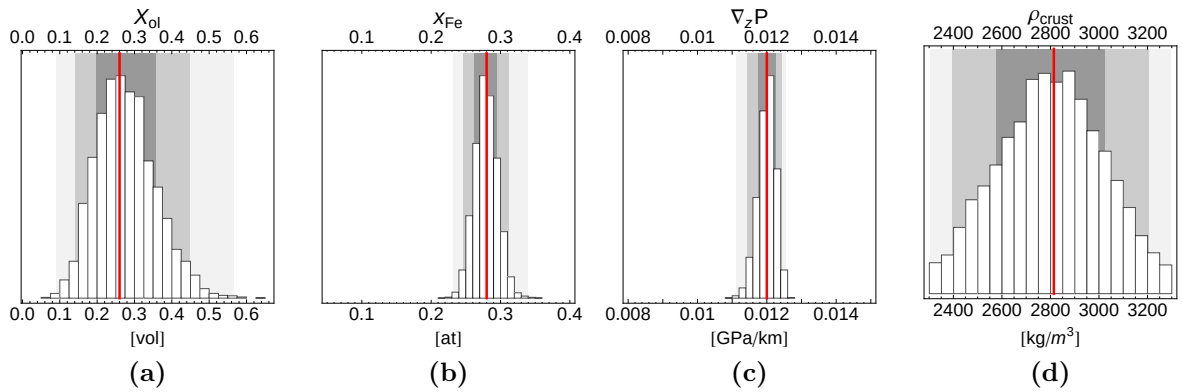


Figure 9.20: Histograms for $X_{\rm ol}$ (a), $x_{\rm Fe}$ (b), ∇P (c), and $\rho_{\rm crust}$ (d). The red lines represent parameter input values. The gray surfaces (lighter to darker) delimit the 0.997, 0.95, and 0.68 probability intervals.

	in	mean	median	0.68	0.95	0.997
$X_{\rm ol}$ [vol]	0.26	0.28	0.275	[0.20, 0.36]	[0.14, 0.45]	[0.09, 0.56]
$x_{\rm Fe}$ [at]	0.28	0.28	0.28	[0.26, 0.3]	[0.25, 0.31]	[0.23, 0.34]
∇P [GPa/km]	0.012	0.0120	0.0120	[0.0117, 0.0122]	[0.0114, 0.0124]	[0.0111, 0.0126]
$\rho_{\rm crust}$ [kg/m^3]	2814	2802	2804	[2577, 3024]	[2395, 3206]	[2304, 3296]

Table 9.6: Initial parameter values versus estimated mean, median, and probability intervals for 0.68, 0.95, and 0.997.

9.5.2 Data availability

The goal of this section is to assess how the knowledge provided by each individual data set, moment of inertia of the silicate shell, bulk sound velocity, and electrical conductivity, influences the posterior inference. This is done by doing inversions leaving out one data set at the time. For all inversions, we have used the 2 point temperature smoother and a hand-set value for λ_T according to the above procedure. The results are compared to those obtained from the whole data set where we have used the 2 point smoother with a hand-set value of $\lambda_T = 0.008$. We refer to those results as 2p08.

Inversion results without I_s

Without I_s, the results are very similar for all the parameters and the posterior data with the exception of the density of the crust. Fig.[9.21] shows the estimated pdf of the moment of inertia of the silicate shell. The estimated 0.68 interval is about the width of the 1σ interval of I_S and about two times larger than the corresponding estimate from 2p08 (see Fig.[9.13]). v_ϕ and $\log(\sigma/\sigma_0)$ do not notably constrain ρ_{crust} since the estimated posterior pdf of ρ_{crust} is nearly as flat as the prior pdf on ρ_{crust} (see Fig.[9.22]). Given the assumed data uncertainties, the constraint provided by the moment of inertia only allows to infer knowledge about the density of the crust and can therefore in our setting be neglected for inferring the mineralogy and the temperature of the mantle.

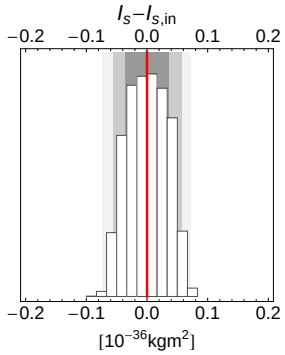


Figure 9.21: Histograms of the posterior silicate shell moment of inertia. The red line is the input value. The gray surfaces (lighter to darker) delimit the 0.997, 0.95, and 0.68 probability intervals.

Inversion results without v_ϕ

In order to reproduce the features in the $\log(\sigma/\sigma_0)$ profile and obtain a plausible realization of the mantel temperature profile we had to reduce the value of λ_T from 0.008 to 0.005.

The estimated pdf for the posterior data I_s shows no visible difference if compared to the 2p08 setting (Fig.[9.23]). However, for the mantle density profile, the estimated posterior confidence intervals are significantly wider (Fig.[9.24a]). Similarly, the estimated mean profile of v_ϕ is different, although, the estimated 0.68 interval is still for most of the mantle within the 1σ interval of the data (Fig.[9.24b]). The 0.997 interval of the $\log(\sigma/\sigma_0)$ profile is only insignificantly wider than the one from 2p08 (Fig.[9.24c]).

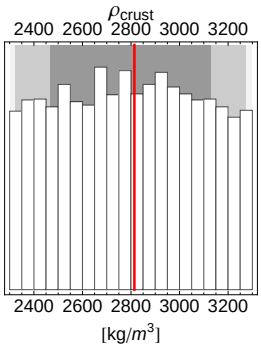


Figure 9.22: Histograms for ρ_{crust}. The red lines represent parameter input values. The gray surfaces (lighter to darker) delimit the 0.997, 0.95, and 0.68 probability intervals.

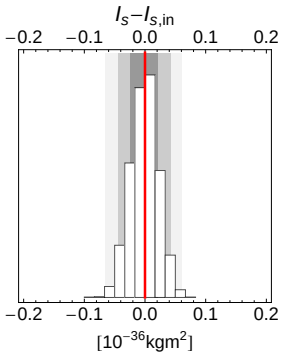
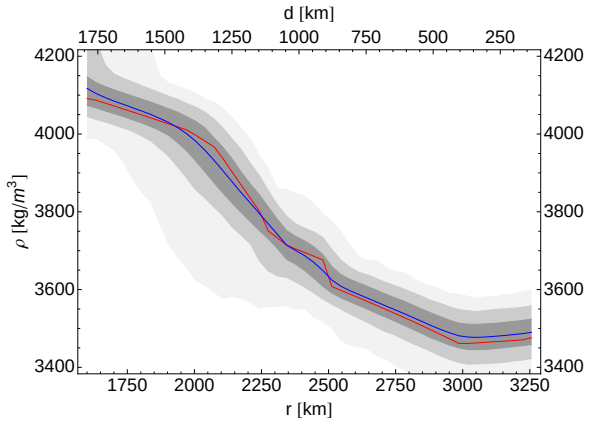
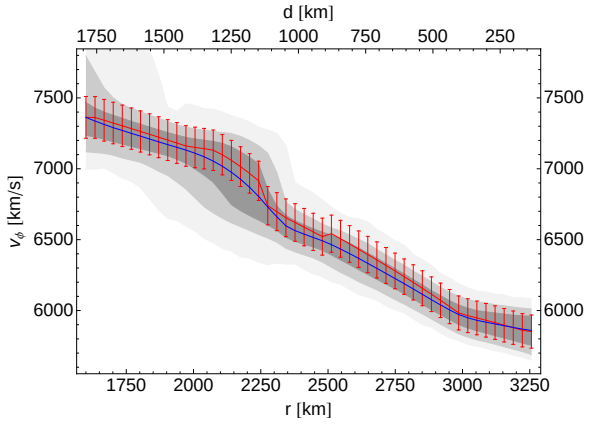


Figure 9.23: Histograms of the posterior silicate shell moment of inertia. The red lines is the input value. The gray surfaces (lighter to darker) delimit the 0.997, 0.95, and 0.68 probability intervals.

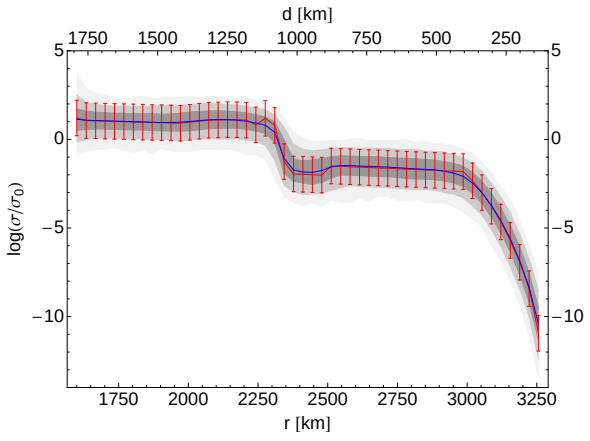
For all parameters, with the exception of ρ_{crust}, the 0.68 intervals are significantly wider than those from 2p08 (see Fig.[9.20]), nevertheless, the 0.68 intervals include the input values of the parameters (Fig.[9.25]). Among all the parameters, the principal mantle mineralogy controlling parameter X_{ol} is the least constrained. The posterior temperature profile, compared to 2p08 (see Fig.[9.16]) the result shows a significant decrease in the confidence of the estimates, i.e., the 0.997 domain is significantly broader (Fig.[9.26]). However, it is narrower than the one estimated without temperature smoother (Fig.[9.6]). The widening of the probability domain is a direct consequence of the decrease of λ_T, from 0.008 to 0.005. The decrease of λ_T was however necessary, since without the v_ϕ data, larger values of λ_T result in over-smoothed temperature profiles and in a less faithful, compared to the data, posterior mean profile for $\log(\sigma/\sigma_0)$. We conclude that, even without the v_ϕ data, it is possible, given the assumed data uncertainties, to infer valuable information about the mantle temperature. However, the uncertainties on X_{ol} are so large, compared to the prior interval, that almost no useful information about the mineralogy of the mantle is gained.



(a)



(b)



(c)

Figure 9.24: Histograms of posterior density (a), v_ϕ (b), and $\log(\sigma/\sigma_0)$ (c). The red curves are the input values and the blue curves are the estimated mean values. The error-bars on v_ϕ and $\log(\sigma/\sigma_0)$ represent the data uncertainties. The contours of the gray surfaces (lighter to darker) are the 0.997, 0.95, and 0.68 probability domains.

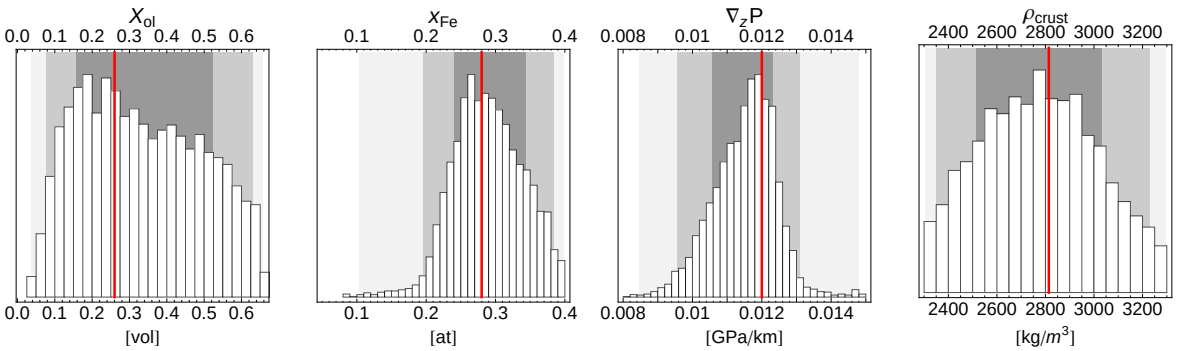


Figure 9.25: Histograms for X_{ol} (a), x_{Fe} (b), ∇P (c), and ρ_{crust} (d). The red lines represent parameter input values. The gray surfaces (lighter to darker) delimit the 0.997, 0.95, and 0.68 probability intervals.

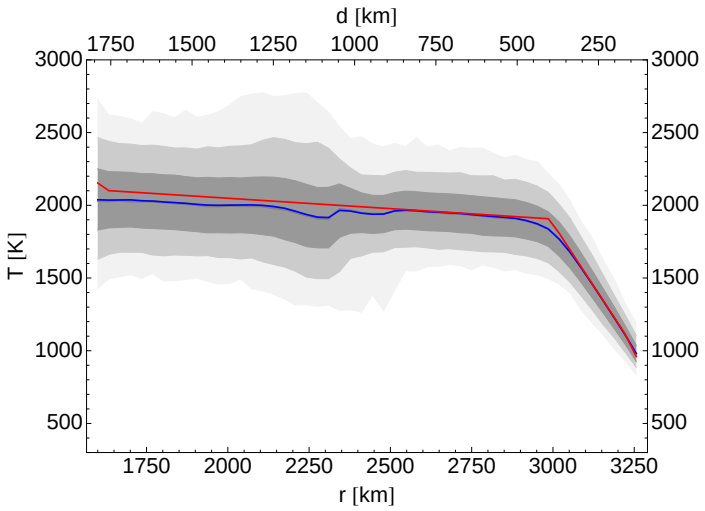


Figure 9.26: Posterior mantle temperature histogram obtained without using v_ϕ data. The red curve is the input temperature and the blue curve is the estimated mean temperature profile. The contours of the gray surfaces (lighter to darker) are the 0.997, 0.95, and 0.68 probability domains.

Inversion result without $\log(\sigma/\sigma_0)$

In the inversion without the $\log(\sigma/\sigma_0)$ data a value of $\lambda_T = 0.004$ has been selected. Larger values of λ_T and data driven values of λ_T result in nearly flat mantle temperature profiles. Smaller values of λ_T produce temperature profiles that are plausible in the conductive part of the mantle but implausible, i.e. with kinks of important amplitude, in the convective part of the mantle. The posterior estimates of v_ϕ are shown in Fig.[9.28b]. The estimated 0.95 domain corresponds to the 1σ domain of the data, whereas for 2p08 the 1σ domain corresponds to the 0.997 domain. The posterior mantle density pdf and $\log(\sigma/\sigma_0)$ profile pdf are shown in Fig.[9.28a] and Fig.[9.28c]. For both profiles, the probability domains are significantly broader. The estimated average $\log(\sigma/\sigma_0)$ values are notably underestimated if compared to the data. Yet, most of the $\log(\sigma/\sigma_0)$ data profile is within the 0.68 domain. The non-availability of the $\log(\sigma/\sigma_0)$ profile does not modify the estimates of I_s, see Fig.[9.27] and Fig.[9.13].

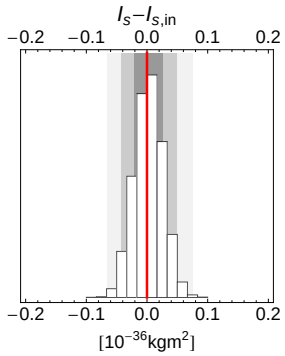
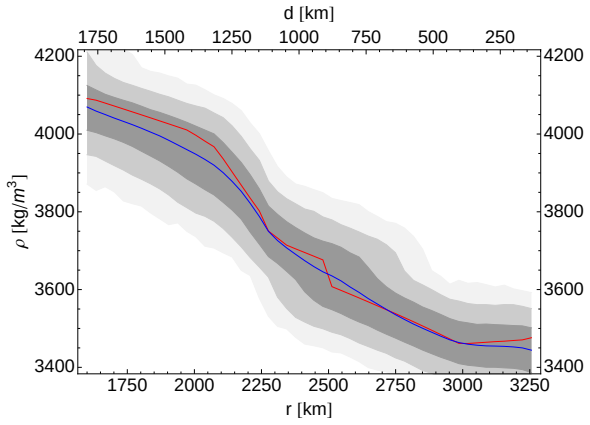


Figure 9.27: Histograms of the posterior silicate shell moment of inertia. The red lines is the input value. The gray surfaces (lighter to darker) delimit the 0.997, 0.95, and 0.68 probability intervals.

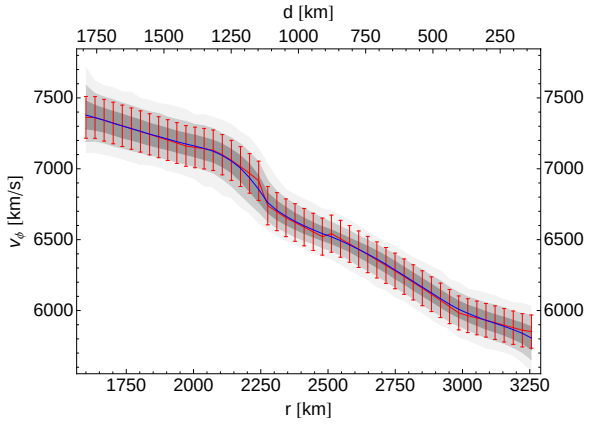
The estimates of the scalar parameters and of the mantle temperature are given in Fig.[9.29] and Fig.[9.30]. Compared to the results of 2p08 the estimated probability domains of the scalar parameters and of the mantle temperature are notably broader, however, the 0.68 domains comprise the input values of the parameters. Although, with the exception of ρ_{crust}, the input values of the parameters are not in the center of the 0.68 domains.

To summarize, without the $\log(\sigma/\sigma_0)$ data, and given the assumed uncertainties, it is neither possible to infer the temperature inside the mantle nor is it possible to obtain useful insight into the mineralogy of the mantle. Moreover, as a result of the combined uncertainties of mantle temperature and the other mantle parameters, the gained knowledge on the crust density, compared to 2p08, is notably degraded, see Fig.[9.29d] and Fig.[9.20d].

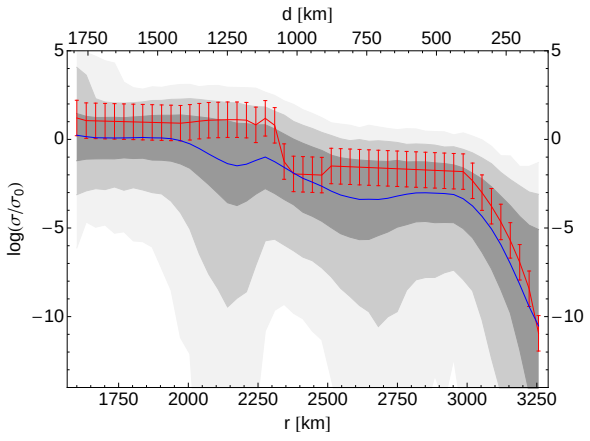
Compared to the setting where the v_ϕ data has been left out, leaving out the $\log(\sigma/\sigma_0)$ data results in strongly degraded inferences on the mantle temperature and on the bulk iron fraction of the mantle since the electrical conductivity is strongly dependent on the local temperature and on the mineral iron content and to a lesser extent on the mantle mineralogy which is primarily controlled by the v_ϕ data.



(a)



(b)



(c)

Figure 9.28: Histograms of posterior density (a), v_ϕ (b), and $\log(\sigma/\sigma_0)$ (c). The red curves are the input values and the blue curves are the estimated mean values. The error-bars on v_ϕ and $\log(\sigma/\sigma_0)$ represent the data uncertainties. The contours of the gray surfaces (lighter to darker) are the 0.997, 0.95, and 0.68 probability domains.

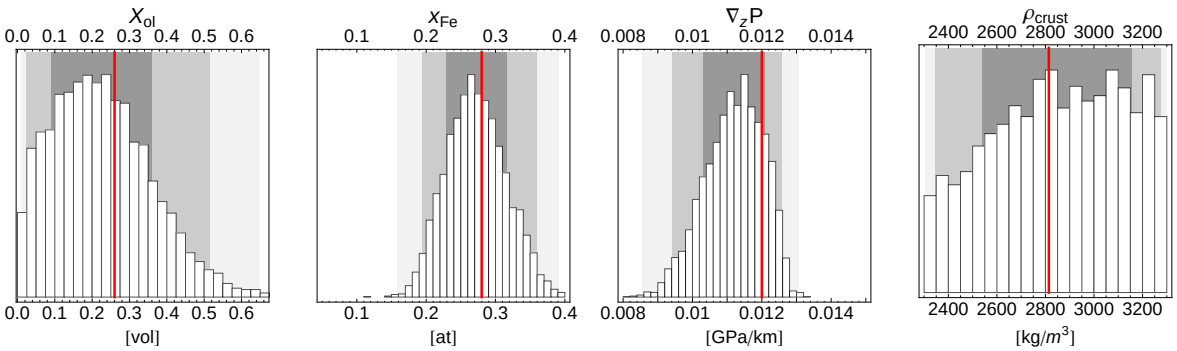


Figure 9.29: Histograms for X_{ol} (a), x_{Fe} (b), ∇P (c), and ρ_{crust} (d). The red lines represent parameter input values. The gray surfaces (lighter to darker) delimit the 0.997, 0.95, and 0.68 probability intervals.

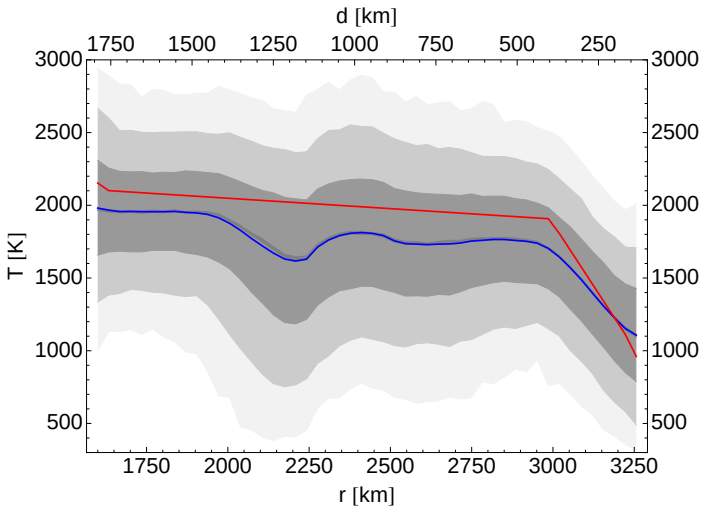


Figure 9.30: Posterior mantle temperature histogram obtained without using v_ϕ data. The red curve is the input temperature and the blue curve is the estimated mean temperature profile. The contours of the gray surfaces (lighter to darker) are the 0.997, 0.95, and 0.68 probability domains.

Wrap up

Our result show that in order to gain precise information about the mantle and the crust all three sets of data, I_S, v_ϕ, and $\log(\sigma/\sigma_0)$, are indispensable. It is however, possible to infer the temperature and the parameters governing the mantle mineralogy without notable degradation, compared to the results obtained with the full data sets, from the data of v_ϕ and $\log(\sigma/\sigma_0)$ alone. Leaving out the data of v_ϕ increases the uncertainties on all parameters, especially on X_{ol}. Since, the mantle mineralogy is controlled by the value of X_{ol} and v_ϕ is strongly dependent on the mantle mineralogy. Nevertheless, it is possible to still gain sensible information about the temperature inside the mantle. Finally, without the $\log(\sigma/\sigma_0)$ data the inferred information on the mantle temperature is significantly reduced. Moreover, for this setting choosing a suitable value for the smoothing parameter is quite challenging. Given the assumed uncertainties it is from the seismic data alone not possible to make a precise inference about the mantle temperature and mantle bulk iron content, since a broad range of local mantle temperature values and x_{Fe} values lead to very similar local bulk sound velocities. However, if the uncertainties on v_ϕ are reduced by about a factor three (results not shown here), then it is possible to obtain constraining knowledge, with respect to the priors, about all the parameters.

9.5.3 Depth dependent data availability

Depth limited data can occur for seismic and electromagnetic induction data as a result of a too short data assimilation period. Since, the sounding depth of electromagnetic waves increases with increasing period, a too short data assimilation period does not allow for whole mantle sampling. Similarly, if during the measuring time the Mars-quakes are not strong enough or too infrequent a reliable whole mantle seismic sound velocity profile cannot be obtained.

We consider two cases of depth dependent data availability. First, we assume that both v_ϕ and $\log(\sigma/\sigma_0)$ have been obtained down to a depth of 810km, i.e. about the first third of the lower mantle. In the second case we assume that the data are only available down to the bottom of the lithosphere, i.e. to a depth of about 400km. For both settings we use the 2 point smoother with hand-set value of λ_T. The results are compared to those obtained with the 2 point smoother with $\lambda_T = 0.008$ and referred to as 2p08.

Data available to a depth of 810km

If the data are only available to a depth of 810km the posterior estimates of the probability intervals of I_s (Fig.[9.31]) are only slightly larger then those of setting 2p08 (Fig.[9.13]). The estimated probability intervals on $\log(\sigma/\sigma_0)$ down to a depth of 800km are only marginally wider than those in 2p08 (Fig.[9.14c]). Conversely, the probability intervals on v_ϕ over the same depth range are larger. In 2p08 the 0.997 domain (Fig.[9.14b]) is narrower than the 1σ interval of the data, whereas here the 0.997 domain is as wide as the 1σ intervals. Also, note that compared to 2p08 (Fig.[9.14a]) the inferred mantle density pdf is notably broader (Fig.[9.32a]). For depths deeper than 810km, the pdf's of both v_ϕ and $\log(\sigma/\sigma_0)$ become wider with increasing depth (Fig.[9.32b] and Fig.[9.32c]). Moreover, the deviation of the input data profiles and the estimated average profiles increase with depth.

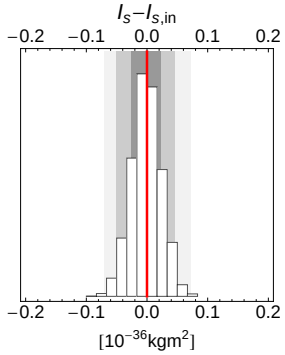


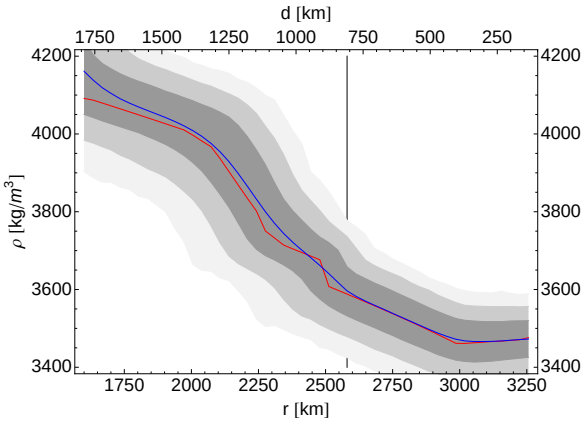
Figure 9.31: Histograms of the posterior silicate shell moment of inertia. The red lines is the input value. The gray surfaces (lighter to darker) delimit the 0.997, 0.95, and 0.68 probability intervals.

Fig.[9.34] shows the estimated pdf of the mantle temperature. For depths shallower than 810km the estimated probability intervals are only marginally wider than those of 2p08 (Fig.[9.16]). This is a consequence of the somewhat smaller value of λ_T, which was here selected to be 0.007 whereas in 2p08 we had 0.008. For depths, deeper than 810km the confidence on the estimated temperature decreases with increasing depth and is nearly as wide as the prior temperature interval at the very bottom of the mantle.

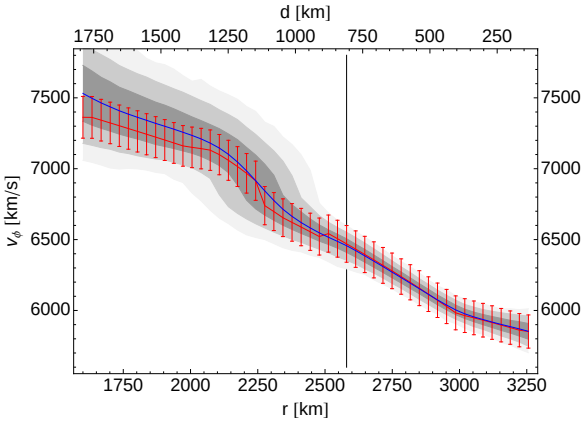
The estimated histograms and the numerical values of the estimates of the scalar parameters are given in Fig.[9.33] and Tab.[9.7]. Compared to 2p08 (Fig.[9.20]) all the estimated probability intervals are wider. The probability intervals are, however, still very much centered about the input values. Since the mantle governing parameters and the mantle temperature deeper than 810km are less well constrained, the confidence in the mantle density is strongly reduced, and consequently, the moment of inertia of the mantle has large variations and the constraint on the crust density is almost nil.

	in	mean	median	0.68	0.95	0.997
X_{ol} [vol]	0.26	0.30	0.29	$[0.18, 0.41]$	$[0.08, 0.6]$	$[0.02, 0.66]$
x_{Fe} [at]	0.28	0.28	0.28	$[0.23, 0.32]$	$[0.20, 0.35]$	$[0.15, 0.38]$
∇P [GPa/km]	0.012	0.0120	0.0120	$[0.0111, 0.0128]$	$[0.0104, 0.0137]$	$[0.0097, 0.0147]$
ρ_{crust} [kg/m^3]	2814	2781	2768	$[2466, 3095]$	$[2325, 3270]$	$[2302, 3299]$

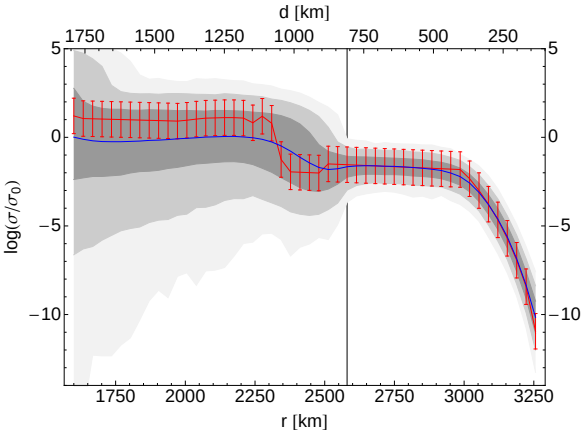
Table 9.7: Initial parameter values versus estimated mean, median, and probability intervals for 0.68, 0.95, and 0.997.



(a)



(b)



(c)

Figure 9.32: Histograms of posterior density (a), v_ϕ (b), and $\log(\sigma/\sigma_0)$ (c). The red curves are the input values and the blue curves are the estimated mean values. The error-bars on v_ϕ and $\log(\sigma/\sigma_0)$ represent the data uncertainties. The contours of the gray surfaces (lighter to darker) are the 0.997, 0.95, and 0.68 probability domains. The black line corresponds to the depth to which the data are available.

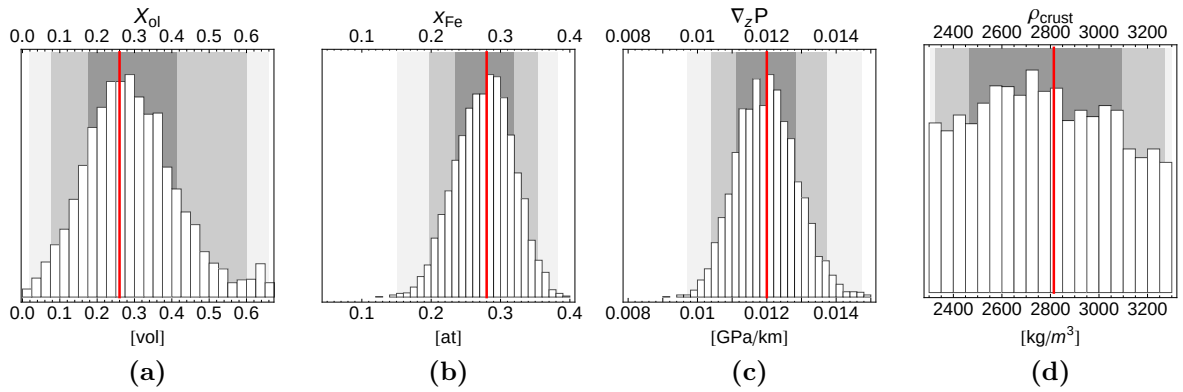


Figure 9.33: Histograms for X_{ol} (a), x_{Fe} (b), ∇P (c), and ρ_{crust} (d). The red lines represent parameter input values. The gray surfaces (lighter to darker) delimit the 0.997, 0.95, and 0.68 probability intervals.

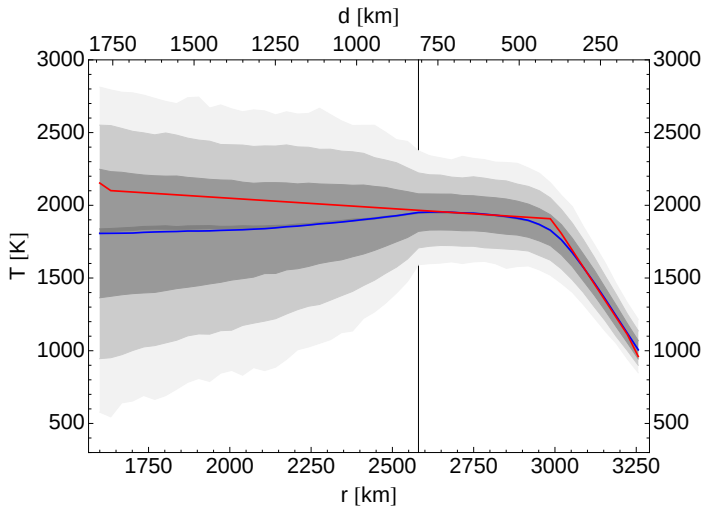


Figure 9.34: Posterior mantle temperature histogram obtained without using v_ϕ data. The red curve is the input temperature and the blue curve is the estimated mean temperature profile. The contours of the gray surfaces (lighter to darker) are the 0.997, 0.95, and 0.68 probability domains. The black line corresponds to the depth to which the data are available.

Data available to a depth of 400km

The estimated posterior data pdf's for this extreme setting are shown in Fig.[9.35] and Fig.[9.36]. Compared to 2p08 the inferred pdf of the shell moment of inertia is not visibly altered, however, the widths of the estimated pdf's of v_ϕ and $\log(\sigma/\sigma_0)$ strongly increase with depth. The results show that the temperature down to the bottom of the lithosphere can be estimated with a high confidence (Fig.[9.38]) and that for depths deeper than 400km the gained information compared to the prior on the temperature is negligible. The results of the scalar parameters, Fig.[9.37] and Tab.[9.8], show that even in this weakly constrained configuration the central estimates are very close to the input values. The confidence in those estimates is, however, drastically reduced.

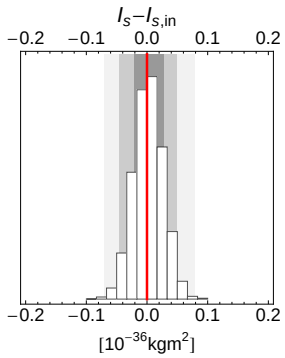


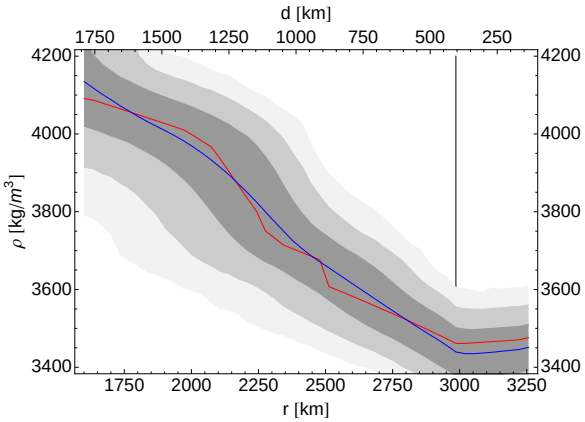
Figure 9.35: Histograms of the posterior silicate shell moment of inertia. The red lines is the input value. The gray surfaces (lighter to darker) delimit the 0.997, 0.95, and 0.68 probability intervals.

	in	mean	median	0.68	0.95	0.997
X_{ol} [vol]	0.26	0.29	0.27	[0.12, 0.46]	[0.03, 0.64]	[0.01, 0.66]
x_{Fe} [at]	0.28	0.25	0.25	[0.21, 0.3]	[0.16, 0.34]	[0.13, 0.39]
∇P [GPa/km]	0.012	0.0116	0.0117	[0.0099, 0.0134]	[0.0085, 0.0146]	[0.0080, 0.0150]
ρ_{crust} [kg/m^3]	2814	2825	2834	[2511, 3137]	[2340, 3270]	[2303, 3298]

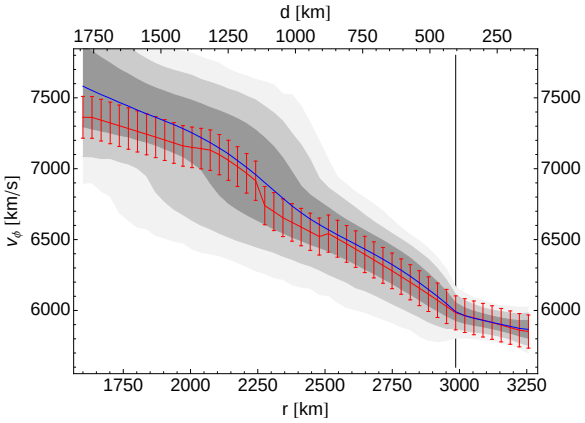
Table 9.8: Initial parameter values versus estimated mean, median, and probability intervals for 0.68, 0.95, and 0.997.

Wrap up

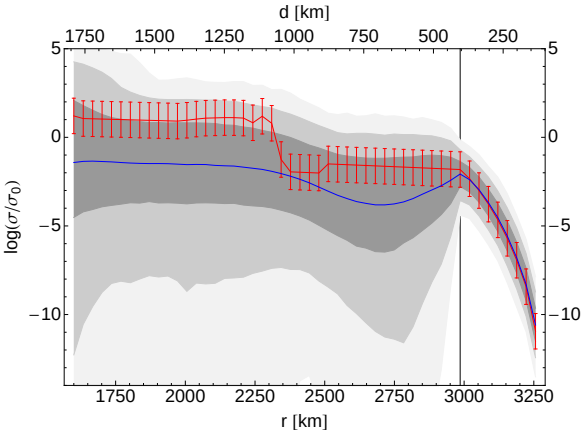
The result show that if the data are available down to a depth of 810km, the mantle mineralogy governing parameters can still be inferred with confidence and the temperature with high confidence to a depth of 810km. However, we cannot gain any appreciable information on the density of the crust. If the data are only available down to the bottom of the lithosphere, it is still possible to infer the temperature in the lithosphere with a relative high confidence, but the inferred knowledge on the remaining parameter is low.



(a)



(b)



(c)

Figure 9.36: Histograms of posterior density (a), v_ϕ (b), and $\log(\sigma/\sigma_0)$ (c). The red curves are the input values and the blue curves are the estimated mean values. The error-bars on v_ϕ and $\log(\sigma/\sigma_0)$ represent the data uncertainties. The contours of the gray surfaces (lighter to darker) are the 0.997, 0.95, and 0.68 probability domains. The black line corresponds to the depth to which the data are available.

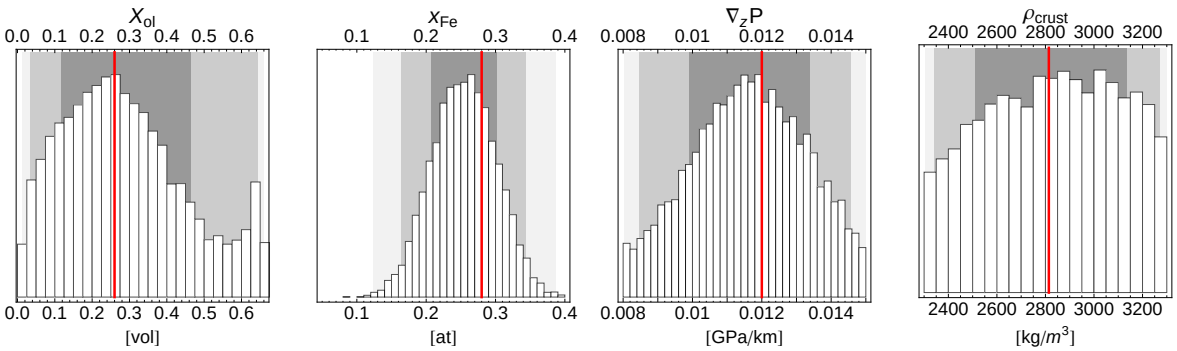


Figure 9.37: Histograms for X_{ol} (a), x_{Fe} (b), ∇P (c), and ρ_{crust} (d). The red lines represent parameter input values. The gray surfaces (lighter to darker) delimit the 0.997, 0.95, and 0.68 probability intervals.

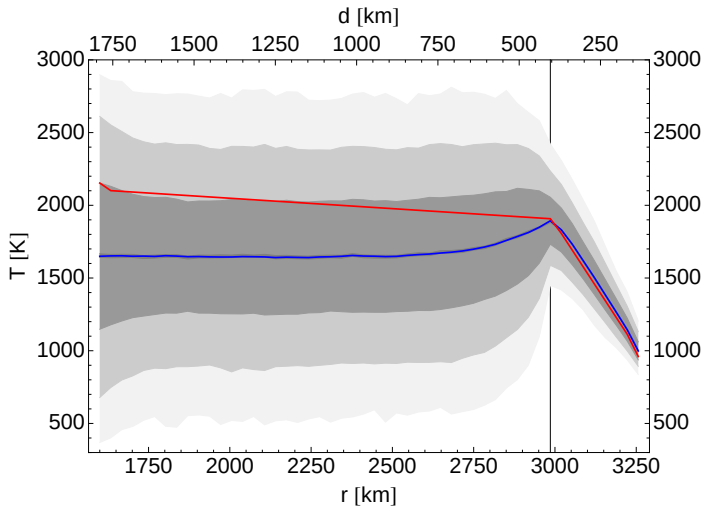


Figure 9.38: Posterior mantle temperature histogram obtained without using v_ϕ data. The red curve is the input temperature and the blue curve is the estimated mean temperature profile. The contours of the gray surfaces (lighter to darker) are the 0.997, 0.95, and 0.68 probability domains. The black line corresponds to the depth to which the data are available.

9.5.4 Increased data uncertainties

We study two cases of increased data uncertainties. In the first case, the uncertainties on the data are larger because we allow for EoS parameter uncertainties. We have seen in Sect.[8.2.5] that because of the EoS parameter uncertainties the model predictions are no longer deterministic but become probabilistic. Here, we consider only the case where model parameter uncertainties lead to normal distributed model predictions. For this setting, the data likelihood function has also a normal distribution, and its variance is the sum of the variance of the model prediction variance and the data variance. Since, compared to the assumed uncertainties on the data the induced variances on I_s and $\log(\sigma/\sigma_0)$ are small (see Sect.[3.7]) we consider only a supplemental uncertainty on v_ϕ. The model induced uncertainty on v_ϕ is about 2%. So compared to the previous setting the uncertainty on v_ϕ is doubled. In the second case, the reference uncertainties on all data are doubled. For both cases, we use the 2 point temperature smoother. For case one, we have used a Jeffrey's prior for λ_T (Fig.[9.39]) and a hand-picked value of $\lambda_T = 0.003$ for case two.

EoS parameter uncertainties

Increasing the uncertainties on v_ϕ does not degrade the quality of the inferred posterior pdf of I_S compared to 2p08 (Fig.[9.40] and Fig.[9.13]). Fig.[9.9] shows the posterior data profiles and the posterior mantle density profile. Even if the uncertainties on v_ϕ are doubled the posterior probability domains are for most depths about as in 2p08 (Fig.[9.14b]). Only in the depth range $[1100, 1300]$km the probability domains are wider. Consequently, the spread of the posterior probability domains of v_ϕ is to a large extend controlled by $\log(\sigma/\sigma_0)$.

Tab.[9.9] gives the numerical values of the scalar estimates and the corresponding estimated pdf's are shown in Fig.[9.42]. The result shows that increasing the uncertainty on v_ϕ does not significantly alter the estimated pdf on ρ_{crust} since it is principally controlled through I_S. The other pdf's show, however, somewhat broader probability intervals. The uncertainties on the temperature and on x_{Fe} are only slightly larger since their values are principally controlled by $\log(\sigma/\sigma_0)$. The most affected parameters are X_{ol} and ∇P. The larger uncertainties in v_ϕ are compatible with a wider range of mantle mineralogies. In order for the resulting mantle densities to be compatible with I_S, and since x_{Fe} and local temperature variations are suppressed by $\log(\sigma/\sigma_0)$, ∇P has to vary accordingly.

With the exception of the temperature for depths below 1000km (Fig.[9.43]) and of the volume fraction of olivine, the central estimates are very close to the input values. The estimated mean temperature is on average for depths deeper than 1000km about 100K lower than the input temperature profile, and the estimated mean value of the olivine fraction is higher by about 7vol%. For a further illustration of the anti-correlation between lower mantle temperature and olivine weight fraction see Fig.[9.19]. Finally, over the whole depth of the mantle the estimated probability domains of the temperature profile are very much alike to those of 2p08 (Fig.[9.16]).

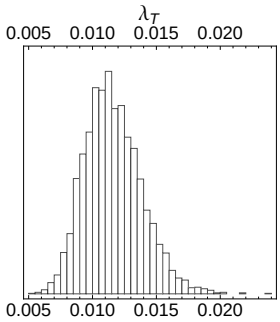


Figure 9.39: Estimated posterior pdf of λ_T for an initial Jeffrey's prior distribution.

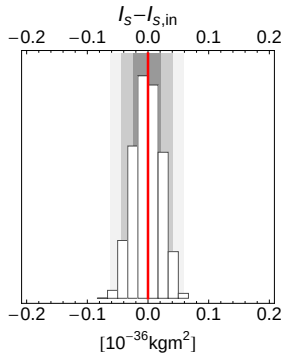
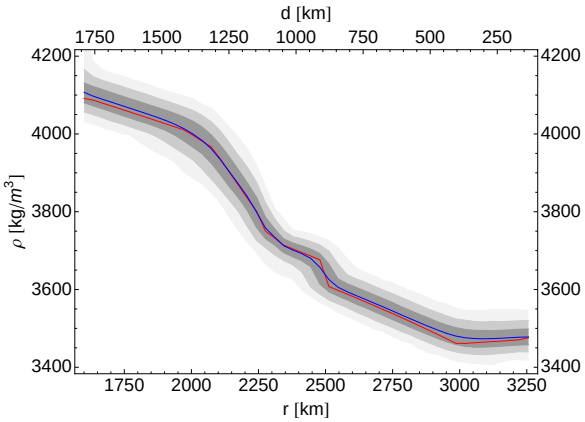


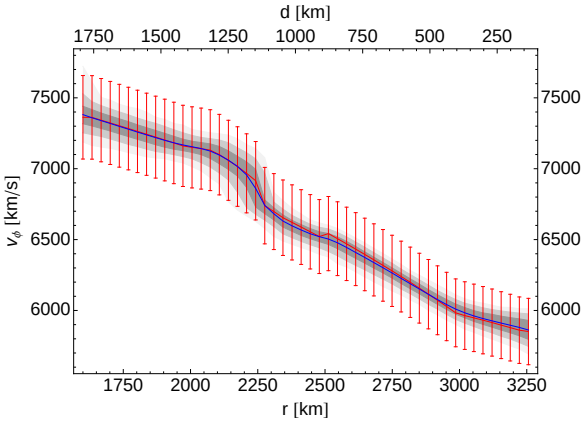
Figure 9.40: Histograms of the posterior silicate shell moment of inertia. The red lines is the input value. The gray surfaces (lighter to darker) delimit the 0.997, 0.95, and 0.68 probability intervals.

	in	mean	median	0.68	0.95	0.997
X_{ol} [vol]	0.26	0.33	0.32	$[0.20, 0.45]$	$[0.12, 0.58]$	$[0.07, 0.64]$
x_{Fe} [at]	0.28	0.28	0.28	$[0.25, 0.30]$	$[0.23, 0.33]$	$[0.21, 0.35]$
∇P [GPa/km]	0.012	0.0119	0.0119	$[0.0115, 0.0123]$	$[0.0110, 0.0125]$	$[0.0106, 0.0128]$
ρ_{crust} [kg/m^3]	2814	2783	2783	$[2541, 3024]$	$[2369, 3212]$	$[2305, 3288]$

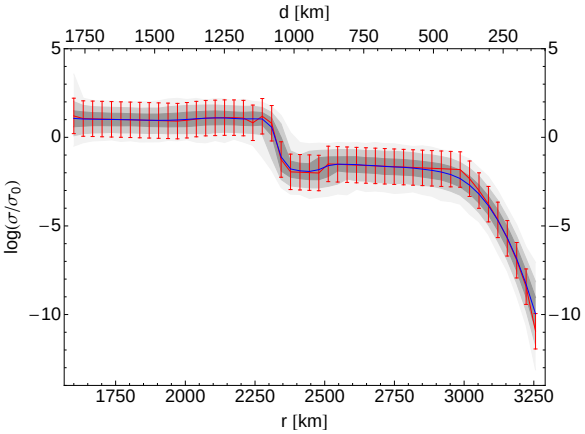
Table 9.9: Initial parameter values versus estimated mean, median, and probability intervals for 0.68, 0.95, and 0.997.



(a)



(b)



(c)

Figure 9.41: Histograms of posterior density (a), v_ϕ (b), and $\log(\sigma/\sigma_0)$ (c). The red curves are the input values and the blue curves are the estimated mean values. The error-bars on v_ϕ and $\log(\sigma/\sigma_0)$ represent the data uncertainties. The contours of the gray surfaces (lighter to darker) are the 0.997, 0.95, and 0.68 probability domains. The black line corresponds to the depth to which the data are available.

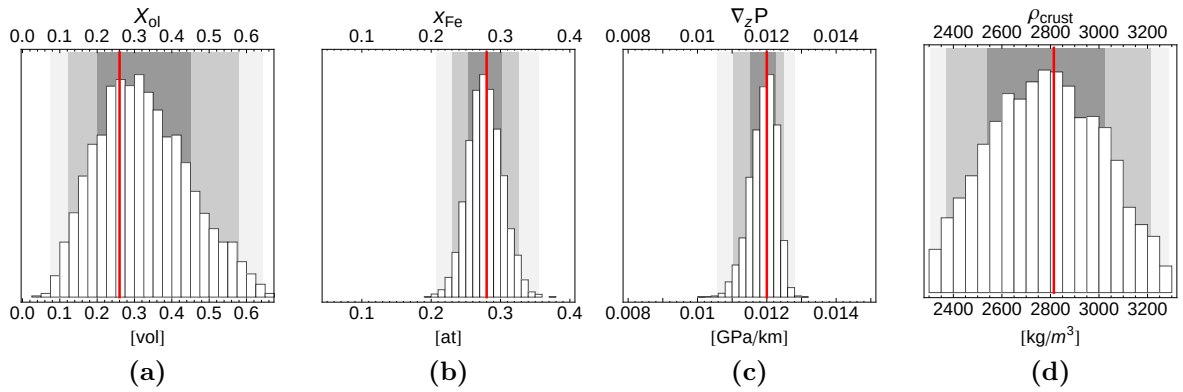


Figure 9.42: Histograms for X_{ol} (a), x_{Fe} (b), ∇P (c), and ρ_{crust} (d). The red lines represent parameter input values. The gray surfaces (lighter to darker) delimit the 0.997, 0.95, and 0.68 probability intervals.

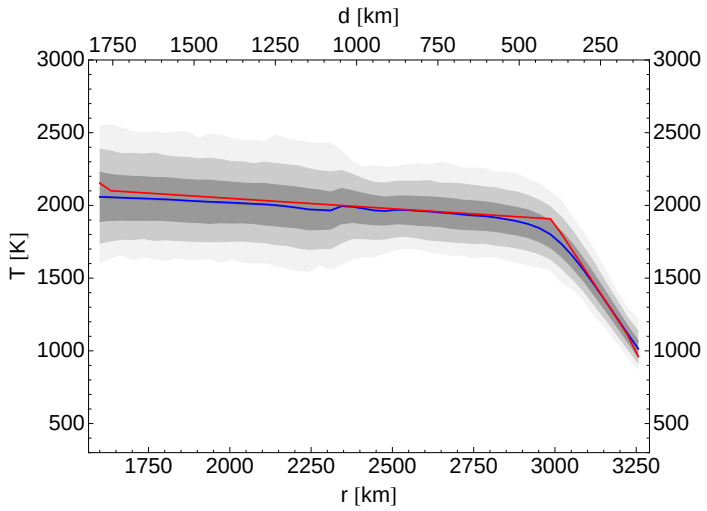


Figure 9.43: Posterior mantle temperature histogram. The red curve is the input temperature and the blue curve is the estimated mean temperature profile. The contours of the gray surfaces (lighter to darker) are the 0.997, 0.95, and 0.68 probability domains.

Doubled data uncertainties

Doubling the uncertainty on all data lessens the relative weight of the likelihood with respect to the prior knowledge in the posterior pdf. For this reason, the value of λ_T has been decreased to 0.003. The value is, however, too large since some of the detailed structure in the data profiles is smoothed out, see Fig.[9.45b] and Fig.[9.45c]. However, smaller values of λ_T result in a too weak smoothing of the possible temperature profiles. The results show that for v_ϕ the estimated 0.997 domains are for most of the mantle smaller than the corresponding 1σ domains of the data, see Fig.[9.45b]. For $\log(\sigma/\sigma_0)$ it is again (Fig.[9.14c]) the 0.95 domain that corresponds to the 1σ domain of the data (see Fig.[9.45c]). The estimated posterior pdf of I_s is given in Fig.[9.44] and the mantle density profile in Fig.[9.45a].

Fig.[9.46] and Fig.[9.47] shows that even if the data uncertainties are doubled the central estimates of the parameters are very close the input parameter values. However, the confidence in the estimates is lowered. Compared to 2p08 (see Tab.[9.6] and Fig.[9.16]), the length of the 0.68 intervals of x_{Fe}, ∇P, and of the mantle temperature are approximatively doubled and those of X_{ol} and ρ_{crust} increase by a factor of about 1.5. The numerical values for the scalar estimates are given in Tab.[9.10].

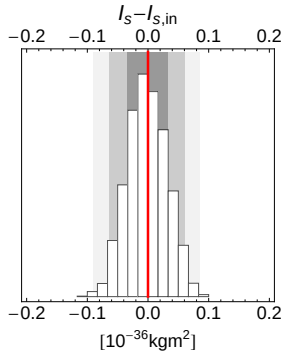
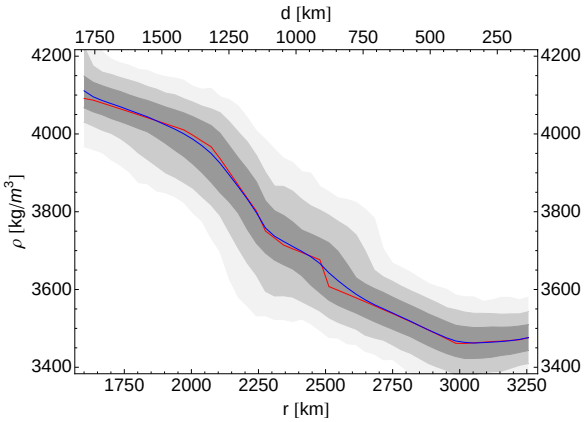


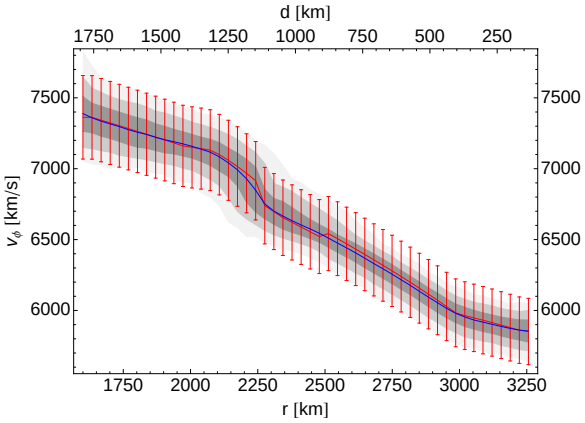
Figure 9.44: Histograms of the posterior silicate shell moment of inertia. The red lines is the input value. The gray surfaces (lighter to darker) delimit the 0.997, 0.95, and 0.68 probability intervals.

	in	mean	median	0.68	0.95	0.997
X_{ol} [vol]	0.26	0.30	0.30	[0.18, 0.43]	[0.10, 0.57]	[0.05, 0.64]
x_{Fe} [at]	0.28	0.28	0.28	[0.21, 0.32]	[0.21, 0.36]	[0.18, 0.39]
∇P [GPa/km]	0.012	0.0118	0.0119	[0.0109, 0.0123]	[0.0109, 0.0126]	[0.0105, 0.0130]
ρ_{crust} [kg/m^3]	2814	2819	2819	[2503, 3122]	[2343, 3270]	[2303, 3299]

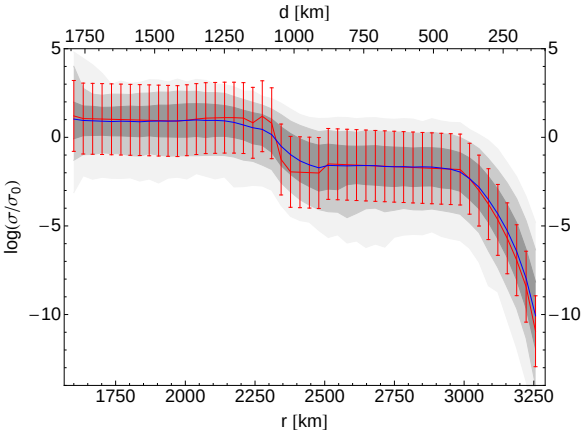
Table 9.10: Initial parameter values versus estimated mean, median, and probability intervals for 0.68, 0.95, and 0.997.



(a)



(b)



(c)

Figure 9.45: Histograms of posterior density (a), v_ϕ (b), and $\log(\sigma/\sigma_0)$ (c). The red curves are the input values and the blue curves are the estimated mean values. The error-bars on v_ϕ and $\log(\sigma/\sigma_0)$ represent the data uncertainties. The contours of the gray surfaces (lighter to darker) are the 0.997, 0.95, and 0.68 probability domains. The black line corresponds to the depth to which the data are available.

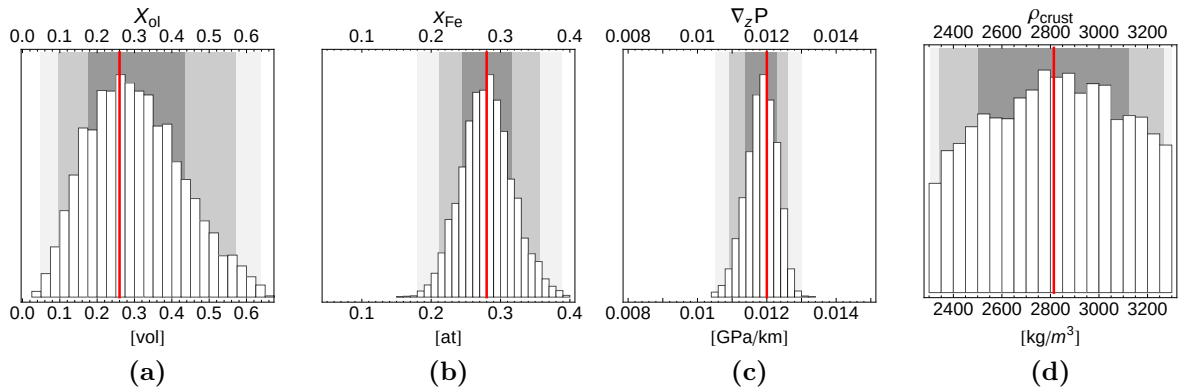


Figure 9.46: Histograms for X_{ol} (a), x_{Fe} (b), ∇P (c), and ρ_{crust} (d). The red lines represent parameter input values. The gray surfaces (lighter to darker) delimit the 0.997, 0.95, and 0.68 probability intervals.

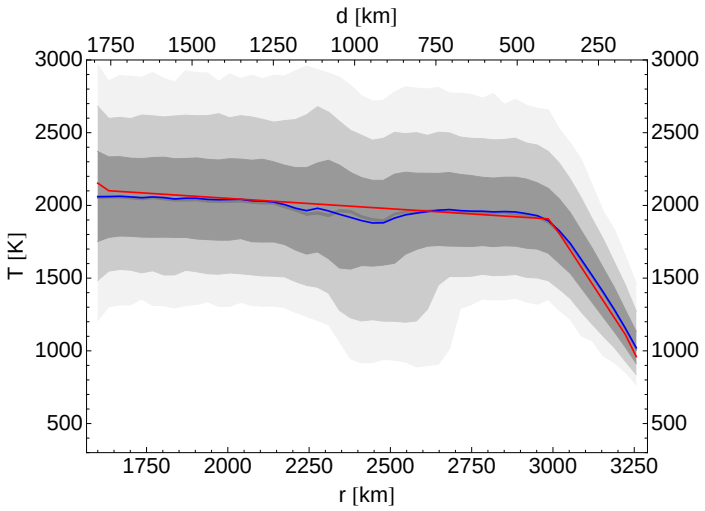


Figure 9.47: Posterior mantle temperature histogram. The red curve is the input temperature and the blue curve is the estimated mean temperature profile. The contours of the gray surfaces (lighter to darker) are the 0.997, 0.95, and 0.68 probability domains.

Wrap up

Including EoS parameter uncertainties in the inversion procedure slightly increases the widths of the probability intervals of the temperature profile for depth deeper than 1000km. The strongest effect is experienced by the parameters $X_{\rm ol}$ and ∇P, for which the length of their 0.68 intervals increases by about 50%. The impact on $x_{\rm Fe}$ and $\rho_{\rm crust}$ are lower. The length of their 0.68 intervals only increase by about 25% and less than 10%, respectively. If the uncertainties on all the data are doubled the length of the 0.68 intervals of $x_{\rm Fe}$ and ∇P are about twice as wide, and those on $X_{\rm ol}$ and $\rho_{\rm crust}$ increase by about 50%. For both settings, the initial parameter values are very close to the center of the 0.68 intervals.

9.6 Extension to the other mantle minerals

The forward problem relating the local mantle density, bulk sound velocity, and mantle electrical conductivity is parameterized by the local temperature, pressure, and bulk mantle mineralogy. The bulk mantle mineralogy is specified by the volume fractions of olivine, orthopyroxene, Ca-pyroxene, and garnet, and the bulk mantle iron content. In order to decrease the number of model parameters we have introduced empirical relations between the mineral fractions (9.3) allowing for the calculation of the pyroxene fractions (orthopyroxene and Ca-pyroxene) from the olivine fraction. In this section we will not use the empirical relation between the mineral fractions (reduced setting) but extend the forward problem to include the fractions of olivine, orthopyroxene, Ca-pyroxene, and garnet as model parameters (extended setting). Note that volume fractions are not independent since $X_{\rm gt} + X_{\rm ol} + X_{\rm opx} + X_{\rm capx} = 100$.

We first give the results for the case without temperature smoother. We use the same uncertainties as those that have been used in the reduced setting (see Tab.[9.2]). The results are compared to those obtained with relations (9.3) using no temperature smoother prior (see Figs. [9.4,9.5,9.6,9.7,9.9]). We refer to them as 2p00.

The estimated posterior pdf's for v_ϕ (Fig.[9.49b]) and $\log(\sigma/\sigma_0)$ (Fig.[9.49c]) are very similar to those of 2p00. However, the estimated average mantle density is systematically larger than the input profile (Fig.[9.49a]). The privileged denser mantle density profiles result in moment of inertia estimates that are larger than the input datum (Fig.[9.48]). The reasons for the overestimated density profile are twofold. They are related to the data privileged mantle mineralogies and temperature profiles. The estimated average value of $x_{\rm Fe}$ (Fig.[9.50e]) is larger than the input value, consequently, the mantle is denser. The estimated average volume fraction of olivine (Fig.[9.50a]) is larger and the estimated volume fraction of orthopyroxene Fig.[9.50b] is smaller than the respective input values. Since olivine is denser than orthopyroxene the upper mantle density profile is larger (Tab.[3.2]). In the lower part of the mantle, the overestimated density can be ascribed principally to the underestimated temperature in the lower mantle. Since the principal stable phases of the lower mantle contain majorite and ringwoodite (Fig.[6.3]) that have about the same density (Tab.[3.2]). The estimated average fractions of garnet and Ca-pyroxene, are found in close vicinity to the input values (Fig.[9.50d] and Fig.[9.50c]).

The estimated pdf's of the crust thickness and mantle pressure gradient are given in Fig.[9.50g] and Fig.[9.50f]. Since the data privileged mantle mineralogies are in a favor of

a somewhat denser mantle, the crust density is driven toward lower values by the planet shell moment of inertia constraint. Moreover, the lower crust density implies that the pressure at the top of the mantle is somewhat reduced. The pressure or depth at which the major phase transitions occur in the middle of the mantle (at about 1000km in Fig.[6.3]) is well constrained by the location of the drastic change in the electrical conductivity in the middle of the mantle (Fig.[9.49c]). Since, for the data privileged higher values of x_{Fe} the occurrences of those phases transitions are moved towards lower pressures [*Mocquet et al.*, 1996], the pressure inside the mantle is pushed toward lower values. The numerical values of the parameter estimates are given in Tab.[9.11] and the correlations between the different parameters are illustrated in Fig.[9.52],

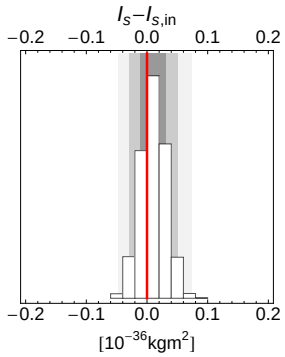
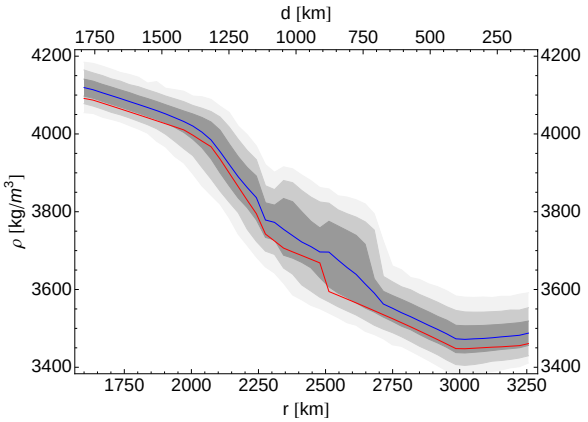


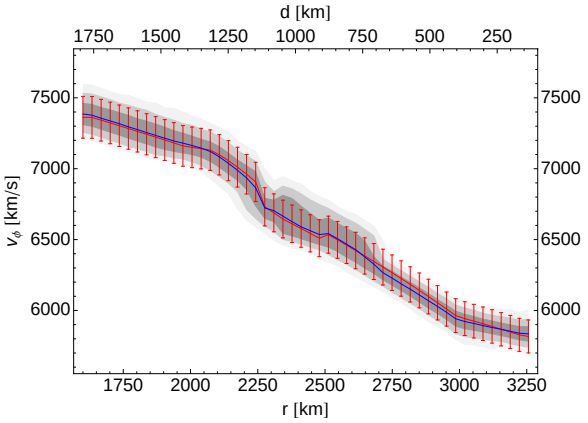
Figure 9.48: Histograms of the posterior silicate shell moment of inertia. The red lines is the input value. The gray surfaces (lighter to darker) delimit the 0.997, 0.95, and 0.68 probability intervals.

	in	mean	median	0.68	0.95	0.997
X_{ol} [vol]	0.26	0.31	0.31	[0.22, 0.41]	[0.15, 0.53]	[0.10, 0.64]
X_{opx} [vol]	0.61	0.48	0.49	[0.36, 0.59]	[0.24, 0.68]	[0.09, 0.76]
X_{capx} [vol]	0.03	0.08	0.06	[0.02, 0.13]	[0, 0.23]	[0, 0.33]
X_{gt} [vol]	0.10	0.13	0.13	[0.06, 0.2]	[0.02, 0.27]	[0, 0.34]
x_{Fe} [at]	0.28	0.3	0.3	[0.27, 0.32]	[0.25, 0.35]	[0.23, 0.39]
∇P [GPa/km]	0.012	0.0117	0.0117	[0.0115, 0.012]	[0.0112, 0.0123]	[0.0108, 0.0125]
ρ_{crust} [kg/m^3]	2549	2714	2717	[2482, 2927]	[2336, 3130]	[2302, 3276]

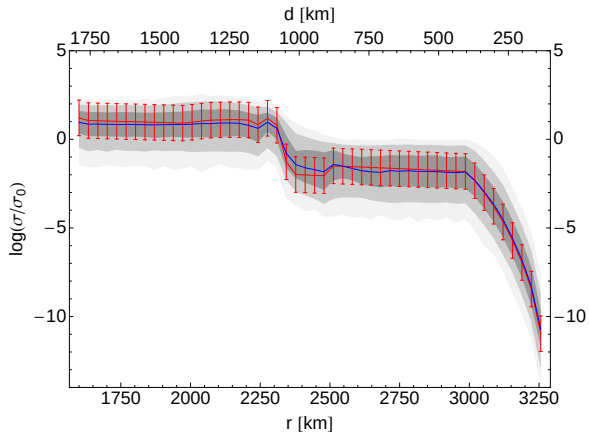
Table 9.11: Initial parameter values versus estimated mean, median, and probability intervals for 0.68, 0.95, and 0.997.



(a)



(b)



(c)

Figure 9.49: Histograms of posterior density (a), v_ϕ (b), and $\log(\sigma/\sigma_0)$ (c). The red curves are the input values and the blue curves are the estimated mean values. The error-bars on v_ϕ and $\log(\sigma/\sigma_0)$ represent the data uncertainties. The contours of the gray surfaces (lighter to darker) are the 0.997, 0.95, and 0.68 probability domains. The black line corresponds to the depth to which the data are available.

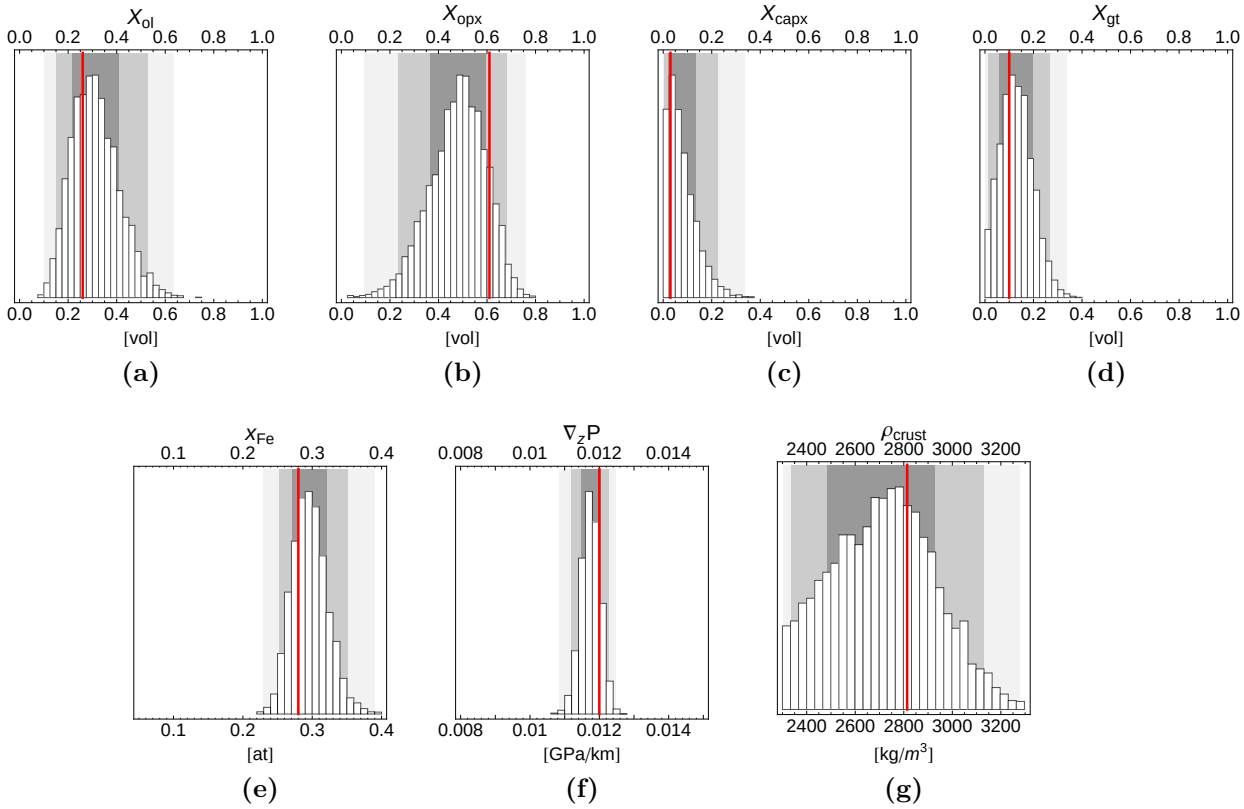


Figure 9.50: Histograms for X_{ol} (a), X_{opx} (b), X_{capx} (c), X_{gt} (d), x_{Fe} (e), ∇P (f), and ρ_{crust} (g). The red lines represent parameter input values. The gray surfaces (lighter to darker) delimit the 0.997, 0.95, and 0.68 probability intervals.

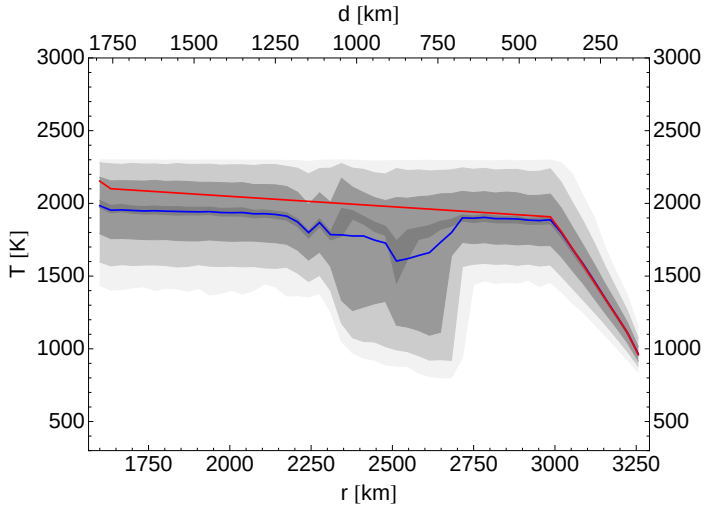


Figure 9.51: Posterior mantle temperature histogram. The red curve is the input temperature and the blue curve is the estimated mean temperature profile. The contours of the gray surfaces (lighter to darker) are the 0.997, 0.95, and 0.68 probability domains.

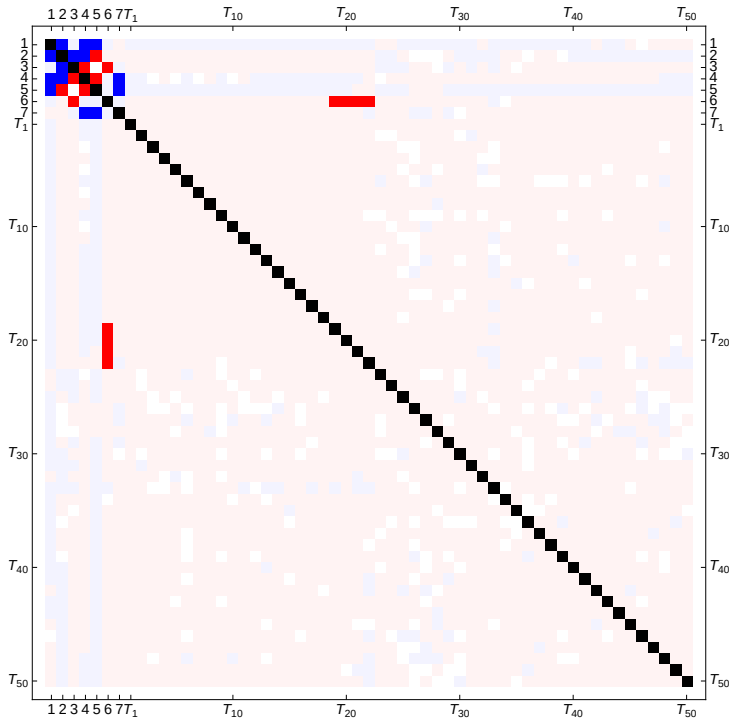


Figure 9.52: Estimated parameter correlation matrix. Black squares have correlation 1, blue squares have negative correlation and red squares have positive correlation. Darker blue or red squares have absolute correlation larger than 0.25. Indices 1 to 7 stand for X_{ol}, X_{opx}, X_{capx}, X_{gt}, x_{Fe}, ∇P, and ρ_{crust}.

Compared to the prior intervals, the data allows, within this extended model setting, to infer relevant information about the parameter distributions. With the exception of X_{opx} the estimated 0.68 probability intervals contain the input values. Compared to the results of the 2p00 setting, the estimated 0.68 probability intervals have about the same width, with the exception of the olivine fraction, whose 0.68 interval increases by about 6vol% (see Tab.[9.4] and Tab.[9.11]). Similarly to the setting 2p00, the constraints provided by the data allow for unwanted temperature fluctuations in the middle of the convective part of the mantle. Likewise to the reduce forward problem setting we here apply the 2-point temperature smoother to suppress the local temperature fluctuations. We have handset λ_T to 0.02.

The resulting posterior data estimates are shown in Fig.[9.54]. Compared to the non-smoothed setting the estimated 0.68 probability intervals are significantly narrower. The estimated posterior mean density profile is notably less overestimated and the posterior pdf of the moment of inertia is centered about the input datum value (Fig.[9.53]).

The estimated temperature profile is smooth over the whole lower mantle, and the input temperature profile is within the 0.68 probability interval (Fig.[9.56]). Although, similar to the non-smoothed setting the estimated mean lower mantle temperatures are underestimated by about 100K. With the exception of X_{opx}, the estimated 0.68 intervals contain the input values and with the exception of X_{ol} and X_{opx} the estimated mean values of the parameters are close to the input values (Fig.[9.55]). The estimated average values of the X_{ol} and X_{opx} are overestimated and underestimated, respectively. The deviations from the input values are even larger than in the non-smoothed setting. The numerical values associated to the scalar parameter estimates are given in Tab.[9.12].

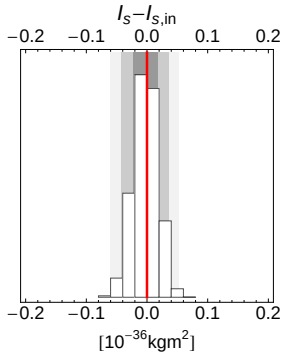
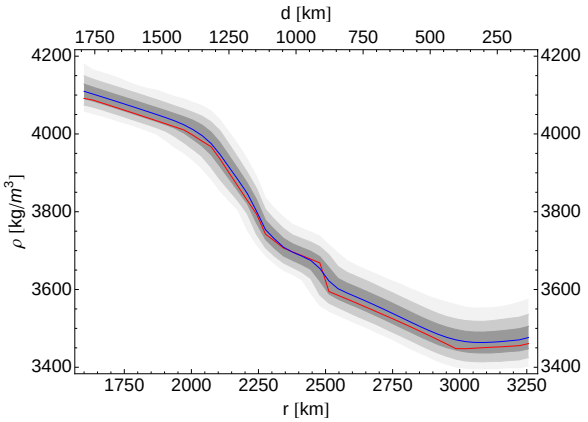


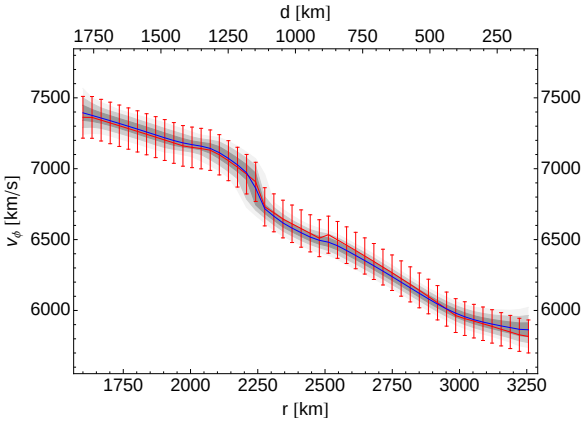
Figure 9.53: Histograms of the posterior silicate shell moment of inertia. The red lines is the input value. The gray surfaces (lighter to darker) delimit the 0.997, 0.95, and 0.68 probability intervals.

	in	mean	median	0.68	0.95	0.997
X_{ol} [vol]	0.26	0.34	0.34	[0.25, 0.44]	[0.18, 0.54]	[0.13, 0.68]
X_{opx} [vol]	0.61	0.44	0.44	[0.32, 0.55]	[0.18, 0.64]	[0.05, 0.71]
X_{capx} [vol]	0.03	0.08	0.07	[0.02, 0.14]	[0, 0.23]	[0, 0.33]
X_{gt} [vol]	0.10	0.14	0.14	[0.07, 0.21]	[0.03, 0.27]	[0, 0.36]
x_{Fe} [at]	0.28	0.28	0.28	[0.26, 0.3]	[0.24, 0.32]	[0.23, 0.34]
∇P [GPa/km]	0.012	0.0118	0.0118	[0.0115, 0.0121]	[0.0113, 0.012]	[0.0108, 0.0125]
ρ_{crust} [kg/m^3]	2549	2757	2756	[2545, 2966]	[2367, 3159]	[2305, 3283]

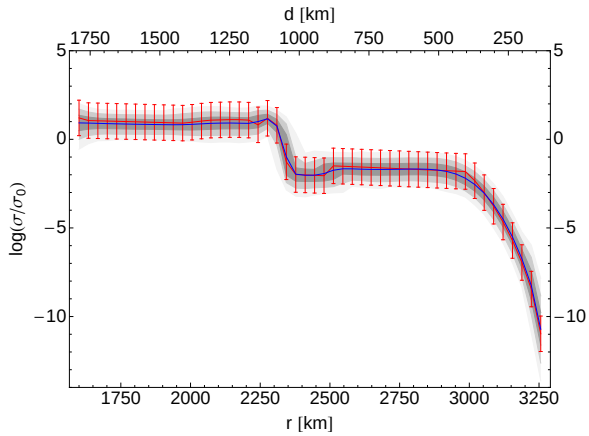
Table 9.12: Initial parameter values versus estimated mean, median, and probability intervals for 0.68, 0.95, and 0.997.



(a)



(b)



(c)

Figure 9.54: Histograms of posterior density (a), v_ϕ (b), and $\log(\sigma/\sigma_0)$ (c). The red curves are the input values and the blue curves are the estimated mean values. The error-bars on v_ϕ and $\log(\sigma/\sigma_0)$ represent the data uncertainties. The contours of the gray surfaces (lighter to darker) are the 0.997, 0.95, and 0.68 probability domains. The black line corresponds to the depth to which the data are available.

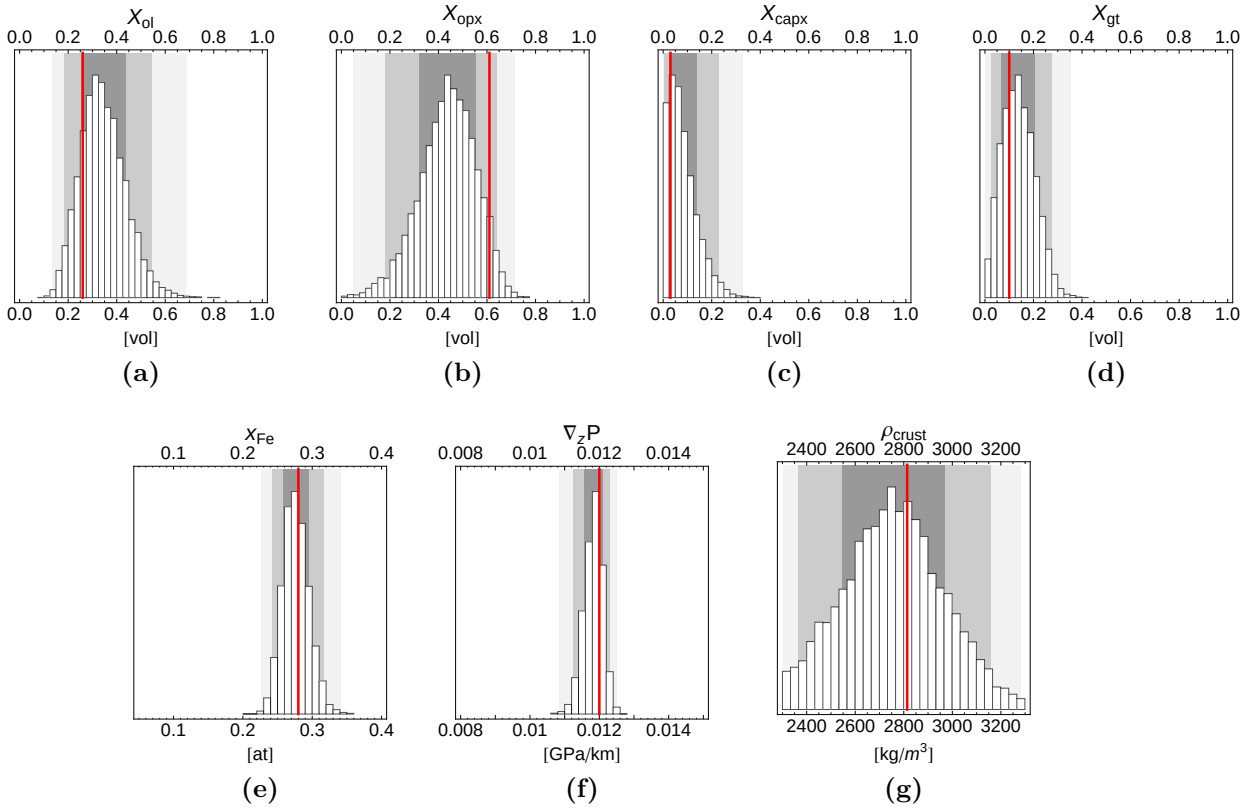


Figure 9.55: Histograms for X_{ol} (a), X_{opx} (b), X_{capx} (c), X_{gt} (d), x_{Fe} (e), ∇P (f), and ρ_{crust} (g). The red lines represent parameter input values. The gray surfaces (lighter to darker) delimit the 0.997, 0.95, and 0.68 probability intervals.

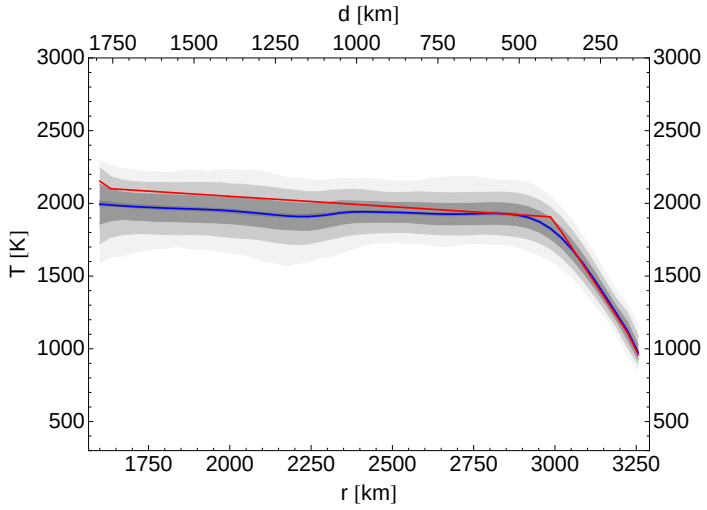


Figure 9.56: Posterior mantle temperature histogram. The red curve is the input temperature and the blue curve is the estimated mean temperature profile. The contours of the gray surfaces (lighter to darker) are the 0.997, 0.95, and 0.68 probability domains.

Wrap up

The result show that given the assumed uncertainties (Tab.[9.2]) on the data it is possible within the above extended setting to gain strongly constraining information, compared to the prior, about the parameters of the model. For all, but X_{opx} the estimated 0.68 probability intervals comprise the input values. Among all the parameters, X_{ol}, X_{opx}, and the temperature of the lower mantle show the largest deviation from the input values. The relative deviations are about 30% for the olivine and orthopyroxene volume fraction, and about 5% for the temperature of the lower mantle. Those deviations can, however, be reduced by more than a factor of two if the relative uncertainty on the v_ϕ data is reduced by a factor two (results not shown here).

Compared to the reduced forward problem setting the estimated widths of the 0.68 probability intervals on the common set of parameters are about the same. The width of the 0.68 probability interval of X_{opx} is similar to that calculated with the empirical relations (9.3) in the reduced setting by using the estimated uncertainty on X_{ol}. The width's on X_{capx} and X_{gt} are, however, about three times as large. Moreover, in the extended setting the bias on the estimated volume fraction of olivine is about four times larger. In the reduced setting the bias on X_{opx}, X_{capx}, and X_{gt} can be estimated by using the bias on X_{ol} with (9.3) together with the deviations of the calculated volume fractions with the intrinsic volume fractions of the EH45 model (Tab.[6.3]). They are about 10vol% and 5vol% lower for X_{opx} and X_{capx}, and about similar for X_{gt}. Note that the estimated pdf of X_{capx} is skewed (see Fig.[9.55c]) and therefore the estimated mean does not provide an informative summary. A more appropriate summary is the mode of the pdf. With this estimator, the bias on X_{capx} is negligible.

In conclusion, with the assumed uncertainties on the data the empirical relations (9.3) allow to retrieve estimated mineral volume fractions that are very close to those used to simulate the data. However, the relations lack any geophysical justification whatsoever and can only be derived if an extended set of mantle mineralogy models is known beforehand. Moreover, the relations are not stable with respect to the set of mineralogy models used. For instance, omitting the pre-SNC model MA79 and the Earth-like pyrolite model will lead to appreciable different parameter values in the relations linking the mineral volume fractions. Performing an inversion with an empirical relation between the mineral volume fractions is similar to using a supplemental strong informative prior. We therefore recommend against using the empirical relations, even if with the assumed data uncertainties the deviations between the estimated mean mineral volume fractions are larger and the temperature in the lowest part of the mantle slightly underestimated. Note that if the pressure inside the mantle is not calculated from pressure gradient parameter, but rather computed by solving the hydrostatic pressure equations (2.1) and (2.2), the deviations between the input and estimated volume fractions of olivine and orthopyroxene are reduced by about 2vol% (results not shown here). Finally, if the uncertainties on v_ϕ are reduced by a factor two the deviations between input parameter values and estimated parameter values are about similar to those obtained by using the empirical relations (results not shown here).

9.7 Conclusions

In this study we have demonstrated that from the joint use of different geophysical data sets (moment of inertia of the silicate shell, mantle seismic velocity and electrical conductivity) detailed information about the composition, temperature, and pressure of the mantle can be gained. In order to achieve this goal we have inverted the non-linear model relating the mantle parameters and the density of the crust to the geophysical data sets by a Bayesian procedure. For realistic data uncertainties we have shown that with exception of the density of the crust, the data significantly increases our knowledge about the model parameters beyond the geophysical plausible but vague prior information adopted.

To obtain plausible realizations of the mantle temperature profiles supplemental prior knowledge has to be assumed. We have shown that with the assumed uncertainties on the data, the central estimates of the inferred posterior pdf's are only in very close vicinity of the input parameters values if a temperature smoothing prior is adopted. We have chosen a parameterized prior probability density function that penalizes sharp local temperature variations and favors smooth temperature profiles. The value of the smoothing parameter controls the smoothness of the mantle temperature profiles.

Among all the data, the moment of inertia of the silicate shell is the least constraining, since its knowledge mostly constrains the density of the crust. The knowledge of the bulk sound velocity constrains principally the volume fraction of olivine and the mantle temperature of the deep mantle, whereas the mantle electrical conductivity strongly constrains the temperature of the upper part of the mantle and the bulk fraction of iron. As could be expected then, from the moment of inertia of the silicate shell and the electrical conductivity profile of the mantle but without seismic data the temperature profile in the mantle can still be estimated with relatively high confidence. However, the knowledge on the other parameters related to the mantle is notably reduced. Slightly better estimates on the scalar parameters of the mantle (X_{ol}, x_{Fe}, ∇P) are obtained from the bulk sound velocity and moment of inertia of the silicate shell alone, but no useful information about the mantle temperature can be obtained. In order to obtain pertinent knowledge about the mantle temperature and about the scalar parameters from the moment of inertia of the shell and from the bulk sound velocity profile, the uncertainty on the sound velocity has to be reduced at least by a factor three. These findings and the fact that the posterior 0.68 intervals of the data are narrower than the 1σ intervals of the data, demonstrates the high complementarity of the data.

Our results corroborate that even if the data are only available for about half the depth of the mantle the temperature profile can be inferred with high confidence to that depth and the scalar parameters of the model, except the density of the crust, are inferred with relatively good confidence. If the data are only available to the depth of the bottom of the lithosphere, only the temperature in that part of the mantle can be estimated with confidence.

We have also investigated how the results are affected if the uncertainties on the data are increased. Our result show that the locations of the central estimates of the parameters are relatively stable to changing data uncertainties. If we allow for EoS parameters uncertainties, which in our setting amounts to increasing the uncertainties on the seismic sound velocity data, all parameters can still be estimated with confidence.

Finally, we have shown that if the forward problem is extended to incorporate the

volume fractions of orthopyroxene, Ca-pyroxene, and garnet as parameters and within the assumed data uncertainties highly relevant informations about all parameters can still be gained. However, in order for the estimated parameters to have about the same accuracy as those obtained by using the empirical relations (9.3) the uncertainties on v_ϕ have to be reduced by about a factor two. This demonstrates the relevance of the empirical relations for settings with larger uncertainties, depth limited data, or missing data. However, for settings with complete data sets and with data uncertainties similar to the above assumed we do not advice to use relations (9.3) since they lack any geophysical justification and necessitate beforehand to know an extended set of possible mantle mineralogy models.

Appendix A

Affinities of chemical elements

Chemical elements can be classified according to their main affinity, i.e. their preferred host phase, into *siderophile* (iron loving), *lithophile* (silicate loving), *chalcophile* (sulfur loving), and *atmophile* (gas loving).

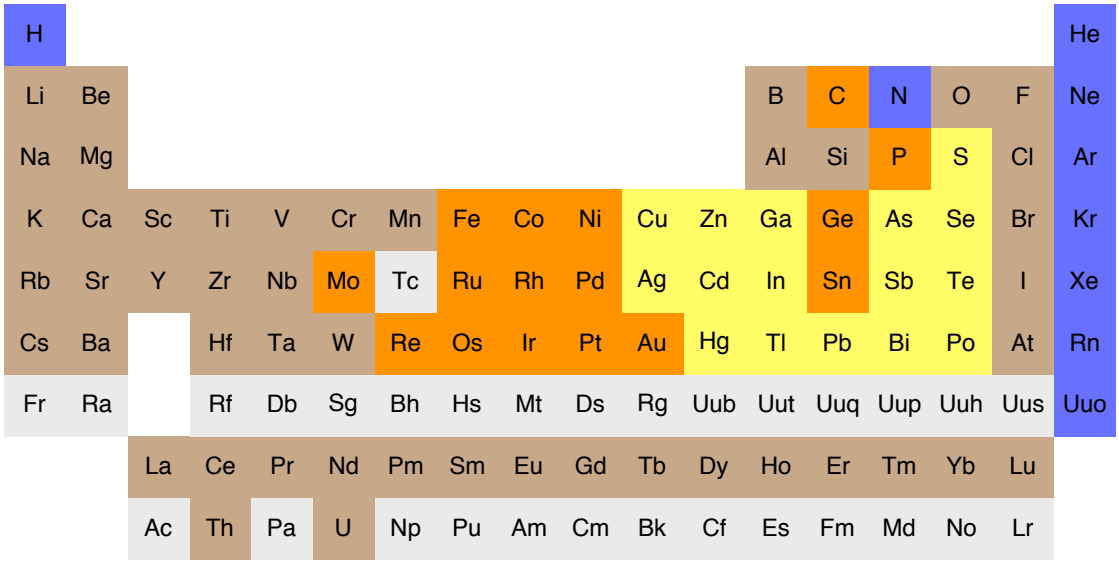


Figure A.1: Chemical affinities of principal elements. Blue shading is for atmophile, brown for lithophile, orange for siderophile, and yellow for chalcophile.

The lithophile elements are mainly confined to the crust and to the mantle, and the siderophile elements to the core. The sulfur loving chalcophile elements are to be found in the crust, mantle, and core.

Conclusion and outlook

The aim of the first part of this thesis has been to devise an interior structure model whose parameters can be constrained by the geodetic measurements, planet mass, average moment of inertia, and tidally induced deformations resulting in external potential variations that are characterized by the Love number k_2. Those observables depend on how the density, the state, solid or liquid, and the elastic properties of the materials comprising the planet body change with depth. In detail, the elastic properties and the density of the planet materials depend on the mineralogical composition and the local temperature and pressure. Additionally, the tidally induced deformation strongly depend on the location of the core mantle boundary if the outer core is liquid. Our constructed whole planet model is therefore parameterized by the crust average density and thickness, the temperature, and the mineralogy of the mantle, the size, state, and composition of the core. For given crust density and thickness, a mantle temperature profile, and a mantle mineralogy, specified by the low pressure phases of olivine, pyroxene, and garnet, and their contents of iron, for a given core light element candidate and core size our model allows to calculate the depth dependent density and elastic moduli for the mantle and the core. Furthermore, the self-consistent thermodynamic liquid solution model used for describing the liquid part of the core allows together with melting data of iron and the candidate light element to decide on the presence or not of a solid inner core. From the resulting whole planet density and elastic moduli profiles, the geodetic observation can then be calculated or predicted.

We have applied our model on the most recent geodetic measurements relative to the planet Mars. The considered geodetic data set does, however, not allow to constrain the temperature and the mineralogy of the mantle, and the nature of the light elements inside the core simultaneously with the other parameters of the model. We therefore have used mantle temperature profiles that are plausible end-members of studies dedicated to the thermal evolution of Mars and five published Mars mantle mineralogies that have been inferred from acquired knowledge about in-situ rock analyses, meteoritic samples and planetary accretion scenarios. Furthermore, we have assumed that the light element in the core is sulfur and has used the most recent melting data on iron-sulfur to construct an empirical melting law. Additionally, we have used the most recent equation of state parameters on solid iron and on iron-sulfur liquids. Note that, in previous published core models about Mars the liquid part of the core has often been described with EoS parameters of solids [*Sohl and Spohn*, 1997; *Bertka and Fei*, 1998; *Zharkov and Gudkova*, 2005, e.g.].

We have found, given the above modeling and from the new melting data, that if Mars had an inner core and if the sulfur concentration were below the eutectic concentration, it would not grow from solidifying iron rich material at the center of the planet, like it does

inside Earth's core, but from precipitating or snowing dense iron-rich solid material expelled from the liquid in the upper part of the core. The reason being that for the Fe − S system, unlike the high pressure range inside the Earth's core, at the Mars core pressures the gradient of the melting temperature is steeper than the adiabatic temperature gradient inside the core and therefore upon cooling the core temperature drops below the melting temperature first in the low pressure upper part of the core [c.f. *Williams*, 2009, for an extended discussion about top-down solidification of small solar system bodies]. Note that this inner core growing scenario has already been anticipated from laboratory results on high pressure melting data of Fe − S systems [*Stewart et al.*, 2007; *Chen et al.*, 2008].

From the geodetic data set, planet mass, moment of inertia, and Love number k_2, we have found that the core size is 1616 ± 137km. The corresponding pressure conditions at the bottom of the mantle and the two considered mantle temperature profiles allow for the occurrence of a perovskite-bearing layer at the bottom of the Martian mantle. The existence of this endothermic phase transition in the deep Martian mantle is favorable for the occurrence of a small number of large mantle plumes, consistent with the interpretation that Tharsis and Elysium are plume-related features [*van Thienen et al.*, 2006].

The data constrains the core sulfur concentration to be in a $[6, 18]$wt% range (at a 1σ level). For such a large fraction of sulfur and given the temperature inside the core, the core is fully molten. The absence of a solid inner core implies that, unlike for the Earth, the past short lived early Martian dynamo [e.g. *Acuña et al.*, 1999] was not driven by compositional convection in the liquid outer but most likely by thermal convection. In absence of iron solidification inside the liquid core, a dynamo can only be driven by thermal convection if the heat flux out of the core exceeds that of adiabatic cooling [*Stevenson*, 2001]. The ability of the core too cool is controlled by the overlying mantle. *Nimmo and Stevenson* [2000] have shown that an early episode of plate tectonics would rapidly cool the mantle and allows enough heat to flow out of the core to drive thermal convection in the core. However, surface geologic evidence of plate tectonics is still missing and present-day crustal thickness estimates and monotonically decreasing rates of crustal production are more in favor of a planet operating in the stagnant lid regime over the whole planet's history [*Breuer and Spohn*, 2003]. In order to reconcile the planets stagnant lid cooling with the early dynamo episode an early superheated core compared to the mantle [e.g. *Breuer and Spohn*, 2003; *Williams and Nimmo*, 2004] is invoked.

The data do not allow to further constrain the range of possible crust densities and thicknesses compared to the most recent estimates [*Wieczorek and Zuber*, 2004]. The result also shows that neither can any of the five mineralogies be excluded nor can the range of possible mantle temperatures be reduced. Even if the core sulfur composition is fixed to the widely presumed 14wt% and the bulk Fe/Si set to about the chondritic value of 1.7. This is in contrast to previous published results who claimed that a DW84 mantle model together with 14wt% of sulfur inside the core cannot fulfill to the moment of inertia constraint and have a chondritic Fe/Si [*Sohl and Spohn*, 1997; *Bertka and Fei*, 1998]. A chondritic Fe/Si can, however, be obtained if the core contains other additionally light elements like FeH [*Zharkov and Gudkova*, 2005]. The differences between our results and those obtained by the above authors are mainly a consequence of their usage of solid core

material properties to describe the liquid part of the core.

The uncertainties on the core size and on the core sulfur concentration estimate can be further reduced if the precision on the determination on k_2 is increased. However, even if the value of k_2 were known with a negligible uncertainty the uncertainty on the estimated core size and the core light element concentration would remain appreciable. This is mainly due to the large range of plausible mantle temperatures and to the large number of plausible mantle mineralogies and to a lesser extend to the uncertainties associated to the crust density and thickness. Additionally, if other light elements together with sulfur are considered for the core then the uncertainties on the core composition will even be larger. The only way to get definite and precise estimates of the core size and the crust thickness that are independent on the mantle mineralogy and temperature, is through seismic sounding. Additionally, from the seismic velocities, the mineralogy and the temperature of the mantle and the composition of the core can be further constrained.

The first part of the thesis was mostly dedicated to construct an interior structure model and estimate from recent geodetic data about Mars the size and composition of the core by assuming a set of plausible mantle mineralogies and two temperature end-members. The aim of the second part of this thesis was to assess if the mantle mineralogy and temperature profile can be inferred by combining the profiles of the electrical conductivity and the bulk sound velocity with the moment of inertia of the planet shell. We have build a model that relates the mantle temperature, the mantle mineralogy, and the density of the crust to the data. For calculating the bulk sound velocity and the density of the mantle, we have applied the mantle model developed in the first part. Since the model relating the parameter is highly non-linear we have used an inversion method that is based on Bayesian inference.

In order to reduce the number of parameters we have introduced an empirical relation between the fractions of minerals that parameterize the mineralogy of the mantle. By assuming realistic uncertainties on the data, we have shown that the temperature and the mineralogy of the mantle can be estimated from data with very high confidence. We have also shown that if the empirical relations are not used all parameters characterizing the mantle mineralogy and the temperature can be estimated with about the same confidence if the uncertainties on the seismic sound velocity are two times smaller.

Bibliography

Acuña, M. H., J. E. P. Connerney, N. F. Ness, R. P. Lin, D. Mitchell, C. W. Carlson, J. McFadden, K. A. Anderson, H. Reme, C. Mazelle, D. Vignes, P. Wasilewski, and P. Cloutier (1999), Global Distribution of Crustal Magnetization Discovered by the Mars Global Surveyor MAG/ER Experiment, *Science*, *284*, 790–793, doi: 10.1126/science.284.5415.790.

Ahrens, T. J., K. G. Holland, and G. Q. Chen (2002), Phase diagram of iron, revised-core temperatures, *Geophys. Res. Lett.*, *29*, 54–1, doi: 10.1029/2001GL014350.

Aki, K., and P. G. Richards (2002), *Quantitative Seismology*, 2nd ed., University Science Books, Sausalito, California.

Anderson, D. L. (1988), Temperature and pressure derivatives of elastic constants with application to the mantle, *J. Geophys. Res.*, *93*(B5), 4688–4700, doi: 10.1029/JB093iB05p04688.

Anderson, D. L. (2005), *New Theory of the Earth*, Cambridge University Press, New York, doi: 10.2277/0521849594.

Anderson, J. D., G. Colombo, P. B. Espsitio, E. L. Lau, and G. B. Trager (1987), The mass, gravity field, and ephemeris of Mercury, *Icarus*, *71*, 337–349, doi: 10.1016/0019-1035(87)90033-9.

Anderson, O. L. (1979), Evidence supporting the approximation $\gamma\rho$=const for the Grüneisen parameter of the earth's lower mantle, *J. Geophys. Res.*, *84*, 3537–3542, doi: 10.1029/JB084iB07p03537.

Anderson, O. L. (2000), The Grüneisen ratio for the last 30 years, *Geophys. J. Int.*, *143*, 279–294, doi: 10.1046/j.1365-246X.2000.01266.x.

Anderson, O. L., and K. Zou (1989), Formulation of the thermodynamic functions for mantle minerals: MgO as an example, *Physics and Chemistry of Minerals*, *16*, 642–648, doi: 10.1007/BF00223312.

Anderson, W. W., and T. J. Ahrens (1994), An equation of state for liquid iron and implications for the Earth's core, *J. Geophys. Res.*, *99*, 4273–4284, doi: 10.1029/93JB03158.

Armitage, P. J. (2009), *Astrophysics of Planet Formation*, Cambridge University Press.

Backus, G. (1986), Poloidal and toroidal fields in geomagnetic field modeling, *Reviews of Geophysics*, *24*, 75–109.

Baker, R., and G. Christakos (2007), Revisiting Prior distributions, Part I: Priors based on a physical invariance principle, *Stochastic Environmental Research and Risk Assessment (SERRA)*, *21*(4), 427–434, doi: 10.1007/s00477-006-0075-0.

Balog, P. S., R. A. Secco, D. C. Rubie, and D. J. Frost (2003), Equation of state of liquid Fe – 10wt%S: Implications for the metallic cores of planetary bodies, *J. Geophys. Res. (Solid Earth)*, *108*, doi: 10.1029/2001JB001646.

Banks, R. J. (1972), The overall conductivity distribution of the Earth., *J.Geomag.Geoelectr.*, *24*, 337–351.

Barriot, J.-P., V. Dehant, W. Folkner, J.-C. Cerisier, A. Ribes, J. Benoist, T. van Hoolst, P. Defraigne, R. Warnant, R. A. Preston, L. Romans, S. Wu, and A. W. Wernik (2001), The Netlander ionosphere and geodesy experiment, *Advances in Space Research*, *28*, 1237–1249.

Basilevsky, A. T., and J. W. Head (1994), Global stratigraphy of Venus: analysis of a random thirty-six test areas, *Earth, Moon, and Planets*, *66*, 285–336, doi: 10.1007/BF00579467.

Berlekamp, E. R. (1968), *Algorithmic Coding Theory*, chap. 7, McGraw-Hill, New York.

Bertka, C. M., and Y. Fei (1997), Mineralogy of the Martian interior up to core-mantle boundary pressures, *J. Geophys. Res.*, *102*, 5251–5264, doi: 10.1029/96JB03270.

Bertka, C. M., and Y. Fei (1998), Density profile of an SNC model Martian interior and the moment-of-inertia factor of Mars, *Earth Planet. Sci. Lett.*, *157*, 79–88, doi: 10.1016/S0012-821X(98)00030-2.

Besag, J., P. Green, D. Higdon, and K. Mengersen (1995), Bayesian computation and stochastic systems (with discussion), *Statistical Science*, *10*, 3–66.

Biot, M. A. (1954), Theory of Stress-Strain Relations in Anisotropic Viscoelasticity and Relaxation Phenomena, *Journal of Applied Physics*, *25*, 1385–1391.

Boehler, R. (1992), Melting of the Fe – FeO and the Fe – FeS systems at high pressure: Constraints on core temperatures, *Earth Planet. Sci. Lett.*, *111*, 217–227, doi: 10.1016/0012-821X(92)90180-4.

Boehler, R. (1996), Fe – FeS eutectic temperatures to 620 kbar, *Phys. Earth Planet. Inter.*, *96*, 181–186, doi: 10.1016/0031-9201(96)03150-0.

Boehler, R., N. von Bargen, and A. Chopelas (1990), Melting, thermal expansion, and phase transitions of iron at high pressures, *J. Geophys. Res.*, *95*, 21,731–21,736, doi: 10.1029/JB095iB13p21731.

Box, G. E. P., and M. E. Muller (1958), A Note on the Generation of Random Normal Deviates, *The Annals of Mathematical Statistics*, *29*(2), 610–611, doi: 10.1214/aoms/1177706645.

Brémaud, P. (1999), *Markov Chains Gibbs Fields, Monte Carlo Simulation, and Queues*, *Texts in Applied Mathematics*, vol. 31, Springer-Verlag, New York.

Brett, R., and P. M. Bell (1969), Melting relations in the Fe-rich portion of the system Fe-FeS at 30 kb pressure, *Earth Planet. Sci. Lett.*, *6*, 479–482, doi: 10.1016/0012-821X(69)90119-8.

Breuer, D., and T. Spohn (2003), Early plate tectonics versus single-plate tectonics on Mars: Evidence from magnetic field history and crust evolution, *J. Geophys. Res. (Planets)*, *108*, 8.1–8.13, doi: 10.1029/2002JE001999.

Burbine, T. H., and K. M. O'Brien (2004), Determining the possible building blocks of the Earth and Mars, *Meteoritics and Planetary Science*, *39*, 667–681, doi: 10.1111/j.1945-5100.2004.tb00110.x.

Cagniard, L. (1953), Basic theory of the magneto-telluric method of geophysical prospecting, *Geophysics*, *18*(3), 605–635.

Callen, B. H. (1985), *Thermodynamics and an Introduction to Thermostatistics*, second edition ed., Wiley & Sons.

Cammarano, F., S. Goes, P. Vacher, and D. Giardini (2003), Inferring upper-mantle temperatures from seismic velocities, *Phys. Earth Planet. Inter.*, *138*, 197–222, doi: 10.1016/S0031-9201(03)00156-0.

Chambers, J. E. (2004), Planetary accretion in the inner solar system, *Earth Planet. Sci. Lett.*, *223*(3-4), 241–252.

Chen, B., L. Gao, K. Funakoshi, and J. Li (2007), Thermal expansion of iron-rich alloys and implications for the Earth's core, *PNAS*, p. 0610474104, doi: 10.1073/pnas.0610474104.

Chen, B., J. Li, and S. A. I. Hauck (2008), Non-ideal liquidus curve in the Fe-S system and Mercury's snowing core, *Geophys. Res. Lett.*, *35*, L07,201, doi: 10.1029/2008GL033311.

Chudinovskikh, L., and R. Boehler (2007), Eutectic melting in the system Fe-S to 44 GPa, *Earth Planet. Sci. Lett.*, *257*(1-2), 97–103, doi: 10.1016/j.epsl.2007.02.024.

Cowles, M. K., and B. P. Carlin (1996), Markov Chain Monte Carlo Convergence Diagnostics: A Comparative Review, *Journal of the American Statistical Association*, *91*(434), 883–904.

Dahlen, F. A., and J. Tromp (1998), *Theoretical Global Seismology*, Princeton University Press, Princeton, New Jersey, Princeton, New Jersey.

de Pater, I., and J. J. Lissauer (2001), *Planetary Sciences*, Cambridge University Press, Cambridge.

DeHoff, R. (2006), *Thermodynamics In Materials Science*, CRC Press, Taylor & Francis, Boca Raton.

Denis, C., M. Amalvict, Y. Rogister, and S. Tomecka-Suchoń (1998), Methods for computing internal flattening, with applications to the Earth's structure and geodynamics, *Geophys. J. Int.*, *132*, 603–642, doi: 10.1046/j.1365-246X.1998.00449.x.

Dreibus, G., and H. Wänke (1985), Mars, a volatile-rich planet, *Meteoritics*, *20*, 367–381.

Dziewonski, A. M., and D. L. Anderson (1981), Preliminary reference Earth model, *Phys. Earth Planet. Inter.*, *25*, 297–356, doi: 10.1016/0031-9201(81)90046-7.

Esposito, P. B., W. B. Banerdt, G. F. Lindal, W. L. Sjogren, M. A. Slade, B. G. Bills, D. E. Smith, and G. Balmino (1992), *Gravity and topography*, pp. 209–248, Mars.

Falzone, A. J., and F. D. Stacey (1980), Second-order elasticity theory: Explanation for the high poisson's ratio of the inner core, *Physics of the Earth and Planetary Interiors*, *21*, 371–377, doi: 10.1016/0031-9201(80)90140-5.

Fei, Y., C. M. Bertka, and L. W. Finger (1997), High-Pressure Iron-Sulfur Compound, Fe_3S_2, and Melting Relations in the Fe – FeS System, *Science*, *275*, 1621 – 1623, doi: 10.1126/science.275.5306.1621.

Fei, Y., J. Li, C. M. Bertka, and C. T. Prewitt (2000), Structure type and bulk modulus of Fe_3S, a new iron-sulfur compound, *American Mineralogist*, *85*(11-12), 1830–1833.

Flegal, J. M., M. Haran, and G. L. Jones (2007), Markov chain Monte Carlo: Can we trust the third significant figure?

Folkner, W. M., C. F. Yoder, D. N. Yuan, E. M. Standish, and R. A. Preston (1997), Interior Structure and Seasonal Mass Redistribution of Mars from Radio Tracking of Mars Pathfinder, *Science*, *278*, 1749–+.

Ganapathy, R., and E. Anders (1974), Bulk compositions of the moon and earth, estimated from meteorites, in *Lunar and Planetary Science Conference*, *Lunar and Planetary Science Conference*, vol. 5, pp. 1181–1206.

Gelman, A., J. B. Carlin, H. S. Stern, and D. B. Rubin (2003), *Bayesian Data Analysis*, Chapman & Hall/CRC, Boca Raton.

Geman, S., and D. Geman (1984), Stochastic relaxation, Gibbs distributions, and the Bayesian restoration of images., *IEEE Transactions on Pattern Analysis and Machine Intelligence*, *6*(6), 721–741.

Ghiorso, M. S. (2004), An equation of state for silicate melts. I. Formulation of a general model, *American Journal of Science*, *304*(8-9), 637–678, doi: 10.2475/ajs.304.8-9.637.

Gilbert, F., and G. Backus (1968), Elastic-gravitational vibrations of a radially stratified sphere, in *Dynamics of Stratified Solids*, edited by G. Hermann, pp. 82–95, American Society of Mechanical Engineers, New York.

Häggström, O. (2002), *Finite Markov Chains and Algorithmic Applications*, no. 52 in London Mathematical Society Student Texts, Cambridge University Press, Cambridge.

Hammersley, J. M., and D. C. Handscomb (1964), *Monte Carlo methods*, Wiley, New York.

Harri, A.-M., O. Marsal, P. Lognonne, G. W. Leppelmeier, T. Spohn, K.-H. Glassmeier, F. Angrilli, W. B. Banerdt, J. P. Barriot, J.-L. Bertaux, J. J. Berthelier, S. Calcutt, J. C. Cerisier, D. Crisp, V. Dehant, D. Giardini, R. Jaumann, Y. Langevin, M. Menvielle, G. Musmann, J. P. Pommereau, S. di Pippo, D. Guerrier, K. Kumpulainen, S. Larsen, A. Mocquet, J. Polkko, J. Runavot, W. Schumacher, T. Siili, J. Simola, and J. E. Tillman (1999), Network science landers for Mars, *Advances in Space Research*, *23*, 1915–1924.

Hastings, W. K. (1970), Monte Carlo sampling methods using Markov chains and their applications., *Biometrika*, *57*, 97–109, doi: 10.1093/biomet/57.1.97.

Hauck, S. A., S. C. Solomon, and A. Smither (2007), Predicted recovery of Mercury's internal structure by MESSENGER, *Geophys. Res. Lett.*, *34*, L18201, doi: 10.1029/2007GL030793.

Helffrich, R., George, and J. Wood, Bernard (2001), The Earth's mantle, *Nature*, *412*(6846), 501–507, doi: 10.1038/35087500.

Hirose, K. (2002), Phase transitions in pyrolitic mantle around 670-km depth: Implications for upwelling of plumes from the lower mantle, *J. Geophys. Res. (Solid Earth)*, *107*, 2078–+, doi: 10.1029/2001JB000597.

Irifune, T., N. Nishiyama, K. Kuroda, T. Inoue, M. Isshiki, W. Utsumi, K.-I. Funakoshi, S. Urakawa, T. Uchida, T. Katsura, and O. Ohtaka (1998), The Postspinel Phase Boundary in Mg2SiO4 Determined by in Situ X-ray Diffraction, *Science*, *279*, 1698–1700, doi: 10.1126/science.279.5357.1698.

Ito, E., and E. Takahashi (1989), Postspinel transformations in the system $Mg_2SiO_4 - Fe_2SiO_4$ and some geophysical implications, *J. Geophys. Res. (Solid Earth)*, *94*, 10,637–10,646, doi: 10.1029/JB094iB08p10637.

Jackson, I. (1998), Elasticity, composition and temperature of the Earth's lower mantle: a reappraisal, *Geophys. J. Int.*, *134*, 291–311, doi: 10.1046/j.1365-246x.1998.00560.x.

Jaynes, E. T. (2003), *Probability Theory: The Logic of Science*, Cambridge University Press, Cambridge.

Jones, G. L., M. Haran, B. S. Caffo, and R. Neath (2006), Fixed-Width Output Analysis for Markov Chain Monte Carlo, *Journal of the American Statistical Association*, *101*(476), 1537–1547, doi: 10.1198/016214506000000492.

Kaiura, G. H., and J. M. Toguri (1979), Densities of the Molten FeS, $FeS - Cu_2S$ and $Fe - S - O$ Systems Utilizing a Bottom-Balance Archimedean Technique, *Canadian Metallurgical Quarterly*, *18*(2), 155–164.

Kasting, J. F. (1988), Runaway and moist greenhouse atmospheres and the evolution of Earth and Venus, *Icarus*, *74*(3), 472 – 494, doi: 10.1016/0019-1035(88)90116-9.

Katsura, T., H. Yamada, T. Shinmei, A. Kubo, S. Ono, M. Kanzaki, A. Yoneda, M. J. Walter, E. Ito, S. Urakawa, K. Funakoshi, and W. Utsumi (2003), Post-spinel transition in Mg_2SiO_4 determined by high P-T in situ X-ray diffractometry, *Phys. Earth Planet. Inter.*, *136*, 11–24, doi: 10.1016/S0031-9201(03)00019-0.

Kennett, B. L. N., E. R. Engdahl, and R. Buland (1995), Constraints on seismic velocities in the Earth from traveltimes, *Geophysical Journal International*, *122*, 108–124, doi: 10.1111/j.1365-246X.1995.tb03540.x.

Khan, A., and J. A. D. Connolly (2008), Constraining the composition and thermal state of Mars from inversion of geophysical data, *J. Geophys. Res. (Planets)*, *113*, E07,003, doi: 10.1029/2007JE002996.

Kittel, C. (2004), *Introduction to Solid State Physics*, 8th ed., Wiley & Sons, New York.

Konopliv, A. S., and C. F. Yoder (1996), Venusian k_2 tidal Love number from Magellan and PVO tracking data, *Geophys. Res. Lett.*, *23*, 1857–1860, doi: 10.1029/96GL01589.

Konopliv, A. S., C. F. Yoder, E. M. Standish, D.-N. Yuan, and W. L. Sjogren (2006), A global solution for the Mars static and seasonal gravity, Mars orientation, Phobos and Deimos masses, and Mars ephemeris, *Icarus*, *182*, 23–50, doi: 10.1016/j.icarus.2005.12.025.

Konopliv, A. S., S. W. Asmar, S. M. Foiles, Ö. Karatekin, D. C. Nunes, S. E. Smrekar, C. F. Yoder, and M. T. Zuber (2011), Mars High Resolution Gravity Fields from MRO, Mars Seasonal Gravity, and Other Dynamical Parameters., *Icarus*, *211*(1), 401 – 428, doi: 10.1016/j.icarus.2010.10.004.

Koot, L., A. Rivoldini, O. de Viron, and V. Dehant (2008), Estimation of Earth interior parameters from a Bayesian inversion of very long baseline interferometry nutation time series, *J. Geophys. Res. (Solid Earth)*, *113*, B08414, doi: 10.1029/2007JB005409.

Kuwayama, Y., and K. Hirose (2004), Phase relations in the system Fe − FeSi at 21 GPa, *American Mineralogist*, *89*(2-3), 273–276.

Lambeck, K., C. Smither, and P. Johnston (1998), Sea-level change, glacial rebound and mantle viscosity fornorthern Europe, *Geophys. J. Int.*, *134*, 102–144, doi: 10.1046/j.1365-246x.1998.00541.x.

Le Mouël, J.-L. (1976), *Traité de géophysique interne*, vol. 2, chap. 29, Dunod, Paris.

Li, J., and C. B. Agee (2001), Element partitioning constraints on the light element composition of the Earth's core, *Geophys. Res. Lett.*, *28*, 81–84, doi: 10.1029/2000GL012114.

Li, J., Y. Fei, H. K. Mao, K. Hirose, and S. R. Shieh (2001), Sulfur in the Earth's inner core, *Earth Planet. Sci. Lett.*, *193*, 509–514, doi: 10.1016/S0012-821X(01)00521-0.

Liu, J. S. (2001), *Monte Carlo Strategies in Scientific Computing*, Springer Series in Statistics, Springer Verlag, New York.

Lodders, K., and B. Fegley (1997), An Oxygen Isotope Model for the Composition of Mars, *Icarus*, *126*, 373–394, doi: 10.1006/icar.1996.5653.

Lognonné, P., D. Giardini, B. Banerdt, J. Gagnepain-Beyneix, A. Mocquet, T. Spohn, J. F. Karczewski, P. Schibler, S. Cacho, W. T. Pike, C. Cavoit, A. Desautez, M. Favède, T. Gabsi, L. Simoulin, N. Striebig, M. Campillo, A. Deschamp, J. Hinderer, J. J. Lévéque, J. P. Montagner, L. Rivéra, W. Benz, D. Breuer, P. Defraigne, V. Dehant, A. Fujimura, H. Mizutani, and J. Oberst (2000), The NetLander very broad band seismometer, *Planet. Space Sci.*, *48*, 1289–1302, doi: 10.1016/S0032-0633(00)00110-0.

Longman, I. M. (1963), A Green's Function for Determining the Deformation of the Earth under Surface Mass Loads, 2, Computations and Numerical Results, *J. Geophys. Res.*, *68*, 485–+.

Love, A. E. H. (1911), *Some Problems of Geodynamics*, Cambridge University Press, Cambridge.

Margot, J. L., S. J. Peale, R. F. Jurgens, M. A. Slade, and I. V. Holin (2007), Large Longitude Libration of Mercury Reveals a Molten Core, *Science*, *316*(5825), 710–714, doi: 10.1126/science.1140514.

Marsaglia, G., and W. W. Tsang (2000), The Ziggurat Method for Generating Random Variables, *Journal of Statistical Software*, *5*(8), 1–7.

Marty, J. C., G. Balmino, P. Rosenblatt, J. Duron, S. Le Maistre, A. Rivoldini, V. Dehant, and T. Van Hoolst (2009), Martian gravity field model and its time variations from MGS and ODYSSEY data, *Planetary and Space Science*, *57*(3), 350–363, doi: 10.1016/j.pss.2009.01.004.

Massey, J. L. (1969), Shift-register synthesis and bch decoding., *IEEE Trans. Information Th.*, *15*, 122–127.

Matas, J., J. Bass, Y. Ricard, E. Mattern, and M. S. T. Bukowinski (2007), On the bulk composition of the lower mantle: predictions and limitations from generalized inversion of radial seismic profiles, *Geophysical Journal International*, *170*, 764–780, doi: 10.1111/j.1365-246X.2007.03454.x.

Matsumoto, M., and T. Nishimura (1998), Mersenne Twister: A 623-dimensionally equidistributed uniform pseudorandom number generator, *ACM Trans. on Modeling and Computer Simulation*, *8*(1), 3–30.

McDonough, W. F., and S.-s. Sun (1995), The composition of the Earth, *Chemical Geology*, *120*, 223–254, doi: 10.1016/0009-2541(94)00140-4.

McSween, H. Y., Jr. (1994), What we have learned about Mars from SNC meteorites, *Meteoritics*, *29*, 757–779.

McSween, H. Y., Jr. (2003), *Treatise on Geochemistry*, vol. 1, chap. Mars, pp. 601–621, Elsevier, doi: 10.1016/B0-08-043751-6/01072-0.

Menvielle, M., G. Musmann, F. Kuhnke, J.-J. Berthelier, K.-H. Glassmeier, M. H. Mandea, U. Motschmann, K. Pajunpaa, J.-L. Pinçon, F. Primdahl, and L. Szarka (2000), Contribution of magnetic measurements onboard NetLander to Mars exploration, *Planet. Space Sci.*, *48*, 1231–1247, doi: 10.1016/S0032-0633(00)00106-9.

Metropolis, N., A. W. Rosenbluth, M. N. Rosenbluth, A. H. Teller, and E. Teller (1953), Equations of state calculations by fast computing machines., *Journal of Chemical Physics*, *21*, 1087–1091.

Metropolis, N. C., and S. M. Ulam (1949), The Monte-Carlo method, *J. Amer. Stat. Assoc.*, *44*, 335–341.

Meyn, S. P., and R. L. Tweedie (1993), *Markov Chains and Stochastic Stability*, Springer-Verlag, London.

Mocquet, A., P. Vacher, O. Grasset, and C. Sotin (1996), Theoretical seismic models of Mars: the importance of the iron content of the mantle, *Planet. Space Sci.*, *44*, 1251–1268, doi: 10.1016/S0032-0633(96)00086-4.

Mohapatra, R. K., and S. V. S. Murty (2003), Precursors of Mars: Constraints from nitrogen and oxygen isotopic compositions of martian meteorites, *Meteoritics and Planetary Science*, *38*, 225–242, doi: 10.1111/j.1945-5100.2003.tb00261.x.

Morard, G., C. Sanloup, G. Fiquet, M. Mezouar, N. Rey, R. Poloni, and P. Beck (2007), Structure of eutectic Fe-FeS melts to pressures up to 17 GPa: Implications for planetary cores, *Earth Planet. Sci. Lett.*, *263*(1-2), 128–139, doi: 10.1016/j.epsl.2007.09.009.

Morard, G., D. Andrault, N. Guignot, C. Sanloup, M. Mezouar, S. Petitgirard, and G. Fiquet (2008), In situ determination of $Fe-Fe_3S$ phase diagram and liquid structural properties up to 65 GPa, *Earth Planet. Sci. Lett.*, *272*(3-4), 620–626, doi: 10.1016/j.epsl.2008.05.028.

Morgan, J. W., and E. Anders (1979), Chemical composition of Mars, *Geochimica et Cosmochimica Acta*, *43*, 1601–1610, doi: 10.1016/0016-7037(79)90180-7.

Neal, R. M. (2005), The short-cut metropolis method, doi: arXiv:math/0508060v1.

Neumann, G. A., M. T. Zuber, M. A. Wieczorek, P. J. McGovern, F. G. Lemoine, and D. E. Smith (2004), Crustal structure of Mars from gravity and topography, *J. Geophys. Res. (Planets)*, *109*, E08,002, doi: 10.1029/2004JE002262.

Nimmo, F. (2007), *Core Dynamics*, *Treatise on Geophysics*, vol. 8, chap. Energetics of the Core, Elsevier, Amsterdam, doi: 10.1016/B978-044452748-6.00128-0.

Nimmo, F., and D. J. Stevenson (2000), Influence of early plate tectonics on the thermal evolution and magnetic field of Mars, *J. Geophys. Res.*, *105*, 11,969–11,980, doi: 10.1029/1999JE001216.

Nishida, K., H. Terasaki, E. Ohtani, and A. Suzuki (2008), The effect of sulfur content on density of the liquid Fe-S at high pressure, *Physics and Chemistry of Minerals*, *35*(7), 417–423, doi: 10.1007/s00269-008-0236-4.

Oates, W. A., and T. B. Flanagan (1981), Thermodynamic properties of regular interstitial solutions, *Journal of Materials Science*, *16*(12), 3235–3243.

Olsen, N. (1998), The electrical conductivity of the mantle beneath Europe derived from C-responses from 3 to 720 hr, *Geophysical Journal International*, *133*, 298–308, doi: 10.1046/j.1365-246X.1998.00503.x.

Papoulis, A. (2002), *Probability, random variables and stochastic processes*, 4th ed., McGraw-Hill, New York.

Peltier, W. R., P. Wu, and D. A. Yuen (1981), *The Viscosities of the Planetary Mantle*, *Geodynamics Series*, vol. 4, pp. 59–77, AGU, Washington, D.C.

Peskun, P. H. (1973), Optimum Monte-Carlo sampling using Markov chains, *Biometrika*, *60*, 607–612.

Poirier, J.-P. (1994), Light elements in the Earth's outer core: A critical review, *Phys. Earth Planet. Inter.*, *85*, 319–337, doi: 10.1016/0031-9201(94)90120-1.

Poirier, J.-P. (2000), *Introduction to the Physics of the Earth's Interior*, Cambridge University Press, Cambridge.

Poirier, J. P., and G. D. Price (1992), Dislocation melting of metals, *Physics of the Earth and Planetary Interiors*, *69*, 153–162, doi: 10.1016/0031-9201(92)90131-E.

Propp, J. G., and D. B. Wilson (1996), Exact Sampling with Coupled Markov Chains and Applications to Statistical Mechanics, *Random Structures and Algorithms*, *9*(1&2), 223–252.

Ranalli, G. (1987), *Rheology of the Earth*, 2nd ed., Chapman & Hall, London.

Righter, K., and M. J. Drake (1996), Core Formation in Earth's Moon, Mars, and Vesta, *Icarus*, *124*, 513–529, doi: 10.1006/icar.1996.0227.

Rivoldini, A., T. Van Hoolst, and O. Verhoeven (2009), The interior structure of Mercury and its core sulfur content, *Icarus*, *201*(1), 12–30, doi: 10.1016/j.icarus.2008.12.020.

Roberts, P. (2007), *Core Dynamics*, *Treatise on Geophysics*, vol. 8, chap. Theory of the Geodynamo, Elsevier, Amsterdam, doi: 10.1016/B978-044452748-6.00133-4.

Rubie, D. C., C. K. Gessmann, and D. J. Frost (2004), Partitioning of oxygen during core formation on the Earth and Mars, *Nature*, *429*, 58–61, doi: 10.1038/nature02473.

Sabadini, R., and B. Vermeersen (2004), *Global Dynamics of the Earth: Applications of Normal Mode Relaxation Theory to Solid-Earth Geophysics*, *Modern Approaches in Geophysics*, vol. 20, Kluwer Academic Publishers, Dordrecht.

Sanloup, C., and Y. Fei (2004), Closure of the Fe − S − Si liquid miscibility gap at high pressure, *Phys. Earth Planet. Inter.*, *147*, 57–65, doi: 10.1016/j.pepi.2004.06.008.

Sanloup, C., A. Jambon, and P. Gillet (1999), A simple chondritic model of Mars, *Phys. Earth Planet. Inter.*, *112*, 43–54, doi: 10.1016/S0031-9201(98)00175-7.

Sanloup, C., F. Guyot, P. Gillet, G. Fiquet, M. Mezouar, and I. Martinez (2000), Density measurements of liquid Fe-S alloys at high-pressure, *Geophys. Res. Lett.*, *27*, 811–814, doi: 10.1029/1999GL008431.

Seagle, C. T., A. J. Campbell, D. L. Heinz, G. Shen, and V. B. Prakapenka (2006), Thermal equation of state of Fe3S and implications for sulfur in Earth's core, *J. Geophys. Res.*, *111*, 6209, doi: 10.1029/2005JB004091.

Seidelmann, P. K., V. K. Abalakin, M. Bursa, M. E. Davies, C. de Bergh, J. H. Lieske, J. Oberst, J. L. Simon, E. M. Standish, P. Stooke, and P. C. Thomas (2002), Report of the IAU/IAG Working Group on Cartographic Coordinates and Rotational Elements of the Planets and Satellites: 2000, *Celestial Mechanics and Dynamical Astronomy*, *82*, 83–111.

Shen, G., H.-k. Mao, R. J. Hemley, T. S. Duffy, and M. L. Rivers (1998), Melting and crystal structure of iron at high pressures and temperatures, *Geophys. Res. Lett.*, *25*(3), 373–376, doi: 10.1029/97GL03776.

Shen, G., V. B. Prakapenka, M. L. Rivers, and S. R. Sutton (2004), Structure of Liquid Iron at Pressures up to 58GPa, *Physical Review Letters*, *92*(18), 185,701–+, doi: 10.1103/PhysRevLett.92.185701.

Simpson, F., and K. Bahr (2005), *Practical Magnetotellurics*, Cambridge University Press, Cambridge, doi: 10.2277/0521817277.

Sivia, D., and J. Skilling (2006), *Data Analysis: A Bayesian Tutorial*, 2nd ed., Oxford University Press, New York.

Sohl, F., and G. Schubert (2007), *Planets and Moons*, *Treatise on Geophysics*, vol. 10, chap. Interior Structure, Composition, and Mineralogy of the Terrestrial Planets, Elsevier B.V., doi: 10.1016/B978-044452748-6.00153-X.

Sohl, F., and T. Spohn (1997), The interior structure of Mars: Implications from SNC meteorites, *J. Geophys. Res.*, *102*, 1613–1636, doi: 10.1029/96JE03419.

Sohl, F., G. Schubert, and T. Spohn (2005), Geophysical constraints on the composition and structure of the Martian interior, *J. Geophys. Res. (Planets)*, *110*(E9), 12,008–+, doi: 10.1029/2005JE002520.

Sokal, A. D. (1996), Monte Carlo methods in statistical mechanics: Foundations and new algorithms, in *Cargèse Summer School on "Functional Integration: Basics and Applications"*, Cargèse Summer School.

Solomon, S. C. (2003), Mercury: the enigmatic innermost planet, *Earth Planet. Sci. Lett.*, *216*, 441–455, doi: 10.1016/S0012-821X(03)00546-6.

Srivastava, S. P. (1966), Theory of the magnetotelluric method for a spherical conductor, *Geophys. J. Roy. Astron.*, *11*, 373–387.

Stacey, F. D. (1995), Theory of thermal and elastic properties of the lower mantle and core, *Phys. Earth Planet. Inter.*, *89*, 219–245, doi: 10.1016/0031-9201(94)03005-4.

Stacey, F. D., and P. M. Davis (2008), *Physics of the Earth*, 4th ed., Cambridge University Press, New York.

Stevenson, D. J. (2001), Mars' core and magnetism, *Nature*, *412*, 214–219, doi: 10.1038/35084155.

Stewart, A. J., M. W. Schmidt, W. van Westrenen, and C. Liebske (2007), Mars: A New Core-Crystallization Regime, *Science*, *316*, 1323–1325, doi: 10.1126/science.1140549.

Stixrude, L. P. (2007), *Mineral Physics*, *Treatise on Geophysics*, vol. 2, chap. Properties of Rocks and Minerals – Seismic Properties of Rocks and Minerals, and Structure of the Earth, Elsevier, Amsterdam, doi: 10.1016/B978-044452748-6.00042-0.

Takahashi, E. (1990), Speculations on the Archean mantle: Missing link between komatiite and depleted garnet peridotite, *J. Geophys. Res.*, *95*, 15,941–15,954, doi: 10.1029/JB095iB10p15941.

Takeuchi, H., and M. Saito (1972), Seismic surface waves, in *Seismology: Surface Waves and Earth Oscillations*, *Methods In Computational Physics*, vol. 11, edited by B. A. Bolt, pp. 217–295, Academic Press, San Diego, Calif.

Tarantola, A. (2005), *Inverse Problem Theory and Methods for Model Parameter Estimation*, Society for Industrial Mathematics, Philadelphia.

Taylor, G. J., W. Boynton, J. Brückner, H. Wänke, G. Dreibus, K. Kerry, J. Keller, R. Reedy, L. Evans, R. Starr, S. Squyresd, O. Gasnault, S. Maurice, C. d'Uston, P. Englert, J. Dohm, V. Baker, D. Hamara, D. Janes, A. Sprague, K. Kim, and D. Drake (2006), Bulk composition and early differentiation of mars, *J. Geophys. Res. (Planets)*, *111*, doi: 10.1029/2005JE002645.

Tikhonov, A. N. (1950), Determination of the electrical characteristics of the deep strata of the earth's crust, *Dokl. Acad. Nauck. SSR*, *73*, 295–297.

Trampert, J., P. Vacher, and N. Vlaar (2001), Sensitivities of seismic velocities to temperature, pressure and composition in the lower mantle, *Phys. Earth Planet. Inter.*, *124*, 255–267, doi: 10.1016/S0031-9201(01)00201-1.

Tsuno, K., E. Ohtani, and H. Terasaki (2007), Immiscible two-liquid regions in the $Fe-O-S$ system at high pressure: Implications for planetary cores, *Phys. Earth Planet. Inter.*, *160*, 75–85, doi: 10.1016/j.pepi.2006.09.004.

Ulmer, P., and R. Stalder (2001), The $Mg(Fe)SiO_3$ orthoenstatite-clinoenstatite transitions at high pressures and temperatures determined by Raman-spectroscopy on quenched sample, *American Mineralogist*, *86*, 1267–1274.

Urakawa, S., K. Someya, H. Terasaki, T. Katsura, S. Yokoshi, K.-I. Funakoshi, W. Utsumi, Y. Katayama, Y.-I. Sueda, and T. Irifune (2004), Phase relationships and equations of state for FeS at high pressures and temperatures and implications for the internal structure of Mars, *Phys. Earth Planet. Inter.*, *143*, 469–479, doi: 10.1016/j.pepi.2003.12.015.

Vacher, P., and O. Verhoeven (2007), Modelling the electrical conductivity of iron-rich minerals for planetary applications, *Planet. Space Sci.*, *55*(4), 455–466, doi: 10.1016/j.pss.2006.10.003.

Vacher, P., A. Mocquet, and C. Sotin (1998), Computation of seismic profiles from mineral physics: the importance of the non-olivine components for explaining the 660 km depth discontinuity, *Phys. Earth Planet. Inter.*, *106*, 275–298, doi: 10.1016/S0031-9201(98)00076-4.

Van Hoolst, T. (2007), Planets and Moons, in *Treatise on Geophysics*, vol. 10, chap. The rotation of the terrestrial planets, pp. 123–164, ELSEVIER, doi: 10.1007/s11214-007-9202-6.

Van Hoolst, T., and C. Jacobs (2003), Mercury's tides and interior structure, *J. Geophys. Res. (Planets)*, *108*(E11), doi: 10.1029/2003JE002126.

Van Hoolst, T., V. Dehant, F. Roosbeek, and P. Lognonné (2003), Tidally induced surface displacements, external potential variations, and gravity variations on Mars, *Icarus*, *161*, 281–296, doi: 10.1016/S0019-1035(02)00045-3.

van Thienen, P., A. Rivoldini, T. Van Hoolst, and P. Lognonné (2006), A top-down origin for martian mantle plumes, *Icarus*, *185*, 197–210, doi: 10.1016/j.icarus.2006.06.008.

Verhoeven, O., A. Rivoldini, P. Vacher, A. Mocquet, G. Choblet, M. Menvielle, V. Dehant, T. Van Hoolst, J. Sleewaegen, J.-P. Barriot, and P. Lognonné (2005), Interior structure of terrestrial planets: Modeling Mars' mantle and its electromagnetic, geodetic, and seismic properties, *J. Geophys. Res. (Planets)*, *110*(E9), E04,009, doi: 10.1029/2004JE002271.

Verhoeven, O., A. Mocquet, P. Vacher, A. Rivoldini, M. Menvielle, P.-A. Arrial, G. Choblet, P. Tarits, V. Dehant, and T. Van Hoolst (2009), Constraints on thermal state and composition of the Earth's lower mantle from electromagnetic impedances and seismic data, *J. Geophys. Res. (Solid Earth)*, *114*, B03,302, doi: 10.1029/2008JB005678.

Vočadlo, L. (2007), *Mineral Physics*, *Treatise on Geophysics*, vol. 2, chap. Mineralogy of the Earth – The Earth's Core: Iron and Iron Alloys, Elsevier, Amsterdam, doi: 10.1016/B978-044452748-6.00032-8.

Wänke, H., and G. Dreibus (1988), Chemical composition and accretion history of terrestrial planets, *Royal Society of London Philosophical Transactions Series A*, *325*, 545–557.

Watt, J. P., G. F. Davies, and R. J. O'Connell (1976), The elastic properties of composite materials, *Rev. Geophys. Space Phys*, *14*, 541–563.

Weidelt, P. (1972), The inverse problem of geomagnetic induction, *Z. Geophys.*, *38*, 257–289.

Wieczorek, M. A., and M. T. Zuber (2004), Thickness of the Martian crust: Improved constraints from geoid-to-topography ratios, *J. Geophys. Res. (Planets)*, *109*(E18), E01,009, doi: 10.1029/2003JE002153.

Williams, J. P., and F. Nimmo (2004), Thermal evolution of the Martian core: Implications for an early dynamo, *Geology*, *32*(2), 97–100, doi: 10.1130/G19975.1.

Williams, Q. (2009), Bottom-up versus top-down solidification of the cores of small solar system bodies: Constraints on paradoxical cores, *Earth and Planetary Science Letters*, *284*, 564–569, doi: 10.1016/j.epsl.2009.05.019.

Xu, Y., T. J. Shankland, and B. T. Poe (2000), Laboratory-based electrical conductivity in the Earth's mantle, *J. Geophys. Res.*, *105*, 27,865–27,876, doi: 10.1029/2000JB900299.

Yoder, C. F., A. S. Konopliv, D. N. Yuan, E. M. Standish, and W. M. Folkner (2003), Fluid Core Size of Mars from Detection of the Solar Tide, *Science*, *300*, 299–303, doi: 10.1126/science.1079645.

Zhang, L., and Y. Fei (2008), Effect of Ni on $Fe-FeS$ phase relations at high pressure and high temperature, *Earth Planet. Sci. Lett.*, *268*(1-2), 212–218, doi: 10.1016/j.epsl.2008.01.028.

Zharkov, V. N., and T. V. Gudkova (2005), Construction of Martian Interior Model, *Solar System Research*, *39*, 343–373, doi: 10.1007/s11208-005-0049-7.

Zschau, J. (1978), Tidal Friction in the Solid Earth: Loading Tides Versus Body Tides, in *Tidal Friction and the Earth's Rotation*, edited by P. Brosche and J. Suendermann, pp. 62–+.

Zuber, M. T. (2001), The crust and mantle of Mars, *Nature*, *412*, 220–227, doi: 10.1038/35084163.